BRNO UNIVERSITY OF TECHNOLOGY
VYSOKÉ UČENÍ TECHNICKÉ V BRNĚ

FACULTY OF MECHANICAL ENGINEERING
FAKULTA STROJNÍHO INŽENÝRSTVÍ

ENERGY INSTITUTE
ENERGETICKÝ ÚSTAV

INTERNAL FLOW OF SPILL-RETURN PRESSURE-SWIRL ATOMIZERS
VNITŘNÍ PROUDĚNÍ V TLAKOVÝCH VÍŘIVÝCH TRYSKÁCH S OBTOKEM

DOCTORAL THESIS
DIZERTAČNÍ PRÁCE

AUTHOR — Ing. Milan Malý
AUTOR PRÁCE

SUPERVISOR — prof. Ing. Jan Jedelský, Ph.D.
ŠKOLITEL

BRNO 2020

Abstract

Pressure-swirl (PS) atomizers are used in many applications where a large surface area of droplets is needed, or a surface must be coated with a liquid, e.g. combustion, spray cooling or spray coating. Spray characteristics of PS atomizers are strongly linked to their internal flow. Spill-return (SR) atomizers enhance the construction of classic PS atomizers (Simplex) by addition of a passage through which the liquid can be spilled away. It allows regulation of an injection flow rate by spilling out a portion of the liquid from the swirl chamber, while the liquid pressure remains high. This ensures a good atomization quality over a wide flow rate range. The SR atomizers were rarely investigated and their internal flow has not been studied at all. In this thesis, both experimental and numerical approach is used to describe the internal flow pattern of several different SR atomizers. The results are then correlated with measured spray parameters. It shows that the addition of the spill passage strongly affects the internal flow even when the spill-line is closed. In some cases, the air-core does not form at all and destabilizes the discharged liquid, which results in the unstable spray. Off-axial SL orifices generate and stabilize the air-core, which leads to the regular formation of a liquid sheet and a high-quality spray. Nevertheless, some configurations changed the breakup nature of the liquid sheet and consequently the spray quality. Moreover, the turn-down ratio of the liquid supply rate and spray stability depend on the distance of the SL orifices from the swirl chamber centreline. Finally, an inviscid analysis of the internal flow, originally derived for the Simplex atomizers, was modified and applied to the SR atomizers. Using this approach, a theoretical prediction of the discharge coefficient and the air-core diameter was derived with spill-to-feed ratio (*SFR*) as the variable. Also, the empirical correlations, originally established for the Simplex type, were transformed to the SR atomizer. This thesis brings a new insight into the understanding of the internal flow of SR atomizers and its results can be directly used by engineers in the design process of the atomizer.

Key words

Atomizer, pressure-swirl, spill-return, spray, intern flow, air-core, liquid sheet

Abstrakt

Tlakové vířivé trysky (TVT) jsou používané v mnoha aplikacích, kde je potřebná velká plocha kapek nebo kde povrch musí být nanesen kapalinou, např. spalování, sprejové chlazení nebo nanášení barev. Parametry spreje z TVT jsou úzce spojené s jejich vnitřním prouděním. Obtokové trysky vylepšují koncepci klasických TVT přítomností otvoru, skrz který může kapalina odtékat zpět do nádrže. Díky této koncepci je možné regulovat vstřikovací množství kapaliny změnou průtoku tímto otvorem, zatímco se ve vířivé komůrce udržuje vysoký tlak, který zaručí dobrou kvalitu spreje. Obtokové trysky byly historicky málo prozkoumány a jejich vnitřní proudění nebylo studováno téměř vůbec. V této práci je popsáno vnitřní proudění několika obtokových trysek jak experimentálně, tak numericky. Tato data jsou následně korelována s měřenými vlastnostmi spreje. Výsledky ukazují, že přidání obtokového otvoru silně ovlivní vnitřní proudění i v případech, kdy obtokem neproudí žádná kapalina. V některých případech se vůbec nezformuje vzdušné jádro a tím se destabilizuje výtok z trysky, čímž vznikne nestabilní sprej. Mimoosé obtokové otvory generují a stabilizují vzdušné jádro, což pomáhá formovat kapalinovou stěnu a vysoce kvalitní sprej. Nicméně některé konfigurace změnily charakter rozpadu kapalinové stěny, což se projevilo i na kvalitě spreje. Navíc regulační schopnost a stabilita spreje závisí na vzdálenosti obtokových otvorů od osy vířivé komůrky. Na závěr byla upravena neviskózní teorie, která analyticky popisuje vnitřní proudění v TVT, tak aby byla aplikovatelná i na obtokové trysky. Pomocí tohoto přístupu byla odvozena teoretická predikce výtokového součinitele a velikosti vzdušného jádra v závislosti na obtokovém poměru (*SFR*). Zároveň byly pro obtokové trysky upraveny empirické korelace původně odvozené pro TVT. Tato práce přináší nový vhled k porozumění vnitřního proudění obtokových trysek a její výsledky najdou uplatnění při jejich návrhu.

Klíčová slova

Atomizér, tryska, tlaková vířivá, obtoková, sprej, vnitřní proudění, vzdušné jádro, kapalinová stěna

Bibliographic citation

MALÝ, M. *Internal flow of Spill-return Pressure-swirl atomizers*. Brno: Vysoké učení technické v Brně, Fakulta strojního inženýrství, 2020. 118 s. Vedoucí disertační práce prof. Ing. Jan Jedelský, Ph.D.

Affirmation

I hereby declare that I have written the PhD thesis on my own according to advice of my supervisor prof. Ing. Jan Jedelský, Ph.D. and all the literary sources are quoted correctly and completely.

In Brno_____ Milan Maly _____

Acknowledgments

Foremost, I would like to express my sincere gratitude to my supervisor prof. Ing. Jan Jedelský Ph.D. for his patience, motivation, enthusiasm, and immense knowledge.

This work has been supported by the project No. GA15-09040S funded by the Czech Science Foundation and the project "Computer Simulations for Effective Low-Emission Energy Engineering" funded as project No. CZ.02.1.01/0.0/0.0/16_026/0008392 by Operational Programme Research, Development and Education, Priority axis 1: Strengthening capacity for high-quality research.

I would like to express my thanks to Ing. Ondrej Cejpek who helped me with the preparation and execution of measurements. My gratitude also belongs to Dr. Graham Wigley for technical consultations and expertise discussions regarding Phase Doppler anemometry.

Finally, I would like to thank to my beloved Jana for her encouragement and patience when writing this thesis, and to my family for the support provided to me throughout my entire life.

Contents

1 Introduction

Pressure-swirl (PS) atomizers are widely used in many industrial applications, e.g. for cooling, painting, food processing or in combustion engines. The atomizer as a fuel delivery device plays an irreplaceable role in the concept of the engine, and more effective atomizers can improve the engine efficiency and reduce emissions. PS atomizers were introduced more than a century ago, but there are still possibilities for further incremental development. The abilities to atomize very viscous liquids or operate at a wide range of injection flow rates are among the parameters where the PS atomizers can further develop.

The simplest design of the PS atomizer is so-called Simplex version. It consists of three parts: tangential port, swirl chamber and exit orifice. The liquid is injected into the swirl chamber via tangential ports, which convert the pressure energy into the kinetic energy. It gains a swirl momentum in the swirl chamber and is consequently discharged by the exit orifice in the form of a hollow-cone liquid sheet. This sheet subsequently breaks up due to aerodynamical forces into filaments and ligaments. The geometry of the internal parts significantly affects the internal flow and, consequently, the discharged spray itself.

The disadvantage of the PS atomizer is that the liquid flow rate is proportional to the inlet liquid pressure. Therefore, the regulation range is limited. To overcome this, the spill-return (SR) modification was introduced more than half a century ago. These atomizers have an orifice in the rear wall of the swirl chamber. The liquid can be spilled away from the swirl chamber by the so-called spill-line (SL) orifice. When the SL orifice is open, only the axial momentum is reduced which results in a lower injection flow rate, but the liquid swirl momentum remains. Due to a high swirl momentum, the spray cone angle widens and the atomization quality remains good over a wide range of injection flow rates. The schematic drawing of a typical SR PS atomizer with outlined flow path is illustrated in Figure 1. These atomizers can be used in various combustion chambers where a wide range of operation regimes is required. However, this concept has some disadvantages. The atomizer design is more complex than that of the Simplex atomizer, and a more complex fuel supply system is required due to the presence of the spill-line.

The SR atomizer can be also used in applications where a very small liquid flow rate is required, such as lubrication applications, painting, and small combustors. For practical purposes, the manufacturing limit is around 0.2 mm of feature dimensions [1]. Moreover, small atomizers have a higher risk of clogging. These issues can be overcome using the SR atomizer and operate it with a high amount of spilled liquid.

This PhD thesis is also motivated by the Czech company První Brněnská Strojírna a.s., where a small-sized SR atomizer is used in their turbojet aircraft engine. However, the former design of the atomizer executed problems with spray stability. This thesis, amongst others, proposes design changes of their SR atomizer to prevent observed instabilities. To reveal more complete picture of the atomization process of the SR atomizers, the external flow and spray characteristics were investigated even though the focus is on the internal flow of SR atomizers.

2 Pressure swirl atomizer

PS atomizers have been widely investigated during the past 30 years due to increasing requirements on the combustion efficiency, and development of new experimental techniques allows for more precise investigations. Due to the complex physics, most of the published works were experimental studies, but in recent years, the number of papers concerning numerical simulations have dramatically increased. The SR atomizers have been investigated marginally; therefore, this section of the thesis focuses on the Simplex atomizers. Then, the findings are transformed to the SR version.

The main advantages of Simplex atomizers are the simple design without any moving parts, high reliability, and energy efficiency. The main disadvantage is that droplet sizes are proportional to the inlet pressure, p_l, and, therefore, the regulation range is limited. The injection flow rate is dependent on the square root of the inlet pressure. To halve the mass flow rate, the p_l must be reduced fourfold, which harms the atomization quality [2]. Despite the simple geometrical design, the PS atomizers have a very complex internal flow. It is a two-phase flow with secondary flow effects, which makes a direct observation difficult [3]. The character of the internal flow directly affects the parameters of the discharged liquid sheet, such as its thickness, t, velocity, and stability. The centrifugal liquid motion inside the swirl chamber generates a low-pressure zone down the swirl chamber centreline. The static pressure drops below the surrounding pressure, and the air from the surrounding atmosphere is sucked into this zone through the exit orifice and forms the air-core. The air-core diameter determines the value of t since the air-core blocks a part of the exit orifice. Moreover, the air-core fluctuations and instabilities affect the liquid sheet perturbations and stability and may consequently change the liquid sheet breakup length. Also, an unstable spray can be observed in some cases [4].

The most of published papers deal with the spray characteristics, but without studying the internal flow. Their outcomes are usually valid only for similar atomizers being investigated. These results are listed in several publications [1, 2, 5, 6]. Note here, that *Atomization and sprays* by A. H. Lefebvre [2] is considered as a standard in nomenclature of the atomizer parts and quantities.

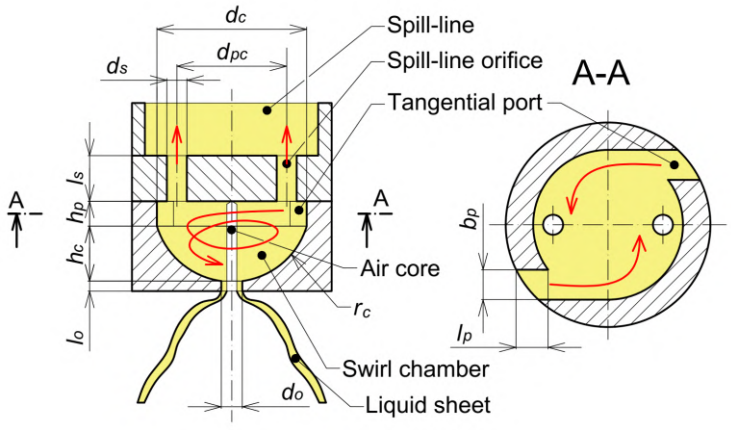

Figure 1 Schematic drawing of PS SR atomizer with two off-axial SL orifices.

These monographies are regularly updated by review manuscripts, e.g.:[7] from 2015. However, the underlying physics of the internal flow is represented only in a part of respective publications. It should be studied in order to establish a link between the atomizer design and spray characteristics.

The spray generated by PS atomizer contains droplets with various velocities and sizes. To evaluate the spray parameters, the size and velocity of individual droplets are usually measured. Droplet sizes are usually described by the Sauter mean diameter, *SMD*, or D_{32}, which can be defined as a diameter of a drop, which has the same volume to the surface ratio as the entire spray. The low *SMD* is useful for combustion applications. Another important parameter is the spray cone angle, *SCA*, which is an apex angle of the spray cone. Its value should be known to avoid the contact of the spray with the combustor wall. The spray temporal stability also affects the combustion process, since the unstable spray can generate an unstable temperature field, which results in excessive engine wear.

2.1 Spray formation from a PS atomizer

A spray formation process can be dived into several parts, see Figure 2. The discharged liquid breaks up into filaments and ligaments in the process called a primary break up. These structures consequently break up further into individual droplets during a secondary break up. The link between *t* and the size of the final droplets was described by Dombrowski and Fraser [8] in 1954. They found that the liquid sheet first breaks into long filaments, the size of which is proportional to *t*. From a simple geometrical consideration, a longer breakup length results in a thinner liquid sheet at the breakup position; therefore, the final droplets tend to be smaller. The initial *t* is dependent on the atomizer geometry, liquid properties, and operating pressure and can be estimated as [2]:

$$t = B\left(\frac{d_o \dot{m}_l \mu_l}{\rho_l p_l}\right)^{0.25}, \tag{1}$$

where d_o is a diameter of the exit orifice, $\dot{m}_l$ is the liquid mass flow rate, μ_l is the liquid viscosity, ρ_l is the liquid density, and p_l is the liquid overpressure. The parameter *B* is an experimental constant dependent on the atomizer used. This equation was derived with $B = 3.66$ [9], but revised later to reach the values of 2.7 [10] and 3.1 [11]. It is evident that the larger atomizer with a larger mass flow rate produces a thicker liquid sheet. The liquid pressure and the liquid density behave opposite. Several modifications of equation 1 were published, e.g.: Moon [12] adds an effect of the inlet port area and the length of the swirl chamber. The size of the final droplet can be roughly estimated as $D_{32} \sim t^{0.39}$ [2].

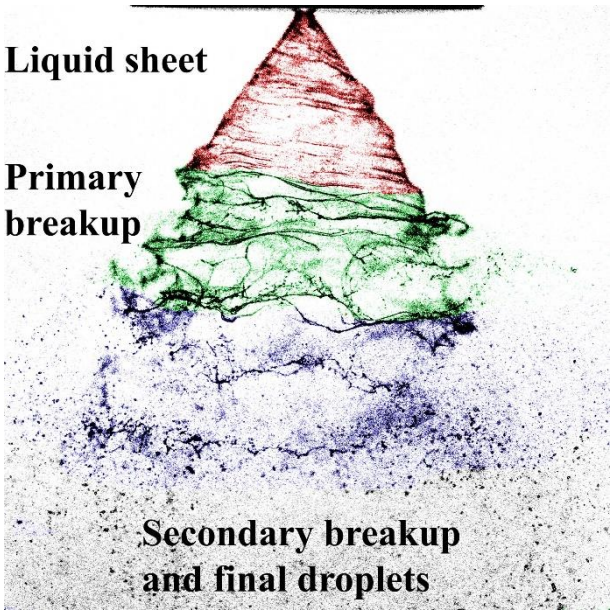

Figure 2 Liquid sheet breakup. The author's diploma thesis [13].

The parameter *t* solely is insufficient for prediction of the spray parameters, since the breakup mode can also change the droplet sizes. Sirignano et al. [13] published an overview where several modes of the liquid sheet breakup modes are described; however, their impact on the spray characteristics is unknown. The sinus waves, which are generated by aerodynamical interaction between the liquid sheet and the surrounding air, play a dominant role in the breakup mechanisms. Moreover, the size of the droplets is to be in the same order of magnitude as the sinus wave wavelength [6].

Hosseinalipour et al. [14] analysed parameters affecting the liquid sheet stability and found that the thinner liquid sheet and the wider *SCA* shorten the breakup length. The presence of crossflow further reduces its stability. Two modes of the liquid sheet breakup were documented by Senecal et al. [15]. They found a transition from the long-wave to the short-wave breakup mode at Weber number value of 27/16. Their definition was based on the liquid sheet half-thickness as the characteristic dimension, see definition of Weber number in eq. 7. A long-wave breakup produces a longer breakup length, and the ligaments are formed twice per wavelength. On the other hand, a short-wave mode produces a short breakup length, and ligaments are formed once per wavelength but with a much higher frequency [14]. The practical impact on the spray quality was not studied.

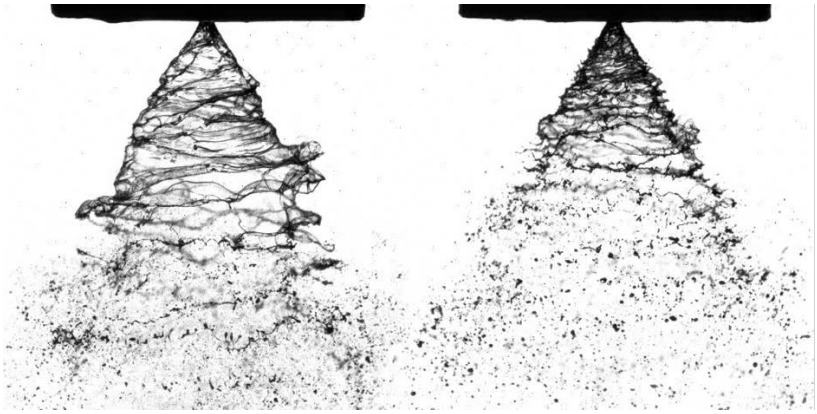

Figure 3 Breakup modes of the liquid sheet [17].

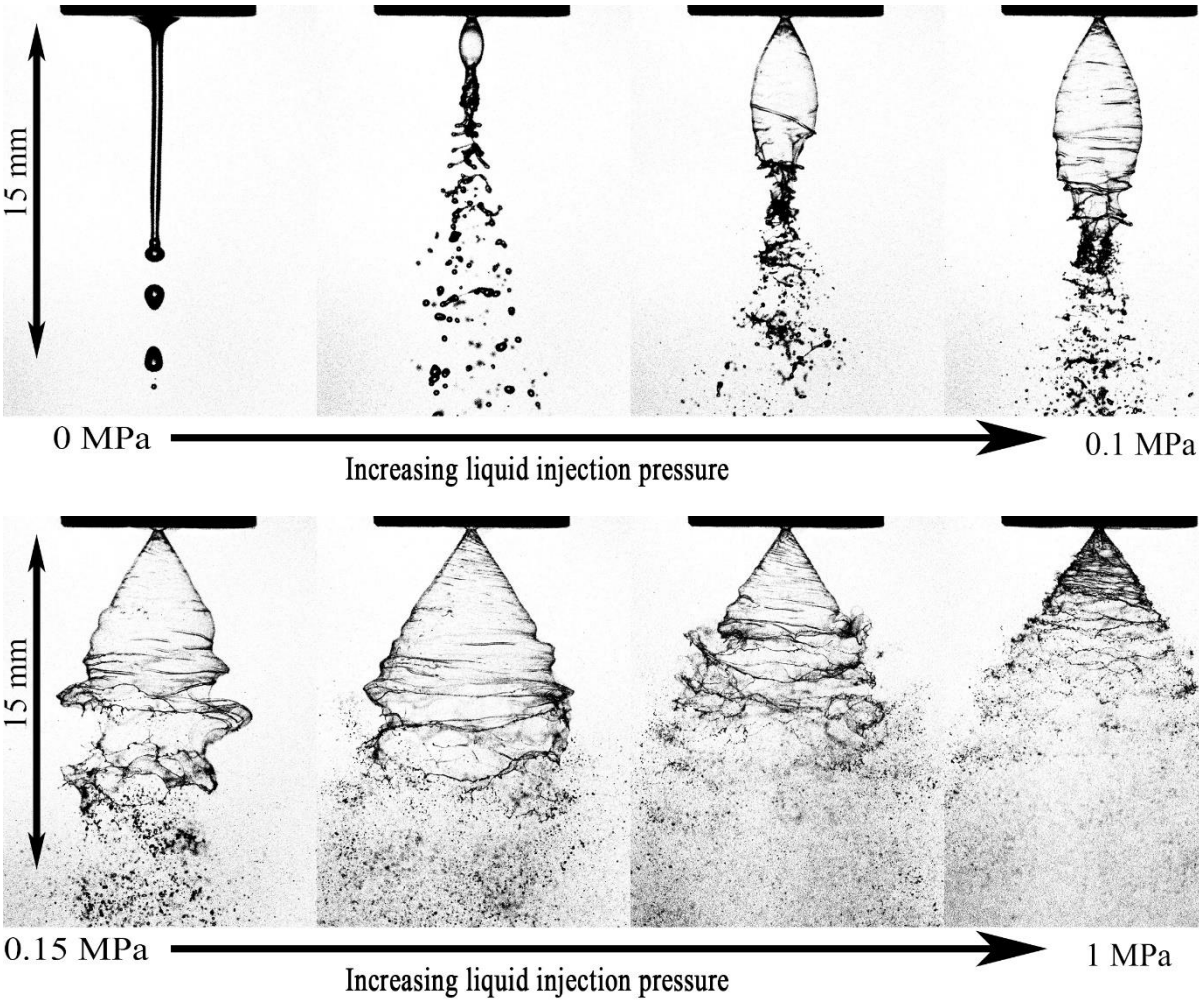

Figure 4 Effect of p_l, on the liquid sheet structure. The author's diploma thesis [13].

The breakup mode is often linked with the internal flow structure [16], but these data are rarely published. The author of this thesis demonstrated that the breakup mode can also be changed due to the presence of the SL orifice [17], see Figure 3, where two atomizers, which differ only in the position of the SL orifice, featured different breakup modes. The left atomizer produces a more stable liquid sheet with a longer breakup distance, which is typical for the long-wave breakup, while the other one has a much less stable sheet and a shorter breakup length. A more stable liquid sheet results in smaller droplets – for details see the paper II. An improper design of the SL orifice can result in highly pulsating spray – see the paper I and II.

Lin et al. [18] analytically described breakup mechanisms using dimensionless criteria. An increase in the ratio of the liquid momentum to viscous (Reynolds number, *Re*) and surface tension forces (Weber number, *We*) decrease the liquid sheet stability. This behaviour can be observed in Figure 4, where the effect of p_l on the liquid sheet structure is shown. At very low p_l, the internal flow is not developed and the Rayleigh breakup mechanism dominates. At $p_l > 0.15$ MPa, a hollow-cone liquid sheet is developed. With further increase in p_l, the breakup distance is rapidly shortened. Despite the short breakup distance, the final droplets are smaller at higher p_l, since the combined effects of smaller *t* and higher relative velocity, which enhance

the secondary break up, dominate [2]. Note here that the secondary break up was studied in detail in [19] and it is out of the scope of this thesis. Similarly, other spray-related effects are not studied here: evaporation [20] and droplet collisions [21].

2.2 Nanofluids sprays

As mentioned above, the spray quality is dependent on the atomizer geometry, operating conditions, and liquid rheology. In recent years, a novel approach for the spray process enhancement was proposed; an addition of nano-sized particles into the liquid can improve the thermal properties of the fluids [22, 23]; this can enhance spray cooling parameters [24, 25]. Moreover, the use of metal nanoparticles as fuel additives can have a positive influence on fuel combustion and emission performance [26]. Since both mentioned applications are spray based, the spray quality is a crucial factor here. The optimal goal is to keep the spray parameters intact, but enhance the liquid thermal properties. The actual effects of adding nanoparticles in the fluid flow characteristics and, particularly in the mechanisms of atomization, are still scarcely reported. A hydrodynamic behaviour of the nanofluids slightly differs from that of the pure liquids, which is mainly related to physical modifications of the local and of the bulk properties of the nanofluids. From the literature reviewed, the only known study related to the spray characteristics of nanofluids was conducted in 2017 by Kannaiyan and Sadr [26], who found only minor effects of alumina nanoparticles on the spray parameters. This topic is addressed within this thesis in Paper V, where the effect of nanoparticle addition on the liquid sheet break up, stability, *SCA,* and spray parameters is studied.

3 Internal flow of pressure-swirl atomizer

The previous chapter discussed the basic principles of the spray formation process. The liquid sheet thickness and its stability have a major role in determination of spray characteristics. The parameters of the liquid sheet are given by the atomizer geometry and operating conditions. The following part focuses on the examination of the internal flow.

3.1 Dimensionless criteria

PS atomizers can have a varied range of sizes, so dimensionless criteria help with their comparison. The discharge coefficient, C_D, and the atomizer constant, k, are probably the most widely used:

Discharge coefficient: $$C_D = \frac{\dot{m}_l}{\dot{m}_{theor}} = \frac{\dot{m}_{inj}}{A_o\sqrt{2\rho p_l}} \quad (2)$$

Atomizer constant: $$k = \frac{A_p}{\pi R_p r_o} \quad (3)$$

where C_D is a ratio of a measured liquid flow rate $\dot{m}_l$ to a theoretical $\dot{m}_{theor}$ rate, which can be derived from the Bernoulli equation. A_o is the area of the exit orifice and p_l is the liquid inlet overpressure. PS atomizers yield usually small values of C_D due to the presence of the internal air-core, which effectively blocks off a part of the exit orifice.

The atomizer constant k links the area of the inlet ports A_p, a mean radius of the liquid entrance to the swirl chamber $R_p = (r_c - r_p)$, and the radius of the exit orifice r_o. It is a characterising number for the given atomizer and the most of discharge parameters can be correlated with K.

Other dimensionless numbers, which are used in the internal flow evaluation [27], are as follows:

Reynolds number $$Re = \frac{\rho_l D V}{\mu_l} \quad (4)$$

Froude number $$Fr = \frac{Q}{2\pi(r_o^2 - r_{ac}^2)\sqrt{r_o g}} \quad (5)$$

Swirl number $$S_0 = \frac{\dot{m}_{inj} v_p R_p}{\dot{m}_{inj} u_o r_o} = \frac{\pi r_o R_p}{A_p} \quad (6)$$

Weber number $$We = \frac{\rho_l d_c V^2}{\sigma_l} \quad (7)$$

The Reynolds number, Re, is a ratio of momentum to viscous forces, where v is the liquid mean velocity and D is a characteristic dimension. Several slightly different definitions of Re are used: Re_c is defined in the swirl chamber and uses d_c and u_o, but Re_p provides a better link with physics within the inlet ports, and uses d_p and v_p.

The Froude number, Fr, describes the effect of gravity. It is a ratio of kinetic to potential energy within the exit orifice, the radius of which is reduced by the air-core radius r_{ac}. Q is a volumetric flow rate and g defines gravitational acceleration. It is useful in the atomizer scaling process, and the values >> 1 ensure a low effect of gravity.

The Swirl number, S_o, is a ratio of the axial flux of angular momentum to the axial flux of axial momentum. For the PS atomizer, it depends solely on the internal geometry; however, the SR

atomizers feature variable S_o as its value increases with *SFR*, see Paper III, where this phenomenon is discussed in detail.
The Weber number, *We*, is a ratio of momentum to surface tension forces. In the case of the internal flow, the surface tension forces can be neglected [27], but this has a great impact on the atomization itself.

3.2 Inviscid assumption

In order to understand the basic flow physics in the PS atomizer, an inviscid assumption is a useful tool. It is an analytical description derived in 1948 by Taylor and in 1953 by Griffen a Muraszew described and revised in detail in [28-30]. The internal flow acts like a non-viscous free vortex with a swirl velocity maximum near the centreline. The internal air-core is then generated in the zone where the static pressure drops below the pressure of surrounding atmosphere. This occurs due to an increase in swirl velocity near the swirl chamber centreline. The rotating air-core behaves like a solid cylinder, with zero swirl velocity within its centreline. Such behaviour is typical for a Rankine vortex.
The vortex behaviour can be described by the Bernoulli equation for an ideal liquid, neglecting the potential part and radial velocity:

$$\frac{u^2 + w^2}{2} = \frac{p_l}{\rho_l} \tag{8}$$

For inviscid free vortex, *wr = constant* and combining with continuity equation:

$$wr = \frac{QR_p}{A_p} \tag{9}$$

where *w* is the tangential velocity, *r* is the radius. In the exit orifice, the axial velocity can be defined as:

$$u_o = \frac{Q}{\pi(r_o^{\,2} - r_{oac}^{\,2})} \tag{10}$$

On the surface of the air-core $r = r_{oac}$. In the exit orifice, $u = u_o$. Combining eqs. 8, 9 and 10:

$$\frac{Q^2}{2\pi^2(r_o^2 - r_{oac}^2)^2} + \frac{Q^2(r_c - r_p)^2}{2A_p^2 r_{oac}^2} = \frac{p_l}{\rho_l} \tag{11}$$

At given p_l, there are two unknowns, Q and r_{oac}. To solve this equation, one more assumption is necessary. The authors of the inviscid model assume a maximal flow principle, where the air-core diameter should adjust itself to keep the flow rate maximal: $\delta Q / \delta r_{oac} = 0$. The equation 11 with the maximal flow assumption can be rewritten in a simplified form [28-30]:

$$X^3 + (2k - 3)X^2 + 3X - 1 = 0 \tag{12}$$

where X is the ratio of the air-core area to the area of the exit orifice: $X = A_{oac}/A_o$. This ratio is dependent solely on the atomizer constant, *k*. Once the X is known, the inviscid discharge coefficient C_{Dinv} can be calculated as:

$$C_{Dinv} = \sqrt{\frac{(1 - X)^3}{1 + X}} \tag{13}$$

The inviscid analysis allows for estimation of how the radius of the swirl chamber, the radius of the exit orifice, and the area of the inlet ports affect the C_D. Taylor (cited in [28]) also derived

that the *SCA* is solely dependent on *k*. Nevertheless, the accuracy of this analysis is relatively low and it can be used for studying purposes or for a very rough design approximation.
Easy to measure, yet very important characteristic of the PS atomizers, is the C_D. Experimental data of the C_D are not in good agreement with the inviscid analysis and illustrate a more complex problem. Rizk and Lefebvre [9] experimentally modified the correlation for the calculation of C_D and added the effect of the ratio of d_c/d_o. Jones [31] studied largescale atomizers and added the length of the swirl chamber and the exit orifice together with liquid viscosity to the correlation. However, these parameters have only a minor impact on the C_D. Ballester et al. [32] found an influence of p_l on the C_D. Benjamin et al. [33] followed the work of Jones [31] and experimentally updated the value of constants. Surprisingly, they found the opposite effect of some parameters. Sakman et al. [34] used the numerical simulation to predict the C_D for different atomizer geometries; however, with constant viscosity and pressure. Lee et al. [35] used a transparent atomizer and defined the C_D as a function of *Re*.
It is evident that the inviscıd assumption simplifies the whole problem and is often unable to predict the elementary parameters such as the C_D. But the experimental correlations are usually valid only for the atomizer with similar geometry as the tested one and they are not universally valid.
Several authors introduced more complex analytical approaches, assuming a viscous flow. Craig et al. [36] modified the inviscid flow analysis using a non-optimal, realistic flow. The ratio of the real C_D to the predicted one was introduced as an efficiency coefficient, *e*, and varies between 0.4 and 0.9 in dependence on the atomizer used. However, the authors claimed that the non-optimal atomizer, which has a smaller air-core than the optimal one, yields surprisingly lower C_D than that predicted by the inviscid analysis. This is the opposite result to that usually presented and, also, opposite to the results from the paper III.
Amini [3] compared the results from viscous and inviscid analysis with CFD results. The viscous analysis assumed the viscous losses within the boundary layer. The accuracy of CFD results outperforms the analytical models. In conclusion, the analytical models can be used for the first approximation of the atomizer geometry which can be fine-tuned by CFD.
Probably the most complex theoretical analysis of the internal flow was made by Wimmer and Brenn [37]. They divided the swirl chamber into three parts and analytically solved the flow including viscous losses. Among the results, the C_D was found to be dependent on the liquid viscosity. The flow rate and C_D increase with increasing liquid viscosity as the frictional losses reduce the swirl velocity component, which consequently shrinks the internal air-core, see Figure 5. This behaviour was experimentally confirmed, amongst others, in our study [38]. Anyway, the air-core temporal behaviour is still unresolved by any analytical model.

3.3 Effect of atomizer geometry and operating conditions on the internal flow

The outputs from the inviscid analysis are limited to global parameters of the atomizer as the C_D, *SCA*, or the air-core diameter. However, these predictions still use several assumptions and the accuracy of the results is often insufficient. Moreover, the temporal behaviour of the internal flow is not captured at all. Several authors investigated the temporal behaviour of the internal flow experimentally. The key studies are summarized in Table 1.

A transparent atomizer operated at several pressure and temperature regimes was used by Lee et al. [35]. The authors found a dependency of the air-core stability on the swirl chamber Re_c, see Figure 6. The unstable regime A with $Re_c < 2400$ features an undeveloped air-core. With increasing Re_c, the air-core is present within the exit orifice, see regime B, and is consequently stretched to the swirl chamber, as in the regimes C and D. At $Re_c > 3500$, the air-core is fully developed and stable. Note here that the spray cone is strongly fluctuating between its min and max angle value in regimes A and B. When the air-core is developed within the exit orifice, the *SCA* fluctuations were inhibited. This conclusion well agrees with findings from the paper I, where the spray instability is studied for a SR atomizer.

Halder et al. [39] experimentally investigated the effect of internal geometry on the air-core stability using 21 different transparent atomizers. Similarly as in [35], the air-core stability was found depended on the Re_p. The authors established two limit values of Re_p, at the first value, the air-core is still undeveloped, while the second one ensures a fully developed and stable air-core.

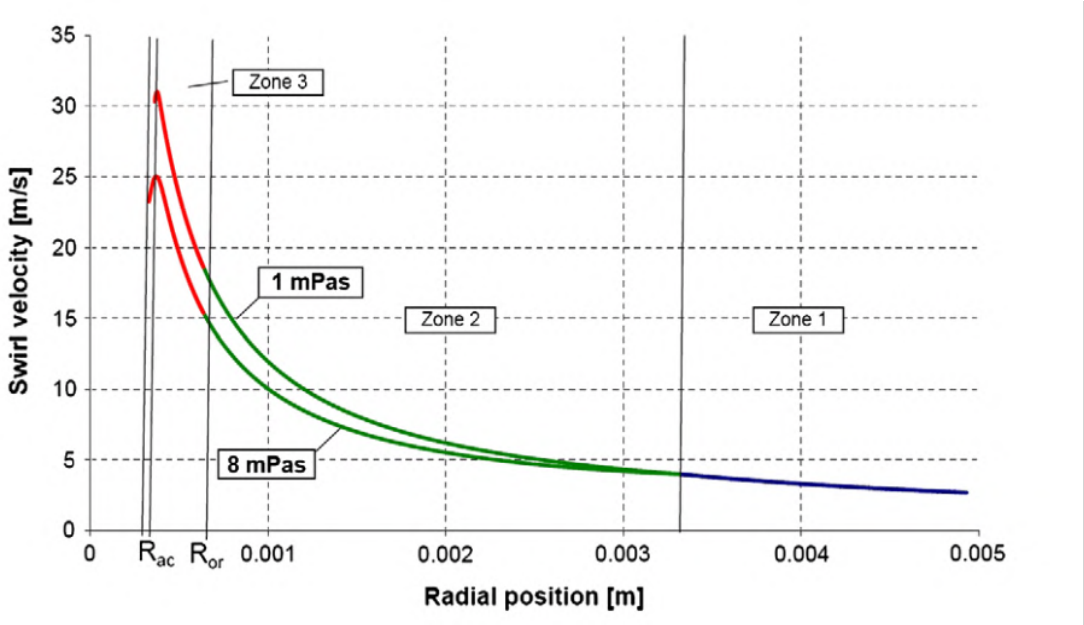

Figure 5 Effect of liquid viscosity on the swirl velocity component. Taken from [37]. R_{ac} is the air-core radius, R_o is the radius of the exit orifice.

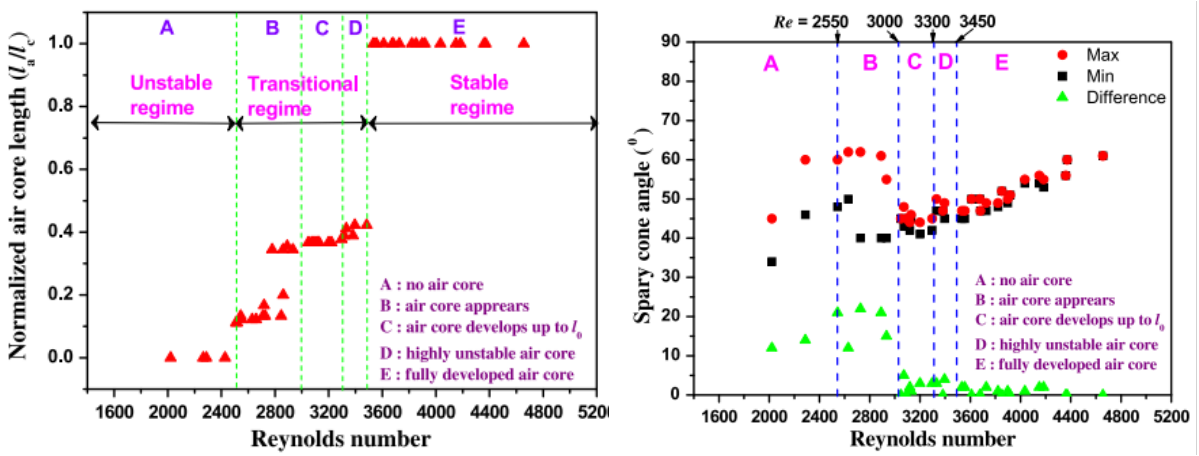

Figure 6 Effect of Re_c on the air-core length (left) and *SCA* (right). Taken from [35].

These limit values decrease with an increase in the ratio of d_o/d_c and a decrease in the ratio of A_p/d_c. The air-core diameter was slightly growing with *Re* and it was larger in diameter within the exit orifice. The atomizer geometry was also studied by Moon et al. [40], who found a critical value of $S_o = 0.6$. The value above this threshold established the stable air-core. Note here, that they used a pulse atomizer. Kim [41] et al. investigated the effect of length and diameter of the swirl chamber. At high ratios of h_c/d_c, the air-core tends to be unstable and even splits into two air-cores, see Figure 7. The unstable regimes cause temporal fluctuations in the liquid film thickness. The stable air-core was achieved for $h_c/d_c < 1.06$, which represents the atomizers with short swirl chambers. Temporal behaviour of the air-core was studied by Sumer et al. [42] using high-speed imaging and numerical simulation. They found a surface wave frequency of around 300 Hz.

Dash et al. [43] described a change in the air-core shape with dependence on *Re*. For *Re* ~ 3 000, the cylindrical shape of the air-core was observed while, for higher *Re*, the helical shape occurs with two revolutions per swirl-chamber length.

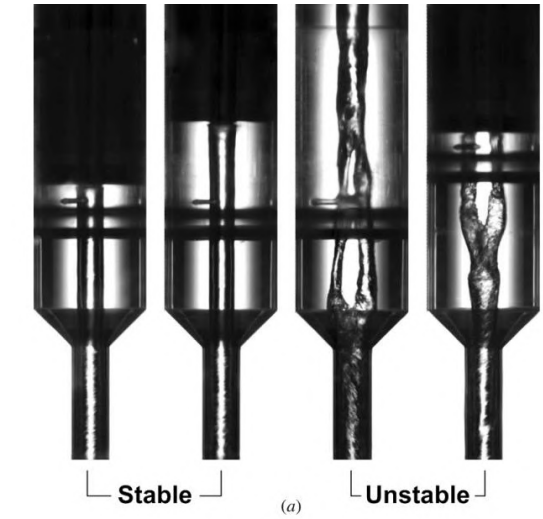

Figure 7 The stable and unstable air-cores as observed in [41].

Table 1 Overview of several key studies of internal flow

Author	Air-core shape	Parameters	Operating liquid
Lee [35]	No air-core	$Re_c < 2400$ $p_l < 0.3$ MPa	Diesel Kerosene
	Unstable	$2400 < Re_c < 3300$ $p_l > 0.3$ MPa	
	Stable	$Re_c > 3300$ $p_l > 0.9$ MPa	
Halder [39]	No air-core	$Re_p < 900$	Water
	Unstable	$900 < Re_p < 2100$	
	Stable	$Re_p > 2100$	
Moon [40]	Unstable	$S_0 < 0.6$	Gasoline
	Stable	$S_0 > 0.6$	
Kim [41]	Stable	$0.7 < h_c/d_c < 1.06$	Water
	Double air-core	$1.27 < h_c/d_c < 3.06$	

Cooper et al. [44] investigated the influence of the shape of convergent part of the swirl chamber on the internal flow and found an impact on the flow dynamics near the walls. However, our recent study [45] found only a negligible effect of the convergent shape on the spray characteristics.

Levante et al. [46] pointed on the presence of air-core surface distortions, which were later studied in detail by Chinn et al. [16], who divided the surface distortion into three categories: helical striations, low-frequency stationary waves, and low amplitude random ripples. The helical waves are the result of discrete number of the inlet ports. Their importance is low when a high number of the inlet ports is used. The stationary waves depend on the inlet velocity. These waves change the liquid sheet thickness within the exit orifice. Moreover, they can also be responsible for the change in the breakup distance.

The presented overview provides design boundaries for the stable Simplex atomizer. These findings are likewise valid for the SR version. However, no relevant study directly describing the effect of air-core stability on the liquid sheet stability and, consequently, on the spray quality was found. So far, all these phenomena have been studied separately.

3.4 Spill-return atomizers

The PS SR atomizers are modified versions of the Simplex types with extended regulation range. The spill-line, SL, orifice positioned in the rear wall of the swirl chamber, is the only geometrical parameters differing from the Simplex type, see a schematic drawing in Figure 1.

The main advantage of the atomizer is a wide regulation range, which can be described by a turn-down ratio. It is a ratio of maximum to minimum injection flow rate, which still satisfies the required spray quality. The turn-down of the Simplex atomizer is achievable only through a change in p_l. The SR atomizer can spill the liquid from the swirl chamber away and reduce the injection flow rate, $\dot{m}_{inj}$, dramatically. The amount of spilled liquid, $\dot{m}_s$, to the pumped amount, $\dot{m}_p$, is defined as a spill-to-feed ratio, $SFR = \dot{m}_p/\dot{m}_p$. The *SFR* can reach the values from 0, where the atomizer operates in the Simplex mode, to 1, where all the liquid is spilled away. This concept benefits from fact that the liquid is always supplied to the swirl chamber under high p_l which ensures a high angular momentum. While the liquid is spilled away, only the axial momentum is reduced. This leads to an increase in the value of S_o, which outcomes in a larger air-core diameter and a thinner liquid sheet. A high ratio of the swirl to the axial momentum also widens the *SCA*. The effect of thinner liquid sheet and wider *SCA* is beneficial for drop size, as discussed previously, but low axial momentum outcomes in low droplets velocities, which inhibits the secondary breakup.

One of the first practical applications of the SR atomizer was in a jet engine [47]. These atomizers benefit from a very good atomization quality at low engine powers, easy regulation, and clogging resistivity.

Kapitaniak [48] studied several design configurations of the spill controlled atomizer. The main influencing parameter was the atomizer constant *k*. The author used a single axially placed spill-orifice and did not study other potential arrangements of the SL orifice.

The SR atomizers were also widely studied in the Soviet Union and the results are available within Borodin's [49] publication from 1967. It contains a vague study on the SL orifice arrangement. It shows that the size and radial position of the SL orifice plays an important role. The authors proved that the radial position of the SL orifice can change the atomizer $C_{D,}$ even

when operated in the Simplex mode at $SFR = 0$. This effect is the strongest for the single axially placed orifice and decreases with the SL orifices being placed further from the swirl chamber centreline. No explanation of this behaviour was provided. The axial orifice suffers from greater pressure losses and necessity for low values of SL pressure, p_s. Finally, the authors compared the turn-down capability of the Simplex and SR atomizers and, for practical applications, they found a turn-down ratio of Simplex atomizer of 4, while the SR version reaches the value of 86. The same results were also used in more recent publications [1, 5].

Rizk et al. [50, 51] experimentally investigated several SR atomizers under various operating conditions. An increase in *SFR* leads to wider *SCA* and a slight decrease in droplet sizes. The authors used a single axially placed SL orifice. However, an opposite trend in the drop size distribution was observed by Dai et al. [52], where an increase in *SFR* caused an increase in the drop sizes.

Loffler-Mang et al. [53] were the first ones to use a transparent SR atomizer with a single axial SL orifice. They found a local minimum for the angular momentum around $SFR = 0.5$. However, they operated the atomizer at a constant inlet mass flow rate. Thus, their results are hard to compare since other authors used the constant *SFR* to compare the atomizers.

Slowik [54] et al. pointed on the problems with spray stability in some SR atomizers, especially at low *SFR*s. Nasr et al. [55, 56] used the SR atomizer for decontamination chambers, where very fine droplets and low $\dot{m}_{inj}$ are required. They used p_l up to 12 MPa. One of the benefits of this atomizer was superior clogging resistance compared to the Simplex atomizers since the exit orifice can be larger. They compared several atomizers with different diameters of the axial SL orifice and used no regulation within the SL. A larger area of SL orifice yields a higher *SFR;* therefore, the $\dot{m}_{inj}$ was decreasing. The droplet sizes were increasing with *SFR*, similarly as in [52].

Despite many advantages of the SR atomizers, there was little interest in research during past years. Some disadvantages, such as a requirement for a more powerful pump, or complicated measurement of $\dot{m}_{inj,}$ limit their use in jet engines [4]. However, with a current trend of energy optimisation, these atomisers may find their place in special applications requiring a superior clogging resistance or very small flow rates. The proper geometrical arrangement of the SL orifice is not clear and its impact on the internal flow is not known. Note here that several configurations of the SR atomizers were found within patents: single axial spill orifice [57-59], off-axial orifices [60], tangentially inclined orifices [61].

3.5 Numerical solution of the internal flow

Chinn in his inviscid analysis review [29, 30] suggests using the inviscid analysis as the first approximation of the atomizer design and recommends the use of CFD tools for final design refinements since it produces more accurate results compared to the analytical models. The number of CFD studies has gradually increased during the last 20 years, mainly due to increasing computational power.

Yule a Chinn in 1997 [62] conducted one of the first 2D simulations of the Simplex atomizer internal flow. They compared the predicted values of *SCA* and C_D with experimental data and found the difference of less than 3%. Note here that they used a laminar solver to calculate the velocity field, even though the internal *Re* reaches the values over 50,000. They discussed this by means of atomizer small dimension where the turbulent flow cannot fully develop. Chinn

discussed this behaviour later in [27], where he calculated that, even for a large scale atomizer (up to a centimetre in the exit orifice radius) and operated at high p_l, the flow is to be laminar. This is further supported by the fact that the swirl dominant flow itself tends to laminarise the flow.

Madsen et al. [63] compared laminar and LES (Large-eddy simulation) simulations using 3D mesh in the range of Re_p = 11,000 – 41,000. The results were validated using experimental data. Both models were able to predict the internal flow including the air-core; however, the LES approach required a much finer mesh and it is more computationally expensive. The authors tried to include the two-equation k-ε model, which is the industry standard; however, this model failed to predict the internal air-core. Nouri-Borujerdi et al. [64] compared the laminar model with the 7-equation Reynolds stress model (RSM) in a 2D simulation The later model is often used in flows where the anisotropic turbulence occurs. This is the case of swirl dominant flow in the Simplex atomizers. The authors compare the CFD results with experimental data in the range of Re_p = 18,000 – 40,000 and also discuss the CFD solution of Datta et al. [65], who used a simpler k-ε model. The laminar model achieved the best match with the experimental data, while the k-ε performed worse than the analytical solution. Both turbulence models overestimated turbulence viscosity.

A review of numerical setups is shown in Table 2. No clear conclusion can be made on selection of the physical model selection. Various authors used both laminar and turbulence approaches for a wide range of Re_p. The most common turbulence models are based on the k-ε family and represented by realizable and renormalization group theory, RNG models. The RSM is also widely used. The air-core interface is usually captured by the Volume of Fluid (VOF) models. To the best of the author's knowledge, so far, any paper regarding CFD simulation of the SR atomizer has been published.

Table 2 Review of published numerical setups

	Software	2D/3D	Transient /steady	Turbulence model	Interface	Re_p
Shaikh [66]	Fluent	2D, 3D		Laminar	VOF Geo-rec.	1000
Laurila [67]	OpenFOAM	3D Full	Transient	Implicit LES	VOF Geo-rec.	420-5300
Galbiati [68]		3D Full	Transient	LES, RSM, RNG *k-ε*	VOF	1700-3800
Ghate [69]	Fluent	3D	Transient	RSM	VOF PLIC	2500-12500
Ibrahim [70]	Fluent	2D		RSM	VOF Geo-rec	5×10^3–5×10^4
Amini [3]	Fluent	2D	Steady	Laminar	VOF	10^4–10^5
Dikshit [71]		3D	Steady	*k-ε*	VOF	~10^4
Madsen [63]	Fluent, CFX	3D		Laminar, LES	VOF	10^4–4×10^4
Hinckel	CFX	3D	Steady	*k-ε*	VOF HEM	>10^4
Sumer [42]	Fluent	2D, 3D	Transient	Laminar	VOF HRIC	$1{,}2\times10^4$
Qian [72]	OpenFOAM	2D		Laminar, RSM	VOF LS coupled	~$1{,}6\times10^4$
Nouri-Borujerdi [64]		2D	Steady /transient	Laminar, RSM	Level set	$1{,}8\times10^4$–4×10^4
Marudhappan [73]	Fluent	2D, 3D		Laminar	VOF HRIC	~2×10^4
Baharanchi [74]		2D	Transient	RNG *k-ε*	VOF	~$2{,}5\times10^4$
Mandal [75]	Fluent	2D		Laminar	VOF	~4×10^4
Vashahi [76]	CCM+	3D	Steady	*k-ε*, *k-ω*	VOF HRIC	

4 Summary of knowledge gap

The pressure-swirl atomizers are currently studied by many research teams even though they were introduced almost a century ago. The researchers focus on both their internal flow characteristics and spray parameters. Despite a simple design of pressure-swirl atomizers, the internal flow is rather complex; it is a two-phase flow with certain secondary flow effects so it is difficult to decide whether the internal flow is laminar or turbulent. This disparity is notable in various setups of the CFD simulations, which boomed during the last two decades.

The Simplex pressure-swirl atomizers are already well documented. The effect of most of the geometrical parameters was experimentally studied, and many empirical correlations were proposed. Therefore, the design process is straightforward: the first geometrical draft can be based on the empirical correlations or analytical solutions, and the fine refinement can be made using the CFD simulation. However, the final design must be experimentally checked before its application, since it is still very hard to perform direct numerical prediction of the spray parameters [77].

The SR atomizers were only rarely studied. The presence of the SL orifices changes the internal flow and may harm the atomization itself. These atomizers can be controlled by setting the two variables; p_l and *SFR*. This makes the SR atomizers more versatile but hard to design and operate properly. They have been applied in very small jet engines, in atomization of very viscous or polluted liquids, or in applications where a wide regulation range is necessary.

The key part of the design process of the SR atomizer is the geometry of SL orifice. A few geometrical arrangements were published, but most authors used a single central orifice. Some authors noticed the unstable spray from these atomizers, especially at low *SFR*s. The off-axial orifices have several parameters to be set, such as their size, number, distance from the atomizer centreline, or their inclination.

It is unknown why the central SL orifice causes the unstable spray, and how the spray instabilities affect the drop sizes. The effect of the SL orifice position of the regulation range is yet to be validated. Moreover, the effect of *SFR* on the drop sizes is unknown, since the authors reported opposite results. This is also linked with the liquid sheet stability which can cause a change in the droplet sizes. From simple geometrical consideration, a hollow liquid cone is getting thinner with distance; therefore, a longer breakup distance should result in smaller droplets. This hypothesis, among others, must be experimentally confirmed.

5 Aim and objectives

5.1 Aim of the thesis

The analysis of geometrical and operational parameters affecting the internal flow stability inside a small pressure-swirl spill-return atomizer and its impact on the final spray.

5.2 Scientific questions and original hypotheses

1. **What is the reason for unstable spray from the atomizers with central SL orifice?**

   The internal air-core is stretched and thus penetrates through the central SL orifice. This causes a decrease in its stability and the air-core may even split or disappear. Since there is no air-core within the exit orifice, the C_D increases shortly. This causes a rapid change in the SCA and can be observed as a spray instability.

   The swirling liquid generates a low-pressure zone along the swirl chamber centreline, where large pressure gradients are present. The liquid can be drained from the SL orifice inside this low-pressure zone fill and the central area with the liquid instead of air. The spray is unstable when no air-core is present.

2. **How does the position of the SL orifices affect the turn-down ratio?**

   The off-axial SL orifices provide a wider regulation range due to higher static pressure on the swirl chamber periphery.

   The axial SL orifice provides a wider regulation range since it is immune to the direct flow from the inlet port to the SL line, which may reduce the turn-down capability of off-axis SL orifice arrangement.

3. **How does *SFR* affects the *SCA* and drop sizes and how does *SCA* depend on the SL orifice configuration?**

   The ratio of angular to axial velocity is increasing with SFR, which causes a wider SCA. Also, the wider SCA should lead to smaller droplets due to the larger interference area of the spray and surrounding air.

   Inclination or position change of SL orifice can change the SCA for the respective SFR.

5.3 Objectives

To support all scientific questions, a set of specific objectives have been formulated:

a) Identify spray stability conditions (*Re*, *SFR*, arrangement of SL orifices)
b) Describe the internal flow of spill-return atomizers using transparent atomizers
c) Correlate the parameters of spray generated from various spill-return atomizers for various p_l and *SFR*s regimes.
d) Predict the atomizer performance using numerical CFD simulation of the internal flow
e) Study the atomization quality and liquid properties by adding of nanoparticles

5.4 Structure of the thesis

The aim and objectives have been addressed in five stand-alone peer-review journal papers. The number of citations taken from Web of Science and Google scholar, excluding auto citation as of November 2020 is given in brackets:

I. **MALÝ, M**.; JEDELSKÝ, J.; SLÁMA, J.; JANÁČKOVÁ, L.; SAPÍK, M.; WIGLEY, G.; JÍCHA, M. Internal flow and air-core dynamics in Simplex and Spill-return pressure-swirl atomizers. *International journal of heat and mass transfer*, 2018, vol. 123, pp. 1-11. ISSN: 0017-9310. **IF = 3.891 (9)**

II. **MALÝ, M**.; SAPÍK, M.; CEJPEK, O.; WIGLEY, G.; KATOLICKÝ, J.; JEDELSKÝ, J. Effect of spill orifice geometry on spray and control characteristics of spill-return pressure-swirl atomizers. EXPERIMENTAL THERMAL AND FLUID SCIENCE, 2019, vol. 106, pp. 159-170. ISSN: 0894-1777. **IF = 3.498 (4)**

III. **MALÝ, M**.; CEJPEK, O.; SAPIK, M.; ONDRACEK, V., WIGLEY, G.; JEDELSKÝ, J. Internal flow dynamics of spill-return pressure-swirl atomizers. EXPERIMENTAL THERMAL AND FLUID SCIENCE, 2021, vol. 120. ISSN: 0894-1777. **IF = 3.498 (0)**

IV. **MALÝ, M**.; SLÁMA, J.; CEJPEK, O.; JEDELSKÝ, J. Comparison of numerical models for prediction of pressure-swirl atomizer. To be published in 2021.

V. **MALÝ, M**.; MOITA, A.S; JEDELSKÝ, J.; RIBEIRO, A. P. C.; MOREIRA, A. L. Effect of nanoparticles concentration on the characteristics of nanofluid sprays for cooling applications. *Journal of Thermal Analysis and Calorimetry*, 2018, ISSN: 1588-2926. **IF = 2.209 (4)**

5.5 The author's contribution to the papers

I. Conducted majority of experimental and numerical work, literature survey, data analysis and writing of the manuscript
II. Conducted majority of experimental work, literature survey, data analysis and writing of the manuscript
III. Conducted majority of experimental work, literature survey, data analysis and writing of the manuscript
IV. Conducted majority of experimental work and numerical work, literature survey, data analysis and writing of the manuscript

V. Conducted all experimental work, part of the literature survey, data analysis and writing of the manuscript

5.6 Other publications of the author related to the topic of the thesis

Two journal papers, which were co-authored during PhD studies and are closely linked to this thesis, but not discussed here due to brevity. Both paper focus on the external flow of Simplex and Spill-return atomizers. The results of this thesis were presented at national and international conferences with more than a dozen conference papers published, some of them are listed below.

JEDELSKÝ, J.; **MALÝ, M**.; PINTO DEL CORAL, N.; WIGLEY, G.; JANÁČKOVÁ, L.; JÍCHA, M. Air–liquid interactions in a pressure-swirl spray. *International journal of heat and mass transfer*, 2018, vol. 121, pp. 1-11. ISSN: 0017-9310. **IF = 3.891 (8)**

JEDELSKÝ, J.; **MALÝ, M**.; JÍCHA, M.; SLÁMA, J.; WIGLEY, G.; Importance of Geometrical Factors on Spray Characteristics of Spill-Return Atomizers. *Journal of Propulsion and Power*, 2021, vol. TBD, p. 11. ISSN: 1533-3876. **IF = 1.940 (0)**

MALÝ, M.; SAPÍK, M.; CEJPEK, O.; LÍZAL, F.; ONDRÁČEK, V.; JÍCHA, M.; JEDELSKÝ, J. *Internal flow characteristics in Spill-return pressure-swirl atomizers.* Paris: ILASS, 2019. p. 1-8.

MALÝ, M.; JEDELSKÝ, J.; SAPÍK, M.; CEJPEK, O.; SLÁMA, J.; WIGLEY, G. *Effect of spill orifice geometry on performance of spill-return pressure-swirl atomizers.* Chicago: 2018. p. 1-8.

MALÝ, M.; JANÁČKOVÁ, L.; JEDELSKÝ, J.; SLÁMA, J.; SAPÍK, M.; WIGLEY, G. Internal flow and air core dynamics in Simplex and Spill-return pressure-swirl atomizers. In *28TH CONFERENCE ON LIQUID ATOMIZATION AND SPRAY SYSTEMS, ILASS-EUROPE 2017.* Valencia: 2017. p. 233-240. ISBN: 978-84-9048-580-4.

MALÝ, M.; SLÁMA, J.; SAPÍK, M.; JEDELSKÝ, J. 2D and 3D numerical modelling of internal flow of Pressure-swirl atomizer. In *EFM18 – Experimental Fluid Mechanics 2018. EPJ Web of Conferences.* EDP Sciences, 2019. pp. 1-6. ISSN: 2100-014X.

MALÝ, M.; SAPÍK, M.; JEDELSKÝ, J.; JANÁČKOVÁ, L.; JÍCHA, M.; SLÁMA, J.; WIGLEY, G. Internal flow characteristics in scaled pressure-swirl atomizer. *EPJ Web of Conferences*, 2018, vol. 180, no. 02059, pp 1-6. ISSN: 2100-014X.

MALÝ, M.; JANÁČKOVÁ, L.; JEDELSKÝ, J.; JÍCHA, M. Influence of operating conditions and atomizer design on circumferential liquid distribution from small pressure-swirl atomizer. In *EPJ Web of Conferences. EPJ Web of Conferences.* EDP Sciences, 2017. pp. 1-4. ISSN: 2100-014X.

MALÝ, M.; JANÁČKOVÁ, L.; JEDELSKÝ, J.; JÍCHA, M. The influence of spill-line geometry on a spray generated by a pressure-swirl atomizer. In *EPJ Web of Conferences. EPJ Web of Conferences.* EDP Sciences, 2016. pp. 1-6. ISSN: 2100-014X.

MALÝ, M.; JANÁČKOVÁ, L.; JEDELSKÝ, J.; JÍCHA, M. Effects of Alternative Fuel characteristics on Spray Generated by Small Pressure- Swirl Atomizer. In *The Application of Experimental and Numerical methods in Fluid Mechanics and Energy 2016.* Žilina: University of Žilina, 2016. pp. 121-125. ISBN: 978-80-554-1193- 4.

5.7 Other publications of the author

During PhD studies, the author contributed to several ongoing researches in the spray laboratory and collaborated with foreign research teams. Only the peer-review journal papers are listed below for brevity.

URBÁN, A.; ZAREMBA, M.; **MALÝ, M**.; JOZSA, V.; JEDELSKÝ, J. Droplet dynamics and size characterization of high-velocity airblast atomization. *INTERNATIONAL JOURNAL OF MULTIPHASE FLOW,* 2017, vol. 95, p. 1-11. ISSN: 0301-9322. **IF = 2.592 (29)**

ZAREMBA, M.; WEIß, L.; **MALÝ, M.**; WENSING, M.; JEDELSKÝ, J.; JÍCHA, M. Low-pressure twin-fluid atomization: Effect of mixing process on spray formation. *INTERNATIONAL JOURNAL OF MULTIPHASE FLOW,* 2017, vol. 89, p. 277-289. ISSN: 0301-9322. **IF = 2.592 (14)**

URBÁN, A.; **MALÝ, M**.; JÓZSA, V.; JEDELSKÝ, J. Effect of liquid preheating on high-velocity airblast atomization: From water to crude rapeseed oil. *EXPERIMENTAL THERMAL AND FLUID SCIENCE,* 2019, vol. 102, p. 137-151. ISSN: 0894-1777. **IF = 3.498 (3)**

URBÁN, A.; GRONIEWSKY, A.; **MALÝ, M**.; JÓZSA, V.; JEDELSKÝ, J. Application of big data analysis technique on high-velocity airblast atomization: Searching for optimum probability density function. FUEL, 2020, vol. 273, no. 1, p. 1-12. ISSN: 0016-2361. **IF = 5.218 (0)**

ÚRBÁN, Á; KATONA, B; **MALÝ, M.;** JEDELSKÝ, J.; JÓZSA, V. Empirical correlation for spray half cone angle in plain-jet airblast atomizers. FUEL, 2020, vol. 277, no. 1, p. 1-11. ISSN: 0016-2361. **IF = 5.218 (0)**

ZAREMBA, M.; KOZÁK, J.; **MALÝ, M**.; WEISS, L.; RUDOLF, P.; JEDELSKÝ, J.; JÍCHA, M. An Experimental Analysis of the Spraying Processes in Improved Design of Effervescent Atomizer. *INTERNATIONAL JOURNAL OF MULTIPHASE FLOW,* 2018, č. 103, s. 1-15. ISSN: 0301-9322. **IF = 2.592 (5)**

6 Summary of conducted work

6.1 Paper I (Objective A and B): The first study of internal flow and air-core dynamics of an unstable SR atomizer.

In this paper, the internal flow of an unstable SR pressure-swirl atomizer was studied using a scaled transparent model of the atomizer and was compared with a Simplex atomizer. The study aims to investigate the internal flow of SR atomizer experimentally and numerically. Firstly, the study examines the possibility to predict the atomizer characteristics such as C_D and *SCA*, and the velocity field in the swirl chamber, using a relatively simple 2D simulation. The primary focus is to elucidate the effect of the central spill orifice on the spray fluctuations as reported in our conference papers [22, 33] and to determine their source. These fluctuations create an uneven temperature field within the combustion chamber of the turbojet aircraft engine, which increases engine emissions and reduces the life span of turbine rotor blades. The spray pulsations were observed at frequencies in a range from 3 to 20 Hz and only for $SFR < 0.15$ or in the Simplex mode.

In order to examine the internal flow, the atomizers were manufactured as scaled transparent copies. Due to the small dimensions of the original atomizers, it was impossible to manufacture them from PMMA and examine their flows directly. To solve this, the transparent versions were designed as ten times scaled copies. It was then necessary to match the flow characteristics of the original and scaled atomizers. This was done by changing the inlet velocity to maintain the same *Re*, which reaches relatively low values in the range from 755 to 1731. The swirl number S_o is the function of the atomizer geometry, which was scaled evenly; therefore, it remains unchanged. The atomizers were operated with kerosene-type fuel jet A-1 and p-cymene (1-Methyl-4-(propan-2-yl) benzene). The main advantage of the p-cymene is proximity of its refractive index to the refractive index of the atomizer body. This index matching technique allows for unbiased velocity measurement using Laser Doppler Anemometry, LDA, and provide high-contrast for imaging techniques. A high-speed camera Photron SA-Z documented the temporal and spatial behaviour of the air-core. The LDA measures the swirl velocity component inside the swirl chamber in several axial planes. The experimental data also served for validation of a simple 2D axisymmetric CFD simulation of the intern flow. Details about the experimental setup, including refractive index matching, and the numerical setup are presented in chapter 3: Experimental and numerical setups in Paper I.

6.1.1 Summary of main findings

The HS images yield the information about the air-core shape, diameter, and temporal stability. The Simplex atomizer generated a fully developed air-core for all the regimes investigated. It was cylindrically shaped and larger in its diameter inside the exit orifice; this shape was also described by other authors. Its behaviour was nearly independent of *Re*. The situation changed dramatically when the SR atomizer was used. The air-core was no longer present in the swirl chamber, and the spray became unstable, even for the highest *Re* values. Only fragments of the core were visible inside the exit orifice. The air-core was unstable and strongly fluctuating and it even occasionally disappeared. The *SCA* was fluctuating between 49 and 88° at a frequency in the range of 10 – 20 Hz with no evident correlation to the air-core behaviour. This was observed for all the regimes with the spill-line closed. With increasing rate of spilled flow, the

swirling momentum increased with respect to the axial momentum and the flow character changed. The standard mean deviation of *SCA*, which measures the rate of fluctuations, was high for $SFR < 0.15$. With a further increase in *SFR*, the fluctuations reduced. The air-core is limited to the exit orifice even at $SFR = 0.4$; however, for *SFR*s higher than 0.15, it was stable enough not to decay. In the relatively narrow range of $SFR = 0.4 – 0.65$, the air-core extends into the swirl chamber. It is evident that the spray stability is linked to the air-core stability within the exit orifice. It is not necessary to provide a fully developed air-core across the entire swirl chamber height to ensure a stable spray. Note that a similar conclusion was proposed by Lee et al. [35] for the Simplex atomizers.

The reason for the undeveloped air-core was derived from the numerical simulation, which captured well the unstable regimes. The liquid from the swirl chamber flows in both directions thought the SL orifice. It is drawn back into the swirl chamber due to the low-pressure zone in the swirl chamber centre and forms a recirculation zone inside the SL. This conclusion disproves the previous hypothesis, which assumed a periodically decaying air-core as based on the external observation of the atomizer spray. The spray parameters were studied in the following paper.

6.2 Paper II (Objective C): Spray characteristics of SR atomizers

Paper II focuses on the spray parameters generated from several SR atomizers. The unstable atomizer, as studied in Paper I, is compared with modified versions that used the off-axial SL orifices. This SL arrangement should prevent the air-core from failure as it blocks the central low-pressure cone, and generates a stable spray even for low *SFR*s. The size and velocity of the spray droplets were probed using the two-component Phase Doppler Anemometry, PDA, and the discharged liquid sheet was documented at high temporal resolution by a Photron SA-Z high-speed camera. Seven different atomizers were investigated. The only difference among them was the position of the SL orifice, as shown in Figure 8. The paper aims to test the hypotheses established at the beginning of the author´s PhD study, see chapter 5.1 of this thesis.

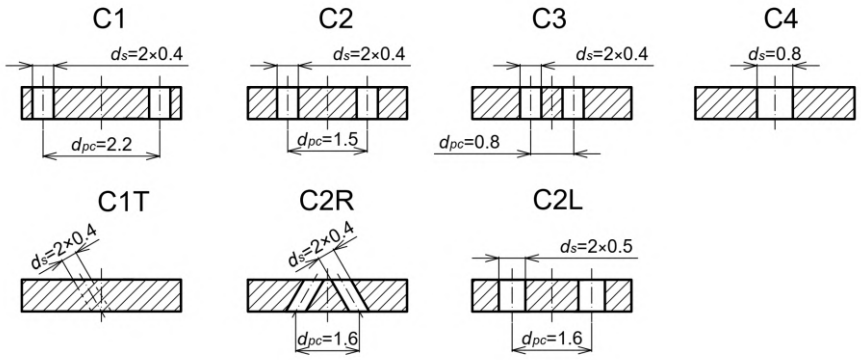

Figure 8 Different SL geometries: off-axis spill orifices with the parallel orifice axes (C1-C3, C2L); axially-positioned (C4); tangentially-inclined toward the main atomizer axis (C1T) and radially-inclined toward the main atomizer axis (C2R)

6.2.1 Discharge parameters

The main advantage of the SR atomizer over the Simplex type is its wide turn-down ratio, which is the ratio of the maximum to minimum injection flow rate suitable for given application. The former hypothesis assumed that placing the SL orifices on the periphery of the swirl chamber, where the static pressure has a maximum, should extend the range where the pressure can be reduced and consequently increases the turn-down ratio. However, this hypothesis was found to be invalid. The opposite is true since the atomizer with central SL orifice yields the greatest turn-down ratio at given *SFR*. The turn-down ratio decreased with increasing d_{pc}. One explanation for this behaviour is that the SL orifices close to the inlet ports tend to drain the liquid directly from the inlet ports. The liquid does not contribute to the atomizer flow but increases an overall liquid consumption. This well agrees with the increased SL orifice discharge coefficient of these SL configurations. Various inclinations of the orifice have a negligible effect on the discharge parameters. For the best spill efficiency and highest turn-down ratio, the atomizers with SL orifices close to the atomizer centreline are recommended.

6.2.2 Spray cone angle and liquid breakup

The discharged spray was found stable for all the atomizers with the exception of the version with a single central orifice, as investigated in the Paper I. Therefore, the spray pulsations can be easily subdued using any atomizer with the off-axial SL orifices, which well supports the

conclusion of Paper I. The spray cone angle, *SCA*, was identical for every stable atomizer and widens with p_l and *SFR* as $SCA \propto p_l^{0.1}$ and $(1\text{-}SFR)^{-0.15}$. The effect of p_l was almost identical as proposed in [78, 79] for the Simplex atomizers.

A surprising difference among the stable atomizers was observed in the breakup nature and breakup length. Two breakup modes were identified; the long wave breakup was performed by the atomizers with SL orifices further from the swirl chamber centreline (C1 and C2), while the C3 and C4 performed rather a short-wave breakup. The breakup length was systematically 25% longer for the long wave mode. The transition into the short wave mode is for *We* smaller than the critical value of 27/16 as proposed in [15] and, in this case, it is related to the internal flow stability. This problem is addressed in detail in the following paper, see Paper III.

6.2.3 Spray quality

The breakup mode and breakup distance change the nature of the resulting spray. The droplet velocity and *SCA* remained the same for all stable atomizers at a given operating regime but the droplet sizes alternated. The integral Sauter mean diameter (*ISMD*) generally decreases with increasing p_l, which was well documented for the Simplex atomizers [80-82] and slightly deteriorates with increasing *SFR*. This is the opposite result to [51] but in line with [52]. Moreover, the *ISMD* decreased with increasing breakup distance, which is responsible for the difference found among the atomizers. The atomizer with a longer breakup distance formed finer droplets. This effect was most evident for low p_l and $SFR = 0.3$ and 0.6. To conclude, Paper II proposed that the optimum SR atomizer features the off-axial parallel orifices. If the spray quality has a high priority, the C2 atomizer with the SL orifice placed on a radius $r_c/2$ is recommended. However, the highest turn-down ratio with stable spray was achieved with the C3 atomizer, but the spray quality was slightly worse at regimes with $SFR = 0.3$–0.6.

6.3 Paper III (Objective A and B): Internal flow of various SR atomizers

Paper III represents the core of this thesis. It addresses an experimental study of the internal flow of several SR atomizers operated under three pressure and four *SFR* regimes. Together with Papers I and II, it provides a complete series, which fills the knowledge gaps regarding the performance of the SR atomizers and delivers a design guideline for the SL orifice.

The second generation of our transparent atomizer was used here. This version allows for a rapid change of an SL orifice plate without the necessity of atomizer disassembly. A new index matching liquid was used. The p-cymene, which was used in Paper I, was replaced by a solution of jet A-1 fuel and 1-Bromonaphthalene. The main advantage of this solution is very accurate matching of the refractive index of liquid and the atomizer body with an error of less than 0.001 for 660 nm wavelength. Moreover, this liquid is less corrosive to the PMMA than p-cymene, which significantly reduced the lifetime of our previous model.

Several geometries of the SL orifice were used; most of them were based on geometries tested in Paper II. The internal flow was observed using a high-speed camera, and three velocity components were measured by LDA.

6.3.1 Modification of the Inviscid Analysis

The internal flow of the Simplex atomizer can be analytically described using the inviscid analysis, which is a useful tool for basic understanding of the internal flow structure and can serve for the first stage of the atomizer design process. This approach has a limited usability of the SR atomizers due to the variable *SFR*, which leads to a change in the axial to swirl momentum ratio. Likewise, the value of the swirl number S_o is changed. The change in S_o was derived in this paper in dependence on the *SFR* as:

$$S_0 = \frac{\pi r_o R_p \dot{m}_p}{A_p \dot{m}_{inj}} = \frac{\pi r_o R_p}{A_p (1 - SFR)} \tag{IV.1}$$

Then, the term $A_{pr} = A_p(1\text{-}SFR)$ represents the reduced area of the inlet ports. This area represents a part of the inlet through which the liquid flows into the swirl chamber and is discharged. The rest of the inlet port serves to feed the liquid directly to the SL orifice. Further, the reduced atomizer constant, k_r, can be derived as a function of *SFR*:

$$k_r = \frac{A_p(1 - SFR)}{\pi R_p r_o} \tag{IV.2}$$

When k_r is established, the classic inviscid analysis can be directly used in the same way as for the Simplex atomizer. This allows for prediction of theoretical C_D or *SCA* in dependence on *SFR*. The predicted values of C_D, C_{Dinv}, captured well the overall trend and were found to be systematically shifted from measured data as $C_D = 1.16 C_{Dinv}$. Therefore, the viscous losses in the swirl chamber reduced the swirl velocity, which resulted in a smaller air-core diameter. The smaller air-core block a lesser portion of the exit orifice and increase C_D.

The approach based on the reduced atomizer constant was validated for calculation of *SCA* using a semi-empirical equation derived by Rizk and Lefebvre for the Simplex atomizers [78]:

$$SCA = B k_{1r}^{-0.15} \left(\frac{p_l d_o^2 \rho_l}{\mu_l^2} \right)^{0.11} \tag{IV.3}$$

where k_{1r} is the atomizer constant used in [78] and can be simply transferred for SR version in the same way as in eq. IV.2. This correlation fitted the experimental data with $R^2 = 0.89$. The most important fact is that the derived exponents in eq. IV.3 are virtually identical to the empirical fit proposed in Paper II for small-scale SR atomizers. Therefore, this approach can be applied to the majority of empirical equations, where the atomizer constant is a variable.

6.3.2 Advanced modification of SL orifice

The modified inviscid theory well connects the existing correlation with a variation in *SFR*. However, the geometrical design of the SL orifice itself is not solved. Similarly, as in Paper II, several designs were compared in terms of the discharge parameters and air-core stability. The turn down ratio was found to be linearly decreasing with d_{pc}, which refines findings from Paper II. Tangential inclination of SL orifices can effectively modify the static pressure in the SL. The orifices inclined towards the swirl motion performed reduced intake losses and higher static pressure in SL for low *SFR*s. This may be disadvantageous in some practical applications since a small change in SL pressure causes a large drop in *SFR.* The opposite inclination ensures a smoother pressure regulation curve, which is beneficial for a pressure regulator. Nevertheless, the orifice inclination had a negligible effect on the *SCA* and the air-core.

This paper also introduced an atomizer with a solid insert along the swirl chamber centreline. As based on the literature review, a shorter air-core should be also more stable. However, the inserts, which aim to shorten the air-core, proved opposite. The air-core was generally less stable and the atomizer yielded a slightly higher C_D. The only beneficial effect is a higher resistance to air leakage inside the SL.

6.3.3 Temporal behaviour of the air-core and liquid sheet

The stability of the air-core was measured using standard mean deviation (SD) of its diameter. The position of SL orifice affected the air-core stability as a decrease in d_{pc} resulted in an increase in the SD of the air-core diameter. It was proved that the air-core instabilities are directly transferred on the emerging liquid sheet. However, no specific frequencies on the air-core surface nor the discharged liquid sheet were found. Two modes of the liquid sheet waves were identified, the partially unstable liquid sheet, which is likely to cause a short-wave breakup, contained a wide spectrum of high-frequency waves. This mode was observed only for atomizers with SL orifice very close to the atomizer centreline.

The essential outcomes of this paper may be used by engineers dealing with the atomizer design. It allows for the SR atomizer to be predicted using a simple analytical approach or empirical correlation derived for Simplex atomizers.

6.4 Paper IV (Objective D): Numerical simulation of internal flow

The numerical CFD simulation of the internal flow is a nowadays tool for designing of the atomizer. It allows for fast and accurate predictions of many characteristics, such as p_l, C_D and *SCA*, without necessity of atomizer manufacturing. As the review in the previous section of this thesis insists (Table 2), there is no consensus on how to treat the internal flow turbulence. Several authors assumed a laminar flow even for very high Re_p, others used industrial standard turbulence models. It is also unknown how the geometry simplification affects the results. The simplification can be done in several steps from a full-scale 3D model over a periodic 3D model to a very simple 2D axisymmetric model. Finally, the flow can be solved in a steady or transient manner, where the transient one requires several times larger computational power, but can capture unsteadiness of the air-core surface. These problems are addressed in Paper IV, which is currently in the final stage of preparation. The CFD results are validated by a comprehensive experiment that used the same modular atomizer as in Paper III, but with the Simplex cap and p-cymene as the liquid. The operating regimes were selected to provide the widest feasible range of Re_p. These regimes should cover a transition from laminar to turbulent pipe flow, since Re_p = 1000, 2000 and 4000. The laminar simulation was compared with turbulence models represented by k-ε RNG and realizable, k-ω SST, Reynolds stress model and Large Eddy Simulation (LES). The simulations were performed in commercial software Ansys Fluent 19.2.

6.4.1 Summary of main finding

The geometry simplification was examined in several steps. The most complex models used full 3D geometry with modelled inlet ports. This model allows for the air-core to divert from the swirl chamber centreline and should provide the most realistic results. Since the atomizer geometry can be divided into three identical parts, the periodic model can be used. The predicted flow parameters were almost identical with the full model, yet the calculation was more stable since the air-core axis was forced to be equal to the swirl-chamber centre line. Further simplification has no discreet inlet port. However, this model diverted from the experimental data and is not viable even if the inlet profile is pre-calculated. The simplest 2D model returns reliable results, but the inlet swirl velocity must be set carefully, since keeping the same angular momentum yielded non-optimal results.

The steady simulations gave comparable data with averaged transient ones, but they were more sensible to a proper mesh selection. However, the steady simulation can produce sufficiently converged results roughly 100× faster than the transient one. The choice of the appropriate physical model is essential. The worst results surprisingly returned the 7-equation RSM model, which should be superior for the swirl dominant flows. The performance of turbulence models was strongly affected by wall functions. The improper wall function prevented the air-core from forming.

The closest results to the experimental data are yielded by the LES model, which was reliable for the whole Re_p range. The laminar model slightly differs at Re_p = 4000, while the k-ω SST overestimated the air-core dimension for the whole Re_p range. Yet, even this model was more accurate than some analytical or empirical correlations. The 3D periodic simulation with steady laminar model was considered as the most cost-effective combination.

The results from this paper served for the preparation of numerical model of the SR atomizers. The preliminary results of SR atomizer simulation show a good agreement with the experimental data presented in Paper III. These simulations will explain some observed phenomena in Paper III and are yet to be published.

6.5 Paper V (Objective E): Effect of nanoparticles on spray parameters

The addition of nanoparticles is a modern way to improve liquid thermo-physical properties. These nanoparticles enhance the thermal properties of a liquid, which e.g. improves heat transfer coefficients of spray cooling [24, 25] or enhances the combustion process [26]. This paper examined the impact of the nanoparticles on the liquid rheology and consequently its effect on the spray generated by the Simplex atomizer. Several different nanofluids were composed of water, surfactant, which improves a mixture stability, and four different types of nanoparticles made from alumina, zinc, copper, and iron oxides. A range of weight concentrations varied between 0.01% and 2%. These nanofluids can be used in spray cooling applications since their thermal properties are better than the base liquid.

The liquid breakup nature and the *SCA* were documented by a high-speed camera, while the PDA system was used to document droplet sizes. Note here that the maximum nanoparticle diameter must not exceed the wavelength of the laser light to prevent noise in the data signal. Therefore, all the nanoparticles including their conglomerates must be smaller than roughly 500 nm. To avoid particle agglomerations, the liquid had to be placed in an ultrasonic bath prior to the measurement.

6.5.1 Summary of main finding

The addition of nanoparticles slightly changes the rheological properties of the base liquid. The nanofluid viscosity increases with particle concentration. The viscosity is considered to have the greatest impact on the spray parameters. The 2% weight concentration changed the liquid viscosity by about 10%. The surface tension was not changed at all, while density slightly increased with the concentration. However, a change in density is usually small and the impact on the spray could be considered as negligible [2].

The camera-based *SCA* differed less than 1° among tested liquids, which is in line with small changes in the liquid rheology. In addition, the difference in the breakup distance was indistinguishable. This suggests that the addition of nanoparticles has no impact on the internal flow, except for a slight change in the liquid rheology, which can be likewise studied using conventional liquids.

The sprayed droplet sizes, discussed by means of integral Sauter mean diameter, differed less than 2 μm among both extremes, which is in a similar order of magnitude as the estimated measurement uncertainty. Hence, the addition of the nanoparticles positively contributes to the spray cooling performance as they enhance the thermal properties of the resulting nanofluid without significantly affecting the hydrodynamic spray characteristics. The results also suggest that further investigation should be focused on higher particle concentrations since the liquid physical properties will be influenced in a more significant way.

7 Conclusion

As formulated in the aim and objectives, this thesis presents an experimental and numerical study of the performance of Pressure-swirl Spill-return (SR) atomizers. The conducted study focused mainly on the internal flow, but the spray parameters were studied to provide a more complete picture.

The summary of the main conclusions from the studies, which fulfils scientific gaps specified in section 4:

- A single central spill-line (SL) orifice inhibits the air-core formation for low *SFR*s, due to recirculation zone, which allows for the liquid from SL to be drained into the swirl chamber and to fill the low-pressure central zone.
- Off axial SL orifices are free of this defect, but the turn-down capability of the atomizer linearly decreases with increasing distance of the SL orifice from the swirl chamber centreline, d_{pc}
- The air-core stability decreases with smaller d_{pc}, yet this effect is only relevant for orifices placed closer to the atomizer axis than half radii of the swirl chamber, $r_c/2$.
- The air-core surface waves are transferred to the discharged liquid sheet; however, the frequencies are in wide spectra without any dominant one.
- These transferred instabilities can change the breakup mode, which consequently harms the atomization quality.
- A shortwave breakup was observed for partially unstable atomizers and produced larger droplets than the stable regime, which generated a long wave breakup with a longer breakup distance.
- The addition of nanoparticle does not change the drop sizes, but may significantly improve liquid thermal properties.
- The CFD simulations proved to be a powerful tool for the atomizer design process. A relatively small sensitivity to the turbulence model selection was found since Laminar, Large Eddy simulation and k-ε models differed by less than 5 %.

The results of this thesis can be beneficial for engineers dealing with atomizer design. It explains several knowledge gaps regarding the design of the Spill-line orifice and reveals its effect on both the internal flow and spray parameters.

7.1 Future research

The basic principles described within this study may found a direct use for many researchers and engineers who deal with the atomizer design. Nevertheless, a map of the SL orifice behaviour is still incomplete. The radial position of SL orifice changes the discharge coefficient of the inlet port, which should be further discussed. It is also still unknown what drives the change in the air-core stability for some off-axial SL configurations. These issues are to be found within CFD simulation, which allows for the fast examination of more geometrical configurations, and reveals unmeasurable characteristics.

Further research within the Spray laboratory is currently focused on the atomizer behaviour in presence of a cross-flow. The liquid sheet stability changes with an airflow and, at certain air velocity, the differences among the atomizers probably diminish.

7.2 Limitations

Due to the complexity of the internal flow, it is unbearable to capture all its features. This study proposed some recommendations on how to design the SR atomizers, but it was focused primarily on the small-scale atomizers. These atomizers found their practical use in e.g. small aircraft turbojet engines. Hence, the liquids with properties similar to the jet A-1 were used. Some geometries may return different results with highly viscous liquids. Moreover, the design of the swirl chamber remained unchanged to isolate the effect of SL orifice. The atomizers that have much higher or lower S_o may show, to some extent, a different flow stability and require a different geometry of the SL orifice.

Further limitations are linked with the laboratory approach itself as several aspects presented in the real-life applications had to be omitted. Such effects are high-temperature environment, elevated surrounding pressure, or presence of ambient airflow. Each of these effects plays a considerable role in the atomizer performance.

8 List of symbols

A	area [mm^2]
b	with [mm]
B	experimental constant [–]
C_D	discharge coefficient [–]
d	diameter [m]
D_{32}	Sauter mean diameter [m]
D	characteristic dimension [m]
Fr	Froude number [–]
g	gravitational acceleration [m/s^2]
h	height [m]
$ISMD$	Integral *SMD* [m]
k	atomizer constant [–]
k_1	atomizer constant as defined in [84] [–]
$\dot{m}$	mass flow rate [kg/s]
p	pressure [MPa]
Q	volumetric flow rate [m^3/s]
r	radius [mm]
R	radial distance [mm]
Re	Reynolds number [–]
SCA	spray cone angle [deg]
SFR	Spill-to-Feed ratio [–]
S_o	Swirl number [–]
u	axial velocity[m/s]
V	velocity [m/s]
w	swirl velocity [m/s]
We	Weber number [–]

Greek symbols

μ	dynamic viscosity [kg/(m·s)]
ρ	density [kg/m^3]
ν	kinematic viscosity [m^2/s]
σ	surface tension [kg/s^2]

Subscripts

a	air-core
c	swirl chamber
inj	injected
inv	inviscid
l	liquid
o	exit orifice
p	inlet port
pc	pitch circle
r	reduced
s	spill-line
$theor$	theoretical

Abbreviations

CFD	Computational fluid dynamics
LDA	Laser Doppler Anemometry
LES	Large Eddy Simulation
PDA	Phase Doppler Anemometry
PS	Pressure-swirl
RSM	Reynolds stress model
SD	Standard Deviation
SL	Spill-line
SR	Spill-return
VOF	Volume of Fluid

9 References

[1] Bayvel, L., and Orzechowski, Z., 1993, Liquid Atomization, Taylor & Francis Inc.

[2] Lefebvre, A. H., and McDonell, V. G., 2017, Atomization and sprays, CRC press.

[3] Amini, G., 2016, "Liquid flow in a simplex swirl nozzle," International Journal of Multiphase Flow, 79, pp. 225-235.

[4] Lefebvre, A. H., and Ballal, D. R., 2010, "Gas turbine combustion alternative fuels and emissions," Taylor & Francis,, Boca Raton, pp. 1 online resource (xix, 537 p.).

[5] Khavkin, Y., 2004, The Theory and Practice of Swirl Atomizers, Taylor & Francis.

[6] Ashgriz, N., and SpringerLink (Online service), 2011, "Handbook of atomization and sprays: Theory and applications," Springer,, New York, pp. xvi, 935 p.

[7] Vijay, G. A., Moorthi, N. S. V., and Manivannan, A., 2015, "Internal and external flow characteristics of swirl atomizers: a review," Atomization and Sprays, 25(2).

[8] Dombrowski, N., and Fraser , P. D., R. P., 1954, "A photographic investigation into the disintegration of liquid sheets," Philosophical Transactions of the Royal Society of London., 247(924), pp. 101-130.

[9] Rizk, N. K., and Lefebvre, A. H., 1985, "Internal flow characteristics of simplex swirl atomizers," Journal of Propulsion and Power, 1(3), pp. 193-199.

[10] Lefebvre, A., and Suyari, M., 1986, "Film thickness measurements in a simplex swirl atomizer," Journal of propulsion and Power, 2(6), pp. 528-533.

[11] Fu, Q.-f., Yang, L.-j., and Qu, Y.-y., 2011, "Measurement of annular liquid film thickness in an open-end swirl injector," Aerospace Science and Technology, 15(2), pp. 117-124.

[12] Moon, S., Abo-Serie, E., and Bae, C., 2010, "Liquid film thickness inside the high pressure swirl injectors: Real scale measurement and evaluation of analytical equations," Experimental Thermal and Fluid Science, 34(2), pp. 113-121.

[13] Sirignano, W. A., and Mehring, C., 2000, "Review of theory of distortion and disintegration of liquid streams," Progress in Energy and Combustion Science, 26(4–6), pp. 609-655.

[14] Hosseinalipour, S. M., Ghorbani, R., and Karimaei, H., 2016, "Effect of liquid sheet and gas streams characteristics on the instability of a hollow cone spray using an improved linear instability analysis," Asia-Pacific Journal of Chemical Engineering, 11(1), pp. 24-33.

[15] Senecal, P. K., Schmidt, D. P., Nouar, I., Rutland, C. J., Reitz, R. D., and Corradini, M. L., 1999, "Modeling high-speed viscous liquid sheet atomization," International Journal of Multiphase Flow, 25(6), pp. 1073-1097.

[16] Chinn, J. J., Cooper, D., Yule, A. J., and Nasr, G. G., 2015, "Stationary rotary force waves on the liquid–air core interface of a swirl atomizer," Heat and Mass Transfer, 52(10), pp. 2037 – 2050.

[17] Maly, M., Jedelsky, J., Sapik, M., Cejpek, o., Slama, J., and Wigley, G., 2018, "Effect of spill orifice geometry on performance of spill-return pressure-swirl atomizers," ICLASS18, p. 8.

[18] Lin, S. P., 2003, Breakup of Liquid Sheets and Jets, Cambridge University Press.

[19] Guildenbecher, D. R., López-Rivera, C., and Sojka, P. E., 2009, "Secondary atomization," Experiments in Fluids, 46(3), pp. 371-402.

[20] Sazhin, S., 2014, Droplets and sprays, Springer.

[21] Santolaya, J. L., García, J. A., Calvo, E., and Cerecedo, L. M., 2013, "Effects of droplet collision phenomena on the development of pressure swirl sprays," International Journal of Multiphase Flow, 56(0), pp. 160-171.

[22] Buongiorno, J., Venerus, D. C., Prabhat, N., McKrell, T., Townsend, J., Christianson, R., Tolmachev, Y. V., Keblinski, P., Hu, L.-w., Alvarado, J. L., Bang, I. C., Bishnoi, S. W., Bonetti, M., Botz, F., Cecere, A., Chang, Y., Chen, G., Chen, H., Chung, S. J., Chyu, M. K., Das, S. K., Paola, R. D., Ding, Y., Dubois, F., Dzido, G., Eapen, J., Escher, W., Funfschilling, D., Galand, Q., Gao, J., Gharagozloo, P. E., Goodson, K. E., Gutierrez, J. G., Hong, H., Horton, M., Hwang, K. S., Iorio, C. S., Jang, S. P., Jarzebski, A. B., Jiang, Y., Jin, L., Kabelac, S., Kamath, A., Kedzierski, M. A., Kieng, L. G., Kim, C., Kim, J.-H., Kim, S., Lee, S. H., Leong, K. C., Manna, I., Michel, B., Ni, R., Patel, H. E., Philip, J., Poulikakos, D., Reynaud, C., Savino, R., Singh, P. K., Song, P., Sundararajan, T., Timofeeva, E., Tritcak, T., Turanov, A. N., Vaerenbergh, S. V., Wen, D., Witharana, S., Yang, C., Yeh, W.-H., Zhao, X.-Z., and Zhou, S.-Q., 2009, "A benchmark study on the thermal conductivity of nanofluids," Journal of Applied Physics, 106(9), p. 094312.

[23] Żyła, G., 2017, "Viscosity and thermal conductivity of MgO–EG nanofluids," Journal of Thermal Analysis and Calorimetry, 129(1), pp. 171-180.

[24] Duursma, G., Sefiane, K., and Kennedy, A., 2009, "Experimental Studies of Nanofluid Droplets in Spray Cooling," Heat Transfer Engineering, 30(13), pp. 1108-1120.

[25] Hsieh, S.-S., Liu, H.-H., and Yeh, Y.-F., 2016, "Nanofluids spray heat transfer enhancement," International Journal of Heat and Mass Transfer, 94, pp. 104-118.

[26] Kannaiyan, K., and Sadr, R., 2017, "The effects of alumina nanoparticles as fuel additives on the spray characteristics of gas-to-liquid jet fuels," Experimental Thermal and Fluid Science, 87, pp. 93-103.

[27] Chinn, J. J., 2008, "The numerics of the swirl atomizer," ILASS, p. 7.

[28] Yule, A. J., and Chinn, J. J., 1994, "Swirl atomizer flow: classical inviscid theory revisited," ICLASS-94, Rouen, France.

[29] Chinn, J. J., 2009, "An appraisal of swirl atomizer inviscid flow analysis, Part 1: The principle of maximum flow for a swirl atomizer and its use in the exposition and comparison of early flow analyses," Atomization and Sprays, 19(3), pp. **263-282**.

[30] Chinn, J. J., 2009, "An appraisal of swirl atomizer inviscid flow analysis, part 2: inviscid spray cone angle analysis and comparison of inviscid methods with experimental results for discharge coefficient, air core radius, and spray cone angle," Atomization and Sprays, 19(3), pp. **283-308**.

[31] Jones, A., 1982, "Design optimization of a large pressure-jet atomizer for power plant," Proceedings of the Second International Conference on Liquid Atomization and Spray Systems.

[32] Ballester, J., and Dopazo, C., 1994, "Discharge coefficient and spray angle measurements for small pressure-swirl nozzles," Atomization and sprays, 4(3).

[33] Benjamin, M., Mansour, A., Samant, U., Jha, S., Liao, Y., Harris, T., and Jeng, S., "Film thickness, droplet size measurements and correlations for large pressure-swirl atomizers," Proc. ASME

1998 International Gas Turbine and Aeroengine Congress and Exhibition, American Society of Mechanical Engineers, p. 8.

[34] Sakman, A., Jog, M., Jeng, S., and Benjamin, M., 2000, "Parametric study of simplex fuel nozzle internal flow and performance," AIAA journal, 38(7), pp. 1214-1218.

[35] Lee, E. J., Oh, S. Y., Kim, H. Y., James, S. C., and Yoon, S. S., 2010, "Measuring air core characteristics of a pressure-swirl atomizer via a transparent acrylic nozzle at various Reynolds numbers," Experimental thermal and fluid science, 34(8), pp. 1475-1483.

[36] Craig, L., Barlow, N., Patel, S., Kanya, B., and Lin, S. P., 2009, "Optimal and Nonoptimal Flows in a Swirl Atomizer," Atomization and Sprays, 19(12), p. 1113.

[37] Wimmer, E., and Brenn, G., 2013, "Viscous flow through the swirl chamber of a pressure-swirl atomizer," International Journal of Multiphase Flow, 53, pp. 100-113.

[38] Malý, M., Janáčková, L., Jedelský, J., and Jícha, M., 2016, "Impact of alternative fuel rheology on spraying process of small pressure-swirl atomizer," AIP Conference Proceedings, AIP Publishing.

[39] Halder, M., Dash, S., and Som, S., 2002, "Initiation of air core in a simplex nozzle and the effects of operating and geometrical parameters on its shape and size," Experimental thermal and fluid science, 26(8), pp. 871-878.

[40] Moon, S., Abo-Serie, E., and Bae, C., 2009, "Air flow and pressure inside a pressure-swirl spray and their effects on spray development," Experimental Thermal and Fluid Science, 33(2), pp. 222-231.

[41] Kim, S., Khil, T., Kim, D., and Yoon, Y., 2009, "Effect of geometric parameters on the liquid film thickness and air core formation in a swirl injector," Measurement Science and Technology, 20(1).

[42] Sumer, B., Erkan, N., Uzol, O., and Tuncer, I., 2012, "Experimental and Numerical Investigation of a Pressure Swirl Atomizer," ICLASS.

[43] Dash, S., Halder, M., Peric, M., and Som, S., 2001, "Formation of air core in nozzles with tangential entry," Journal of fluids engineering, 123(4), pp. 829-835.

[44] Cooper, D., Yule, A., and Chinn, J., 1999, "Experimental measurements and computational predictions of the internal flow field in a pressure swirl atomizer," ILASS 1999.

[45] Jedelsky, J., Maly, M., Jicha, M., Slama, J., and Wigley, G., 2021, "Importance of Geometrical Factors on Spray Characteristics of Spill-Return Atomizers," Journal of Propulsion and Power, TBD, p. 11.

[46] Von Lavante, E., and Maatje, U., 2002, "Investigation of unsteady effects in pressure swirl atomizers," ILASS, p. 11.

[47] Carey, F. H., 1954, "The Development of the Spill Flow Burner and Its Control System for Gas Turbine Engines," Journal of the Royal Aeronautical Society, 58, pp. 737-753.

[48] Kapitaniak, A., 1967, "The Influence of Chosen Construction Parameters on the Performance of Spill-Control Pressure-Jet Atomizers," Journal of the Institute of Fuel, pp. 24-35.

[49] Borodin, V., Dityakin, Y. F., Klyachko, L., and Yagodkin, V., 1968, "Atomization of Liquids," DTIC Document.

[50] Rizk, N. K., and Lefebvre, A. H., 1985, "Drop-size distribution characteristics of spill-return atomizers," Journal of Propulsion and Power, 1(1), pp. 16-22.

[51] Rizk, N. K., and Lefebvre, A. H., 1985, "Spray characteristics of spill-return atomizers," Journal of Propulsion and Power, 1(3), pp. 200-204.

[52] Dai, X. F., Lefebvre, A. H., and Rollbuhler, J., 1989, "Spray Characteristics of a Spill-Return Airblast Atomizer," Journal of Engineering for Gas Turbines and Power, 111(1), pp. 63-69.

[53] Löffler-Mang, M., and Leuckel, W., 1991, "Atomization with Spill-Controled Swirl Pressure-Jet Nozzles," ICLASS, pp. 431-440.

[54] Slowik, G., and Kohlmann, J., 2006, "A swirl controlled hollow cone nozzle and its technical applications," ICLASS06.

[55] Nasr, G. G., Yule, A. J., and Lloyd, S. E., "The Characterisation of the Spray from a New Fine Spray Spill Return Swirl Atomiser," Proc. Proceedings of the 21st ILASS–Europe Meeting.

[56] Nasr, G. G., Yule, A. J., Stewart, J. A., Whitehead, A., and Hughes, T., 2011, "A new fine spray, low flowrate, spill-return swirl atomizer," Proceedings of the Institution of Mechanical Engineers, Part C: Journal of Mechanical Engineering Science, 225(4), pp. 897-908.

[57] W, P. A., 1954, "Spill burner unit for continuous combustion turbine engines," Google Patents.

[58] Tanasawa, Y., Muto, N., Saito, A., and Kawamura, K., 1981, "Spill type swirl injector," Google Patents.

[59] Archetti, M., 2010, "Spill return nozzle," Google Patents.

[60] Schindler, E. S., Lindemann, S., and Dale, J., 2007, "Advanced Mechanical Atomization For Oil Burners," Google Patents.

[61] Hicks, P. G., and Lee, F. P., 2015, "Dual action fuel injection nozzle," Google Patents.

[62] Yule, A. J., and Chinn, J. J., 1997, "Pressure swirl atomizer internal flow and performance," ILASS, Americas, pp. 205-209.

[63] Madsen, J., Hjertager, B. H., and Solberg, T., 2004, "Numerical simulation of internal flow in a large-scale pressure-swirl atomizer," ILASS, pp. 183-188.

[64] Nouri-Borujerdi, A., and Kebriaee, A., 2012, "Numerical simulation of laminar and turbulent two-phase flow in pressure-swirl atomizers," AIAA journal, 50(10), pp. 2091-2101.

[65] Datta, A., and Som, S., 2000, "Numerical prediction of air core diameter, coefficient of discharge and spray cone angle of a swirl spray pressure nozzle," International journal of heat and fluid flow, 21(4), pp. 412-419.

[66] Shaikh, S., Banaszak, U., Von Lavante, E., Cooper, D., and Yule, A., 2004, "CFD prediction of the Effects of Viscosity on the Internal Flow of a Scale Pressure-swirl Atomiser," ILASS.

[67] Laurila, E., Roenby, J., Maakala, V., Peltonen, P., Kahila, H., and Vuorinen, V., 2019, "Analysis of viscous fluid flow in a pressure-swirl atomizer using large-eddy simulation," International Journal of Multiphase Flow, 113, pp. 371-388.

[68] C. Galbiati, S. Tonini, P. Conti, and Cossali, G. E., 2016, "Numerical Simulations of Internal Flow in an Aircraft Engine Pressure Swirl Atomizer," Journal of Propulsion and Power(6), p. 9.

[69] Ghate, K., and Sundararajan, T., 2019, "Effects of orifice divergence on hollow cone spray at low injection pressures," Proceedings of the Institution of Mechanical Engineers, Part G: Journal of Aerospace Engineering, 233(11), pp. 4091-4105.

[70] Ibrahim, A., 2006, "Comprehensive study of internal flow field and linear and nonlinear instability of an annular liquid sheet emanating from an atomizer," PhD Thesis, University of Cincinnati.

[71] Dikshit, S. B., Kulshreshtha, D., and Chaniwala, S., 2011, "Numerical predictions of internal flow through pressure swirl atomizer," Indian Journal of Science and Technology, 4(2), pp. 72-75.

[72] Qian, W., Hui, X., Zhang, C., Xu, Q., Lin, Y., and Sung, C.-J., 2017, "A Numerical Study of the Internal Flow in a Pressure Swirl Atomizer," ASME Turbo Expo 2017: Turbomachinery Technical Conference and Exposition.

[73] Marudhappan, R., Chandrasekhar, U., and Hemachandra Reddy, K., 2016, "Optimization of Simplex Atomizer Inlet Port Configuration through Computational Fluid Dynamics and Experimental Study for Aero-Gas Turbine Applications," Journal of The Institution of Engineers (India): Series C, pp. 1-12.

[74] Abbasi Baharanchi, A., Nordin Darus, A., Ansari, M., and Abbasi Baharanchi, E., 2012, "An Optimum Method of Capturing Interface and a Threshold Weber Number for Inclusion of Surface Tension Force in Simulation of Nozzle Internal Flow in Pressure Swirl Atomizers," (ASME International Mechanical Engineering Congress and Exposition), p. 12.

[75] Mandal, A., Jog, M., Xue, J., and Ibrahim, A., 2008, "Flow of power-law fluids in simplex atomizers," International journal of heat and fluid flow, 29(5), pp. 1494-1503.

[76] Vashahi, F., Dafsari, R. A., Rezaei, S., Lee, J. K., and Baek, B. J., 2019, "Assessment of steady VOF RANS turbulence models in rendering the internal flow structure of pressure swirl nozzles," Fluid Dynamics Research, 51, p. 045506.

[77] Shao, C., Luo, K., Chai, M., and Fan, J., 2018, "Sheet, ligament and droplet formation in swirling primary atomization," AIP Advances, 8(4), p. 045211.

[78] Rizk, N. K., and Lefebvre, A. H., 1987, "Prediction of velocity coefficient and spray cone angle for simplex swirl atomizers," International Journal of Turbo and Jet Engines, 4(1-2), pp. 65-74.

[79] Taeock Khil and Sunghyuk Kim and Seongho Cho and Youngbin, Y., 2009, "Quantification of the transient mass flow rate in a simplex swirl injector," Measurement Science and Technology, 20(7), p. 075405.

[80] Jasuja, A. K., 1979, "Atomization of crude and residual fuel oils," Journal of Engineering for Power-Transactions of the Asme, 101(2), pp. 250-258.

[81] Radcliffe, A., 1960, Fuel Injection, High Speed Aerodynamics and Jet Propulsion, Princenton University Press, Princenton, N.Y.

[82] Babu, R. K., Narasimhan, M. V., and Karayanaswamy, K., 1982, "Prediction of Mean Drop Size of Fuel Sprays from Swirl Spray Atomizers," ICLASS, pp. 99-106.

10 Appendices

10.1 Paper I

International Journal of Heat and Mass Transfer 123 (2018) 805–814

Contents lists available at ScienceDirect

International Journal of Heat and Mass Transfer

journal homepage: www.elsevier.com/locate/ijhmt

Internal flow and air core dynamics in Simplex and Spill-return pressure-swirl atomizers

Milan Maly [a,*], Jan Jedelsky [a], Jaroslav Slama [b], Lada Janackova [a], Marcel Sapik [a], Graham Wigley [c], Miroslav Jicha [a]

[a] Faculty of Mechanical Engineering, Brno University of Technology, Czech Republic
[b] Provyko s.r.o, Czech Republic
[c] Loughborough University, United Kingdom

ARTICLE INFO

Article history:
Received 21 December 2017
Received in revised form 22 February 2018
Accepted 22 February 2018

Keywords:
Internal flow dynamics
Pressure-swirl
Transparent nozzle
CFD
Spill return atomizer
Air core

ABSTRACT

Spill-return (SR) atomizers enhance the construction of Simplex atomizers by addition of a passage in the rear wall of the swirl chamber through which the liquid can be spilled away. It allows to discharge the liquid always at a high pressure and to spray well over a wide flow rate range. The spray characteristics of pressure-swirl atomizers are strongly linked to the internal flow, and the air-core dynamics affect the spray stability. The SR atomizers are rarely investigated and their internal flow is not studied at all. Therefore, in this paper, the Simplex and SR atomizers with a central SR orifice were examined comparatively.

Transparent polymethyl methacrylate (PMMA) models of both atomizers scaled 10:1 were manufactured for the visualization and velocity measurements of the flow inside the swirl chamber. The atomizers were examined by means of high-speed imaging, laser-Doppler anemometry and computational fluid dynamics tools. The experimental and numerical results were analysed and compared in terms of the spray cone angle (SCA), discharge coefficient (C_D), and the morphology and temporal stability of the air core. The internal flow characteristics between the original and the model atomizer were matched using the Reynolds, Swirl and Froude numbers. The test conditions were limited to inlet Reynolds numbers from 750 to 1750.

The results show that the addition of the spill passage strongly affects the internal flow even when the spill-line is closed. The air core in the Simplex atomizer is fully developed and stable for all flow regimes. The SR atomizer behaves differently; with the closed spill-line (spill-to-feed ratio, SFR = 0), the air core does not form at all; therefore, the spray is unstable. The reason is that the liquid, contained in the spill-line, is drained back into the swirl chamber due to a recirculation zone found inside the spill-line. Increasing the SFR stabilizes the internal flow, and the spray becomes stable if SFR > 0.15. The air core begins to form for SFR > 0.4. The results suggest that the axially positioned spill orifice is inappropriate and its placing off-axis would improve the spray stability. The results of the 2D numerical simulation matched closely with the experiments in terms of SCA, C_D, velocity profiles, and air core morphology which proved its prediction capabilities.

1. Introduction

Pressure-swirl (PS) atomizers are used in many applications where a large surface area of droplets is needed, or a surface must be coated with a liquid, e.g. combustion, fire suspension or air conditioning. PS atomizers are easy to manufacture, reliable and provide a good atomization quality. They convert the pressure energy of the pumped liquid into kinetic and surface energy of the resulting droplets. The liquid is injected via tangential ports into a swirl chamber where it gains a swirl motion under which it leaves the exit orifice as a conical liquid sheet. The centrifugal motion of the swirling liquid creates a low-pressure zone in the centre of the swirl chamber and generates an air core along the centreline. The flow inside the atomizer is rather complex; it is two-phase with secondary flow effects. There is a strong link between internal flow conditions and the resulting spray characteristics. However, not all aspects of the internal flow are well understood. A drawback of the Simplex atomizer is that the droplet size depends on the inlet pressure, hence on the liquid flow rate.

* Corresponding author.
E-mail address: milan.maly@vutbr.cz (M. Maly).

https://doi.org/10.1016/j.ijheatmasstransfer.2018.02.090
0017-9310/

Nomenclature

A	area [mm^2]
b	width [mm]
C_D	discharge coefficient [–]
d	diameter [m]
f	frequency [–]
g	gravitational acceleration [m/s^2]
k	atomizer constant [–]
k_{vel}	correction factor [–]
Fr	Froude number [–]
h	height [mm]
$\dot{m}$	mass flow rate [kg/s]
n_1	refractive index of PMMA [–]
n_2	refractive index of the liquid [–]
Q	volumetric flow rate [–]
r	radial distance [mm]
R	radius of the swirl chamber at the measurement plane [mm]
Re	Reynolds number [–]
SCA	spray cone angle [deg]
SFR	Spill-to-Feed ratio [–]
S_1	virtual distance of the measurement volume from the atomizer wall [mm]
S_2	real distance of the measurement volume from the atomizer wall [mm]
S_o	Swirl number [–]
w	velocity [m/s]

Greek characters

Δp	pressure drop at the nozzle [MPa]
μ	dynamic viscosity [kg/(m·s)]
ρ	density [kg/m^3]
ν	kinematic viscosity [m^2/s]
σ	liquid/gas surface tension [kg/s^2]

Subscripts and superscripts

l	atomized liquid
o	exit orifice
s	swirl chamber
p	inlet port
a	air core

The flow rate varies as the square root of the injection pressure. Thus, doubling the flow rate demands a fourfold increase in injection pressure, which means that the range of applicable flow rates is limited and thus the turn-down ratio (defined as the ratio of maximum liquid flow rate to minimum liquid flow rate), which satisfies the requirement of atomization quality, is usually low [1]. This disadvantage can be eliminated using a Spill-return (SR) atomizer which is basically a Simplex type with a passage added in the rear wall of the swirl chamber, see Fig. 1. When the spill-line is closed, the atomizer operates as a standard Simplex type. When a low injection flow rate is required, the liquid is spilled away through the spill orifice while the inlet pressure and the swirl momentum keep high, and the atomization quality remains such as previously. However, an increase in spilled flow rate causes a reduction in the axial momentum of the discharged liquid; this consequently leads to a change in the spray cone angle (SCA), as the SCA is determined by the ratio of the swirl momentum to the axial momentum. Other drawbacks are the requirement for increased pump power and complicated flow metering. For these reasons, the interest in SR atomizers for aircraft combustors has declined. However, if the aromatic content of gas turbine fuels rises, a gum formation in the small sized atomizers could pose serious problems in terms of the atomizer blockage [2,3]. The SR atomizers are virtually free of this defect as they have no small passages. Beside the aircraft combustors, the SR atomizers were used in stationary gas turbines [4] and industrial burners [5]. Also, the above-mentioned advantages of SR atomizers are crucial for special applications that require a fine spray at very low flow rate, e.g. decontamination devices [6], or for atomization of waste fuels and liquids containing impurities where large dimensions of flow cross-sections are necessary to prevent the atomizer from clogging, or for applications where pneumatic atomizers are not allowed

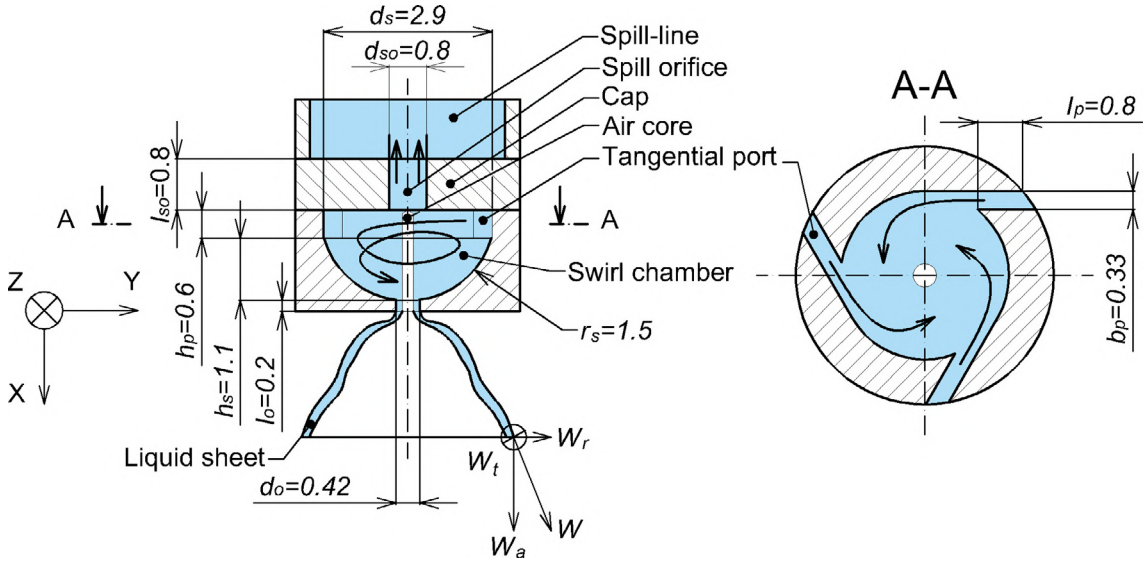

Fig. 1. A sketch of the original SR atomizer with the main dimensions in millimetres. The Simplex atomizer has the same geometry and size, but the spill-line orifice is missing. The transparent atomizer has the same shape, and all dimensions are 10 times larger.

while a wide regulation range is required. The studied SR atomizer is originally used in a combustion chamber of a commercially produced small turbojet aircraft engine.

Before the advent of computational fluid dynamics (CFD), a number of authors attempted to describe the internal flow of Simplex atomizer by relatively simple analytical approaches. One of the first was presented by Taylor [7] who focused on an inviscid analysis using Bernoulli's equation and the principle of maximal flow. Taylor derived an equation for the discharge coefficient (C_D) and the SCA solely dependent on the atomizer constant $k = 2A_p/(\pi d_o d_s)$, where A_p is the total area of the inlet ports, d_o, and d_s are defined in Fig. 1. Similar results were found independently by other authors, and these works have been compared and reviewed by Chinn [8,9]. Results obtained by the inviscid theory are not generally in good agreement with experiments. However, the inviscid theory findings may be used as a basis for design improvements.

The experimental correlations for C_D were found to be more complex than the inviscid theory predicted. Rizk and Lefebvre [10] derived a semi-empirical correlation where, besides the constant k, the ratio d_s/d_o had a strong influence. Jones [11] found a weak dependence of C_D on the length of the swirl chamber and exit orifice, and liquid viscosity. Ballester [12] added a dependence on the inlet pressure. Benjamin [13] followed the work of Jones [11] and found inverse trends for some parameters. Wimmer and Brenn [14] theoretically uncovered a relatively strong effect of the liquid viscosity on C_D, which was later experimentally confirmed by Maly et al. [15].

The internal flow characteristics, especially the air core stability, were addressed by a few authors. Halder [16] investigated the air core shape in 21 different transparent atomizers at various inlet mass flow rates of water. Two limiting values of Reynolds number (Re) were conducted for the inception of the air core for each atomizer. Below the lower limit, the air core was not formed at all, while above the upper limit, it was always found to be stable. He observed that the limiting Re decreases with an increase in d_o/d_s and a decrease in A_p/d_s. The stable air core had a cylindrical shape, and for large Re values, it was almost constant in diameter. For Re close to the limiting value, the diameter of the air core increased sharply with increasing Re. A similar concept of limiting values of Re was introduced by Lee et al. [17]. In this experimental work, a transparent atomizer with diesel and kerosene was used over a range of inlet pressures and temperatures. They deduced that the air core stability was a function of Re related to the exit orifice, Re_o. It was stable for $Re_o > 3300$; at lower values it became unstable until for Re_o below 2400, where there was no air core at all due to insufficient centrifugal forces, and the spray fluctuated strongly. Kim et al. [18] investigated the influence of diameter and length of the swirl chamber on the air core stability. Atomizers with a ratio of the swirl chamber height to its diameter, h_s/d_s, higher than 1.27 demonstrated an unstable air core. The authors [18] described the unstable air core as having a rotating and double helical structure. Moon [19] found a limiting value of the swirl number $S_0 = 0.6$, which ensured a stable air core. The same limiting value of S_0 was also proposed by Park [20] for swirling jets.

SR atomizers have rarely been studied, and their internal flow has not been documented so far to the best of our knowledge. Especially the effect of the spill orifice arrangement on the internal flow is not at all clear. The liquid spill can be realized by a single axial orifice, by several off-axis orifices, or by an annular slot [21]. The simplest designs use a single, axially placed spill orifice but the difficulties with spray stability were reported [21–23], especially under operating regimes with a closed spill-line.

The former approaches to study the internal flow were mostly experimental [24,25] and analytical [8,9,26]. The application of CFD has greatly simplified atomizer design process due to increase in computing performance in recent years. In 1997, Yule and Chinn [27] conducted one of the first numerical studies using a 2D simulation. They assumed a laminar flow even for Re = 50,000; an internal air-core was captured by the Volume of Fluid (VOF) method. They reported the difference between numerical calculations and the experiment to be less than 3%. Similarly a 2D laminar setup was used by Amini [28] and Mandal [29]; both authors reported a close match with experimental data. Summer [30] compared 2D and 3D simulations with a laminar solution and found only small differences between them. Madsen [31] tested laminar and turbulent k-ε models together with a Large Eddy Simulation (LES). The turbulent model overestimated the turbulent viscosity; the air-core was not formed at all. The laminar model was comparable to the LES predictions. Various models to capture the liquid–air interface were investigated by Baharanchi [32]. A geometrical reconstruction scheme was found to be an optimal method for capturing the air core. While there are some papers providing CFD simulations of Simplex atomizers, no numerical simulations of SR atomizer were found.

Due to the lack of published results on SR atomization, the present study aims to investigate the internal flow of SR atomizer experimentally and numerically. Firstly, the study examines the possibility to predict the atomizer characteristics such as C_D and SCA, and the velocity field in the swirl chamber, using a relatively simple 2D simulation. The main focus is to elucidate the effect of the central spill orifice on the spray fluctuations as reported in our previous works [22,33], and to determine their source. Furthermore, the internal flow characteristics are compared with a Simplex atomizer.

2. Atomizer geometries and liquid properties

The experiments were performed using both Simplex and SR atomizer designs. In order to examine the internal flow, the atomizers were manufactured as transparent copies. Due to the small dimensions of the original atomizers (see Fig. 1), it was impossible to manufacture them and to examine their flows directly. To solve this issue, the transparent versions were designed as ten times scaled copies. The scaled atomizers have a modular construction (Fig. 2, right). The assembly consists of three parts, each made from PMMA. The bottom part contains the swirl chamber with the exit orifice, the central one forms the tangential inlet ports, while the top part is a plain wall, in the case of Simplex atomizer or, it contains the axial spill orifice in the case of the SR atomizer. This modular construction allows for each part to be replaced by another one of a different geometry or shape. The surfaces of each part were ground and polished to achieve the transparency sufficient for optical access.

Due to the ten times model scale, it is necessary to match the flow of the original and scaled atomizers so the relevant dimensionless numbers must be considered. Re is defined as the ratio of inertial force to the viscous force. In the case of the swirl atomizer, the most common definition of Re is related to the inlet ports [34] as:

$$Re = w_p d_p / \nu, \tag{1}$$

where w_p is the mean velocity in the inlet ports, calculated as a volumetric flow rate divided by the total cross-section of inlet ports, ν is the liquid kinematic viscosity, and d_p is the hydraulic diameter of the inlet ports:

$$d_p = 2h_p b_p/(h_p + b_p), \tag{2}$$

for the dimensions, see Fig. 1. The Swirl number S_0 is useful to determine the ratio of the angular momentum to the axial momentum. It can be calculated as a function of the internal geometry [34]:

$$S_0 = \pi R r_o / A_p, \tag{3}$$

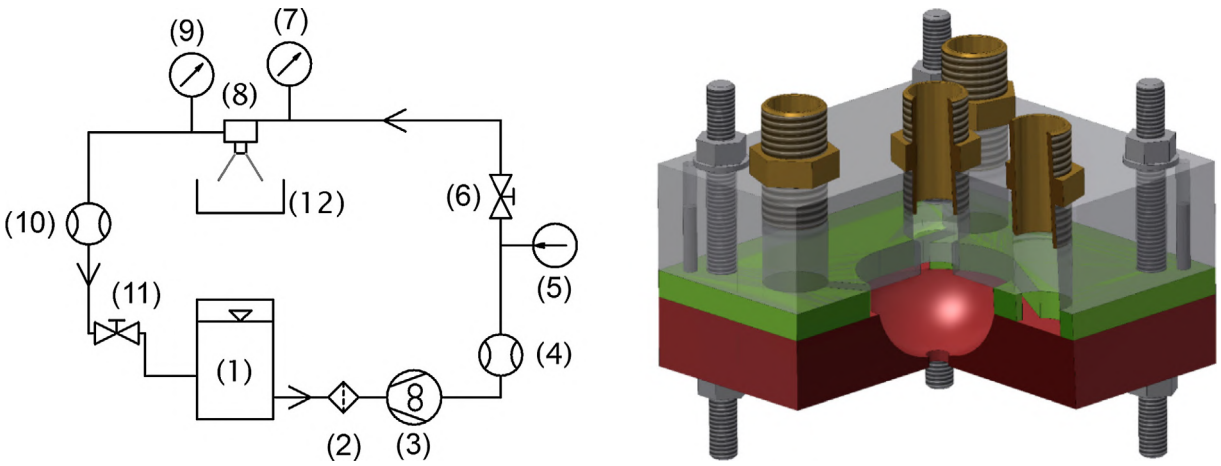

Fig. 2. Left: Schematic layout of liquid supply. Right: A Schematic of the scaled transparent atomizer.

where R is the radius of flow entry to the swirl chamber and A_p is the total cross-section of the inlet ports. It is obvious that the swirl numbers for the original and scaled atomizers are identical. The Froude number (Fr) shows the effect of gravity in comparison with the energy of the bulk flow and is calculated as:

$$Fr = \frac{Q}{2\pi(r_o^2 - r_{oa}^2)\sqrt{r_o g}}, \tag{4}$$

where Q is the volume flow rate and r_{oa} is the radius of the air core in the exit orifice. To minimize the effect of gravity, it is necessary to keep $Fr >> 1$, as in the case of the original atomizer. The Fr for the lowest pressure used was 6.9, thus the effect of gravity was small. Spray related dimensionless numbers, such as Weber number and Ohnesorge number differ between the original and scaled atomizers by an order of magnitude; so, the spray parameters were not investigated, except for the SCA close to the exit orifice.

Table 1 lists the experimental flow regimes with their dimensionless numbers. The operating regimes were derived from those used in the previous study [22]. The main control parameters were the inlet pressures of the original Simplex and SR atomizers. The Re was consequently calculated from measured mass flow rates. The SR atomizer was evaluated with both the closed spill-line to simulate the maximum injection rate and various spill-to-feed (SFR) regimes. Kerosene-type Jet A-1 representing the commonly used fuel was used in both the original and modelled atomizer. However, the refractive index of kerosene differs from the refractive index of the PMMA by about 0.05 at 660 nm wavelength at 25 °C which disturbs the optical measurement close to the internal surfaces of the transparent model. A liquid with a refractive index very close to the PMMA should be used to reduce the optical distortions. For this purpose, several different liquids and mixtures were evaluated to determine the most suitable one. Based on this, Paracymene (p-cymene or 1-Methyl-4-(propan-2-yl)benzene) was chosen. It is a colourless, transparent organic compound with a refractive index different from Plexiglas by less than 0.001 at 660 nm wavelength and at 25 °C. It also has a relatively low aggressiveness to PMMA; however, after a few hours of measurement, it caused cracks in those parts where increased internal stresses may be anticipated, i.e. in the vicinity of bolts and threads; thus, it was only used for high-speed imaging. The physical properties of Jet A-1 are $\sigma = 0.029$ kg/s^2, $\mu_l = 0.0016$ kg/(m·s), $\rho_l = 795$ kg/m^3 and p-cymene: $\sigma = 0.028$ kg/s^2, $\mu_l = 8 \times 10^{-4}$ kg/(m·s), $\rho_l = 850$ kg/m^3.

Two similarly designed test benches were used for testing of both the original and scaled atomizers, see Fig. 2. The test liquids were supplied to the atomizer (8) from a fuel tank (1) via a filter (2) by a gear pump or a centrifugal pump (3) for the original and the scaled atomizer respectively. The mass flow was controlled by varying the pump speed. The fuel flowing through the inlet line was metered by the Coriolis mass flow meter Mass 2100 Di3 fitted with the Mass 6000 transmitter (Siemens AG, GE) (4) with an accuracy ±0.1% of the actual flow rate. Static inlet over-pressure was measured by a piezo-resistive pressure sensor DMP 331i (BD SENSORS s.r.o., CZ) (7). The uncertainty in pressure sensing was 0.05 kPa and 2 kPa for the scaled and the original atomizer respectively as different sensors were used in each case. The inlet line was also equipped with a temperature sensor PR-13 made by OMEGA Engineering, INC., USA with an error of 0.2 °C. The spill-line used a piezo-resistive pressure sensor DMP 331i (BD SENSORS s.r.o., CZ) (9), a ball valve (11) and a positive displacement flow meter KOBOLD DOM-S05 with ±1% accuracy of the actual flow rate (KOBOLD Messring GmbH, GE) (10). The calculated uncertainty of C_D at $Re = 1021$ was 0.14% and 0.25% for the original and scaled

Table 1
Operating flow regimes, kerosene, $S_0 = 3.87$.

		Original atomizer				Scaled atomizer			
	Re [–]	Δp [MPa]	m_l [kg/h]	C_D [–]	Fr [–]	Δp [kPa]	m_l [kg/h]	C_D [–]	Fr [–]
Simplex	755	0.5	5.4	0.387	137	5	53.8	0.378	6.9
Simplex	1021	1	7.3	0.369	293	10	73.1	0.366	9.3
Simplex	1252	1.5	9.0	0.365	359	15	88.2	0.362	11.4
SR, SFR 0.0	1075	0.5	7.7	0.542	308	5	69.4	0.483	9.8
SR, SFR 0.0	1431	1	10.3	0.519	411	10	93.4	0.466	13.0
SR, SFR 0.0	1731	1.5	12.4	0.510	497	15	110.0	0.454	15.7
SR, SFR 0.4	1676	1	12.0	0.378	481	10	103.9	0.261	15.0

Simplex atomizer respectively. The atomized liquid was captured into a collection chamber and routed back into the fuel tank. Fuel mist and vapours were ventilated out by a fan. The atomizer was mounted to a CNC positioning system with a positional error less than 0.1 mm.

3. Experimental and numerical setups

Following subchapters document the setups of the experimental approach using a high-speed camera and laser-Doppler anemometry (LDA) and the CFD simulations.

3.1. Experimental setup

The experiments were performed on the cold test bench at room temperature. A Photron SA-Z high-speed camera was used to document the spatial and temporal behaviour of the air core. The atomizer was illuminated by a background light using a LED panel. Three record types were provided at each operating regime; the first was a general image showing the whole atomizer while the other two observed the exit orifice and the top of the swirl chamber in a close up, see Fig. 3. The camera frame rate was 4,000 and 20,000 fps for the general image; the resolution was 1024 × 1024 px, and the shutter speed was set to 20 µs. The close-up records used a frame rate of 28,000 fps, resolution 768 × 904 px, and a shutter time of 10 µs. Mean and RMS images were calculated for each case. The air core dimensions were captured by MATLAB code based on the Canny edge detector. The air core fluctuations were analysed using the Fast Fourier Transform (FFT) in the cross-section b. The FFT was applied to the time-resolved air core surface captured by the Canny edge detector. Another FFT was used on the average pixel intensities over a rectangle 3 × 3 px placed near the air core boundary to verify the previous FFT approach. The air core dimensions were measured at three cross-sections (a, b and c) over the swirl chamber and one cross-section at the tip of the exit orifice.

The LDA, a FlowExplorer (Dantec Dynamics A/S, Skovlunde, DK), was employed for the point-wise measurement of the velocity of individual particles inside the transparent atomizer. The swirl velocity component was measured in three cross-sections across the swirl chamber (see Fig. 3). The axial distances from the top of the swirl chamber were 2.5, 8 and 13 mm for cross-sections a, b and c respectively, and 50, 38 and 25 measurement points were taken on each cross-section. The distance between two surrounding points was 0.25 mm. The LDA was configured in the backscatter mode. A built-in, diode-pumped solid-state laser generated a beam with wavelength of 660 nm. The beam was split into two parallel beams with the power of 30 mW each. One of the beams was shifted by 80 MHz. A converging transmitting/receiving lens with focal length of 150 mm was used to form an ellipsoidal measurement volume with the size of app. 0.1 × 0.1 × 0.8 mm. Dantec BSA P80 signal processor was used to process the measured signal. BSA flow software v5.20 was used to control the data acquisition and the following setting was used: Photomultiplier sensitivity 700 V, signal gain 20 dB, velocity centre 2.4 m/s, velocity span 4.8 m/s. The measurement was limited to 10,000 samples acquired or a 10-s acquisition duration at each measured point. A repeatability error based on three consequent measurements was less than 4%. The measuring volume position relative to the LDA positioning system had to be corrected due to the different refractive index of the atomizer body and the liquid as [35]:

$$S_2 = R \Big/ \left(1 + \frac{n_1}{n_2}\left(\frac{R}{n_1 S_1} - 1\right)\right), \tag{5}$$

where S_1 is the virtual distance of the measurement volume from the atomizer wall, S_2 is the real distance of the measurement volume, R is the diameter of the swirl chamber at the measurement plane, n_1 and n_2 are the refractive indices of PMMA and kerosene, respectively. The measured velocity was multiplied by a correction coefficient k_{vel} based on the simplified approach from [35] as:

$$k_{vel} = 1 + \frac{S_2}{R}\left(\frac{n_1}{n_2} - 1\right) \tag{6}$$

The correction factor reached the maximum of 1.04 for kerosene at the atomizer axis. In positions close to the air-core, the raw velocity data were filtered since a strong noise was generated by the reflection from the air core surface. The filtration process seeks for the Gaussian distribution in the velocity histogram, and the mean velocity was calculated only from the data which satisfied the Gaussian distribution.

The flow tracer particles were SL75 e-spheres with a mean diameter of 45 µm. Their Stokes number, based on the swirl velocity and diameter of the swirl chamber, was less than 0.01 for each regime, which ensured a sufficiently small flow traceability error.

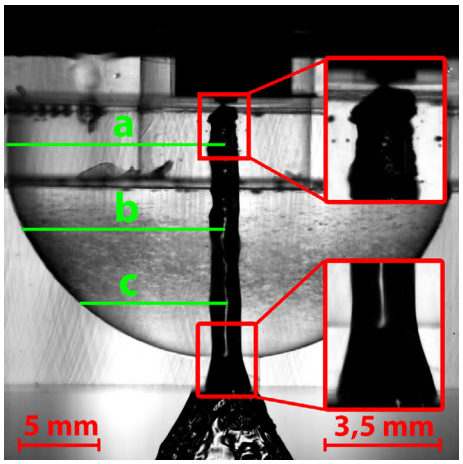

Fig. 3. High-speed visualization, p-cymene, 1 MPa, Simplex, cross-section a, b and c placed 2.5, 8 and 13 mm from the top of the swirl chamber.

3.2. Numerical setup

Conservation of mass (continuity) and conservation of momentum (Navier–Stokes) equations were solved numerically using Ansys Fluent 17.2. The flow simulation was conducted using a transient 2D axisymmetric model. A VOF model with the geo-reconstruct scheme was used to capture the boundary of the air core. The 3D inlet boundary condition was set to conserve the mass flow rate in the radial direction and ensure the same angular momentum in the tangential direction. The pressure outlet boundary condition was applied on the outer boundaries with no-slip conditions applied on the wall boundaries. A laminar flow was assumed due to the low *Re* values inside the inlet ports, and also because the radial forces of the swirl inside the swirl chamber tend to laminarise the flow [34]. The simulations were performed for both the original and scaled atomizers. The SR atomizer was simulated including a 4-mm long part of the spill-line geometry (see Fig. 10 in Section 4.3). The spill flow in the regime with SFR = 0.4 was set as a negative liquid source across the entire spill-line. It was not possible to set the pressure boundary condition to the spill-line wall as the solution was very unstable.

The all quad structured mesh with an average skewness of 0.058 and an average aspect ratio of 1.18 was created (Fig. 4); the mesh independence test was carried out for four different element base sizes in terms of C_D, SCA and the air core diameter (d_a) at

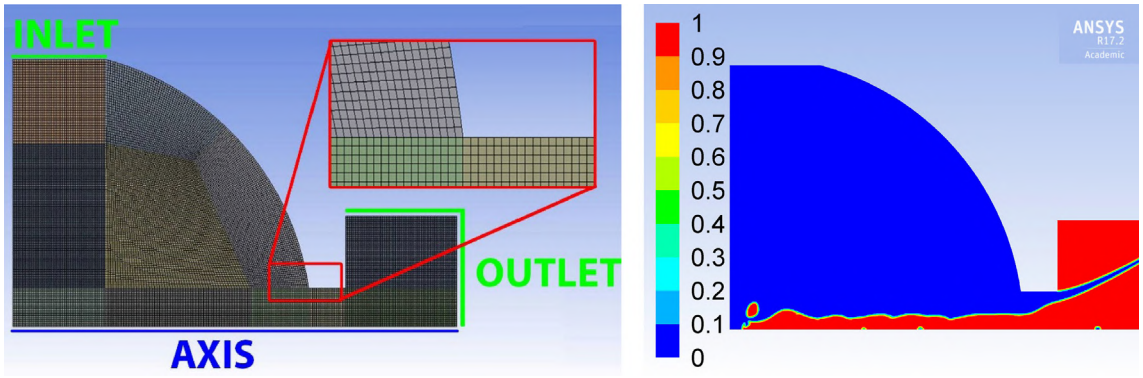

Fig. 4. Left: Numerical domain and its mesh. Right: Typical results obtained with the wavy surface of the air core, phase distribution: 1 = air, 0 = liquid.

Table 2
Mesh independence test.

Number of elements	C_D [–]	d_a/d_o [–]	SCA [deg]
11,684	0.392	0.655	58
22,669	0.365	0.707	58
46,765	0.358	0.710	57
68,610[a]	0.359	0.710	57
90,684	0.356	0.711	56

[a] The base size of the elements was the same as in the case of 46,765 elements. The outflow area was four times larger.

the end of the exit orifice (d_o) in a dimensionless form as d_a/d_o (see Table 2). There was a significant difference between the meshes of 11,684 and 22,669 elements. This difference decreased with further increase in the number of elements, and the mesh of 46,765 elements was chosen as a good compromise between the accuracy and the calculation speed. Two sizes of an outflow area, which is an artificial area downstream of the atomizer outlet, were also tested. A calculation of four times larger outflow area revealed the same results as the original one, see the results for meshes with 68,610 and 46,765 elements.

4. Results and discussion

The air core shape and stability play a key role in the formation of the liquid sheet at the discharge orifice. A description of the air core dynamics is based on high-speed image records and numerical simulations. The discharge parameters are discussed in terms of C_D and SCA. The measured swirl velocity profiles served for consequent validation of the numerical simulations.

4.1. Air core shape and spray cone angle

In a comparative manner, the high-speed records with both kerosene and p-cymene as the working liquid are shown in Fig. 5. For the kerosene image, there are darker regions towards the edge of the swirl chamber. These are caused by light refraction at the swirl chamber wall. It is not evident in the atomizer centre due to the small relative curvature there. This issue is solved using the liquid with the same refractive index as the atomizer body which can be seen for the results of p-cymene.

The air core was found fully developed in the case of the Simplex atomizer. It was cylindrically shaped and increased in its diameter inside the exit orifice; such behaviour was also described by other authors [16,17,28]. The dimensionless diameter of the air core in the exit orifice was $d_a/d_o = 0.72 \pm 0.02$ for all the inlet pressures and both liquids with no evident correlations to *Re*. Inside the swirl chamber, $d_a/d_o = 0.47 \pm 0.03$ and it was also almost independent of *Re*. Both findings are in accordance with other authors [16,36,37] who reported the independent air core size for high *Re* regimes, while Halder and Som [16] found a slightly increasing air core diameter with *Re*. Instabilities, in the form of air core fluctuations, both in the axial and radial direction (Fig. 6), were observed at the top of the swirl chamber. These fluctuations are linked with the wavy structure on the air core surface. The frequency of the surface waves $f = 32 \pm 4$ Hz was estimated using the FFT analysis of images for the Simplex atomizer with p-cymene at $Re = 1021$. A similar analysis was reported by Sumer et al. [30] who used a similarly sized atomizer, but with the velocity in the inlet ports approximately ten times higher; they found wave frequencies of $f = 273$ Hz. Chinn et al. [38] studied the surface waves on the air core and described three distinctive types of surface waves: helical striations, stationary waves and random ripples. They noted that the stationary waves were responsible for changes in the liquid sheet thickness. The same phenomenon was also evident in our records. The helical striations, which are caused by the finite number of the inlet ports, were not observed here.

The situation changed dramatically when the SR atomizer was used. The air core was no longer present in the swirl chamber, and the spray become unstable, even for the highest *Re* values. Only fragments of the core are visible inside the exit orifice (see Fig. 7). The air core was unstable and strongly fluctuating and it even occasionally disappeared. The SCA was fluctuating between 49 and 88 deg with a frequency in the range of 10–20 Hz with no evident correlation to the air core behaviour. This was observed for all the regimes with the spill-line closed.

With increasing spilled flow rate, the swirling momentum increases with respect to the axial momentum, and the flow character changes. The standard mean deviation of SCA featured a high value up to spill-to-feed ratio (SFR) 0.15 as shown in Fig. 8, which corresponds to strong fluctuations. With further increase in SFR, the fluctuations reduced, and the SCA correlates with SFR as $SCA = 62.1 + 23.8 \times SFR^{1.5}$ (see the correlation line in Fig. 8). However, at high SFRs, where the injection flow rate was very low, the fluctuations of SCA become stronger again. The air core is limited to the exit orifice even at SFR 0.4; however, for SFRs higher than 0.15, it was stable enough not to decay. In the relatively narrow range of SFR 0.4–0.65, the air core extends into the swirl chamber. With further increase in SFR, the air core penetrated through the spill orifice so it was not possible to make a further measurement of its length. It is evident that the spray stability is linked to the air core stability within the exit orifice, but it is not necessary to provide a fully developed air core across the entire swirl chamber height to ensure a stable spray. The standard mean deviations of SCA for Simplex and SR atomizers at SFR 0.3–0.4 are approximately equal even if the air core is not fully developed as in the case of SR atomizer.

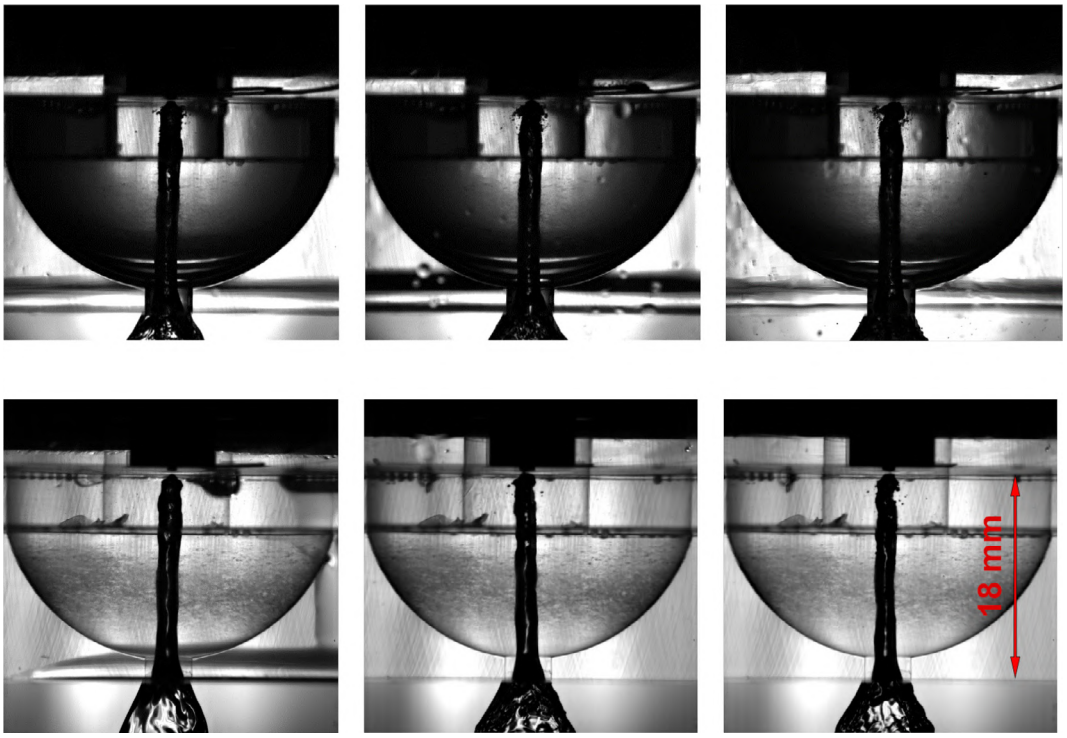

Fig. 5. Simplex atomizer, Top: Kerosene, Bottom: P-cymene. From left to right: flow regime equivalent to 0.5 MPa (*Re* = 755), equivalent to 1 MPa (*Re* = 1021), equivalent to 1.5 MPa (*Re* = 1252).

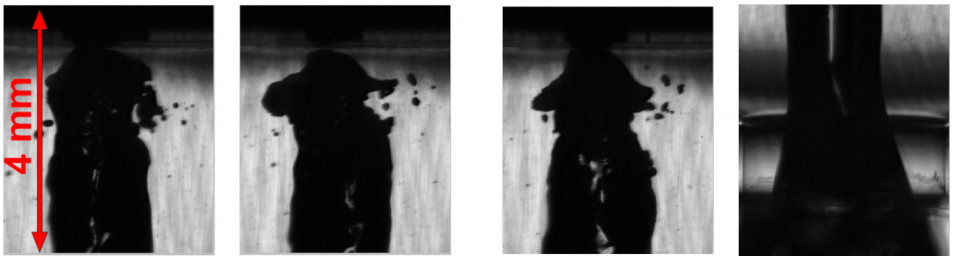

Fig. 6. Simplex, p-cymene, *Re* = 1021, the temporal evolution of the air core tip. Right: the detail on the exit orifice.

Fig. 7. The exit orifice in detail. SR atomizer, SFR 0, p-cymene, flow regime from left to right: equivalent to 0.5 MPa (*Re* = 1075), equivalent to 1 MPa (*Re* = 1431), equivalent to 1.5 MPa (*Re* = 1731).

4.2. Velocity profile inside the swirl chamber

The measured profiles of the swirl velocity (Fig. 9, left) show a disparity between the Simplex and SR atomizers. The velocity profile for the Simplex version features a relatively sharp maximum near the air core interface, which is typical for the Rankine vortex. The central air core behaves like a solid body of the vortex core. In the outer region, a potential vortex distribution can be found. Several authors published a similar velocity profile [39,40]. The swirl velocities are almost identical for all axial distances in both the experiment and simulation (see Fig. 9, right). This is in agreement with the inviscid theory where the swirl velocity depends on the inlet velocity and radial distance from the axis of the swirl chamber out to the mid-point of inlet ports.

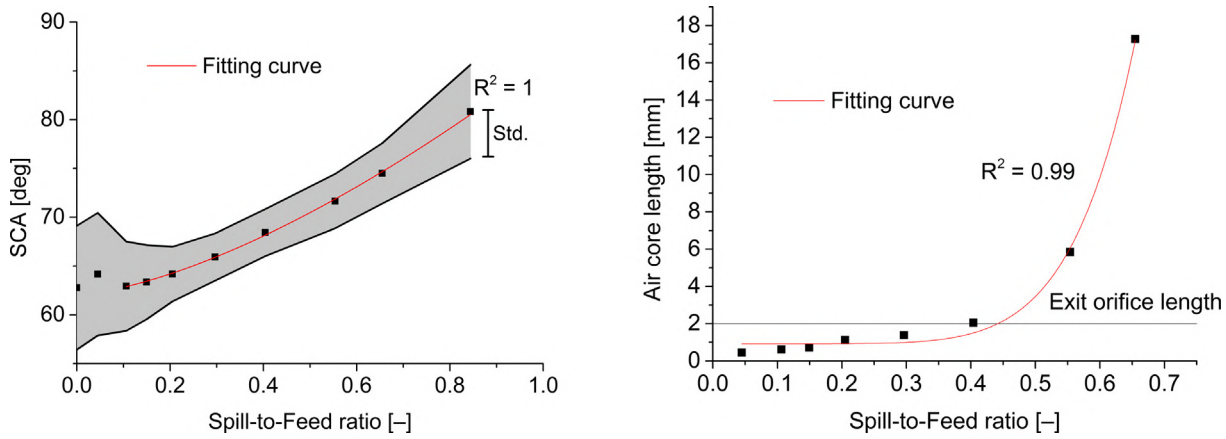

Fig. 8. SCA (left) and air core length (right) in dependence on SFR.

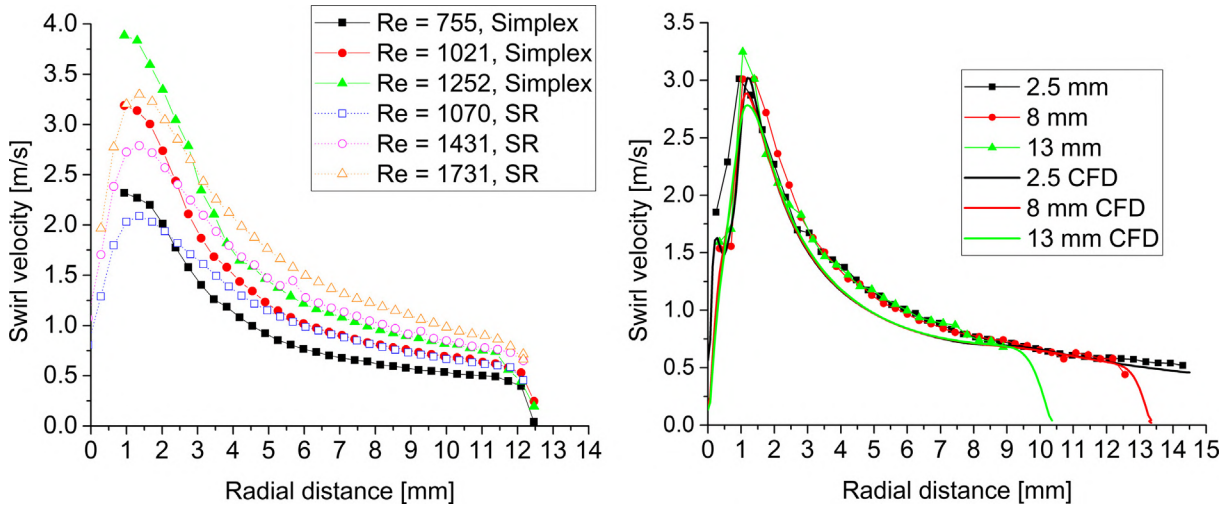

Fig. 9. Swirl velocity profiles from Simplex and SR atomizer; left: kerosene, cross-section b (8 mm from the top), right: comparison of numerical and experimental profiles of swirl velocity, kerosene, Simplex, *Re* = 1021.

In contrast to the Simplex atomizer, the SR type at similar *Re* values has no air core formed and so the atomizer centre is filled with the viscous liquid. This causes a viscous decay of the velocity; thus the velocity maximum is lower and its peak is flatter.

The trends in the swirl velocity profiles were almost identical between experiments and simulations. The simulation slightly underestimates the velocity magnitude at the air core boundary. Similar studies were carried out by Hansen and Madsen [31,39] who conducted both experimental and 3D computational studies of a large-scale PS atomizer. Their earlier study [39] showed that the 3D numerical simulation significantly underestimated the swirl velocity magnitude. In their following work [31], the numerical grid was modified and the inlet tangential ports were properly modelled, which reduced the differences between the experimental and numerical velocity magnitude. This is in contrast to our case where the simple 2D simulation was able to closely predict the swirl velocity even if the inlet ports were substituted by an annular slot.

The numerical simulation reveals some secondary flow effects in the swirl chamber. Görtler vortices can be seen in the near-wall region for both the Simplex and SR atomizers (see the path lines in Fig. 10). A similar behaviour was described in [41].

4.3. Discharge characteristics

Both the original and scaled Simplex atomizers have virtually the same C_D (see Table 1). This is expected as they have the same atomizer constant *k*, operating liquid, and *Re*. However, the SR version shows some disparity between the original and scaled atomizer in the C_D. The scaled atomizer featured a noticeably smaller C_D. This behaviour was attributed to the diameter of the outflow area behind the spill orifice, which was not sized proportionally in the transparent model according to the original atomizer.

The numerical results of Simplex atomizer, when compared with the experiments in terms of global characteristics (C_D and SCA), give a very good agreement (Table 3). The most significant difference was found in the case of low *Re* values where the numerical solution overestimated the C_D by 5%. An increase in *Re* results in a slight decrease in C_D for both the experimental and numerical solutions. The results based on the inviscid theory are dependent only on the atomizer geometry and were calculated in accordance to Chinn [8,9]. The C_D was underestimated by about 15%, and the SCA was overestimated by about 35–65% depending on the equation used. These results can be expected as observed in the real viscous flow; the friction forces cause a decrease in angular momentum. Due to this, the air-core is smaller in diameter, which causes an increase in flow cross-section over the exit orifice, and thus the C_D is increased. Similarly, the SCA is smaller as the angular momentum is decreased. Rizk and Lefebvre [10] published modified correlations for C_D and SCA which show a fair agreement with our experimental and numerical results (see Table 3). However, they did not consider the effect of *Re* in their correlation.

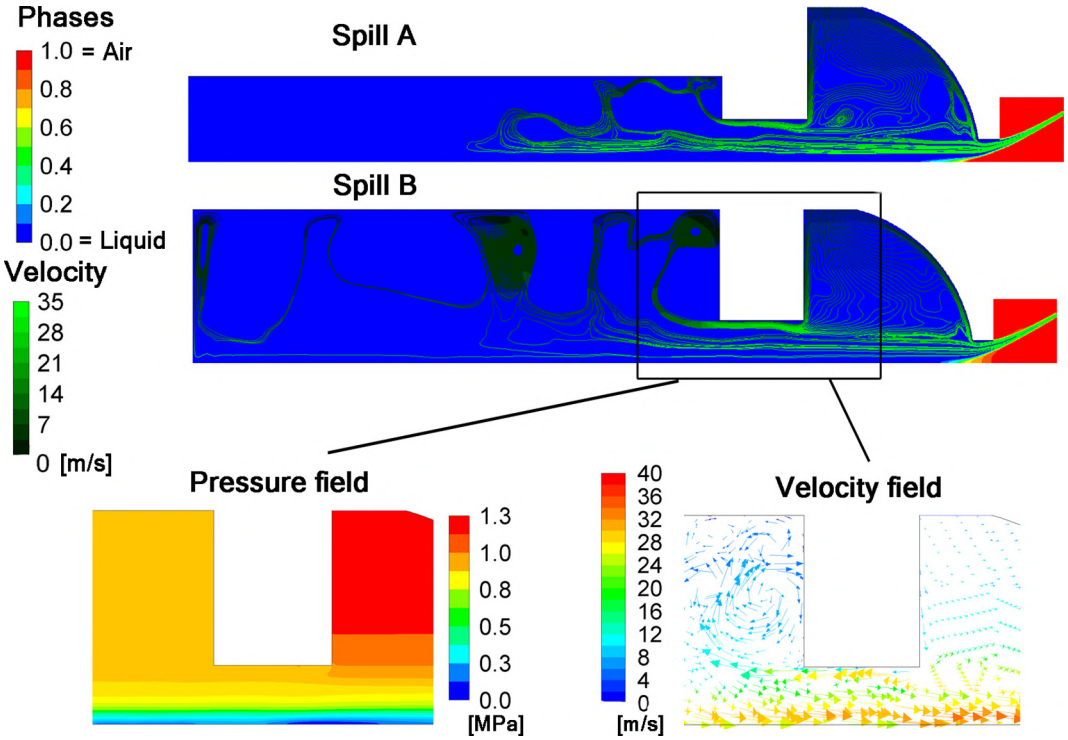

Fig. 10. Spill A and Spill B: Mean phase distributions and path lines, different spill-line geometry. Bottom: a detail of the spill-line: left: pressure field, right: 2D velocity vector field (vector count reduced 50 times).

Table 3
Comparison of numerical and experimental results of the Simplex atomizer.

	Re = 755		*Re* = 1021		*Re* = 1252			
	Num.	Exp.	Num.	Exp.	Num.	Exp.	Inviscid [8,9]	Rizk [10]
C_D [–]	0.410	0.387	0.359	0.369	0.366	0.365	0.312	0.359
SCA [deg]	56.7	58.6	58	59.5	58.7	60.3	80–100	51.6[a]
d_a/d_o [–]	0.62	0.70	0.71	0.71	0.71	0.71	0.7–0.8	–

[a] *Re* = 1021.

In all the numerical simulations of the Simplex atomizers, the wavy interface between the liquid and gas phases was unsteady, see Fig. 4, right. The frequency of the surface wave in the centre of the swirl chamber was, in the case of p-cymene, for *Re* = 1021, app. 25 ± 4 Hz, which agrees well with $f = 32 \pm 4$ Hz in the experiment. However, the fluctuations of the air core tip were overestimated in the simulation as the air core was periodically detaching from the rear wall of the swirl chamber (see Fig. 4).

The unstable behaviour of the SR atomizer was captured well by the simulation. The air core was limited to the exit orifice area in a similar way to the experiments (see Fig. 10 and Table 4). However, the dimension of the spill-line outflow area affected the numerical results. A larger outflow area, as shown in Fig. 10, increased the instabilities of the air core and C_D. This is in agreement with Table 1 where the original atomizer had a relatively large spill outflow area compared to the transparent atomizer. The analysis of the velocity fields inside the spill orifice (see Fig. 10) reveals a recirculation zone inside the spill-line. The liquid flows in both directions thought the spill orifice as it is drawn back into the swirl chamber due to the low-pressure regime in the swirl chamber centre. This flow nature was also observed in the high-speed records. The off-axis replacement of the spill orifice will change the flow behaviour as the pressure distribution across the spill orifice will be uniform; thus, the backflow will be unfeasible.

It shows that our former hypothesis, as regards to a periodically decaying air core as based on the external observation of the original atomizer spray [22], was misleading; the air core is not formed at all. This study is consistent with the fact that the atomizers with the off-axis spill-orifice provide a stable spray under all regimes [22] and under the regimes with a closed spill-line, they behave in the same way as the Simplex type.

Table 4
Comparison of numerical and experimental results of SR atomizer.

	SR, *Re* = 1431, SFR 0			SR, *Re* = 1676, SFR 0.4	
	Exp.	Num. Spill A	Num. Spill B	Exp.	Num. Spill B
C_D [–]	0.519	0.448	0.460	0.378	0.342
SCA [deg]	62.8	57.6	58.2	68	60
d_a/d_o [–]	Decaying	0.45	Decaying	0.56	0.57

5. Conclusions

The discharge and internal flow characteristics of Simplex and SR atomizer, with a central SR orifice, were examined both experimentally and numerically. The numerical results were validated against the results obtained from the high-speed images and point-wise LDA measurements.

The Simplex atomizer featured a stable, cylindrically shaped air core. Its diameter was found independent of *Re* under the measured range of operating conditions.

The numerical simulation, assuming a laminar flow, was able to closely predict the global characteristics (C_D, SCA). The trends and magnitude in mean swirl velocity were both well captured. Unstable waves were observed on the surface of the air core using high-speed imaging and were also captured by the numerical simulation.

The SR atomizer with axially placed spill orifice produced an internal flow without the air core; therefore, the spray fluctuated strongly. A recirculation zone was found inside the spill-line and the liquid flow through the spill orifice in both directions. The velocity profiles showed lower and flatter peak values in comparison to the Simplex atomizer at similar *Re* values. Spill orifices placed off-axis will stabilize the internal flow.

This study provides the primary groundwork for the internal flow analysis of SR atomizers. Further investigations including a more realistic 3D computational model, several different arrangements of the spill orifice and a range of SFRs will follow. The numerical approach proved to be a strong tool for further atomizer design.

Conflict of interest

The authors declares that there is no conflict of interest.

Acknowledgements

This work has been supported by the project No. GA15-09040S funded by the Czech Science Foundation and the project no. CZ.1.05/2.1.00/19.0397, NETME Centre TechUp with the financial support from the Ministry of Education, Youth and Sports of the Czech Republic under the "National Sustainability Programme I" and project Reg. No. FSI-S-17-4444 funded by the Brno University of Technology.

Appendix A. Supplementary material

Supplementary data associated with this article can be found, in the online version, at https://doi.org/10.1016/j.ijheatmasstransfer.2018.02.090.

References

[1] A.H. Lefebvre, Atomization and Sprays, Hemisphere Pub. Corp, New York, 1989.
[2] A.H. Lefebvre, D.R. Ballal, Gas Turbine Combustion, Taylor & Francis, 2010.
[3] N. Rizk, A. Lefebvre, Drop-size distribution characteristics of spill-return atomizers, J. Propuls. Power 1 (1) (1985) 16–22.
[4] F.H. Carey, The development of the spill flow burner and its control system for gas turbine engines, J. Royal Aeronaut. Soc 58 (1954) 737–753.
[5] A. Kapitaniak, The influence of chosen construction parameters on the performance of spill-control pressure-jet atomizers, J. Inst. Fuel (1967) 24–35.
[6] G. Nasr, A. Yule, J. Stewart, A. Whitehead, T. Hughes, A new fine spray, low flowrate, spill-return swirl atomizer, Proc. Inst Mech. Eng., Part C: J. Mech. Eng. Sci. 225 (4) (2011) 897–908.
[7] G.I. Taylor, The Mechanics of Swirl Atomizers, International Congress of Applied Mechanics London, 1948.
[8] J.J. Chinn, An appraisal of swirl atomizer inviscid flow analysis, Part 1: The principle of maximum flow for a swirl atomizer and its use in the exposition and comparison of early flow analyses, Atomizat. Sprays 19 (3) (2009).
[9] J.J. Chinn, An appraisal of swirl atomizer inviscid flow analysis, part 2: inviscid spray cone angle analysis and comparison of inviscid methods with experimental results for discharge coefficient, air core radius, and spray cone angle, Atomizat. Sprays 19 (3) (2009).
[10] N.K. Rizk, A.H. Lefebvre, Internal flow characteristics of simplex swirl atomizers, J. Propuls. Power 1 (3) (1985) 193–199.
[11] A. Jones, Design optimization of a large pressure-jet atomizer for power plant, Proceedings of the Second International Conference on Liquid Atomization and Spray Systems, 1982.
[12] J. Ballester, C. Dopazo, Discharge coefficient and spray angle measurements for small pressure-swirl nozzles, Atomizat. Sprays 4 (3) (1994).
[13] M. Benjamin, A. Mansour, U. Samant, S. Jha, Y. Liao, T. Harris, S. Jeng, Film thickness, droplet size measurements and correlations for large pressure-swirl atomizers, in: Proc. ASME 1998 International Gas Turbine and Aeroengine Congress and Exhibition, American Society of Mechanical Engineers, p. 8.
[14] E. Wimmer, G. Brenn, Viscous flow through the swirl chamber of a pressure-swirl atomizer, Int. J. Multiphase Flow (2013).
[15] M. Malý, L. Janácková, J. Jedelský, M. Jícha, Impact of alternative fuel rheology on spraying process of small pressure-swirl atomizer, AIP Conference Proceedings, AIP Publishing, 2016.
[16] M. Halder, S. Dash, S. Som, Initiation of air core in a simplex nozzle and the effects of operating and geometrical parameters on its shape and size, Exper. Therm. Fluid Sci. 26 (8) (2002) 871–878.
[17] E.J. Lee, S.Y. Oh, H.Y. Kim, S.C. James, S.S. Yoon, Measuring air core characteristics of a pressure-swirl atomizer via a transparent acrylic nozzle at various Reynolds numbers, Exper. Therm. Fluid Sci. 34 (8) (2010) 1475–1483.
[18] S. Kim, T. Khil, D. Kim, Y. Yoon, Effect of geometric parameters on the liquid film thickness and air core formation in a swirl injector, Measur. Sci. Technol. 20 (1) (2009).
[19] S. Moon, E. Abo-Serie, C. Bae, Air flow and pressure inside a pressure-swirl spray and their effects on spray development, Exp. Therm. Fluid Sci. 33 (2) (2009) 222–231.
[20] S.H. Park, H.D. Shin, Measurements of entrainment characteristics of swirling jets, Int. J. Heat Mass Transf. 36 (16) (1993) 4009–4018.
[21] Y. Khavkin, The Theory and Practice of Swirl Atomizers, Taylor & Francis, 2004.
[22] J. Jedelsky, M. Malý, L. Janáčková, M. Jícha, Effect of Geometric Factors on Spray Characteristics and Stability for Small Spill-Return Pressure-Swirl Atomizers, ILASS 2016 Brighton, 2016, p. 12.
[23] G. Slowik, J. Kohlmann, A Swirl Controlled Hollow Cone Nozzle and its Technical Applications, ICLASS06, 2006.
[24] M. Horvay, W. Leuckel, LDA-measurements of liquid swirl flow in converging swirl chambers with tangential inlets, in: 2nd International Symposium on Applications of Laser Anemometry to Fluid Mechanics, 1985, p. 11.
[25] M. Kraemer, M. Horvay, M. Loeffler-Mang, W. Leuckel, Velocity profile measurements within swirl pressure-jet nozzles using LDA, Laser Anemom.-Adv. and Appl. (1988) 141–152.
[26] A.J. Yule, J. Chinn, Swirl atomizer flow: classical inviscid theory revisited, ICLASS-94, Rouen, France, 1994.
[27] A. Yule, J. Chinn, Pressure swirl atomizer internal flow and performance, ILASS, Americas, 1997, pp. 205–209.
[28] G. Amini, Liquid flow in a simplex swirl nozzle, Int. J. Multiph. Flow 79 (2016) 225–235.
[29] A. Mandal, M. Jog, J. Xue, A. Ibrahim, Flow of power-law fluids in simplex atomizers, Int. J. Heat Fluid Flow 29 (5) (2008) 1494–1503.
[30] B. Sumer, N. Erkan, O. Uzol, I. Tuncer, Experimental and Numerical Investigation of a Pressure Swirl Atomizer, ICLASS, 2012.
[31] J. Madsen, B.H. Hjertager, T. Solberg, Numerical simulation of internal flow in a large-scale pressure-swirl atomizer, ILASS (2004) 183–188.
[32] A. Abbasi Baharanchi, A. Nordin Darus, M. Ansari, E. Abbasi Baharanchi, An Optimum Method of Capturing Interface and a Threshold Weber Number for Inclusion of Surface Tension Force in Simulation of Nozzle Internal Flow in Pressure Swirl Atomizers, (ASME International Mechanical Engineering Congress and Exposition), 2012. p. 12.
[33] L. Durdina, J. Jedelsky, M. Jicha, Investigation and comparison of spray characteristics of pressure-swirl atomizers for a small-sized aircraft turbine engine, Int. J. Heat Mass Transf. 78 (2014) 892–900.
[34] J.J. Chinn, "The numerics of the swirl atomizer," ILASS, 2008.
[35] Z. Zhang, LDA Application Methods: Laser Doppler Anemometry for Fluid Dynamics, Springer, 2010.
[36] A. Datta, S. Som, Numerical prediction of air core diameter, coefficient of discharge and spray cone angle of a swirl spray pressure nozzle, Int. J. Heat Fluid Flow 21 (4) (2000) 412–419.
[37] S. Moon, E. Abo-Serie, C. Bae, Liquid film thickness inside the high pressure swirl injectors: Real scale measurement and evaluation of analytical equations, Exp. Therm Fluid Sci. 34 (2) (2010) 113–121.
[38] J. Chinn, D. Cooper, A. Yule, G. Nasr, Stationary rotary force waves on the liquid–air core interface of a swirl atomizer, Heat Mass Transf. (2015) 1–14.
[39] K. Hansen, J. Madsen, C. Trinh, C. Ibsen, T. Solberg, B. Hjertager, A computational and experimental study of the internal flow in a scaled pressure-swirl atomizer, Zaragoza 9 (2002) 11.
[40] M. Horvay, W. Leuckel, Experimental and theoretical investigation of swirl nozzles for pressure-jet atomization, German Chem. Eng. 9 (5) (1986) 276–283.
[41] D. Cooper, A. Yule, J. Chinn, "Experimental measurements and computational predictions of the internal flow field in a pressure swirl atomizer," ILASS, 1999.

10.2 Paper II

Experimental Thermal and Fluid Science 106 (2019) 159–170

Contents lists available at ScienceDirect

Experimental Thermal and Fluid Science

journal homepage: www.elsevier.com/locate/etfs

Effect of spill orifice geometry on spray and control characteristics of spill-return pressure-swirl atomizers

M. Maly[a,*], M. Sapik[a], O. Cejpek[a], G. Wigley[b], J. Katolicky[a], J. Jedelsky[a]

[a] Brno University of Technology, Czech Republic
[b] Loughborough University, United Kingdom

ARTICLE INFO

Keywords:
Spill-return atomizer
Spray cone angle
PDA
Sauter mean diameter
Spill orifice
Break up

ABSTRACT

Many spray process technologies require variable liquid flow rates or droplet sizes. Frequently used Simplex atomizers, favoured for their simple construction, reliability and fine spray, have a limited regulation range due to their flow rate dependency on the square root of the inlet overpressure, p_l. To overcome this drawback, spill-return versions of the atomizer were developed in the past but so far rarely investigated in depth. In this paper, small spill-return atomizers (SRAs) were designed and investigated experimentally using Phase Doppler Anemometry (PDA) and high-speed imaging with the aim to determine the effect of the spill orifice design, e.g. the positioning of the axial and off-axis spill orifices, their number and inclination on the control characteristics, nozzle efficiency and spray characteristics. Such detailed data were not to be found in the open literature.

The off-axial spill orifice version produced a stable spray under all flow regimes investigated while the axially positioned spill orifice provided an unstable spray for low spill-to-feed ratios (*SFR*). However, the axially placed spill orifice was found to be more energy efficient as it required a lower spill flow rate to achieve the same injection flow rate. The radial position of the spill orifices affected the turndown ratio and liquid breakup nature. The atomizers with spill orifices placed close to the swirl chamber centreline generated a liquid sheet which disintegrated in short-wave breakup mode while the other atomizers demonstrated a long-wave breakup mode. This mode produced longer liquid breakup length and formed droplets with smaller Sauter mean diameters. Atomization efficiency was found to decrease linearly with *SFR* and almost inversely proportional to p_l. These findings have produced practical guidelines and recommendations for atomizer designs to suit specific goals and are addressed to both atomizer designers and application engineers. The experimental data form a significant base to validate advanced numerical simulations of the SRA sprays.

1. Introduction

Pressure-swirl atomizers are common in numerous engineering applications where a large surface area of droplets is required, e.g. in combustion, where the atomizer design directly affects the combustion efficiency, flame stability and pollutant emissions. Simplex pressure-swirl atomizers typically produce a hollow-cone spray with droplet sizes inversely proportional to the inlet overpressure, p_l, hence to the mass flow rate. Doubling the flow rate requires fourfold increase in p_l, which means that the range of applicable flow rates is limited. This disadvantage can be overcome using a pressure-swirl spill-return atomizer (SRA). It is basically a Simplex pressure-swirl atomizer that contains a bypass in the rear wall of the swirl chamber known as the spill-line (SL) orifice. The liquid is injected via tangential ports into the swirl chamber where it is divided into two streams; one of them is discharged into the surroundings and atomized while the other one is "spilled" back to the reservoir through the SL orifice. The spilled amount is controlled by a regulator in the SL. The main advantage of this versatile system is that the liquid is supplied to the swirl chamber at a constant and high pressure providing good atomization over a wide span of injection flow rates. This feature allows the use of SRAs in applications requiring a wide regulation range, such as industrial burners and gas turbine combustors [1–3]. Other attractive features come from there being no moving components, and, since the flow passages are designed to handle large flow rates, there is a resistance to clogging. An important operating parameter of SRAs is the ratio of spilled liquid amount $\dot{m}_s$ to the total flow rate through the inlet ports $\dot{m}_p$, called the spill-to-feed ratio: $SFR = \dot{m}_s/\dot{m}_p$. When $SFR = 0$, the atomizer is operated as in the Simplex mode, while with increasing *SFR*, the injected flow rate decreases.

* Corresponding author.
E-mail address: milan.maly@vutbr.cz (M. Maly).

https://doi.org/10.1016/j.expthermflusci.2019.04.014
Received 22 December 2018; Received in revised form 11 March 2019; Accepted 14 April 2019
Available online 16 April 2019

Nomenclature

A	area [m^2]
b	width [m]
B	empirical constant [–]
C_c	Cunningham correction factor [–]
C_{DS}	SL discharge coefficient [–]
d	diameter [m]
D_{20}	surface mean diameter [m]
D_{30}	volume mean diameter [m]
d_{pc}	Pitch Circle Diameter [m]
f_i	data-rate [–]
k	atomizer constant [–]
h	height [m]
ISMD	Integral Sauter mean diameter [m]
L	distance from the breakup point to the measurement point [m]
l_b	breakup length [m]
$\dot{m}$	mass flow rate [kg/h]
r	radial distance [m]
Re	Reynolds number [–]
SCA	spray cone angle [°]
SFR	Spill-to-Feed ratio [–]
SMD	Sauter mean diameter [m]
t	liquid sheet thickness [m]
U	axial velocity [m/s]
v	relative velocity [m/s]
We_g	gas Weber number [–]
Z	axial distance [m]

Greek characters

p	pressure drop at the nozzle [Pa]
μ	dynamic viscosity [kg/(m·s)]
ρ	density [kg/m^3]
ν	kinematic viscosity [m^2/s]
σ	liquid/gas surface tension [kg/s^2]
η_a	atomization efficiency [–]

Subscripts and superscripts

c	swirl chamber
g	surrounding gas
inj	injected
l	atomized liquid
p	inlet port
s	spill-line

A number of studies have focused on the improvement of the spray characteristics of the simplex atomizers, but only a few have investigated the SRA and even fewer studies have examined the effect of the configuration of the SL orifices on the spray quality and stability. A study of SRAs by Carey [4] in 1954 discussed the optimal position of the SL orifice and suggested the use of off-axial orifices. It was also noted that the axial SL orifice might cause penetration of the internal air-core into the SL and consequently the air may leak into the fuel-line and pump. Rizk and Lefebvre [5,6] used a light scattering technique to measure the droplet sizes produced by three SRAs with different swirl chamber geometries and a single axially placed SL orifice at various inlet pressures and *SFR*s. The Sauter mean droplet diameter (*SMD*) and size distribution were found to be almost independent of *SFR* but the spray cone angle, *SCA*, widened sharply with increasing *SFR*. This behaviour is typical for the SRA, where the axial momentum of the discharged liquid reduces with increases in *SFR*, but the tangential component remains the same. Dai and Lefebvre [7] in a later study found increasing droplet sizes with *SFR*. Nasr et al. [8] investigated several different diameters for the SL orifice in terms of *SMD* and mass flow rate. Their atomizers were run with a fully open SL without any regulation. The *SFR* was controlled by changing the cross-section of the SL orifice. They found an increase in *SMD* with *SFR*; i.e. similar to the results in [7].

The internal flow of SRAs was investigated by Loefer-Mang et al. [9]. They used a transparent atomizer with a central SL orifice operated at relatively high Reynolds number in the range of *SFR* = 0–0.9. The air-core was found to be fully developed under all operating regimes and its diameter enlarged with increasing *SFR*. Droplet sizes in the spray were also measured, but the atomizer was only operated at a constant pumped flow rate. Thus, these results are not comparable with the other papers cited since most kept the inlet pressure constant.

The effect of an axially placed SL orifice on the internal flow was recently documented by Maly et al. [10]. In contrast to [9], the axial SL orifice caused decay of the internal air-core in the regimes of *SFR* < 0.15, and the spray fluctuated strongly. In these regimes, a recirculation zone was found inside the SL as the liquid was drained back from the SL into the swirl chamber due to the low-pressure zone along the swirl chamber centreline. Khavkin [11] suggested placing the SL orifice at a radius $r_s/2$, where r_s is the radius of the swirl chamber. In this case, the amount of the spilled liquid is proportional to the square root of the pressure difference between the inlet and SL, and the atomizer is expected to be resistant to spray fluctuations.

In general, there are several mechanisms which affect the droplet sizes which are linked with the parameters of the discharged liquid sheet; its thickness, relative velocity to surrounding gas and SCA [1]. The liquid sheet disintegration process has been mathematically described by several authors [12–15]. Linear stability theory, based on the wave growth on the liquid sheet surface, caused by aerodynamic forces, was mostly used. The results of these analyses show the correlations of the breakup length with sheet parameters which could serve as estimators of the ligament size and consequently droplet size [16]. For the SRA, an increase in *SFR* results in a wider spray cone and, also, in a thinner liquid sheet at the discharge orifice since the swirl velocity component is high but the flow rate is low. From a simple geometric consideration, increasing *SCA* further reduces the thickness of the conical liquid sheet at the breakup distance [7]. As the droplet sizes are a function of the liquid sheet thickness then, increasing *SFR* should improve the atomization quality. However, the breakup length is similarly affected and is shorter for the thinner liquid sheets [12], which may counterbalance the positive effect of the wider spray cone. Moreover, the discharge velocity decreases with increasing *SFR*, which reduces the intensity of secondary breakup [17] but also decreases the growth rate of the surface waves and increases the breakup length [18]. Finally, the stability of the internal flow affects the breakup length since the instabilities of the liquid sheet are driven by the initial perturbances prior discharge.

To the best of our knowledge, there has been no systematic study comparing different geometries of the SL orifices. The purpose of this study is to investigate the effect of the SL orifice geometry on the performance of the SRA such as the regulation range and spray parameters. Various SRAs have been investigated for a range of p_l = 0.25–1 MPa and *SFR* from 0 to 0.9. The only difference among the atomizers was the geometry of the SL orifices. The single axially placed SL orifice, used originally in a combustion chamber, was compared with several modifications with the off-axial SL orifices.

2. Experimental methods

The experimental data included in this paper were acquired using a cold test bench in the Spray laboratory at the Brno University of Technology. The following paragraphs describe the equipment and instrumentation used and include discussion of the atomizers, the test bench, PDA system and high-speed imaging.

2.1. The atomizer designs

The SRAs investigated have tangential entry ports of a rectangular cross-section, see Fig. 1. The original atomizer, with an axially positioned SL orifice, was found prone to spray fluctuations. Therefore, the atomizer cap was modified and investigated here with several SL modifications to improve the spray stability by preventing the air core failure. There are many possibilities as to how to design the SL orifice. The number, size and inclinations of the orifices together with their pitch circle diameter affect the atomizer performance foremost. The flow area of the SL orifices changes the regulation range as more liquid can be spilled away through the larger orifices. Although the flow area increases with the number and size of the orifices, in this paper, a maximum of two orifices is used due to manufacturing simplicity. Inclined SL orifices are investigated here for the first time. Thus, their effect is an unknown. However, the inclination should help with the liquid intake into the orifice as the standard SL orifices are perpendicular to the flow and energy loss would occur here. Finally, the distance from the swirl chamber centreline to the orifices, defined by the pitch circle diameter, influences the regulation range as the static pressure is changing across the swirl chamber.

Several caps with two off-axial SL orifices were designed. For the sake of simplicity, the diameter of the off-axial orifices was kept constant. It is important for all the flow passages to prevent clogging; therefore, minimal diameter of the SL orifices should be similar to the diameter of the exit orifice. Two off-axial orifices were used to keep the symmetry and circumferential periodicity of the swirl chamber, which is beneficial for the manufacturing simplicity and provides the flow and spray symmetry. Larger spill-orifices enable greater flow rates and consequently greater *SFR*. Theoretically, at very high *SFR*s, the spray cone angle approaches 180°. However, our preliminary experiments showed that the spray tends to be very unstable and asymmetric if $SFR > 0.92$. Also, the flow rate requirements grow, the atomization efficiency drops with *SFR* increase and the regulation is more problematic as small difference in spill-line pressure, p_s, causes greater differences in $\dot{m}_s$. Thus, these regimes are not suitable for this small-sized atomizer if operated at relatively low p_l. Hence, the flow area of the SL orifices was designed to reach $SFR \sim 0.9$ with fully open spill-line.

The SL orifice axes were parallel, or inclined, to the main swirl chamber axis, see the lower row in Fig. 2. The atomizers C1, C2 and C3 used parallel SL orifices placed at different distances from the swirl chamber centreline; C1 had the SL orifice placed on an outer boundary of the swirl chamber at a pitch circle diameter $d_{pc} = 2.2$ mm, C2 on $d_{pc} = r_s/2$, and C3 closer to the swirl chamber centreline at $d_{pc} = 0.8$ mm. A modified version of the C1 atomizer, C1T, was also introduced with tangentially inclined SL orifices. Similarly, C2R and C2L atomizers based on the C2 atomizer, were designed but with the SL orifices radially inclined, or larger in the diameter, respectively. The original atomizer C4 used a single axially placed orifice with flow area twice as large compared to the off-axial orifices. In operation the air-

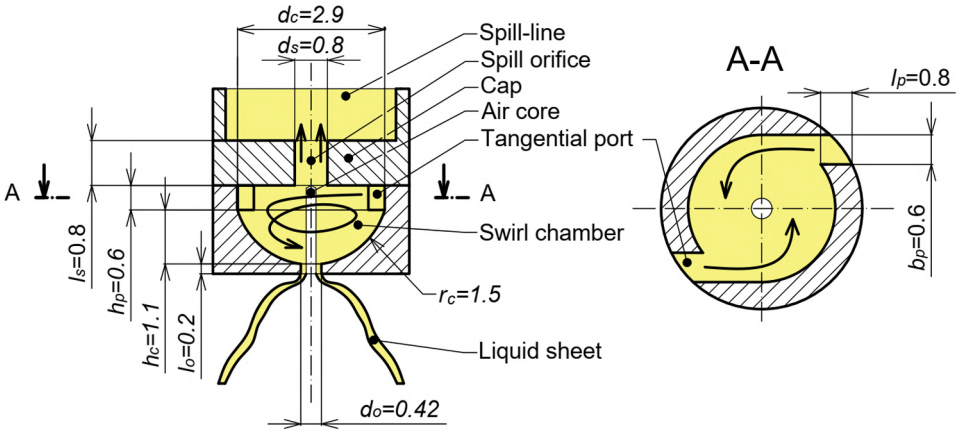

Fig. 1. Sketch of the original SRA (C4) with the main dimensions given in millimetres; side section (left) and top section (right).

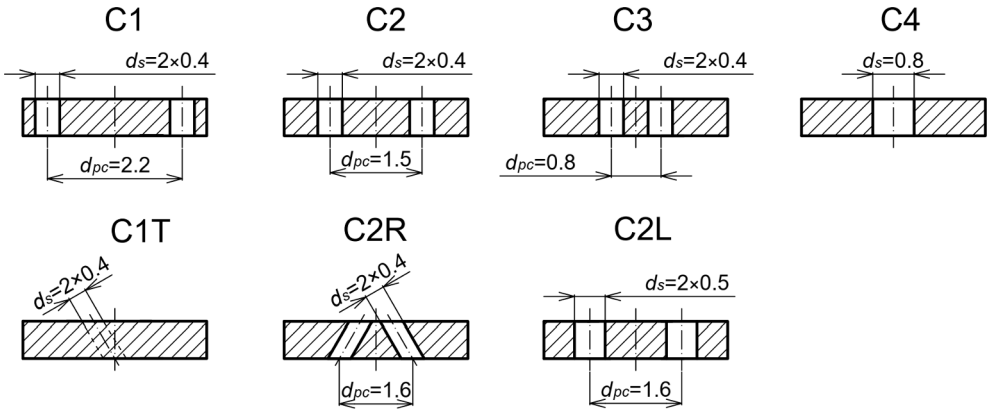

Fig. 2. Different SL geometries: off-axis spill orifices with the parallel orifice axes (C1-C3, C2L); axially-positioned (C4); tangentially-inclined toward the main atomizer axis (C1T) and radially-inclined toward the main atomizer axis (C2R).

core penetrates through the axial orifice, and partially blocks its cross-section so the effective flow area is significantly reduced. Therefore, the effective flow areas of the axially placed orifice and the off-axial orifices are comparable. The geometrical dimensions were inspected using an optical microscope and the maximal geometrical deviation from Fig. 2 was found to be ± 0.01 mm for the SL orifice diameter and ± 0.05 mm for the pitch circle diameter.

Jet A-1 fuel (Kerosene) was used as the test liquid. Physical properties of Jet A-1 at room temperature are as follows: surface tension $\sigma = 0.029\,kg/s^2$, liquid dynamic viscosity $\mu_l = 0.0016\,kg/(m{\cdot}s)$, and liquid density $\rho_l = 795\,kg/m^3$. The experiments were performed for p_l between 0.25 and 1 MPa and for several *SFR*s in the range of *SFR* = 0–0.9. The atomizer was mounted to a three-axis computer controlled traverse mechanism. The alignment accuracy of the atomizer with the measurement volume of the PDA system was ± 0.3 mm. The spray was discharged from the atomizer into stagnant surrounding air at room temperature of 23 °C with gas density $\rho_g = 1.2\,kg/m^3$.

2.2. The test bench

The test liquid was supplied to the atomizer (8) from a fuel tank (1) by a gear pump (3) via a filter (2), see Fig. 3. The liquid flow rate was controlled by varying the pump speed. The amount of the pumped liquid was metered using a Coriolis mass flow meter Mass 2100 Di3 fitted with a Mass 6000 transmitter (Siemens AG, GE) (4) with an accuracy of ± 0.1% of the actual flow rate. Static over-pressures in the inlet (7) and spill (9) line were measured with piezo-resistive sensors BD Senzor DMP 331i (BD SENSORS s.r.o., CZ) with an accuracy of ± 2 kPa. The inlet line was also equipped with a temperature sensor PR-13 (OMEGA Engineering, INC., USA) with an error of 0.2 °C. The SL contained a needle valve (11) used to control the spilled flow rate and a positive displacement flow meter DOM-S05 (KOBOLD Messring GmbH, GE) (10) with an accuracy of ± 1% of the actual flow rate. The atomized liquid was captured in a collection chamber (12) and flowed back into the fuel tank. Spray mist and vapours were captured by an oil mist separator.

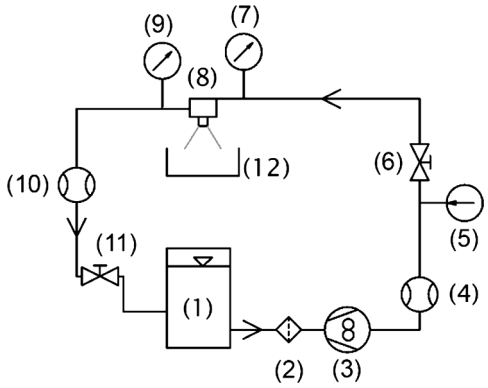

Fig. 3. Schematic layout of the cold test bench.

2.3. Droplet sizing

The size and velocity of the spray droplets were probed using a two-component fibre-based commercial PDA (Dantec Dynamics A/S Skovlunde, DK), see Fig. 4. The PDA acquires the axial and radial or tangential velocity components in the coincidence mode along with the simultaneous drop sizes. The spray was probed at axial distances of Z = 12.5 and 25 mm from the exit orifice along two radially orthogonal axes. There were 17 and 25 radial positions on each axis for Z = 12.5 and 25 mm respectively; the step size was 2 mm between two adjacent points. In each measurement point either 35,000 samples were acquired, or a 15-second acquisition duration was achieved, whichever required the shorter time interval. The PDA measurement was controlled by the Dantec BSA software 5.2; for the detailed setup see Fig. 4, right.

The integral Sauter mean diameter, *ISMD*, ID_{32}, provides the global representation of the Sauter mean diameter by its mass-weighted averaging over the entire radial profile [19]:

$$ISMD = ID_{32} = \sum_{i=1}^{n} r_i f_i D_{30,i}^3 / \sum_{i=1}^{n} r_i f_i D_{20,i}^2 \quad (1)$$

where r_i is a radial distance from spray centerline, f_i is the data-rate, D_{20} is a surface mean diameter and D_{30} is a volume mean diameter. The error in the consistency of the *ISMD* measurements was less than ± 2 μm.

2.4. Spray visualization

A high-speed camera FASTCAM SA-Z (Photron, Japan) was used to document the liquid breakup and spray macrostructure. The spray was background illuminated by a pulsed LED light model HPLS-36DD18B (Lightspeed Technologies, USA). The light pulse duration was 300 ns, the camera frame rate was 60,000 fps, and the shutter speed was 350 ns. For each imaging sequence, 3000 frames were captured, each of them was analysed individually and the results were consequently averaged. The *SCA* was detected using an in-house MATLAB® code based on the Canny edge detector. In this paper, the *SCA* is represented by the subtended angle between two straight lines drawn along the

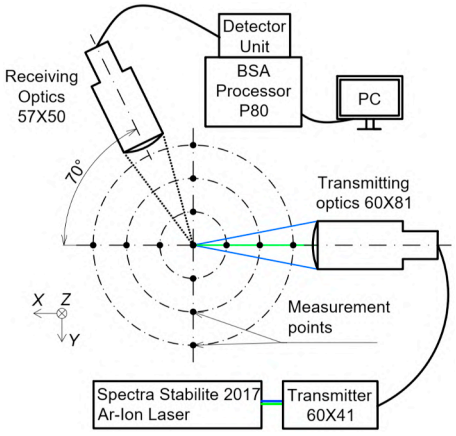

Parameter		Value	
Laser power output		0.3 W (total)	
Wavelength		488 and 514.5 nm	
Focal length of optics:	transmitting	310 mm	
	receiving	800 mm	
Scattering angle		70°	
Receiver mask		B	
Receiver spatial filter		0.1 mm	
Processor setup			
Velocity component		Axial	Radial
Velocity centre		18 m/s	0 m/s
Velocity span		48 m/s	45 m/s
Sensitivity		800 V	1000 V
SNR		0 dB	0 dB
Signal gain		14 dB	14 dB
Level validation ratio		8	2

Fig. 4. A setup of the PDA measurement with a coordinate system (left) and the main system parameters (right).

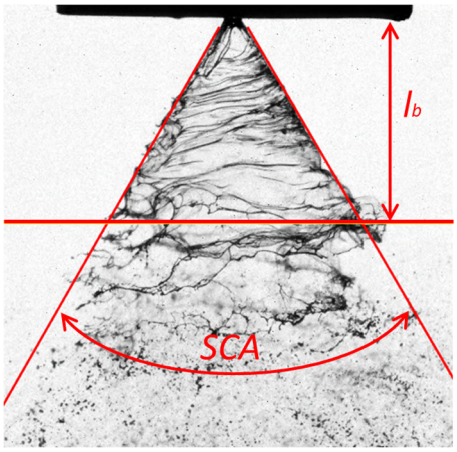

Fig. 5. Spray cone angle and breakup length measurement.

liquid sheet up to $Z = 3$ mm from the atomizer – see Fig. 5. The uncertainty of the *SCA* measurements was ± 2°. The breakup length was determined as the axial distance from the atomizer exit orifice to a point, where the liquid sheet starts to be ruptured (see l_b in Fig. 5). It was estimated with a statistical error of ± 1 mm.

3. Results and discussion

This chapter is divided into three parts. The first part is focused on the discharge parameters of the atomizers. The second one deals with the spray cone angle, breakup length and breakup structure while the third one documents the spray characteristics of four representative atomizers. All the proposed empirical correlations use basic SI units as listed in Nomenclature.

3.1. Discharge characteristics

The SRAs are favoured for their ability to reduce the injection flow rate while the inlet pressure remains constant. This capability can be described by the turn-down ratio, which is the ratio of the maximum to minimum injection flow rate for a given range of operating conditions. As the static pressure at the back wall of the swirl chamber is a function of the distance from the atomizer centreline [20] the positioning of the SL orifice will modify the flow rates and the turn-down ratio. The change of the pressure can be simply estimated using the ratio of the SL and inlet pressure at $SFR = 0$, p_{smax}/p_l, which reaches values of 0.99, 0.97, 0.9 and 0.7 for the C1, C2, C3 and C4 atomizer respectively. Our former hypothesis assumed that placing the spill-orifices to the periphery of the swirl chamber, where the static pressure has a maximum, should have extended the range in which the pressure can be reduced, and consequently increase the turn-down ratio. However, this hypothesis was found not to be valid since the atomizers perform differently as it is explained in the following chapter.

The discharge parameters were measured at $p_l = 0.25$, 0.5 and 1 MPa and for several *SFR* regimes in a range from a closed spill line to fully open. The total liquid consumption and injection mass flow rate for $p_l = 1$ MPa is shown in Fig. 6 left. There is little variation in the flow rates for low *SFR*s except for the C4 atomizer at $SFR = 0$ which produces an unstable spray and has a noticeably higher flow rate at this regime due to the unstable air core which is smaller in diameter than in the stable case [10]. Consequently, the smaller air core causes an increase in the flow cross-section of the exit orifice. However, with increasing *SFR*, spray stability improves and becomes fully stable at $SFR > 0.15$. A slight decrease in the flow rate was observed at $SFR = 0.2$ as the air core was assumed to be stable [10]. With further increases in *SFR*, the differences amongst the atomizers rise. The C1 and C1T consume a considerably greater amount of pumped liquid, while the C3 and C4 feature only a mild increase of $\dot{m}_p$ with *SFR*. The atomizers C1 and C2 are unable to reach $SFR = 0.9$ even if operated with a fully open SL. Note that the demand for the pump power grows with $\dot{m}_p$ and thus the atomizers with the lower $\dot{m}_p$ are favoured.

The flow rates are shown in detail for $p_l = 1$ MPa and $SFR = 0.8$ in Fig. 6, right. The atomizers can be divided into three groups which correspond to the distance of the SL orifice from the swirl chamber centreline. The inclination of the orifice produces negligible changes in the flow rates. The C3 and C4 atomizers feature both the lowest inlet and injection flow rates, thus less amount of the liquid is spilled away, and they can be attributed as to the most spill-efficient.

The turn-down ratio is shown in Table 1. The C1 and C1T have the lowest turn-down capability and are able to reduce the injection flow rate three times by controlling the spill flow rate at $p_l = 1$ MPa and about 4.4 times when both the pressure is reduced fourfold to 0.25 MPa and the SL is fully open. For comparison, the simplex atomizers have a turn-down capability of 2 when the pressure is reduced fourfold. The greatest the turn-down capability was achieved in the C3 and C4 cases which can reduce the flow rate 5.9 and 7.2 times respectively for a constant p_l. However, the C4 atomizer offers a larger maximal flow rate which biased the results. When its flow rate is normalized with that of C3, its turn down ratio at constant p_l is similar to C3. A fourfold reduction in p_l extended the turn-down ratio from 5.9 to 11.2 and from 5.9 to 15 for C3 and normalized C4 respectively.

The discharge coefficient of the SL orifices C_{DS} was calculated in order to assess the pressure losses through these orifices. Knowledge of C_{DS} can be used for prediction of $\dot{m}_s$ or sizing of the SL orifices. It is defined as a ratio of the measured flow rate to the theoretical flow rate

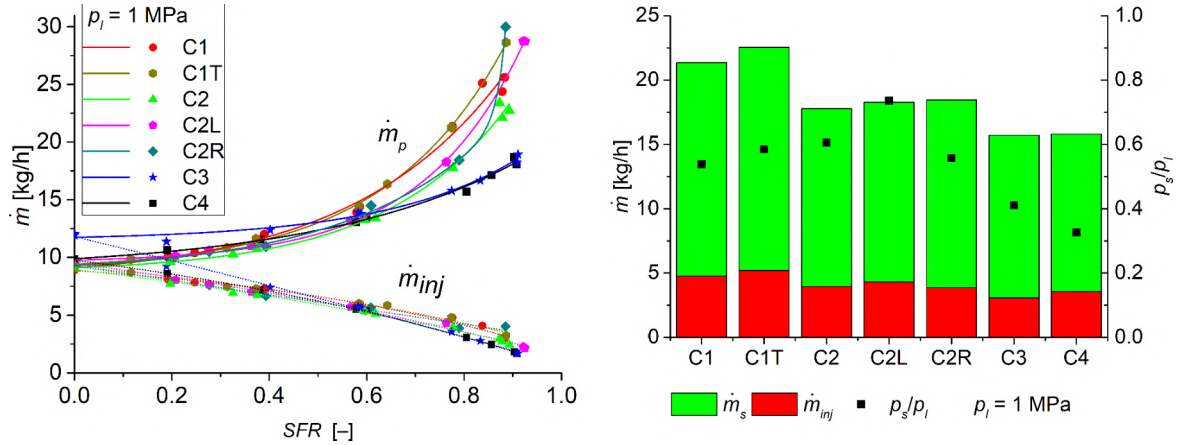

Fig. 6. Left: total ($\dot{m}_p$) and injection flow ($\dot{m}_{inj}$) rates at $p_l = 1$ MPa. Right: detail on the flow rates and pressure ratio at $p_l = 1$ MPa and $SFR = 0.8$.

Table 1
Turn-down ratio for fully open SL.

Ratio of p_l	Simplex	C1	C1T	C2	C2L	C2R	C3	C4	C4 norm.
1×	1	3.0	2.9	3.7	4.6	2.3	5.9	7.2	5.9
4×	2	4.4	4.5	6.5	6.9	5.3	11.2	18.7	15.0

through the SL orifice:

$$C_{DS} = \dot{m}_s/(A_s\sqrt{2\rho_l(p_{smax} - p_s)}) \quad (2)$$

where $\dot{m}_s$ is the measured flow rate through the SL, A_s is the total area of the SL orifices, p_{smax} is the maximal static pressure in the SL at $SFR = 0$, and p_s is the actual static pressure in the SL. The p_s and p_{smax} were measured at constant p_l. A change in p_l does not affect C_{DS}, see Fig. 7, where the combined measurements from $p_l = 0.25$, 0.5 and 1 MPa are shown. The C1T atomizer has the highest C_{DS} overall, however, the differences diminish with increasing *SFR*. This atomizer uses the tangentially inclined SL orifices which are inclined towards to the swirling liquid; thus, the flow resistance is expected to be lower. Changing the inclination rate or direction are likely to change the slope of C_{DS} and *SFR* correlation and a suitable setup may be beneficial for the spill-flow regulator since the atomizer flow-rates could be driven more precisely.

Placing the SL orifice closer to the atomizer centreline results in a decrease in C_{DS}. Furthermore, the area of the SL orifice influences the C_{DS} as the C2L has noticeably lower C_{DS} compared to the C2 version. The single central SL orifice in the C4 produces the lowest C_{DS} due to the decrease in the static pressure in the centre of the swirl chamber [10]. Surprisingly, for $SFR > 0.6$, the air-core is expected to be penetrating through the SL orifice [10], but no evident effect on C_{DS} was observed. The lack of the effect of the air-core penetration on the observed C_{DS} is attributed to a counter flow, which was evidenced inside the SL orifice in [10] for low *SFRs*. This counter flow reduces the effective spill flow cross-section; thus, the flow area has similar size to that at the regimes when the air-core is present inside the SL orifice in the case of higher *SFRs*.

Note that the C_{DS} can be inversely correlated with the turn-down ratio as the atomizers with greater C_{DS} yield reduced turn-down ratios as shown in Fig. 8 for $p_l = 1$ MPa and $SFR = 0.9$. A similar correlation can also be obtained for other pressure regimes.

3.2. Liquid breakup and spray cone angle

Since the geometry of the inlet ports and swirl chamber remains the same, the *SCA* is only dependent on the ratio of the axial and swirl velocity of the emerging liquid sheet; it thus changes with *SFR*. The *SCA* was found to be almost independent of the atomizer used, as shown in

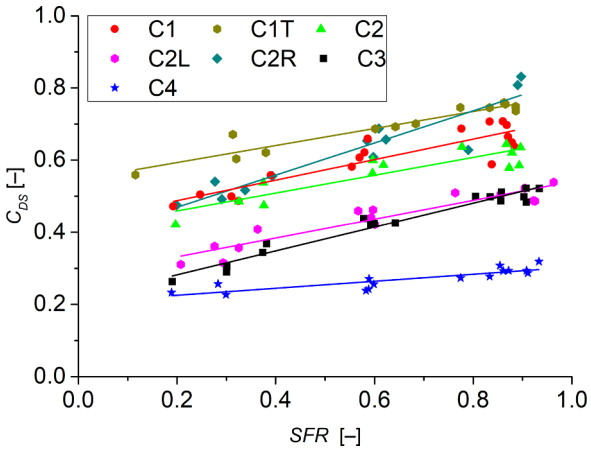

Fig. 7. SL orifice discharge coefficients, data for all inlet pressures.

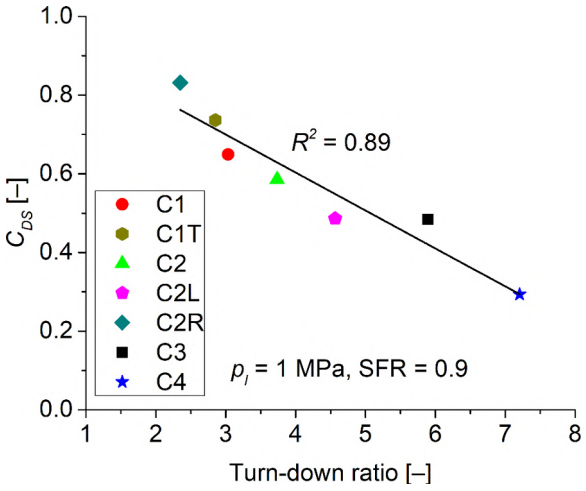

Fig. 8. A correlation of C_{DS} with the turn-down ratio.

Fig. 10 left for $p_l = 1$ MPa, while it increased with *SFR* and p_l. All the atomizers with the off-axial SL orifice generated a stable spray at $SFR = 0$. The mean *SCA* at $p_l = 1$ MPa is 61.4° ± 1° depending on the atomizer used. The temporal variation of the *SCA* based on the standard mean deviation is approximately 1.4° for all of the atomizers except C4. This atomizer showed an unstable spray with the $SCA = 72.2°$ and the *SCA* variation of approximately 11.6°. With increasing *SFR*, the spray stabilized and at $SFR > 0.3$, the spray stability was found to be almost identical among all the atomizers. With further increases in *SFR*, the spray fluctuations start to increase and at $SFR > 0.8$, they are approximately twice as high as at $SFR = 0.4$ (see Fig. 11).

Several empirical correlations for the *SCA* were proposed in the past for the Simplex atomizers [21–24], however, none was found for the SRAs. The experimental data for the *SCA* can be empirically correlated with p_l and *SFR* using exponential equation as proposed e.g. in [21,24]:

$$SCA = 16.3p_l^{0.1}(1 - SFR)^{-0.15} \quad (3)$$

where 16.3 is an empirical constant related to the geometry of the atomizer and the rheology of the liquid used. The difference between the calculated and measured *SCA* is shown in Fig. 10 right, the unstable regimes of the C4 atomizer were excluded from the correlation. The *SCA* is slightly increasing with the inlet pressure as $SCA \propto p_l^{0.1}$ for all spill-regimes. This correlation is also valid for the Simplex atomizers substituting $SFR = 0$. Note that similar correlation of $SCA \propto p_l^{0.11}$ was published in [21] for Simplex atomizers and it was later confirmed in [22]. Different exponents of 0.06 [23] and 0.39 [24] were derived for large scale Simplex atomizers and high-viscosity liquids respectively.

The character of the liquid breakup varies between the atomizers; see Fig. 9, where the instantaneous spray images are displayed for $p_l = 0.5$ MPa. The radially and tangentially inclined SL orifices (C1T and C2R) and the large area SL orifice (C2L) produce identical *SCA* and breakup structure as their base variants (C1 and C2 respectively), so they are not shown in Fig. 9.

The differences in the spray images at $SFR = 0$ for the stable atomizers are small; however, the C1 and C2 atomizers feature a longer breakup length compared to the C3 atomizer. The unstable C4 atomizer has a very chaotic breakup nature at $SFR = 0$ i.e. for a closed SL. At $SFR = 0.3$ and 0.6, the C3 and C4 atomizers have a very similar structure of the liquid breakup. Nevertheless, the C1 and C2 have a noticeably better stability of the liquid sheet with a larger breakup length. The regime with $SFR = 0.9$ is strongly affected by the injection flow rate, which is the highest in the case of the C1 atomizer and thus the liquid sheet is expected to be thicker and consequently the breakup length longer [12]. At most of the tested regimes, the gas Weber number, based on the liquid sheet half-thickness, defined as: $We_g = \rho_g U_l^2 t/2\sigma$, where U_l is the axial velocity and t is the thickness of

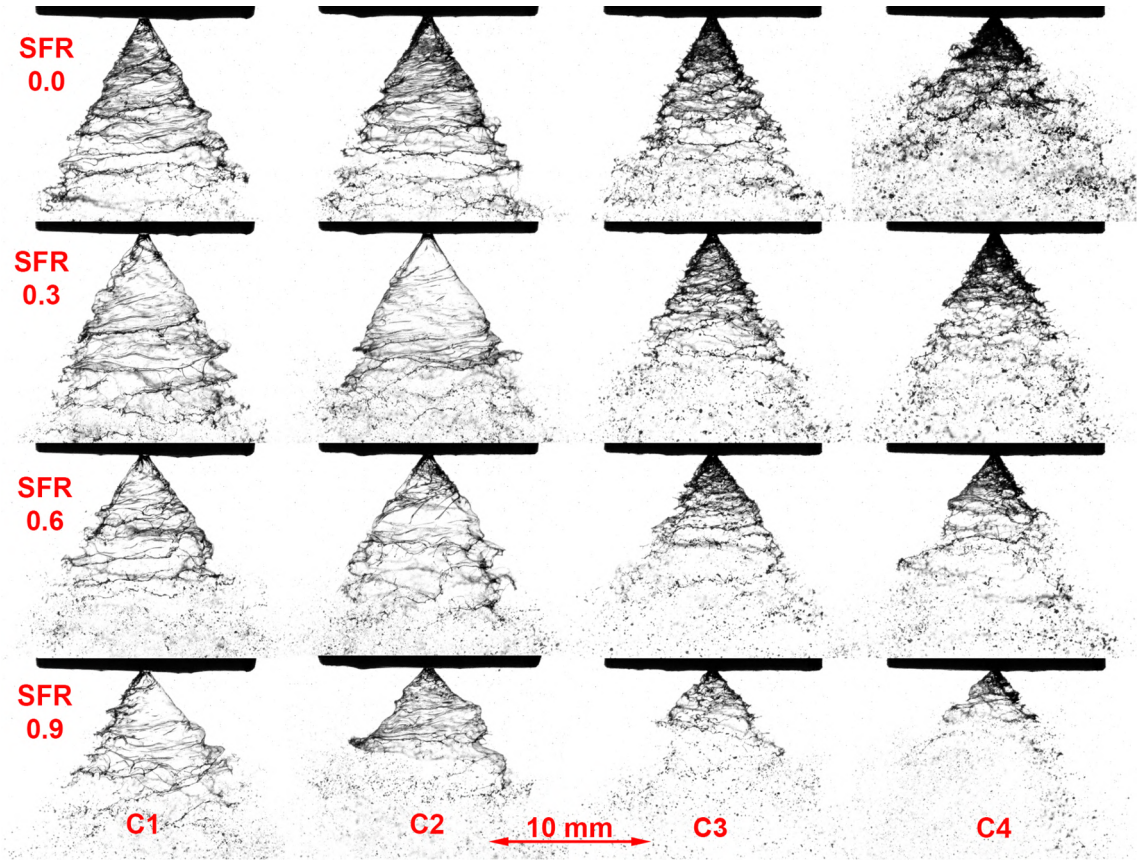

Fig. 9. Instantaneous images of the liquid breakup, p_l = 0.5 MPa, from top: *SFR* = 0, 0.3, 0.6 and 0.9. From left: atomizer C1, C2, C3 and C4.

the liquid sheet respectively (see Appendix A), was lower than 27/16, where the transition from the long-wave to the short-wave breakup mode was observed [14]. The only regime where $We_g > 27/16$ was for p_l = 1 MPa, *SFR* = 0. The short-wave breakup was observed there for all the atomizers.

The breakup regime can affect the droplet sizes since the long-wave breakup produces a longer breakup length and the ligaments are formed twice per wave length. On the other hand, the short-wave mode produces a short breakup length and ligaments are formed once per wave length but with a much higher frequency [14]. The long-wave regime can be observed in the case of C1 and C2 atomizer. The short-wave breakup can be attributed to the C3 and C4 at all the regimes, even when $We_g < 27/16$. It is evident here, that the transition between the long and short mode is not caused by the aerodynamic forces but rather by the high frequency instabilities of the internal flow. The shape and stability of the internal air-core predetermine the thickness of the liquid sheet as well as its temporal fluctuations, which modify the frequency and amplitude of the initial disturbances [25]. The axially placed SL orifice can cause a decay of the internal air core and generate strong spray fluctuations [10].

In order to assess the effect of p_l and $\dot{m}_{inj}$ on the breakup length l_b and describe the variance among the atomizers, l_b was correlated with p_l and $\dot{m}_{inj}$ as:

$$l_b = B p_l^{-0.75} \dot{m}_{inj}^{0.47}, \tag{4}$$

where B is a constant dependent on the atomizer used. For C1, C1T C2,

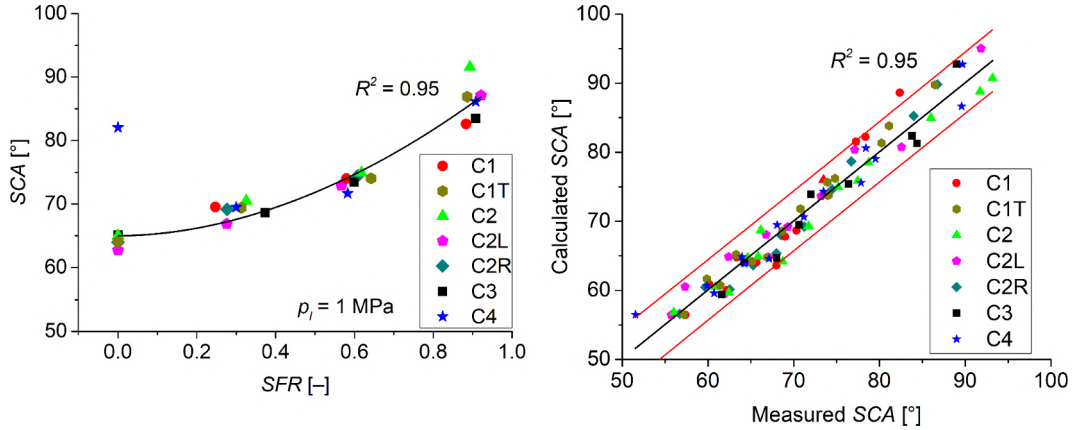

Fig. 10. Left: the effect of *SFR* on camera-based *SCA* at p_l = 1 MPa. Right: comparison of calculated and measured *SCA* according Eq. (3) with 95% prediction band. Unstable regimes of the C4 atomizer are excluded from the correlations.

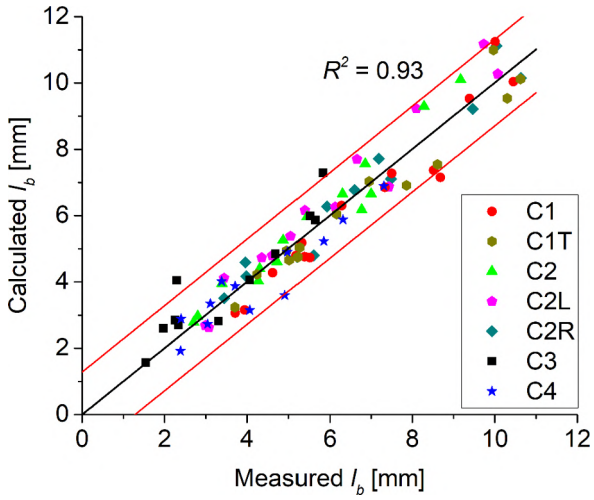

Fig. 11. Comparison of measured and calculated l_b with 95% prediction bands.

C2L, and C2T is $B = 58$ while for the C3 and C4 is $B = 39$. The constant B clearly highlights the difference among the atomizers, as it is adjusted from the influence of p_l and $\dot{m}_{inj}$. The C1 and C2 would have l_b about 25% longer at given p_l and $\dot{m}_{inj}$. This is attributed to the better stability of the internal flow. For all the atomizers, the same dependency on p_l and $\dot{m}_{inj}$ applies, as increasing p_l results in a shorter breakup length, due to an increasing liquid sheet velocity. An increase in injection mass flow rate, $\dot{m}_{inj}$, results in a thicker liquid sheet which has better stability and therefore l_b is extended.

A semi-empirical correlation proposed in [13,26], correlating l_b with t, U_l and wave grow rate was able to capture the trends, but its fit quality was as poor as $R^2 \sim 0.5$. Nevertheless, the empirical constant had to be changed in a similar way as it is proposed in Eq. (4). To properly describe the differences in the breakup nature, the amplitude of the disturbances on the liquid sheet has to be evaluated together with measurements of t and U_l inside the exit orifice. This is beyond the scope of this current paper.

3.3. PDA results

The PDA measurements were made for four atomizers – C1, C2, C3 and C4 – with the operating parameters of $p_l = 0.25$, 0.5 and 1 MPa and $SFR = 0$, 0.3, 0.6 and 0.9. The atomizers C1T, C2R and C2L were excluded from the PDA investigation in order to reduce the measured parameters. These atomizers produced sprays with identical macroscopic spray features, such as SCA and breakup length as their base variants. Moreover, they provided worse turn-down ratio and higher pump power requirements.

The effect of the injection mass flow rate and SFR on the $ISMD$ is shown in Fig. 12. An increase in SFR results in a slight decrease in the $ISMD$ at $p_l = 0.5$ and 1 MPa for all the atomizers. However, at $SFR = 0.9$, the C1 and C2 exhibit an increase in the $ISMD$. This effect is stronger at the lower pressures. Both atomizers give very similar trends and values of $ISMD$. The C4, compared to the other atomizers, provides the largest $ISMD$ at $p_l = 0.25$ MPa, probably due to the unstable internal flow and consequent spray fluctuations. Nevertheless, the fluctuating spray from the C4 provides the smallest droplets at higher pressures, which was not expected. The C3 and C4 atomizers perform similarly at $p_l = 0.5$ and 1 MPa and $SFR > 0$. For the regimes with moderate SFR, the C1 and C2 atomizers have a lower $ISMD$ compared to C3 and C4. In particular, at $p_l = 0.5$ and $SFR = 0.6$, the C1 and C2 produce the spray with $ISMD$ about 15% smaller.

For a given regime, all the atomizers have the same SCA and also the same velocity of the discharged liquid sheet (for the velocity calculations, see Appendix A). The mean axial velocity of the sprayed droplets at $Z = 25$ mm are 10% higher in the case of C3 and C4. Higher droplet velocities should improve the spray quality; however, in this case, it is assumed that the breakup structure and stability affect the droplet sizes [1] foremost. The C1 and C2 atomizers provide a more stable liquid sheet, so, at the point of breakup the liquid film could be thinner, and therefore, the droplets generated would be smaller. Similarly, the larger droplets from the C3 and C4 have greater initial momentum. Thus, their velocity remains high further downstream from the exit orifice. As the p_l increases, the breakup length generally decreases and the difference among atomizers diminishes. Note here, that for $p_l = 1$ MPa and $SFR = 0$ the C1, C2 and C3 atomizers feature the same $ISMD$, because it is the only operating regime, in which all the atomizers operate at the same sheet breakup mode.

Rizk and Lefebvre [6] studied three SRAs and found that the SMD was slightly decreasing with SFR but the p_l played a dominant role which agrees with our results. However, Dai and Lefebvre [7] found a reverse effect of SFR where the drop sizes were about 10% larger at $SFR = 0.7$ compared to $SFR = 0$. The injected mass flow rate, plotted

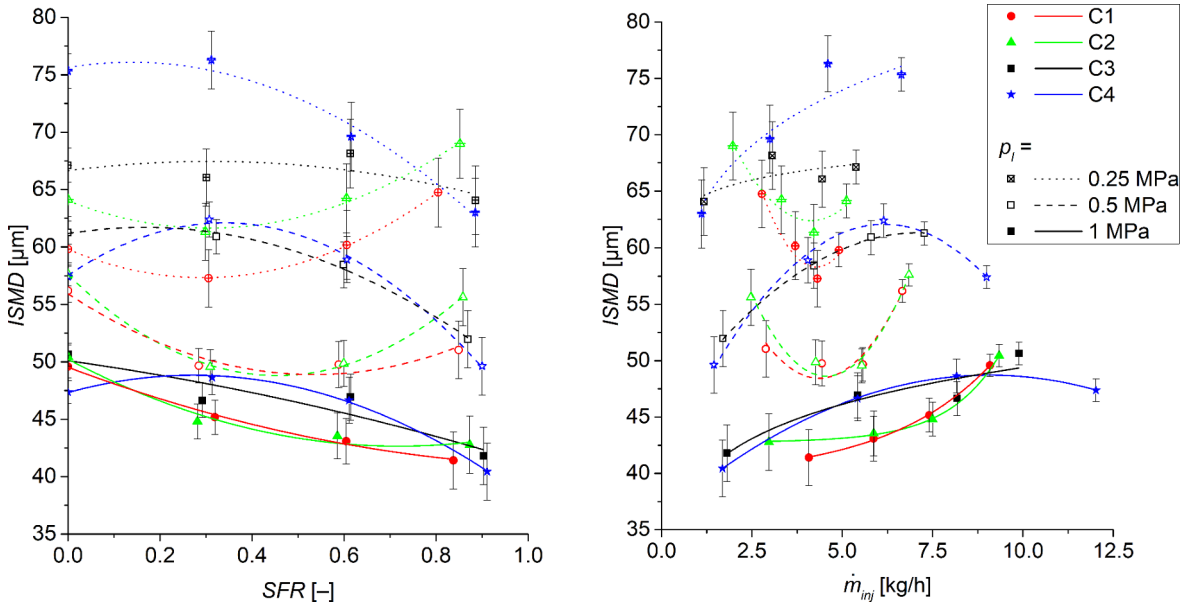

Fig. 12. $ISMD$ plotted with SFR (left) and injection mass flow rate (right).

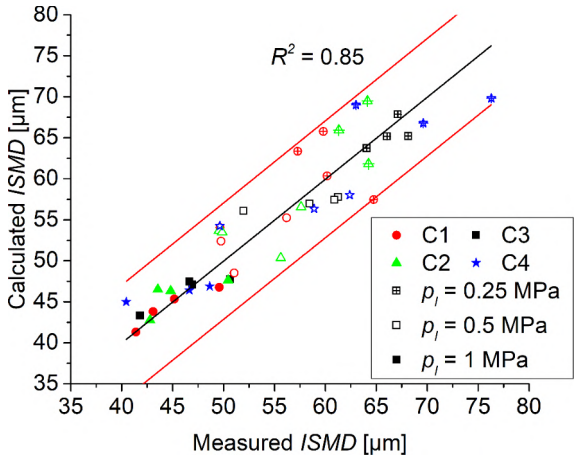

Fig. 13. Comparison of measured and calculated *ISMD* from Eq. (5a).

with *ISMD* in Fig. 12 left, presents a different view on the results. The *ISMD* in general decreases slightly with decreasing injection flow rates; nevertheless, the effect of the p_l is obviously much stronger. Also, for a given atomizer, a different *ISMD* can be obtained at a constant injection rate with different combinations of inlet pressure and *SFR*. This feature may find practical applications e.g. in soot control of combustor.

Due to the difference in *SMD* among the atomizers studied, it was not possible to obtain a simple correlation combining p_l, *SFR* and atomizer geometrical parameters. Introducing the breakup length as a differentiating parameter between the two atomizer groups, then the following correlation can be derived:

$$ISMD = 1.72 \times 10^{-3} p_l^{-0.33} l_b^{-0.18} (1 - SFR)^{0.1} \quad (5a)$$

A substitution of l_b from Eq. (4) results in:

$$ISMD = 1.72 \times 10^{-3} B p_l^{-0.2} m_{inj}^{0.09} (1 - SFR)^{0.1} \quad (5b)$$

Nevertheless, the quality of the fit between the measured and the calculated values is only moderate with $R^2 = 0.85$, see Fig. 13. It is evident, that the increases in p_l and l_b result in smaller droplets. The effect of p_l has been investigated in the literature, where the pressure exponent for Simplex atomizers varies from −0.23 to −0.44 [27–29] depending on the geometry and liquid used and agrees well with the findings presented here. The values reported here are after correction for the effect of the mass flow rate on *SMD*, as the flow rate was considered as an independent factor in these papers and has a minor effect here. The effect of l_b was expected, since the liquid sheet thickness with l_b decreases and consequently the ligaments and droplets generated should be smaller.

The camera based *SCA* indicates only the outer boundaries of the spray and provides no information of the radial distribution of the liquid further downstream. For these reasons, the effective *SCA* is often determined [30]. The effective *SCA* was estimated from the PDA data as the apex angle of a virtual cone which covers 90% of the liquid volume flux inside the spray at $Z = 25$ mm downstream the atomizer.

The effective *SCA* shows lower values compared to the camera based *SCA*. However, their trends are very similar as evident in Fig. 14, especially for higher p_l values. The C1 and C2 atomizers produce a smaller effective *SCA* at $p_l = 0.25$ MPa compared to the C3 and C4, which is in contrast to the camera based *SCA*, where all the atomizers performed in similarly. The increase in *SCA* with *SFR* is less prominent here. To explain this phenomenon, the droplet size and velocity correlations need to be considered. The sprays generated by the C1 and C2 atomizer contain much smaller droplets than for the C3 and C4 atomizers. The smaller droplets have less momentum which decay faster and reduces their axial and radial penetration. The droplets generated at $p_l = 0.25$ MPa already have small initial momentum. Therefore, the

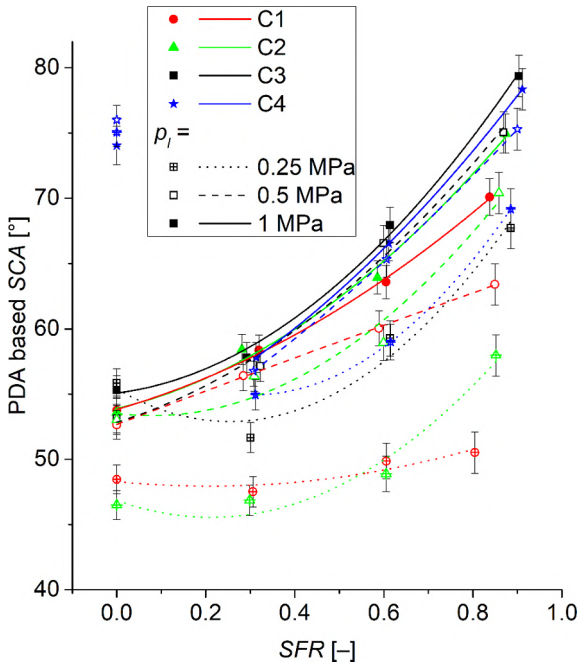

Fig. 14. Effective *SCA* based on PDA mass radial flux.

effective *SCA* as measured with PDA narrows with distance downstream from the atomizer.

3.4. Nozzle efficiency

The efficiency of the conversion of the inlet potential energy into kinetic energy within the atomizer exit orifice was derived from the Bernoulli equation:

$$\eta_n = \rho_l U_l^2 / 2 p_l, \quad (6)$$

This so-called nozzle efficiency is strongly dependent on the *SFR*, as it is evident from Fig. 15. This is expected, as a portion of the energy is spilled out. The nozzle efficiency decreases from its maximum of $\eta_n = 0.52$ for $SFR = 0$ to as low value as 0.15 for the fully open SL. The C4 atomizer behaves differently as it shows a noticeable drop in η_n for $SFR = 0$. It is evident, that the unstable internal flow negatively affects η_n. The p_l weakly affects η_n as it was found independent on p_l for $p_l = 0.5$ and 1 MPa and it was only 5% greater for $p_l = 0.25$ when compared to the other regimes. The C3 and C4 atomizers yield lower η_n for $SFR = 0.6$. For these atomizers, it is assumed that the liquid sheet

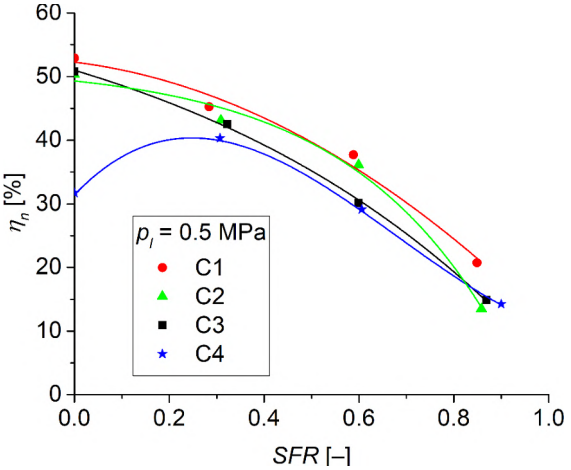

Fig. 15. Nozzle efficiency for $p_l = 0.5$ MPa.

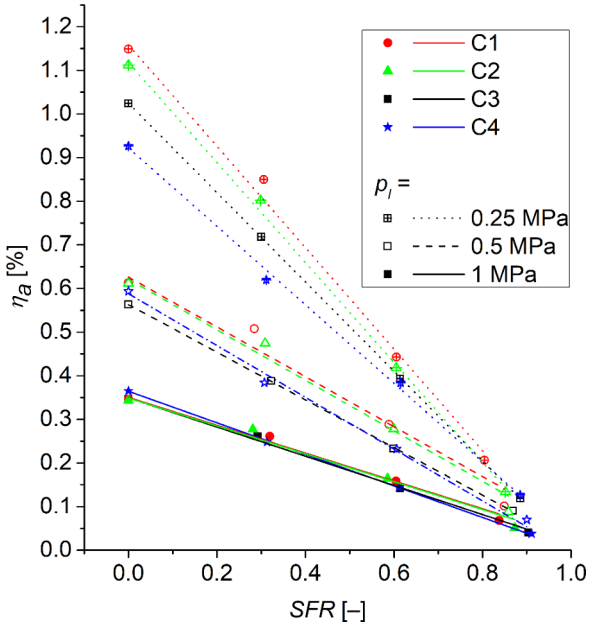

Fig. 16. Influence of the atomization efficiency on *SFR*.

within exit orifice is unstable, hence the energy inside the atomizer dissipates readily.

Other authors reported nozzle efficiencies for Simplex atomizers of η_n = 0.42–0.66 with a dependence on the shape of the convergent part of the swirl chamber [31,32], which is in good agreement with our results. For large scaled Simplex atomizers η_n = 0.55–0.59 [19] and η_n = 0.73–0.86 [33] was reported. This difference to our results can be explained by the small scale of the atomizer used here, which has large area of internal surfaces compared to the internal volume, hence a larger frictional loss.

3.5. Atomization efficiency

The SRAs usually have a lower atomization efficiency compared to the Simplex atomizers due to the energy taken by the spilled liquid. The atomization efficiency, η_a, is defined as a ratio of surface energy increase to potential energy of pumped liquid and can be calculated as follows [19]:

$$\eta_a = 6\sigma(1 - SFR)/(p_l \cdot ISMD) \quad (7)$$

As shown in Fig. 16, η_a almost linearly declines with *SFR*. The effect of *ISMD* is weak as it remained almost constant with *SFR* change. The increase in p_l causes a drop in η_a, approximately as $\eta_a \propto p_l^{-0.8}$ due to the reduction in *ISMD* with p_l. The variation in η_a among the atomizers is larger at lower inlet pressure due to a greater variation in *ISMD*, where η_a reaches the maximum of 1.1% for the C1 atomizer at p_l = 0.25 MPa and *SFR* = 0. With raising p_l, the atomization efficiency drops to 0.35% at p_l = 1 MPa and *SFR* = 0. With opening the SL, η_a drops as low as to 0.05% for p_l = 1 MPa and *SFR* = 0.9. The results given in Fig. 16 are in good agreement with other authors. Loffler-Mang and Leuckel [9] obtained η_a = 0.1–0.4% in dependence on *SFR* for the SRAs and Petela [34] for Simplex atomizers found η_a = 0.08–0.2%. Despite the low η_a at high *SFR*, the SRAs have a relatively high η_a compared to other types of atomizers., e.g. Jedelsky and Jicha [35] investigated a twin-fluid effervescent atomizer and found η_a = 0.02–0.1%.

4. Conclusions

Seven small pressure-swirl spill-return atomizers with different geometries of the spill-line (SL) orifice were investigated experimentally using high-speed imaging and Phase Doppler Anemometry.

The radial position, on which the SL orifices are located, plays a crucial role in the performance of the SRAs as it affects the spray quality, stability and turn-down ratio. The single axially located orifice causes spray fluctuations at regimes close to a spill to feed ratios, *SFR*, of zero; however, the spray is stable for *SFR* > 0.15. The atomizers with off-axial orifices are free of this defect, but their turn-down ratio range deteriorates with the increasing distance of the SL orifices from the swirl chamber centreline. The inclination of the SL orifices has a negligible effect on the discharge parameters, spray cone angle and breakup structure. However, the tangential inclination can affect the discharge coefficient of SL orifices.

The inlet pressure plays a dominant role over *SFR* in the spray formation. The integral Sauter mean diameter, *ISMD,* was found to be decreasing with *SFR* increase for p_l = 0.5 and 1 MPa. The atomizers with the SL orifice further from the swirl chamber centreline (C1 and C2) produce a finer spray at moderate *SFR*; however, the *ISMD* deteriorates at the highest *SFR*s. This behaviour was attributed to better stability of the liquid sheet at moderate *SFR* values as the long-wave breakup mode was observed compared to the C3 and C4 atomizers which show the liquid sheet break up in the short-wave mode even for gas Weber numbers, We_g < 27/16.

The atomization efficiency was found to be in the range of η_a = 0.05–1.1%. It decreases linearly with increasing *SFR* and is almost inversely proportional to p_l. It is also weakly dependent on the atomizer used at p_l = 0.5–1 MPa.

From this study it is proposed that the optimum configuration for spill-return atomizers is with off-axial parallel orifices. If the spray quality has a high priority, the C2 atomizer with the SL orifice placed on a radius $r_s/2$ is recommended. The highest turn-down ratio was achieved by the C3 atomizer, but the spray quality was slightly worse at regimes with *SFR* 0.3–0.6.

The study presented reveals some effects of SL orifice geometry on the SRAs characteristics, and, it also indicates the complexity of the internal flow. Further experimental and numerical analysis of the internal flow will follow to explain the breakup mechanism in detail.

Acknowledgements

The authors acknowledge the financial support from the project No. 18-15839S funded by the Czech Science Foundation and the project “Computer Simulations for Effective Low-Emission Energy” funded as project No. CZ.02.1.01/0.0/0.0/16_026/0008392 by Operational Programme Research, Development and Education, Priority axis 1: Strengthening capacity for high-quality research.

Appendix A

The axial velocity of the discharged liquid sheet, U_l, is a required parameter for the calculation of the gas Weber number, We_g. As a direct measurement of U_l was not performed in this paper, it was estimated indirectly from the PDA measurements and the high-speed imaging records.

The PDA measurement was provided at Z = 12.5 mm downstream the atomizer exit orifice. As the droplets interact with the surrounding gas, their flow behaviour is linked to their size and velocity. A dimensionless parameter, describing the behaviour of the particles in the flow, is the Stokes number, *Stk*, defined as the ratio of characteristic time of a droplet to a characteristic time of the flow and can be estimated as [36]:

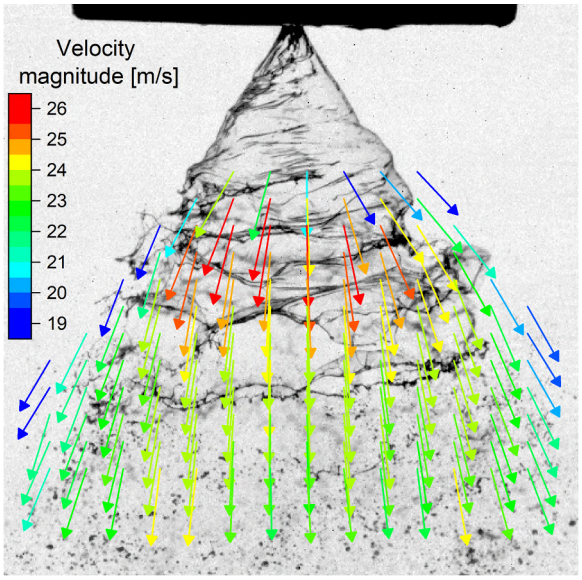

Fig. A.1. Typical result from PIVlab®, mean velocity vectors calculated from 200 frames.

$$Stk = \frac{\rho_l C_c \bar{D}_p^2 \Delta\bar{v}}{18\mu_g L}, \tag{A.1}$$

where C_c is the Cunningham correction factor and it is ≈ 1 in this case, L represents the distance from the breakup point to the measurement point, $\Delta\bar{v}$ is the difference between the local air velocity and the droplet velocity, μ_g is the air dynamic viscosity. Both, $\Delta\bar{v}$ and L were calculated in the same way as described in [36]. The droplets with $Stk >> 1$ move ballistically and are resistant to turbulent eddies. In this paper, the droplets at $Z = 12.5$ mm with $D_p > 80$ µm feature $Stk > 100$ for all the operating regimes and atomizers. The mean axial velocity was calculated for those large droplets at each measured point. Consequently, the radial position with the maximal droplet axial velocity was selected if more than 100 analyzed droplets were analyzed. This velocity was then considered to be a good approximation of the discharge velocity of the liquid sheet.

To validate these results, a Particle Image Velocimetry, PIV, analysis of the high-speed images was performed with the open software PIVlab® [37], Typical flow vector results are shown in Fig. A.1. Since direct measurement of the wave velocity on the liquid sheet surface can bias the results [38], the axial velocity was measured just downstream of the breakup position. Thus, with $L \to 0$ the Stk is expected to be very high and the axial velocity should not be affected by the droplet interaction with surroundings.

Comparison of both approaches is shown in Fig. A.2 for all the atomizers and operating regimes measured by PDA. The results correlate with $R^2 = 0.98$ and the velocities from PIVlab® were some 3% smaller than PDA results which could be caused by the uncertainty in the vector spatial and temporal scaling. It can be concluded that the axial velocity of the largest droplets can be used for the estimation of the liquid sheet axial velocity.

The liquid sheet thickness, t, is related to the injection mass flow rate, $\dot{m}_{inj}$, and from the Continuity equation:

$$\dot{m}_{inj} = \pi\rho_l U_l t (d_o - t) \tag{A.2}$$

The U_l is expected to be equivalent to the axial liquid velocity within the exit orifice.

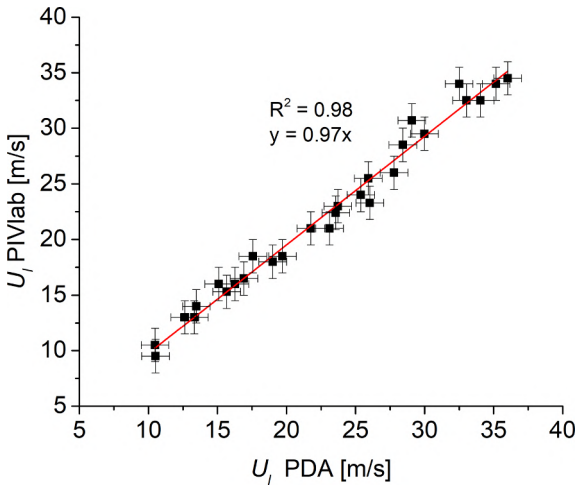

Fig. A.2. Correlation of U_l from PIVlab® and PDA.

References

[1] A.H. Lefebvre, V.G. McDonell, Atomization and sprays, CRC Press, 2017.
[2] L. Durdina, J. Jedelsky, M. Jicha, Investigation and comparison of spray characteristics of pressure-swirl atomizers for a small-sized aircraft turbine engine, Int. J. Heat Mass Transf. 78 (2014) 892–900.
[3] B. Becker, F. Bonsen, G. Simon, A simple and reliable combustion control system, ASME 1990 International Gas Turbine and Aeroengine Congress and Exposition, American Society of Mechanical Engineers, 1990.
[4] F.H. Carey, The development of the spill flow burner and its control system for gas turbine engines, J. Royal Aeronaut. Soc. 58 (1954) 737–753.
[5] N. Rizk, A. Lefebvre, Drop-size distribution characteristics of spill-return atomizers, J. Propul. Power 1 (1) (1985) 16–22.
[6] N.K. Rizk, A.H. Lefebvre, Spray characteristics of spill-return atomizers, J. Propul. Power 1 (3) (1985) 200–204.
[7] X.F. Dai, A.H. Lefebvre, J. Rollbuhler, Spray characteristics of a spill-return airblast atomizer, J. Eng. Gas Turbines Power 111 (1) (1989) 63–69.
[8] G. Nasr, A. Yule, J. Stewart, A. Whitehead, T. Hughes, A new fine spray, low flowrate, spill-return swirl atomizer, Proc. Inst. Mech. Eng., Part C: J. Mech. Eng. Sci. 225 (4) (2011) 897–908.
[9] M. Loffler-Mang, W. Leuckel, Atomization with spill-controled swirl pressure-jet nozzles, ICLASS (1991) 431–440.
[10] M. Maly, J. Jedelsky, J. Slama, L. Janackova, M. Sapik, G. Wigley, M. Jicha, Internal flow and air core dynamics in Simplex and Spill-return pressure-swirl atomizers, Int. J. Heat Mass Transf 123 (2018) 805–814.
[11] Y. Khavkin, The Theory and Practice of Swirl Atomizers, Taylor & Francis, 2004.
[12] S.M. Hosseinalipour, R. Ghorbani, H. Karimaei, Effect of liquid sheet and gas streams characteristics on the instability of a hollow cone spray using an improved linear instability analysis, Asia-Pacific J. Chem. Eng. 11 (1) (2016) 24–33.
[13] Q.-F. Fu, L.-J. Yang, Y.-Y. Qu, B. Gu, Linear stability analysis of a conical liquid sheet, J. Propul. Power 26 (5) (2010) 955–968.
[14] P.K. Senecal, D.P. Schmidt, I. Nouar, C.J. Rutland, R.D. Reitz, M.L. Corradini, Modeling high-speed viscous liquid sheet atomization, Int. J. Heat Mass Transf 25 (6) (1999) 1073–1097.
[15] A. Ibrahim, M.A. Jog, S. Jeng, Effect of liquid swirl-velocity profile on the instability of a swirling annular liquid sheet, Atomization Sprays 16 (3) (2006).
[16] Ashgriz, N., and SpringerLink (Online service), 2011. Handbook of atomization and sprays: Theory and applications, Springer, New York, pp. xvi, 935 p.
[17] D.R. Guildenbecher, C. López-Rivera, P.E. Sojka, Secondary atomization, Exp. Fluids 46 (3) (2009) 371–402.
[18] A.H.A. Hamid, R. Atan, Spray characteristics of jet–swirl nozzles for thrust chamber injector, Aerosp. Sci. Technol. 13 (4) (2009) 192–196.
[19] J. Jedelsky, M. Jicha, Energy considerations in spraying process of a spill-return pressure-swirl atomizer, Appl. Energy 132 (2014) 485–495.
[20] E. Wimmer, G. Brenn, Viscous flow through the swirl chamber of a pressure-swirl atomizer, Int. J. Multiph. Flow (2013).
[21] N. Rizk, A. Lefebvre, Prediction of velocity coefficient and spray cone angle for simplex swirl atomizers, Int. J. Turbo Jet Engines 4 (1–2) (1987) 65–74.
[22] Taeock Khil, Sunghyuk Kim, Seongho Cho, Y. Youngbin, Quantification of the transient mass flow rate in a simplex swirl injector, Meas. Sci. Technol. 20 (7) (2009) 075405.
[23] M. Benjamin, A. Mansour, U. Samant, S. Jha, Y. Liao, T. Harris, S. Jeng, Film thickness, droplet size measurements and correlations for large pressure-swirl atomizers, Proc. ASME 1998 International Gas Turbine and Aeroengine Congress and Exhibition, American Society of Mechanical Engineers, 1998 p. 8.
[24] J. Ballester, C. Dopazo, Discharge coefficient and spray angle measurements for small pressure-swirl nozzles, Atomization Sprays 4 (3) (1994).
[25] J. Chinn, D. Cooper, A. Yule, G. Nasr, Stationary rotary force waves on the liquid–air core interface of a swirl atomizer, Heat Mass Transf. (2015) 1–14.
[26] Z. Han, S.E. Parrish, P.V. Farrell, R.D. Reitz, Modeling atomization processes of pressure-swirl hollow-cone fuel sprays, Atomization Sprays 7 (6) (1997) 663–684.
[27] A.K. Jasuja, Atomization of crude and residual fuel oils, J. Eng. Power-Trans. Asme 101 (2) (1979) 250–258.
[28] A. Radcliffe, Fuel Injection, Princenton University Press, Princenton, N.Y, High Speed Aerodynamics and Jet Propulsion, 1960.
[29] R.K. Babu, M.V. Narasimhan, K. Karayanaswamy, Prediction of mean drop size of fuel sprays from swirl spray atomizers, Proceedings of the second International Conference on Liquid Atomisation and Spray SystemsMadison, 1982, pp. 99–106.
[30] S. Chen, A. Lefebvre, J. Rollbuhler, Factors influencing the effective spray cone angle of pressure-swirl atomizers, ASME Trans. J. Eng. Gas Turbines Power 114 (1992) 97–103.
[31] M. Horvay, W. Leuckel, Experimental and theoretical investigation of swirl nozzles for pressure-jet atomization, German Chem. Eng. 9 (5) (1986) 276–283.
[32] M. Horvay, W. Leuckel, LDA-measurements of liquid swirl flow in converging swirl chambers with tangential inlets, 2nd International Symposium on Applications of Laser Anemometry to Fluid Mechanics, (1985) p. 11.
[33] A. Yule, J. Chinn, The internal flow and exit conditions of pressure swirl atomizers, Atomization Sprays 10 (2) (2000) 121–146.
[34] R. Petela, Exergetic analysis of atomization process of liquid, Fuel 63 (3) (1984) 419–422.
[35] J. Jedelsky, M. Jicha, Energy conversion during effervescent atomization, Fuel 111 (2013) 836–844.
[36] J. Jedelsky, M. Maly, N.P. del Corral, G. Wigley, L. Janackova, M. Jicha, Air–liquid interactions in a pressure-swirl spray, Int. J. Heat Mass Transf. 121 (2018) 788–804.
[37] W. Thielicke, E. Stamhuis, PIVlab–towards user-friendly, affordable and accurate digital particle image velocimetry in MATLAB, J. Open Res. Software 2 (1) (2014).
[38] K. Siddharth, M.V. Panchagnula, T.J. Tharakan, Feature correlation velocimetry for measuring instantaneous liquid sheet velocity, J. Fluids Eng. 139 (9) (2017) 091401.

10.3 Paper III

Experimental Thermal and Fluid Science 119 (2020) 110210

Contents lists available at ScienceDirect

Experimental Thermal and Fluid Science

journal homepage: www.elsevier.com/locate/etfs

Internal flow dynamics of spill-return pressure-swirl atomizers

Milan Maly[a,*], Ondrej Cejpek[a], Marcel Sapik[a], Vladimir Ondracek[b], Graham Wigley[c], Jan Jedelsky[a]

[a] Brno University of Technology, Technicka 2, 616 69 Brno, Czech Republic
[b] PBS Velka Bites, a. s., Vlkovska 279, 595 01 Velka Bites, Czech Republic
[c] Loughborough University, LE11 3TU, United Kingdom

ARTICLE INFO

Keywords:
Internal flow
Spill-return
Air-core
Liquid sheet
Temporal stability

ABSTRACT

The sprays produced by spill-return pressure-swirl atomizers are strongly dependent on the nature of the internal fluid dynamics. Several spill-return atomizers were compared in terms of the spatial and temporal behaviour of the internal air-core, liquid sheet thickness and its perturbations. The only difference amongst the test configurations was the geometrical arrangement of the spill-line (SL) orifice through which the liquid was spilled away. The flow field inside the swirl chamber was examined using high-speed imaging with image post processing using an in-house Matlab code and three orthogonal velocity components acquired using Laser Doppler Anemometry. The dimensions of the production atomizers did not allow direct visualization of their internal flow, so a scaled, modular, transparent plexiglass model was used. Its flow characteristics were equivalent to the original atomizer. The refractive index of the atomizer body was matched to the test liquid using a solution of 1-Bromonaphthalene and kerosene fuel type JET A-1. The test conditions were derived from the original atomizer and were limited to inlet port Reynolds numbers, from 700 to 2000 and spill-to-feed ratios, *SFR*, from 0 to 0.75. An inviscid analysis, originally derived for Simplex atomizers, was modified and applied to the spill-return version. This approach allows a theoretical prediction of the discharge coefficient and air-core diameter dependent solely on *SFR*. An axially located SL orifice inhibits any internal air-core forming in the swirl chamber. Off-axial SL orifices generate and stabilize the air-core, which leads to the regular formation of a liquid sheet and a high-quality spray. Nevertheless, some configurations changed the breakup nature of the liquid sheet and consequently the spray quality. Moreover, the turn-down ratio of the liquid supply rate and spray stability depend on the distance of the SL orifices from the swirl chamber centreline. The flow energy losses increase with *SFR*. The outcomes from this analysis allow the optimization of the SL configuration for specific application and extend the classical inviscid analysis.

1. Introduction

Many industrial spray applications require a high liquid surface area to volume ratio, which is usually accomplished by an atomizing device. Numerous atomizer designs have been proposed in past, and yet, the most common type introduced more than a century ago, is the pressure-swirl type known as a Simplex atomizer. The injection flow rate, $\dot{m}_{inj}$, of the Simplex atomizer depends solely on the square root of the injection pressure p_l. Therefore, a halving in $\dot{m}_{inj}$ requires a fourfold decrease in the p_l, which affects droplet sizes dramatically [1]. Several enhanced versions were derived in order to improve operating and spray parameters. This paper focuses on pressure-swirl Spill-return atomizers, which are based on the Simplex geometry, but contain an additional passage, the spill-line, in the rear wall of the swirl chamber. The liquid is injected in to the swirl chamber via tangential ports. In the swirl chamber it is divided into two streams, one is discharged outside and atomized while the second one is spilled away through the spill-line passage. The liquid can be supplied into the swirl chamber under a high inlet overpressure, p_l, and the $\dot{m}_{inj}$ is regulated by changing the spill flow rate, $\dot{m}_s$. This allows a high swirl momentum to be maintained for a wide range of $\dot{m}_{inj}$. Due to this feature, spill-return atomizers have a large turn-down ratio. This is the ratio of the maximum to minimum $\dot{m}_{inj}$ appropriate for the given application of acceptable spray quality and operational pressure. The operating regime of the spill-return atomizer is typically characterised by a bypass ratio known as the spill-to-feed ratio, *SFR*. It is the ratio of the spilled flow rate, $\dot{m}_s$, to the pumped flow rate, $\dot{m}_p$ and can have values from $SFR = 0$, where all the liquid is injected and the atomizer operates in a Simplex mode to

* Corresponding author.
E-mail address: milan.maly@vutbr.cz (M. Maly).

https://doi.org/10.1016/j.expthermflusci.2020.110210
Received 6 February 2020; Received in revised form 27 May 2020; Accepted 23 June 2020
Available online 24 June 2020
0894-1777/

Nomenclature

A	area [m^2]
b	width [m]
B	experimental constant for *SCA* [–]
C_D	discharge coefficient [–]
d	diameter [m]
d_{pc}	Pitch Circle Diameter [m]
h	height [m]
k	Atomizer constant used in [8,9] [–]
k_1	Atomizer constant used in [31] [–]
l_b	breakup length [m]
$\dot{m}$	mass flow rate [kg/h]
n	refractive index [–]
p	pressure drop at the atomizer [Pa]
r	radius [m]
R_p	distance of inlet port axis to swirl chamber axis [m]
Re	Reynolds number [–]
S_0	Swirl number [–]
S_1	virtual distance of the measurement volume [m]
S_2	real distance of the measurement volume [m]
SCA	spray cone angle [°]
SFR	Spill-to-Feed ratio [–]
t	liquid sheet thickness [m]
U	axial velocity [m/s]
v	velocity [m/s]
W	swirl velocity [m/s]
We_g	gas Weber number [–]
X	ratio of air-core to of exit orifice area [–]
Z	axial distance [m]

Greek characters

μ	dynamic viscosity [kg/(m·s)]
ρ	density [kg/m^3]
σ	liquid/gas surface tension [kg/s^2]

Subscripts and Superscripts

ac	air-core
acc	air-core within the swirl chamber
ace	air-core within the exit orifice
c	swirl chamber
cal	calculated
g	surrounding gas
inj	injected
inv	inviscid analysis
l	atomized liquid
o	exit orifice
p	inlet port
r	reduced variable by 1-*SFR*
s	spill-line
sc	spray cone
y	experimental constant for swirl velocity [–]

$SFR \rightarrow 1$, where most of the liquid is spilled away.

Both the Simplex and Spill-return atomizers typically discharge a hollow cone liquid sheet [1]. The parameters of the liquid sheet, such as liquid sheet thickness, t, velocity and perturbations are related to the internal flow characteristics. The centrifugal liquid motion inside the swirl chamber generates an internal air-core due to a low-pressure zone up down the swirl chamber centreline. Air from the surrounding atmosphere is sucked into this zone through the exit orifice to form the air-core. The diameter of the air-core determines the value of t since the air-core blocks a part of the exit orifice. Moreover, any air-core fluctuations and instabilities affect the liquid sheet perturbations and stability [2] and may consequently change the liquid sheet breakup length. Better stability of the liquid sheet prolongs the breakup length [3]. From a simple geometric consideration, where the liquid sheet is considered as the hollow-cone, the longer breakup length results in a thinner liquid sheet at the breakup position. Therefore, the generated ligaments are smaller and so are the final droplet sizes [4]. Also, the breakup mode can change the size of the ligaments. Both long and short wave breakup modes have been observed [5] being dependent on the gas Weber number. It is based on the liquid sheet half thickness: $We_g = \rho_g U_l^2 t/2\sigma$, where ρ_g is air density, U_l is axial velocity of the liquid sheet, t is the liquid sheet thickness and σ is surface tension. The We_g reaches a critical value of 27/16, where a transition from the long to the short wave breakup mode appears. The long wave breakup mode produces a longer breakup length and tends to create smaller ligaments and droplets. This was confirmed in our previous work [4]. The initial amplitude of the liquid sheet perturbations is an important parameter for theoretical breakup models [3,5,6], but, due to a limited number of experimental results, it is often approximated.

Before the development of Computational Fluid Dynamics, many analytical approaches were derived assuming both inviscid flow [7–9] or viscous flow [10,11]. These models are suitable for prediction of the air-core diameter; however, the air-core dynamics is not usually captured. Experimental studies generally reveal a complex nature of the air-core shape and stability. The air-core surface may contain several types of surface waves and distortions, described in [2], as helical striations, stationary waves and random ripples. The stationary waves were found to be responsible for the temporal change in the liquid sheet thickness. The air-core stability varies with the geometrical design of the atomizer and its operating conditions. For low Re, the centrifugal forces are weak and thus the air-core is less developed and can even disappear [12]. The same applies for low Swirl numbers, S_0 [13]. The length of the air-core is also an important parameter since a long swirl chamber reduces the stability of the air-core and could produce an unstable spray [14]. Note that the air-core must be developed and stable within the exit orifice in order to achieve a stable spray. However, the spray stability has been found almost independent on the air-core stability further upstream within the swirl chamber [12,15].

Spill-return atomizers feature even more complex internal flow characteristics, since it can be affected by the presence of the SL orifice. Moreover, the internal flow conditions, such as S_0 and Re change with SFR. The SL orifice can have many geometrical configurations, e.g. a single orifice placed at the swirl chamber centreline, or several off-axial orifices placed around the swirl chamber. The single axially placed SL orifice was found to be prone to the air-core fluctuations, especially at low SFR regimes, and produced an unstable spray. The air-core periodically decayed and was developed only within the exit orifice [15]. This behaviour was attributed to the presence of a low-pressure zone across the SL orifice, through which the liquid could be drained from the SL into the swirl chamber and consequently fill the air-core with liquid. Off-axial SL orifices solve this problem, but their distance from the swirl chamber centreline can change the liquid sheet breakup mode [4]. The transition from the long to short wave breakup was observed even for We_g smaller than the critical We_g. It was assumed that this phenomenon was related to the fluctuations or stability of the inner air-core. This paper aims to test this hypothesis.

The turn-down capability of the Spill-return atomizer is hugely dependent on the size and position of the SL orifices. Despite the problems with the liquid sheet stability, the SL orifices located closer to the swirl chamber centreline yielded a wider turn-down capability while for the axially placed SL orifices this was maximised [4]. With its simple geometry, the single axially placed SL orifice has been used in many

studies [16–20]. Nevertheless, a few authors have pointed out that spray instabilities can occur [21,22] and suggest the use of the off-axial SL orifices. Khavkin [22] recommended placing the SL orifices at a radius $r_s/2$. Since this literature review identifies several contradictory conclusions, these are addressed within this study and, together with our previous work [4] should provide a more complete understanding of this problem.

In the current trend of increasing process efficiency, the leakage of the pressure energy with the spilled liquid is often inconvenient. To minimize the energy losses, it is beneficial to connect the SL directly to the suction side of a fuel pump and recover a portion of the pressure energy. The construction of the atomizer must prevent the air leakage to the pump suction. This was found challenging for some geometrical arrangements of the spill-return atomizers [23]. However, as no relevant literature was found to deal with this problem in detail, it is also addressed in this paper.

2. Experimental setup

The experiments were performed at special facility designed for cold atomizer testing at Brno University of Technology, Czech Republic.

2.1. The atomizer designs

The atomizer geometries were derived from an original geometry studied in our previous work [4]. However, to aid manufacturing simplicity the converging part of the swirl chamber was modified and three ports are to be used. Due to the small dimensions of the original atomizers, it was impossible to manufacture them and to examine their flows directly. To solve this issue, a transparent version was designed as a ten times scale model. The transparent atomizer has a modular construction. The assembly consists of two transparent parts made from cast polymethyl methacrylate, PMMA, which were ground and polished to achieve transparency, and three metal parts, including exchangeable caps, see Fig. 1. The operating regimes were based from the original atomizer [4] as follows: the Re_p was calculated for three p_l regimes and $SFR = 0$, which yielded $Re_p = 700$, 950 and 1250 for $p_l = 0.25$, 0.5 and 1 MPa respectively. The same Re_p was consequently used in this study, which results in $p_l = 3$, 6 and 12 kPa for the scaled atomizer and the test liquid. The spill regimes use a constant p_l and the regime is defined by changing the SFR values from 0 to the fully open SL. The Swirl number was the same for both the original and scaled atomizer due to design similarity.

Twelve caps with different arrangements of the SL orifices were designed; see Fig. 2. For sake of simplicity, the diameter of the SL orifices, d_s, was kept constant at $d_s = 3$ mm. Three off-axial orifices were used to maintain the circumferential periodicity of the swirl chamber. The caps C8, C9, C11, C15 and C22 use three off-axial, parallel orifices. The orifices are placed at different distances from the swirl chamber centreline; C8 has the orifices closest to the atomizer centreline, at a pitch circle diameter $d_{pc} = 8$ mm, C11, C15 and C22 use $d_{pc} = 11$, 15 and 22 mm respectively. Note here, that the cap number denotes d_{pc}, e.g. the atomizer C15 uses the cap with $d_{pc} = 15$ mm. The values for d_{pc} are based on the results from [4]. The C8B1 and C8B2 versions are based on C8 but contain an insert along the swirl-chamber centreline, which, in theory should reduce the air-core length and increase its stability [14]. Tangentially inclined SL orifices are introduced into the C8TG and C8TGC caps, where the C8TG uses orifices inclined towards the swirl motion, which reduces intake losses, while C8TGC uses the opposite inclination. The C14R cap contains a large insert where three spill-orifices are located and configured perpendicular to the atomizer main axis. Similarly, as for the C8B1 and C8B2 caps, the air-core length is reduced. The C8C version is also a modification of the C8 cap with the addition of an extra orifice located on the swirl-chamber centreline. The CC, on the other hand, uses a single axially placed orifice. Spray instabilities are expected in the case of both C8C and CC according to [15].

2.2. The test bench

A solution of Jet A-1 fuel (Kerosene type fuel) and 1-Bromonaphthalene was used as the test liquid. This solution maintains the similar rheological properties as the Jet A-1 fuel, but also simplifies the optical measurement within the atomizer, since its refractive index is closely matched to that of the PMMA. The physical properties of the solution at room temperature are as follows: surface tension $\sigma = 0.032$ kg/s^2, liquid dynamic viscosity $\mu_l = 0.0018$ kg/(m·s), and liquid density $\rho_l = 932$ kg/m^3. The test liquid was supplied to the atomizer from the fuel tank by a centrifugal pump. The mass flow was regulated by varying the pump speed. The fuel flowing through the inlet line was metered by the Coriolis mass flow meter Mass 2100 Di3 fitted with the Mass 6000 transmitter (Siemens AG, GE) with an accuracy ± 0.1% of the actual flow rate. A piezo-resistive pressure sensor DMP 331i (BD SENSORS s.r.o., CZ) measured the static inlet overpressure. The uncertainty in pressure sensing was 0.05 kPa. The inlet line was also equipped with a temperature sensor PR-13 (OMEGA Engineering, INC., USA) with an error of 0.2 °C. The spill-line used a piezo-resistive pressure sensor DMP 331i (BD SENSORS s.r.o., CZ), a regulation valve and a positive displacement flow meter FPD3202 with ± 1% accuracy of the actual flow rate (OMEGA Engineering, Inc., USA). The calculated uncertainty of discharge coefficient, C_D, was 0.25% of actual value. The atomized liquid was captured in a collection chamber and routed back to the fuel tank. The atomizer was mounted to a CNC positioning system with a positional error less than 0.1 mm.

2.3. High-speed imaging

A FASTCAM SA-Z high-speed camera (Photron, Japan) with a long-distance microscope 12X Zoom lens (NAVITAR, New York, USA) which composed of a 2X F-mount adapter (type 1-62922), a 12 mm F.F zoom

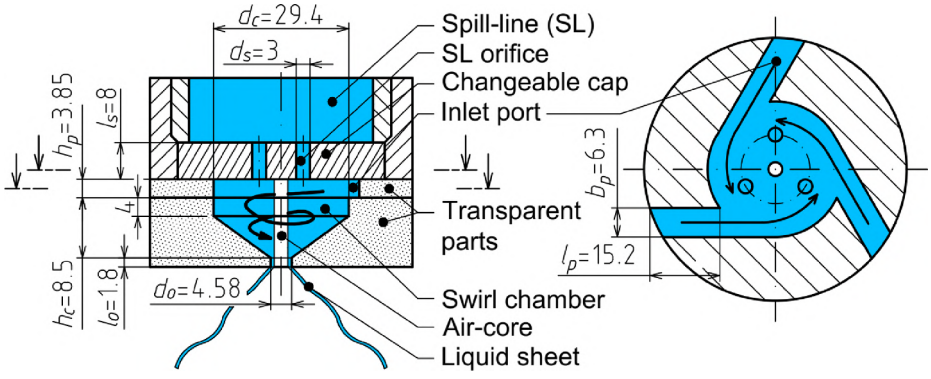

Fig. 1. Atomizer schematic drawing with main dimensions in millimetres.

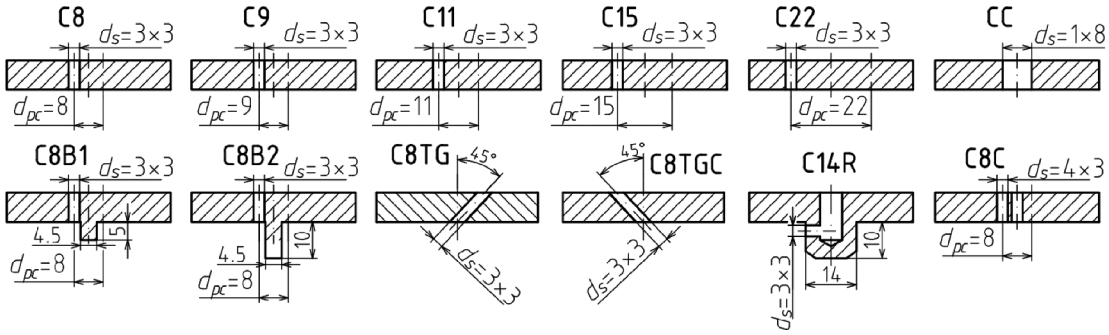

Fig. 2. Schematic drawing of tested caps with main dimensions in millimetres.

lens (type 1-50486) together with 0.25X lens (type 1-50011) was used to document the spatial and temporal behaviour of the air-core and discharged liquid sheet. A background LED panel illuminated the atomizer. The camera frame rate was 10,000 frames per second, the resolution was 1024 × 1024 px and the shutter speed was set to 40 μs. The air-core dimensions and the spray cone angle, *SCA*, were measured by an in-house MATLAB code using a threshold based detection technique. Two axial locations, for which the air-core diameter and its surface waves and fluctuations are discussed in this paper, are shown in Fig. 3. Similarly, the position where the spray cone fluctuations are evaluated is discussed there. The temporal fluctuations and waves were processed using Fast Fourier Transform technique, FFT.

2.4. Laser Doppler Anemometry

Point-wise velocity measurements inside the swirl chamber were carried out using a 2D LDA FlowExplorer (Dantec Dynamics A/S, Skovlunde, DK). Two perpendicular axes were measured at a single axial distance, see Fig. 3. Two orthogonal velocity components were acquired simultaneously. The traversed distance between two neighbouring measurement points was 0.25 mm. The LDA contains two built-in diode pumped solid state lasers with wave lengths of 660 nm and 785 nm wavelength. The beam from each laser was split into two parallel beams with a separation of 60 mm and power of 30 mW per beam. The wavelength of 660 nm was used for the swirl and radial velocity measurements, while the 785 nm wavelength measured the axial velocity component. The LDA, configured in the backscatter mode has a lens focal length of 150 mm. The measurement volume had the size of 0.1 × 0.1 × 0.8 mm. The LDA signals were processed using a Dantec P80 processor and the data acquisition was controlled using BSA flow software v5.2.

The refractive index of the atomizer body and working liquid differed by less than 0.005 for both 660 nm and 785 nm wavelength. Therefore, the velocity error is expected to be less than 0.4% [15,24]. However, the real position of the measurement volume inside the atomizer body had to be corrected as $S_2 = nS_1$, where S_2 is the real distance of the measurement volume from the atomizer wall and S_1 is the traversed distance of the measurement volume from the atomizer wall. The measurements near the air-core surface were affected by light reflections, which generate noise on the LDA signals and the subsequent velocity estimates. Therefore, these data were processed by a filtration algorithm, which seeks for a Gaussian distribution in the velocity histogram, and calculates the mean velocity only from the data which satisfies the Gaussian distribution.

Flow tracer particles SL75 e-spheres (Envirospheres, AU) with a mean diameter of 45 μm were used as tracers for the LDA measurements. Their Stokes number, based on the highest swirl velocity and air-core diameter, which is the worst scenario case for the particle movement, was less than 0.1 for each regime, which ensured a sufficiently high flow fidelity.

3. Results and discussion

Presentation of the results is divided into five parts. The first part is focused on the discharge parameters of the atomizers. The second one deals with the air-core characteristics. The third one focuses on the *SCA* and stability of the discharged liquid sheet. The fourth compares the temporal characteristics of the air-core and liquid sheet for two atomizers in detail, while the fifth discusses the measured velocity profiles within the swirl chamber.

3.1. Discharge characteristics

The discharge parameters were measured at p_l = 3, 6 and 12 kPa and for several *SFR* regimes in the range from an *SFR* = 0 to a fully open SL for spill overpressure, p_s = 0. There are two ways as how to evaluate the flow rates of the atomizers: at constant *SFR* or constant p_s. The former is better linked to the physics of the spray formation and parameters such as droplet size or *SCA*, while, in practical applications, the atomizers are likely to be driven by the pressure regulator.

The main difference between the Simplex and Spill-return atomizers is that the Spill-return version features a variable swirl number, S_O, dependent on the *SFR*. The S_O can be defined as the ratio of axial flux of angular momentum to axial flux of axial momentum and it can be calculated as [25]:

$$S_0 = \frac{\dot{m}_{inj} v_p R_p}{\dot{m}_{inj} U_o r_o}, \tag{1}$$

where v_p is a mean velocity inside the inlet port, U_o is an axial velocity inside the exit orifice and R_p is the mean radius at which the flow enters the swirl chamber: $R_p = \left(r_s - \frac{b_p}{2}\right)$. Neglecting the presence of the air-core, the velocities can be calculated as:

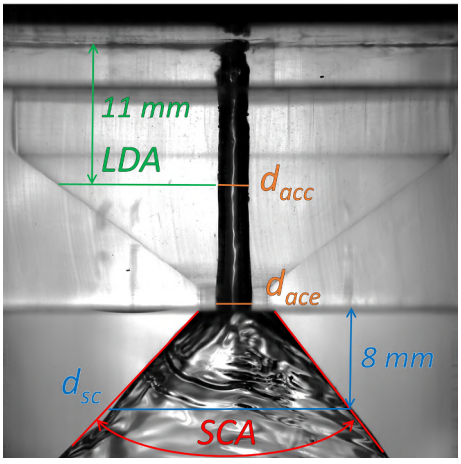

Fig. 3. The typical high-speed image with measurement positions.

$$v_p = \frac{\dot{m}_p}{A_p \rho_l}, \; U_o = \frac{\dot{m}_{inj}}{\rho_l \pi r_o^2} \tag{2}$$

Substituting Eq. (2) into Eq. (1) together with $SFR = (\dot{m}_p - \dot{m}_{inj})/\dot{m}_p$:

$$S_0 = \frac{\pi r_o R_p \dot{m}_p}{A_p \dot{m}_{inj}} = \frac{\pi r_o R_p}{A_p (1 - SFR)} \tag{3}$$

Then, the term $A_{pr} = A_p(1\text{-}SFR)$ represents the reduced area of the inlet ports, which can be interpreted as the inlet port virtually divides into two parts. Only the liquid flowing through A_{pr} contributes to the swirl chamber inflow, while the rest drains to the SL directly. Then, the reduced atomizer constant, k_r, is considered as a function of *SFR*:

$$k_r = \frac{A_{pr}}{\pi R_p r_o} = \frac{A_p (1 - SFR)}{\pi R_p r_o} \tag{4}$$

This simple assumption allows classical inviscid analysis and empirical equations derived for the Simplex atomizer to be applied to the spill-return version. The inviscid analysis is based on the Bernoulli equation of the inviscid flow and principle of maximum flow, which ensure, that the air-core diameter will adjust itself for optimum flow rate. This analysis was among others proposed by Giffen and Muraszew in 1953 [26] and is reviewed in detail in [8,9], where it is also compared with approaches derived by other authors. Only the final equations are mentioned here due to brevity. The ratio of the real mass flow rate to the theoretical can be measured by a discharge coefficient, C_D:

$$C_D = \frac{\dot{m}_{inj}}{A_o \sqrt{2 \rho_l p_l}} \tag{5}$$

In practical applications, C_D less than 1, due to viscous energy dissipation. The C_D calculated from the inviscid analysis is still applicable for pressure-swirl atomizers even when the viscous losses are neglected. The presence of the air-core effectively blocks off a portion of the exit orifice and reduces the C_D. Therefore, the C_D is solely dependent on the air-core dimensions and can be calculated using eq. 41 from [8,9] or eq. 5.37 from [1]. Both equations return identical results, but the latter is presented here due to its straightforwardness. The C_{Dinv} represents the C_D based on the inviscid analysis:

$$C_{Dinv} = \sqrt{\frac{(1 - X)^3}{1 + X}} \tag{6}$$

where X is the ratio of the air-core area to the area of the exit orifice: $X = A_{ac}/A_o$. The X can be calculated, when the principle of maximum flow, eq. 44 in [8,9], is applied:

$$X^3 + (2k_r - 3)X^2 + 3X - 1 = 0 \tag{7}$$

The only unknown parameter in Eq. (7) is the X , which can be calculated for each k_r. Then, the C_{Dinv} can be calculated from Eq. (6) and it depends only on the k_r, which is a function of atomizer geometry and *SFR*. This value can be used as a target value for atomizer design optimization since it neglects all the internal energy losses and represents an ideal atomizer. The viscous losses have two opposite effects. First, it reduces the axial velocity and tends to lower C_D. Second, the friction reduces the swirl velocity and consequently, the air-core diameter. It leads to a higher C_D. Our measurements give $C_D = 1.16 C_{Dinv}$ with $R^2 = 0.96$, see Fig. 4. Therefore, the second effect dominates, which is in agreement with general consensus [1,8–10]. However, Craig et al. [27] claimed, that non-optimal flows have a lower C_D that predicted by inviscid analysis, which is the opposite conclusion.

All of the atomizers, except the unstable CC and C8C, yield similar flow rates for $SFR = 0$ of $\dot{m}_{inj} = 71$, 96 and 131.6 kg/h with a standard mean deviation of ± 2, 3.5 and 5 kg/h but dependent on the atomizer used for $p_l = 3$, 6 and 12 kPa respectively. This leads to a discharge coefficients of $C_D = 0.50$, 0.48 and 0.46 ± 0.02. The variance among atomizers is likely caused by the complexity of flow near the SL orifices for some geometries, which increases overall energy losses in the swirl chamber or partially destabilizes the air-core. Therefore, the atomizer with inserts or tangentially inclined SL orifices typically exhibit slightly larger C_D values and a slightly smaller air-core diameter within the exit orifice. Unlike in the inviscid analysis, C_D decreases with increasing p_l as $C_D \propto p_l^{-0.06}$, see a notable data point classification according to p_l in Fig. 4. This is a well-known phenomenon as documented in [12]. The CC and C8C atomizers produce an unstable spray with $\dot{m}_{inj} = 86$, 112 and 143 kg/h for the CC atomizer and $\dot{m}_{inj} = 90$, 122 and 166 kg/h for C8C for $p_l = 3$, 6 and 12 kPa respectively which results in high C_D values of 0.59, 0.55, and 0.51 for CC and 0.63, 0.61 and 0.59 for C8C. This was expected, since no stable air-core was developed for this regime (as discussed later) and the flow cross-section at the exit orifice is therefore larger. Note here, that C8C yields a considerably higher C_D for $p_l = 12$ kPa than the CC. This can be attributed to the developing air-core in the CC case for higher p_l. Both atomizers are excluded from the inviscid analysis, since, with no air-core, the inviscid $C_{Dinv} \rightarrow 1$, which is in huge disparity with measured data. This could be explained by a large swirl velocity component that reduces the static pressure across the centre of the exit orifice, which consequently reduces the flow rate. The phenomenon of the undeveloped air-core was studied in detail in [15].

When the spill-line opens, the stable atomizers start to differ. The $\dot{m}_s$, $\dot{m}_{inj}$ and *SFR* are plotted for each atomizer for a fully open SL in Fig. 5. It is evident, that the overall liquid consumption grows with increasing d_{pc}. This trend was discussed in our previous work [4]. The C8 and C9 atomizers feature both the lowest $\dot{m}_s$ and $\dot{m}_{inj}$, thus, they can be attributed as to the most spill-efficient. The inserts into the swirl chamber, in the case of C8B1, C8B2 and C14R atomizers, have almost negligible effect on the flow-rates for all regimes tested. The C8C atomizer reaches the lowest value of *SFR*; despite it having one additional orifice. The atomizers with the inserts generally reach a lower *SFR* for a given pressure compared to their base variants.

The turn-down ratio, calculated here as the ratio of $\dot{m}_{inj}$ for $SFR = 0$ to $\dot{m}_{inj}$ for $SFR = 0.6$, likewise differs, see Fig. 6, where it is shown for $p_l = 6$ kPa. Similar results are also obtained for other p_l values. Since all of the atomizers were able to reach an $SFR = 0.6$, the difference comes only from the position of the SL orifices. The turn-down ratio is found to linearly decrease with d_{pc}. Note that for all the atomizers with $d_{pc} = 8$ mm an almost identical turn-down ratio of 2.05 was achieved. This was true even for the C8C version with flow rates 25% higher in comparison to the C8 atomizer under all *SFRs* investigated. The CC atomizer achieved the highest turn-down capability for a given *SFR*, followed by all the C8 versions and C9.

The tangential inclination of the SL orifice changes the pressure

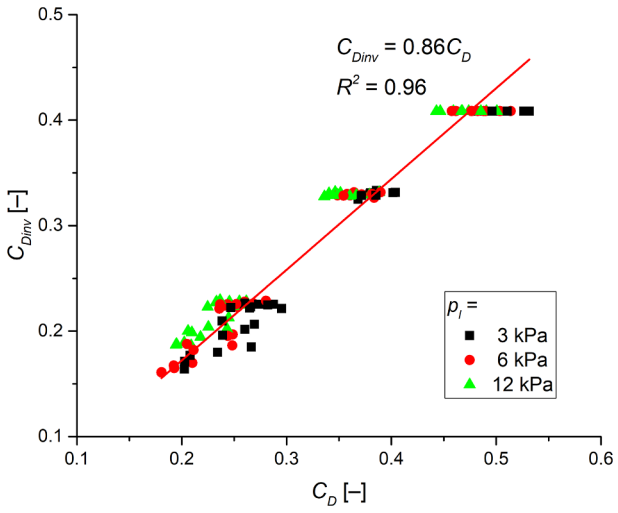

Fig. 4. Comparison of measured and calculated C_D.

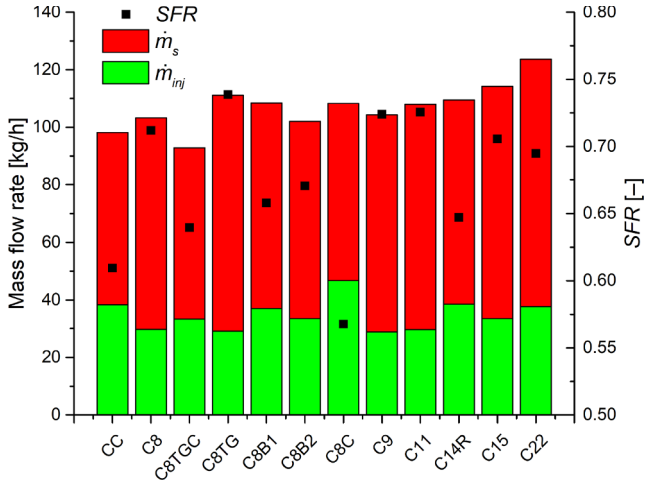

Fig. 5. Mass flow rates and *SFR* for $p_l = 3$ kPa and $p_s = 0$ kPa.

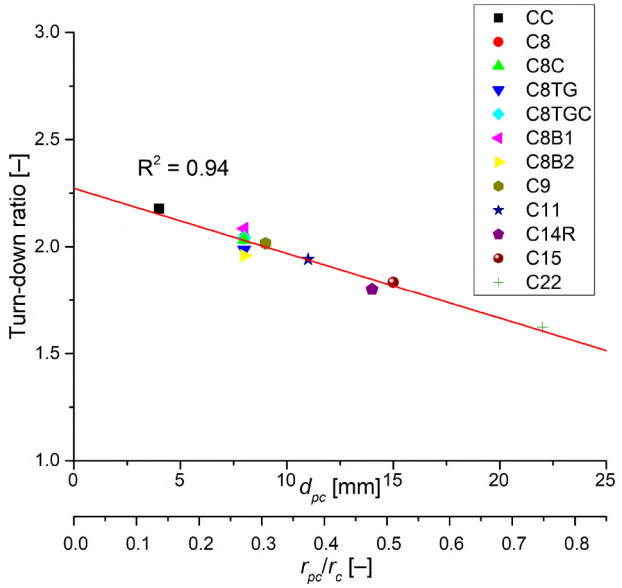

Fig. 6. Turn-down ratio for $p_l = 6$ kPa and $SFR = 0.6$.

drop with respect to the direction of inclination, see Fig. 7, where *SFR* is plotted with p_s. The SL orifices inclined towards the internal swirl motion in the case of C8TG, reduce the pressure drop and this version can reach higher *SFRs* and thus have a greater turn-down capability with fully open SL – see Fig. 5. However, no difference was found in the flow-rate at constant *SFR* despite inclination of the SL orifices. Another aspect for practical operation is the p_s value at a given *SFR*. The pressure regulator setting is very sensitive when a small change in p_s causes a large drop in *SFR*. This is the case for C8TG version, where the p_s is almost identical for $SFR = 0$ and 0.3. Thus, if the overall turn-down capability is not a priority, the SL orifices inclined opposite to the internal swirl motion ensure a smoother pressure regulation curve.

3.2. Internal air-core

The investigation of the internal flow plays a key role in understating the mechanisms responsible for the atomizer performance. The strong swirling motion inside the swirl chamber forms an air-core whose size and stability affects the whole spraying process, as discussed in the introduction. The high-speed imaging showed that the internal air-core is cylindrically shaped, being larger in diameter, see the stable C22 atomizer in Fig. 8, with the exit orifice which is well known phenomenon [28,29]. With increasing p_l the air-core diameter slightly increases as discussed in [10]. The presence of the air-core effectively blocks a portion of the exit orifice and causes relatively low C_D values, typical for pressure-swirl atomizers. The unstable C8C and CC atomizers have undeveloped air-cores, which agrees with the findings discussed in the previous section.

In all other cases, the air-core is developed across the whole length of the swirl chamber. The difference between the air-core size within the swirl chamber and the exit orifice is plotted in Fig. 9. With increasing *SFR*, the difference between d_{acc} and d_{ace} is decreasing and both increase almost linearly with *SFR*. This is due to a rising liquid flow rate through the tangential ports, which produces a stronger swirl motion and a lower axial velocity component as the spilled amount increases. The dimensionless air-core diameter, $\sqrt{X}$, from the inviscid analysis was overestimated for all the regimes, as predicted and with a nonlinear trend. When the calculated $\sqrt{X}$ is multiplied by the same correction coefficient as used for C_{Dinv}, 0.86, the values of $0.86\sqrt{X}$ match well at higher *SFRs* but are still overestimated for $SFR = 0$ and 0.3. These results confirmed that the smaller air-core leads to the higher C_D.

For low p_l, the helical striations, as described in [2], can be found as the result of three inlet ports which creates discrete flow patterns within the swirl chamber. The prominence of the helical striations decreases downstream in the swirl chamber and they are not detectable within the exit orifice. The greatest variance in the air-core diameter among the atomizers can be found for d_{acc} at low *SFRs* – Fig. 9. These differences diminish inside the exit orifice; as shown by small variations among atomizers for the d_{ace}.

The air-core stability is affected by the atomizer geometry, in this paper, the configuration of the SL orifice and the presence of the inserts which reduce the air-core length are the only different parameters. The air-core stability can be quantified by the standard mean deviation, SD, of the air-core diameter fluctuations at a given location. The air-core fluctuations inside the swirl chamber measured at d_{acc} only moderately affect the air-core stability within the exit orifice d_{ace} with $R^2 = 0.69$. The air-core stability slightly decreases with increasing d_{pc}, as shown in Fig. 10. This phenomenon was discussed in [4], by means of differences in the breakup mode. It is evident here, that the air-core stability slightly decreases for $d_{pc} < 11$ mm. The SL orifices for the less stable atomizers are placed in the zone, where the pressure gradient is increasing. Therefore, an apparent pressure change can be generated across the SL orifice diameter. As it was discussed in [15], this pressure gradient can create a two-way flow through the SL orifice and generate vortices, which consequently reduce the air-core stability. This behaviour can be readily observed in the case of the C8C atomizer, where

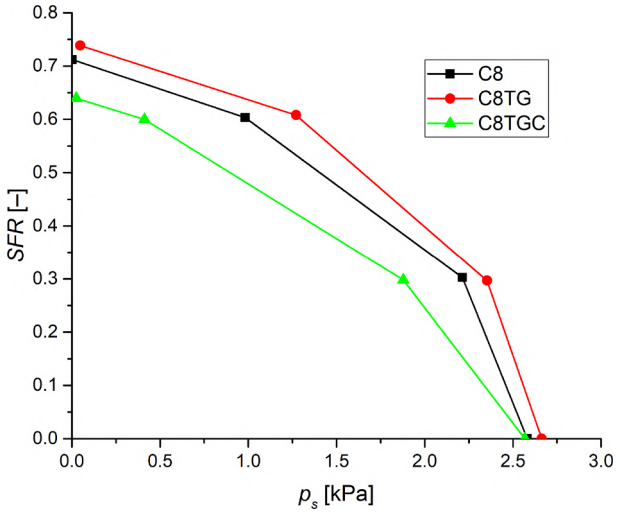

Fig. 7. Comparison of *SFR* for inclined SL orifices dependent on p_s, $p_l = 3$ kPa.

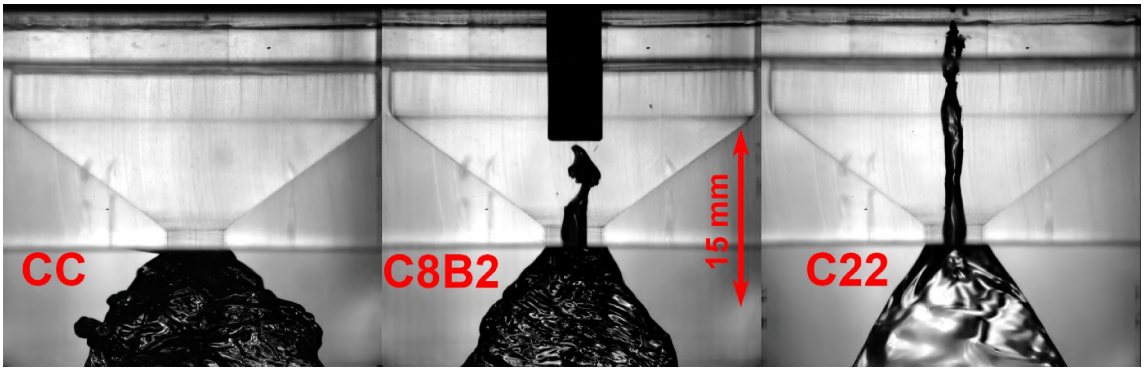

Fig. 8. Comparison of the air-core behaviour of the CC, C8B2 and C22 atomizers for p_l = 3 kPa and SFR = 0.0.

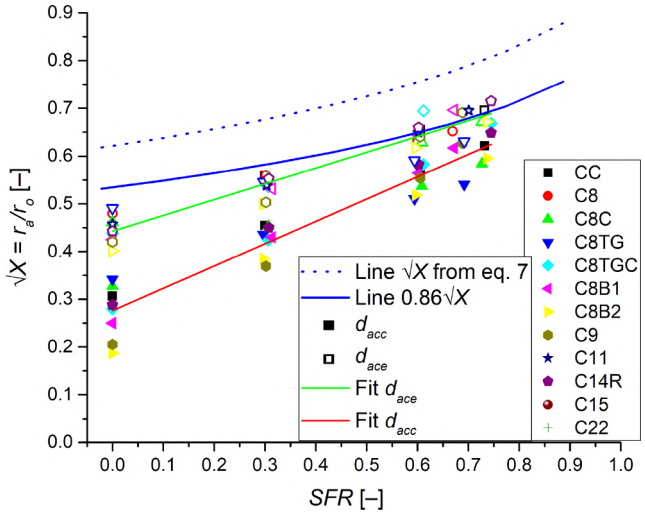

Fig. 9. Effect of SFR on the air-core diameters d_{ace} and d_{acc} for p_l = 6 kPa. The unstable regimes excluded. Dotted line is based on the inviscid analysis.

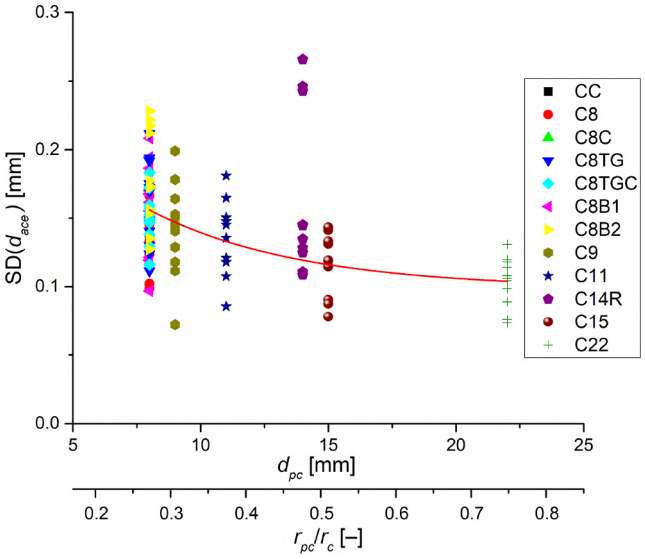

Fig. 10. The air-core stability, the unstable CC, C8C are excluded from the plot and the C14R is excluded from the fit curve.

the liquid flows into the SL via the distant orifices due to the higher pressure there, and is sucked back into the swirl chamber by the central orifice due to a low pressure zone along atomizer centreline. This atomizer is the only one which had no air-core under any operating regime, since the low pressure zone was always filled by the liquid.

The air-core diameter fluctuations and surface dislocations can be assessed from the high-speed images for a given location as a function of time. The similarity of the air-core surface distortions along its length is then evaluated using a cross-correlation method. Results shown here are time varying data related to the d_{acc} position which is cross-correlated with positions downstream of the air-core. For each data pair a maximum in the correlation coefficient was obtained (Fig. 11) together with its representative time shift (Fig. 12). Air-core diameter fluctuations for two atomizers with different air-core stability (see following sections of this paper) are only shown here for brevity. Results suggest that the signal correlation is lost after just 2.5 mm downstream which is in the same order of magnitude as the air-core diameter itself. Also, the correlation coefficient drops sharply below a value of 0.3 which points to a poor correlation quality. The same result was obtained for both surface wave and air-core diameter fluctuations. This may be caused by a rapid change in the air-core surface shape due to its rotation. However, an interesting phenomenon can be observed in the time shift values, which are positive for the regimes with SFR = 0 and 0.3 but change to negative values for SFR = 0.6 and 0.7. A negative value corresponds to a downwards movement in the swirl chamber. This result was unexpected and suggests the presence of a large rotating vortex which modifies the motion of the surface waves. Nevertheless, this should be investigated further e.g. using numerical simulations. Note here, that the cross-correlation method performed on the discharged liquid sheets show negative time shift values for all tested regimes and atomizers, but yields much higher correlation coefficients. The cross-correlation performed inside the exit orifice demonstrates a rapid

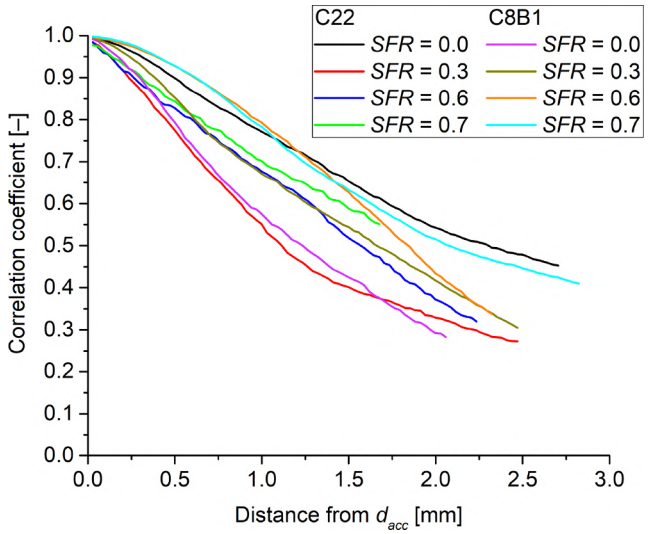

Fig. 11. Correlation coefficient as a function of distance from d_{acc} position. p_l = 6 kPa.

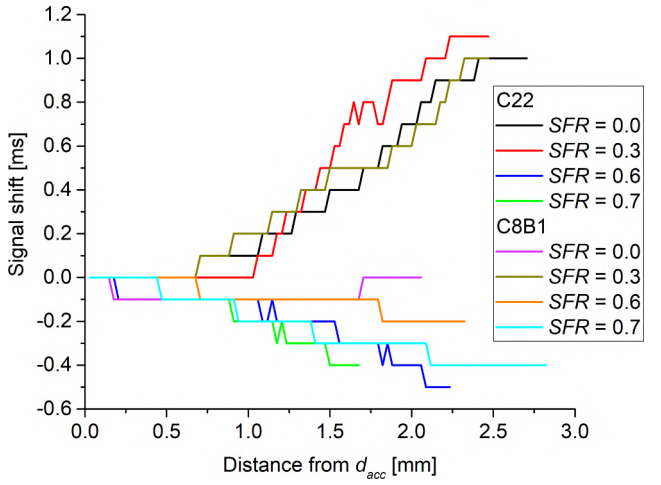

Fig. 12. Temporal shift of surface waves as a function of distance from d_{acc} position. p_l = 6 kPa.

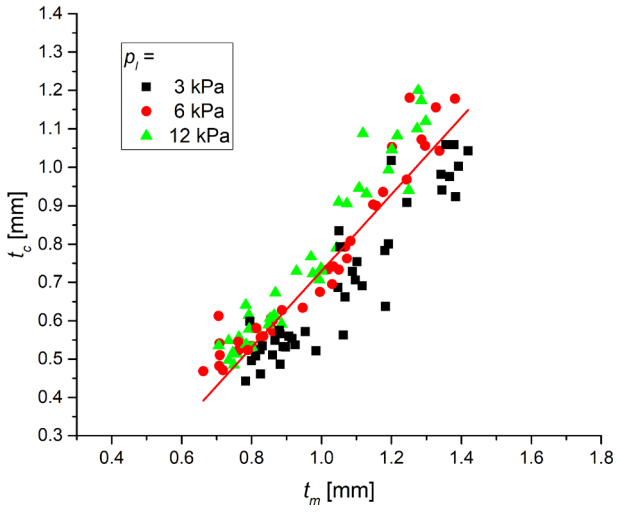

Fig. 13. Comparison of the measured and calculated t from Eq. (8).

movement of the surface waves since the time shift was virtually zero along the whole exit orifice length for all cases tested.

The inserts inside the swirl-chamber used in the C8B1, C8B2 and C14R atomizers change the air-core behaviour, e.g. in the case of the C8B1 atomizer at $SFR = 0$ the air-core occasionally splits into several parts. The overall stability of the air-core for these atomizers was lower compared to their base variants, see C8B2 in Figure 8 and C14R in Fig. 10. This result was unexpected since the shorter air-core should be rather more stable as described in [14]. The C_D of these atomizers was slightly higher than their base variants, which agrees well with the less stable air-core. The only beneficial effect is a higher resistance to the air leakage, which may be important in applications where the SL is connected directly to the pump suction to recover a portion of p_s energy.

Air leakage through the SL line is often one of the limiting factors of spill-return atomizers as the air may feed into the pump inlet. In this paper, the presence of air inside the SL was visually observed through a transparent SL tube. The only atomizer which leaked air was the CC atomizer under the operating condition of $p_l > 6$ kPa and $SFR > 0.6$. This was expected since the air-core penetrates through the SL orifice and brings air into the SL. The other atomizers had to be tested under more extreme conditions to reveal their limits. First, the operating regime was set to $p_l = 3$ kPa and $p_s = 0$ kPa. Then the $\dot{m}_s$ was kept constant and p_{in} was reduced until the air bubbles were observed inside the SL. The C22 atomizer shows the greatest leak resistance, which has to be operated at $p_l = 0.2$ kPa and $SFR > 0.9$ and the liquid has to be sucked from the SL at p_s = -3 kPa. On the other hand, for the C8 version, the leakage was observed at $p_l = 2$ kPa and $SFR = 0.8$, which is still much better than CC version. The atomizer with inserts – C8B1, C8B2 and C14R – show a greater air leak resistance compared to their base variants. The air leakage can practically occur for all possible geometries of the spill-return atomizers and their resistance must be checked experimentally dependent on the application.

3.3. Spray cone angle and liquid sheet stability

The liquid sheet thickness, t, is one of the crucial parameters which determines the sheet breakup mode [3] and the subsequent sizes of the droplets in the spray. It is easily calculated if the air-core diameter is known just by subtracting the measured air-core radius from the exit orifice radius. In addition, the inviscid analysis can provide an estimate on the value of t, but some correction factors must be applied, as mentioned above. If no direct measurement of d_{ace} can be performed, then t could be also estimated from the continuity equation:

$$\dot{m}_{inj} = \pi \rho_l U_l t (d_o - t), \tag{8}$$

where U_l is axial velocity of the liquid sheet inside the exit orifice. Determination of U_l is the crucial aspect here. For practical applications, it is convenient to approximate U_l from the axial velocity of the discharged liquid sheet, which can be easily measured using cross-correlation of high-speed images using e.g PIVlab®, or Laser/Phase Doppler Anemometry. The relationship between the PIVlab® and Laser Doppler measurement was discussed in [4], where both the approaches were found to be reliable with differences of less than 2%. However, the moving waves on the liquid sheet can bias the results from image cross-correlation methods, as described in [30]. Therefore, the regimes with a very smooth liquid sheet emerging at low p_l may cause errors in velocity values in the range of several percent. The correlation between the measured, t_m and calculated, t_c, values is shown in Fig. 13. It is evident that the calculated values are comparable with measured values, but there is a notable separation of the data according to p_l. Moreover, the calculated results underestimate, on average, the liquid sheet thickness by a constant value of 0.2 mm. The approximated velocity U_l would therefore be greater than the real velocity of the liquid sheet. It can be explained by the presence of boundary layers on the air-core interface and near the atomizer wall. Also, the low p_l regime may exhibit a more laminar flow profile and therefore the bias is larger. This approach is suitable for higher Re and it gives rather an estimate in liquid sheet thickness.

The SCA was evaluated from images obtained from the high-speed imaging. Since the only geometrical variation among the atomizers tested is the position of the SL orifices, the change in the SCA is only possible through the change of the swirl to axial momentum ratio, which varies with SFR. This phenomenon has been addressed in several papers [4,17,20]. Assuming the reduced k_r, the correlations established for the Simplex atomizers can also be used for the spill-return version. The widely used correlation proposed by Rizk and Lefebvre for the Simplex atomizers [31]:

$$SCA = Bk_{1r}^{-0.15}\left(\frac{p_l d_o^2 \rho_l}{\mu_l^2}\right)^{0.11} \tag{9}$$

where $k_{1r} = A_{pr}/(d_o d_c)$ is the Atomizer constant as used in [31], B is an experimental constant, and it is set here as $B = 10$ while in [31] it has a value of 6. The difference may partially result from the different measurement method used here. In our recent paper [4], a simple empirical correlation for the SCA of small spill-return atomizers was proposed with variance on SFR and p_l solely. Note that both the variables have almost identical exponents in [4] where $SCA \propto p_l^{0.1}$ and $(1\text{-}SFR)^{-0.15}$ as presented in Eq. (9), which were originally derived for Simplex atomizers. The fit quality for all combinations and regimes is $R^2 = 0.89$,

see Fig. 14. The *SCA* is almost identical for all the atomizers except the unstable CC and C8C for $SFR = 0$ and the same p_l. The *SCA* calculation according the inviscid theory over predicts its value similarly as in [8,9] and also neglects the effect of p_l. Hence, it has little practical applicability and it is not discussed here for brevity.

The spray stability was evaluated using the SD of the *SCA*. The unstable regimes reach an SD of about 10°, which corresponds to a significantly fluctuating spray. The SD is weakly dependent on the d_{pc}, since the C8 atomizer reaches 3.5° and it decreases to 2.5° for the C15 and C22 atomizers for $SFR = 0$. However, for $SFR \geq 0.6$, the spray fluctuations increase by 60% for all atomizers.

The scaled atomizers used here ensures similar conditions of the internal flow as in the original version [15], but the We_g, which governs the nature of the liquid sheet breakup, is not replicated here and so the breakup is not directly comparable. In addition, the breakup point lies beyond the recorded image frame height. Thus, the discharged liquid sheet is discussed by means of the temporal stability just downstream from the exit orifice. The We_g reaches values in the range from 0.02 to 0.50 with a dependency on *SFR* and p_l, which are an order of magnitude lower than those investigated in [4] and also much lower than the critical We_g value of 27/16. Therefore, the long wave breakup should occur for each operating regime.

Temporal wave oscillations can be obtained by fixing a location and observing the surface change as a function of time. In this way, spatio-temporal diagrams of the liquid sheet and air-core were obtained, where each vertical line corresponds to a fixed line from the high-speed images at different time steps. The spatio-temporal diagram in Fig. 15 shows the liquid sheets discharged from three different atomizers operated under the same condition: $p_l = 3$ kPa and $SFR = 0.0$. As the surface wave propagates downstream, its amplitude increases, but the frequency remains the same which was confirmed by cross-correlation evaluation of the discharge liquid sheet and it agrees with findings in [32]. For the sake of simplicity, only one axial position, as shown in Fig. 3, is discussed here. The most unstable pattern shown in Fig. 15 top was produced by the CC and C8C atomizers. It is characterised by large surface wave amplitude and a wide range of frequencies. The more stable mode, middle figure, has much lower amplitudes but still relatively high frequencies of surface waves. This mode was generated by the whole C8 series, C9 and C14R atomizers. The only stable mode (bottom figure) has a very smooth surface with small disturbances at a very low frequency. This mode is likely to be the only one which results in the long wave breakup mode as described in [4]. It diminishes with $p_l > 6$ kPa even for the most stable atomizers, C15 and C22.

Since the operation conditions such as *Re* and We_g are virtually identical, the stability difference has to be linked with the internal air-core stability. A similar conclusion was proposed in [4], where two different atomizers, operated under identical conditions, demonstrated both short and long wave breakup-modes and also produced a spray with different droplet sizes. The change in the breakup mode was attributed to the differences in the initial amplitude and frequency of the liquid sheet surface waves. To test this hypothesis, the air-core fluctuations are correlated with the liquid sheet fluctuations. The relative SD of the liquid sheet thickness within the exit orifice represent the internal fluctuations. It was obtained by measuring the SD of liquid sheet divided by the liquid sheet thickness, *t*. These data are compared with the spray fluctuations, represented by a relative SD of the spray width at given axial distance, d_{sc}. The correlation of both measures is in Fig. 16. Despite only a moderate R^2, it is obvious that the initially unstable liquid destabilizes the discharged sheet. This confirms our previous hypothesis that the internal fluctuations affect the liquid sheet. Note that in Fig. 16, there is no stable regime for $p_l = 12$ kPa which corresponds with a prior discussion as regards the stable liquid sheet modes. A partial correlation using a constant p_l returns $R^2 = 0.60$, 0.77 and 0.4 for $p_l = 3$, 6 and 12 kPa respectively. The correlations of the frequency spectra are described in the following section of this paper.

3.4. Air-core and liquid sheet dynamics

Two atomizers with a relatively stable air-core but with different liquid sheet breakup patterns were subjected to a frequency analysis of the air-core and liquid sheet fluctuations. The stable atomizers are represented by the C22 versions and a partially unstable by the C8B1, both were operated at $p_l = 6$ kPa, $SFR = 0.0$. This regime was selected due to the more prominent wave amplitudes than reported in Fig. 15. Both atomizers achieved almost identical flow-rates and mean air-core diameters. The spatio-temporal diagrams of the air-core and liquid sheet are shown in Fig. 17. Note, that the air-core surface, at a given time step, is very smooth – see Fig. 8, but its shape is rapidly changing in the temporal domain. Since the air-core is not perfectly cylindrical, it changes its diameter and position slightly during each revolution and, due to the finite camera frame-rate, a sharp change in the temporal domain can occur.

For both atomizers, the air-core diameters are seen to expand and contract in the swirl chamber, d_{acc}, but this behaviour diminishes within the exit orifice. To quantify the fluctuating frequency, an FFT was applied to the data of air-core and discharged liquid sheet width changes, which corresponds to the contractions and expansions, and boundary movement which also captures the spatial dislocation of the air-core or liquid sheet. A binomial smoothing filter was applied on the FFT signal for clarity, see Fig. 18. Despite a relatively strongly fluctuating liquid sheet, no dominant frequency or wave mode was observable here. Similarly, rather random waves are observed for the rest atomizers and regimes. A comprehensive study of liquid sheet waves was performed [32], where the dominant wave frequency was obtainable only for relatively high-viscous liquids, which is not the case here. The waves with frequencies up to 100 Hz are dominant on both the liquid sheet width and edge. These waves are related to the air-core spatial movements rather than with the diameter fluctuations, see d_{acc} and d_{ace} in the bottom part of Fig. 18. The frequency peaks for the air-core expansion/contraction for d_{acc} are located at 175 and 303 ± 3 Hz and they are identical for both the atomizers. However, their amplitudes diminish rapidly within the exit orifice.

The only notable difference between the stable and partially unstable atomizer are the high-frequency waves, present on the liquid sheet in the case of C8B1 atomizer, see the frequency range of 500–1000 Hz. These waves are insignificant in the case of the C22 atomizer. The high-frequency waves may be responsible for the short-wave breakup mode, observed in [4]. Nevertheless, detection of these fluctuations on the d_{ace} is difficult due to their small amplitudes, rapid changes and very low contrast.

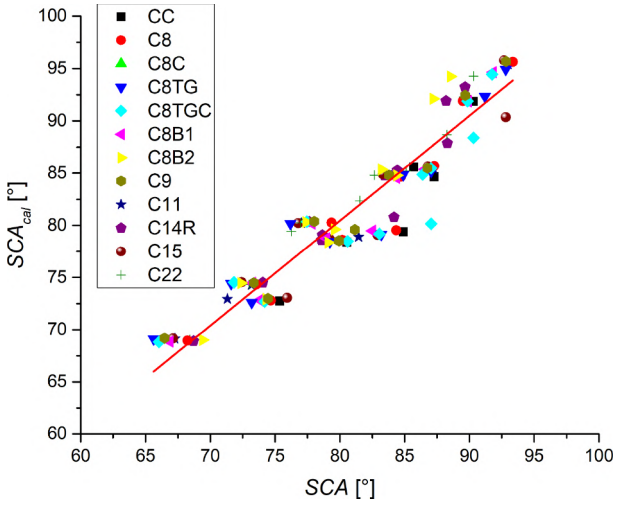

Fig. 14. Comparison of calculated and measured SCA.

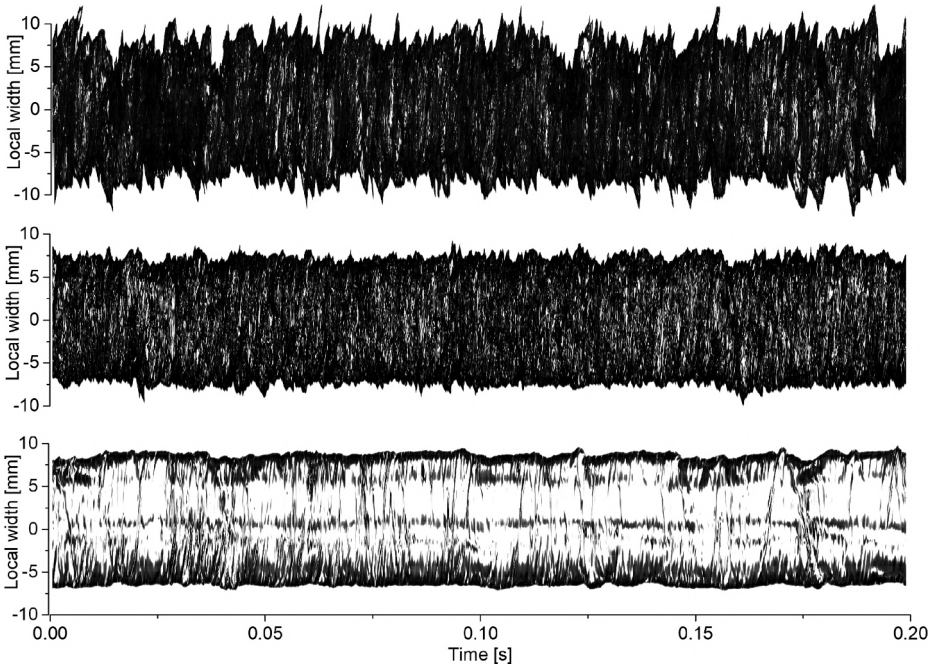

Fig. 15. The spatio-temporal diagrams for three typical breakup patterns, p_l = 3 kPa, *SFR* = 0.0. Top: CC atomizer, middle: C8 atomizer, bottom C22 atomizer.

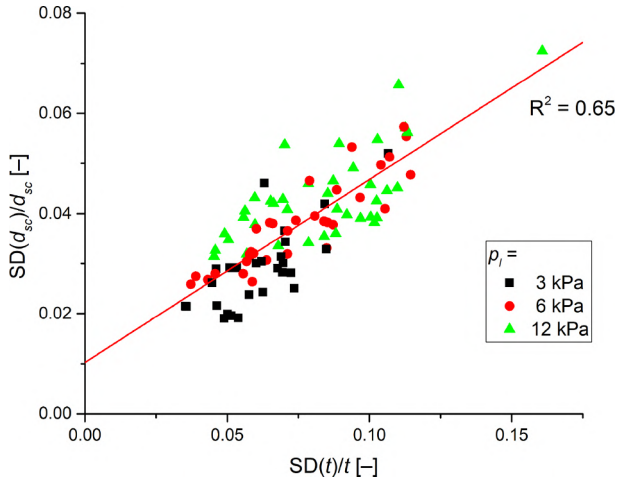

Fig. 16. Correlation of the internal liquid sheet and discharged liquid fluctuations. The regimes without developed air-core are excluded.

3.5. Velocities inside the swirl chamber

All three velocity components were measured using the LDA. Since the swirl velocity is similar across the whole swirl chamber height [10,15,33], only one cross-section is subject to analysis. The selection of the cross-section was based on the best optical transmission of the laser beams paths through the atomizer body. The beams for measurement of the axial velocity component could be distorted by the surface interfaces of the model body.

The atomizers with the stable air-core show a relatively sharp maximum in the swirl velocity profiles, *W*, which was located near to the air-core surface. This corresponds well with other observations [15,19] and it is typical for a Rankine vortex, where the air-core behaves like a rotating solid body and the swirl velocity decreases with distance from the rotating centre. The relative swirl velocity profiles were almost identical for all the pressure regimes and thus only data for p_l = 6 kPa are discussed here for clarity. With increasing *SFR*, the velocity within the inlet port, v_p, increases but the swirl velocity component rather remains similar. Thus, the relative velocity is decreasing. In addition, due to a larger d_{ac}, the velocity maximum is shifted from the swirl chamber centre line. When the different atomizers are compared, the swirl velocity component depends mainly on the air-core presence. If the air-core is not developed, the swirl velocity reaches a lower and flatter maximum, see the case of the CC and C8C atomizer in Fig. 19. With increasing *SFR*, the air-core inside the CC atomizer stabilizes and the atomizer behaves similarly to the rest. Only minor variations are to be found among the stable atomizers. The value of *W* can be calculated simply if an inviscid flow is assumed. Then *W* varies across the swirl chamber for a Rankine vortex as Wr = constant. However, this equation over predicts the *W* since it neglects the viscous losses. Khavkin [22] suggested a simple modification as Wr^y = constant, where *y* is an empirical constant, which can be physically interpreted as an approximation of hydraulic losses [22]. The value of *y* reaches 0.88 for *SFR* = 0 with virtually no difference among the tested atomizers. It decreases with *SFR* as *y* = 0.8 for *SFR* = 0.6 and *y* = 0.65 for *SFR* = 0.7. This sharp decrease indicates exponentially increasing hydraulic losses with increasing *SFR*. Note here, that the Khavkin's approach matched the measured swirl velocity well up to $r = r_o/r_c$. The flow complexity in the zone near the air-core is high [10], and the viscous effect plays a more dominant role there. Furthermore, the precision of the measured data is affected by the light reflections from the air-core surface.

The measured turbulence intensity of the swirl velocity component (TI) reaches minimum values of about 7% at the half radius of the swirl chamber, $r = r_c/2$, and it increases towards the walls or the air-core. Comparable values were obtained for all regimes with only a slight trend where the TI rather decreases with *SFR* and p_l. Note here that the LDA tends to overestimate the TI due to the relatively long measurement volume and also to the fact that periodic oscillations can be considered falsely as turbulence.

The axial velocity component, *U,* reaches two local maxima, the first one is located close to the swirl chamber wall while the second one, which is more prominent, lies near the air-core interface. This wall maximum is almost independent of the *SFR*, p_l and the atomizer used and reaches values of about $0.25v_p$. The maximum at the air-core is decreasing with *SFR* as a results of lower $\dot{m}_{inj}$. The local minimum of *U* for positions located around $r_s/2$ even show negative values for *SFR*

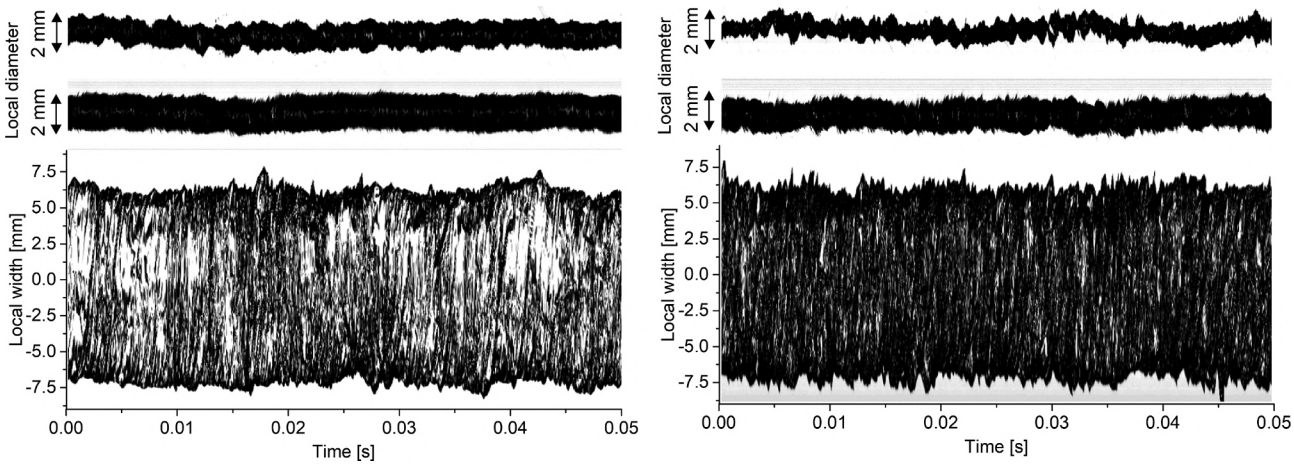

Fig. 17. Spatiotemporal diagrams. Top and middle: Comparison of surface waves on the air-core surface of C22 and C8B1 atomizer for $SFR = 0$, d_{acc} and d_{ace}. Bottom: Temporal stability of the liquid sheet.

$= 0.6$ and 0.7. This indicates the presence of a large rotating vortex within the swirl chamber and it agrees well with a change in direction of the time shift from the cross-correlation results. This minimum was found for all the atomizers and p_l but the unstable C8C exhibits the lowest U values.

The radial velocity was found to be very low compared to U and W and can be considered as almost negligible so it is not shown here for brevity. It reaches maximum values of about $0.2v_p$ near the air-core and rapidly decreases to values of roughly $0.05v_p$ within the rest of the swirl chamber with the velocity direction towards to the swirl chamber centreline. Moreover, the measurement uncertainty of the radial velocity at the position near the air-core interface is relatively high due to

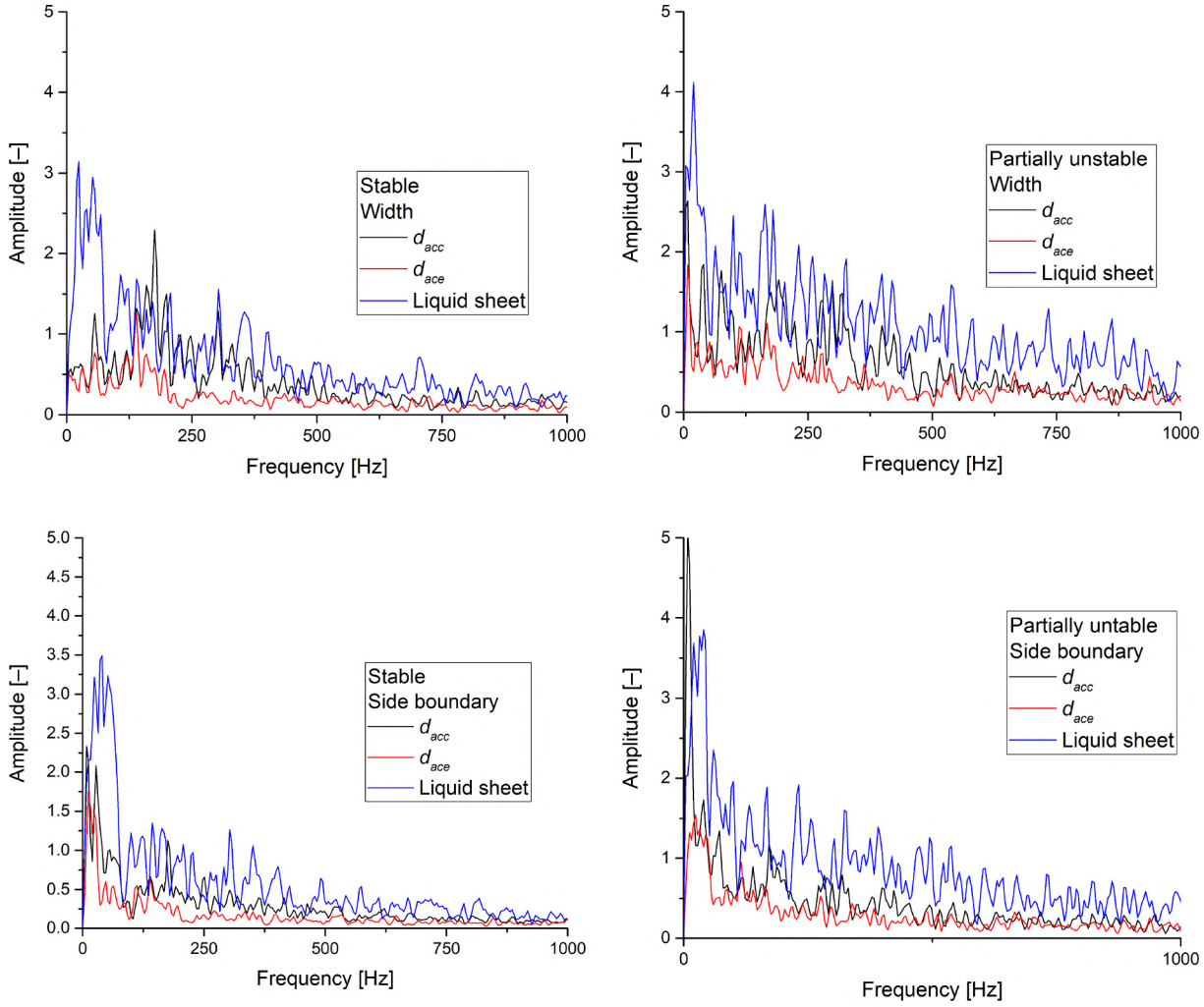

Fig. 18. The FFT of the air-core width (top) and edge (bottom). The C22 (left) and C8B1 (right) atomizers.

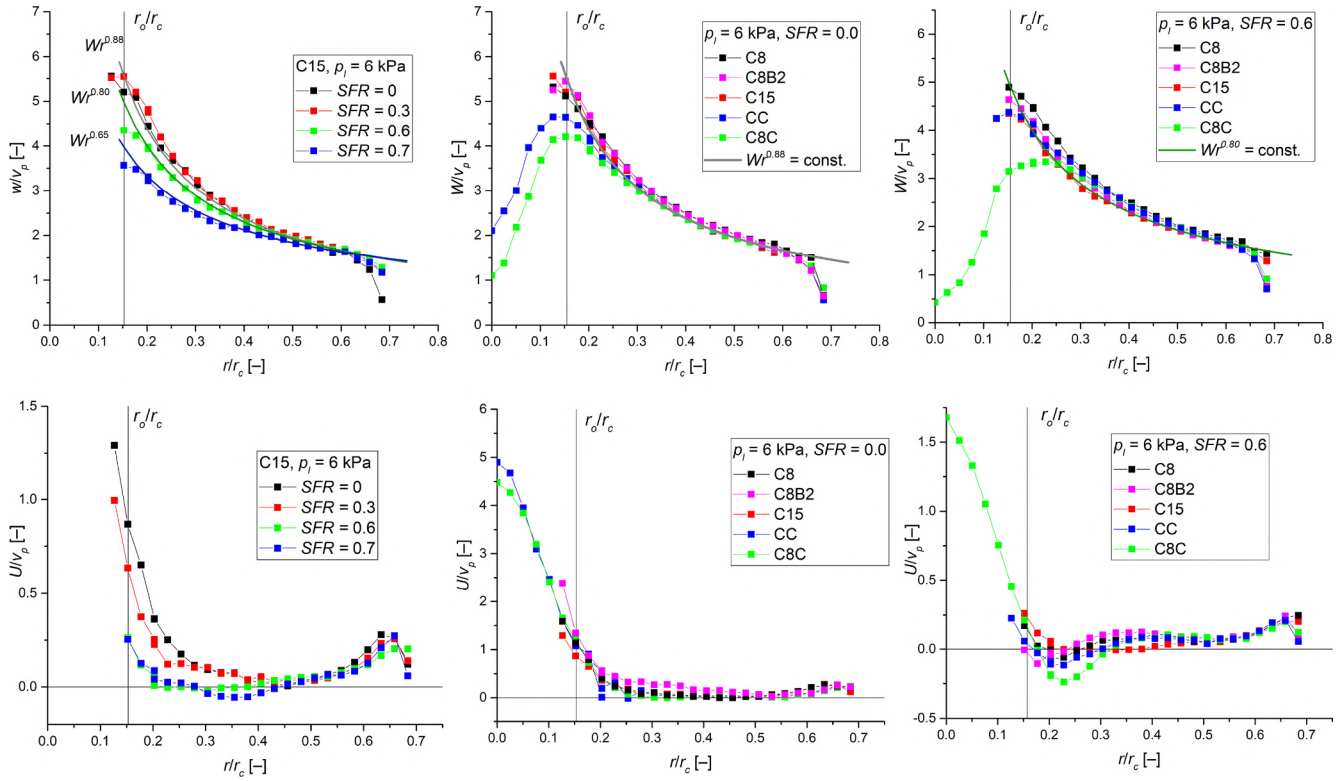

Fig. 19. Swirl (top) and Axial (bottom) velocity profiles. Left: The C15 atomizer at $p_l = 6$ kPa and various *SFR*. Middle: $p_l = 6$ kPa, $SFR = 0$, various atomizers, right: $p_l = 6$ kPa, $SFR = 0.6$, various atomizers. The ratio r_o/r_c marks the position of the exit orifice.

positioning error, which may result in occasional measurements of a partial swirl velocity component. This error diminishes with distance from the atomizer centre line. No correlation of frequency spectra between measured velocity fluctuations and the air-core temporal surface dislocations was found.

4. Conclusions

Experimental investigations on 12 transparent Spill-return pressure-swirl atomizers were performed using high-speed imaging and Laser Doppler Anemometry. A scaled transparent PMMA model of a modular construction was used. To overcome optical distortions, refractive index of the atomizer body and the working liquid was matched using a solution of JET A1 and 1-Bromonaphthalene.

The reduced area of the inlet ports was used to modify the inviscid analysis originally derived for the Simplex atomizers. The modified analysis was used for predictions of C_D and air-core diameter in the Spill-return atomizer. The measured C_D was higher, approximately by 16%, due to viscous friction, which reduced the air-core diameter compared to the inviscid assumption. Furthermore, the reduced area of the inlet port can be used in the empirical correlations, derived for Simplex atomizers. Its predictive capability was proven for estimates of the spray cone angle.

The turn-down ratio, the ratio between the minimum and maximum injection flow rates, was found to be affected by the pitch circle diameter, d_{pc}, on which the spill-line (SL) orifices were located. An increase in d_{pc} reduces the turn-down capability. The spray cone was stable for all atomizers, except the CC and C8C versions, which featured a central SL orifice. These atomizes have no air-core inside the swirl-chamber. The cylindrically shaped air-core, wider in its diameter within the exit orifice than in the swirl chamber, was found for all the other atomizers. The air-core diameter increases linearly with spill to feed ratio, *SFR*, while the difference between the air-core diameters inside the swirl chamber and the exit orifice decreases with *SFR*.

Inserts in the swirl chamber, which aim to reduce the air-core length, destabilise the air-core and provide no beneficial effect apart from a slightly increased resistance to air-leakage through the spill-line. Tangential inclination of the SL orifices changes the pressure difference losses through the SL orifice and can enhance regulation of pressure setting or increase the maximum turn-down capability, but with a dependence on inclination direction.

The measured liquid sheet thickness, *t*, was compared with the calculation based on the Continuity equation but using the axial velocity of the discharged liquid sheet instead of the axial velocity of the liquid sheet within the exit orifice. The correlation between measured and calculated values of *t* proved, that *t* can be estimated but validation by direct measurement is still recommended.

The temporal characteristics of the air-core and discharged liquid sheet were examined in detail for two atomizers. High-frequency waves were found for the partially unstable atomizer. An FFT analysis did not reveal any dominant frequency, for neither the air-core nor the liquid sheet, but showed slightly higher magnitudes of air-core fluctuations for the C8 atomizer. The high-frequency waves may cause changes in the liquid sheet breakup mode, as described in [4].

CRediT authorship contribution statement

Milan Maly: Conceptualization, Investigation, Data curation, Writing - original draft, Writing - review & editing, Visualization. **Ondrej Cejpek:** Investigation. **Marcel Sapik:** Resources, Methodology. **Vladimir Ondracek:** Resources, Methodology. **Graham Wigley:** Supervision. **Jan Jedelsky:** Conceptualization, Supervision, Funding acquisition, Project administration.

Declaration of Competing Interest

The authors declare that they have no known competing financial interests or personal relationships that could have appeared to

influence the work reported in this paper.

Acknowledgements

The authors acknowledge the financial support from the project No. 18-15839S funded by the Czech Science Foundation and the project "Computer Simulations for Effective Low-Emission Energy Engineering" funded as project No. CZ.02.1.01/0.0/0.0/16_026/0008392 by Operational Programme Research, Development and Education, Priority axis 1: Strengthening capacity for high-quality research.

References

[1] A.H. Lefebvre, V.G. McDonell, Atomization and sprays, CRC Press, 2017.
[2] J.J. Chinn, D. Cooper, A.J. Yule, G.G. Nasr, Stationary rotary force waves on the liquid–air core interface of a swirl atomizer, Heat Mass Transf. 52 (10) (2015) 2037–2050.
[3] Q.-F. Fu, L.-J. Yang, Y.-Y. Qu, B. Gu, Linear stability analysis of a conical liquid sheet, J. Propul. Power 26 (5) (2010) 955–968.
[4] M. Maly, M. Sapik, O. Cejpek, G. Wigley, J. Katolicky, J. Jedelsky, Effect of spill orifice geometry on spray and control characteristics of spill-return pressure-swirl atomizers, Exp. Therm Fluid Sci. 106 (2019) 159–170.
[5] P.K. Senecal, D.P. Schmidt, I. Nouar, C.J. Rutland, R.D. Reitz, M.L. Corradini, Modeling high-speed viscous liquid sheet atomization, Int. J. Multiph. Flow 25 (6) (1999) 1073–1097.
[6] A. Ibrahim, Comprehensive study of internal flow field and linear and nonlinear instability of an annular liquid sheet emanating from an atomizer, PhD Thesis, University of Cincinnati, 2006.
[7] G.I. Taylor, The Mechanics of Swirl Atomizers, International Congress of Applied Mechanics, London, 1948, pp. 280-285.
[8] J.J. Chinn, An appraisal of swirl atomizer inviscid flow analysis, Part 1: The principle of maximum flow for a swirl atomizer and its use in the exposition and comparison of early flow analyses, Atomization Sprays 19 (3) (2009) 263–282.
[9] J.J. Chinn, An appraisal of swirl atomizer inviscid flow analysis, part 2: inviscid spray cone angle analysis and comparison of inviscid methods with experimental results for discharge coefficient, air core radius, and spray cone angle, Atomization Sprays 19 (3) (2009) 283–308.
[10] E. Wimmer, G. Brenn, Viscous flow through the swirl chamber of a pressure-swirl atomizer, Int. J. Multiph. Flow 53 (2013) 100–113.
[11] S. Som, S. Mukherjee, Theoretical and experimental investigations on the formation of air core in a swirl spray atomizing nozzle, Appl. Sci. Res. 36 (3) (1980) 173–196.
[12] E.J. Lee, S.Y. Oh, H.Y. Kim, S.C. James, S.S. Yoon, Measuring air core characteristics of a pressure-swirl atomizer via a transparent acrylic nozzle at various Reynolds numbers, Exp. Therm Fluid Sci. 34 (8) (2010) 1475–1483.
[13] S. Moon, E. Abo-Serie, C. Bae, Air flow and pressure inside a pressure-swirl spray and their effects on spray development, Exp. Therm Fluid Sci. 33 (2) (2009) 222–231.
[14] S. Kim, T. Khil, D. Kim, Y. Yoon, Effect of geometric parameters on the liquid film thickness and air core formation in a swirl injector, Meas. Sci. Technol. 20 (1) (2009).
[15] M. Maly, J. Jedelsky, J. Slama, L. Janackova, M. Sapik, G. Wigley, M. Jicha, Internal flow and air core dynamics in Simplex and Spill-return pressure-swirl atomizers, Int. J. Heat Mass Transf. 123 (2018) 805–814.
[16] N.K. Rizk, A.H. Lefebvre, Drop-size distribution characteristics of spill-return atomizers, J. Propul. Power 1 (1) (1985) 16–22.
[17] N.K. Rizk, A.H. Lefebvre, Spray characteristics of spill-return atomizers, J. Propul. Power 1 (3) (1985) 200–204.
[18] X.F. Dai, A.H. Lefebvre, J. Rollbuhler, Spray characteristics of a spill-return airblast atomizer, J. Eng. Gas Turbines Power 111 (1) (1989) 63–69.
[19] M. Löffler-Mang, W. Leuckel, Atomization with spill-controled swirl pressure-jet nozzles, ICLASS (1991) 431–440.
[20] G.G. Nasr, A.J. Yule, J.A. Stewart, A. Whitehead, T. Hughes, A new fine spray, low flowrate, spill-return swirl atomizer, Proc. Inst. Mech. Eng., Part C: J. M. Eng. Sci. 225 (4) (2011) 897–908.
[21] G. Slowik, J. Kohlmann, A swirl controlled hollow cone nozzle and its technical applications, ICLASS06, 2006.
[22] Y. Khavkin, The Theory and Practice of Swirl Atomizers, Taylor & Francis, 2004.
[23] F.H. Carey, The development of the spill flow burner and its control system for gas turbine engines, J. Royal Aeronautical Soc. 58 (1954) 737–753.
[24] Z. Zhang, LDA Application Methods: Laser Doppler Anemometry for Fluid Dynamics, Springer, 2010.
[25] J.J. Chinn, The numerics of the swirl atomizer, ILASS, 2008, p. 7.
[26] E. Giffen, A. Muraszew, The Atomization of Liquid Fuels, Chapman & Hall, 1953.
[27] L. Craig, N. Barlow, S. Patel, B. Kanya, S.P. Lin, Optimal and nonoptimal flows in a swirl atomizer, Atomization Sprays 19 (12) (2009) 1113.
[28] M. Halder, S. Dash, S. Som, Initiation of air core in a simplex nozzle and the effects of operating and geometrical parameters on its shape and size, Exp. Therm. Fluid Sci. 26 (8) (2002) 871–878.
[29] G. Amini, Liquid flow in a simplex swirl nozzle, Int. J. Multiph. Flow 79 (2016) 225–235.
[30] K.S. Siddharth, M.V. Panchagnula, T.J. Tharakan, Feature correlation velocimetry for measuring instantaneous liquid sheet velocity, J. Fluids Eng. 139 (9) (2017) 091401.
[31] N.K. Rizk, A.H. Lefebvre, Prediction of velocity coefficient and spray cone angle for simplex swirl atomizers, Int. J. Turbo Jet Engines 4 (1–2) (1987) 65–74.
[32] S. Yao, J. Zhang, T. Fang, Effect of viscosities on structure and instability of sprays from a swirl atomizer, Exp. Therm. Fluid Sci. 39 (2012) 158–166.
[33] A.J. Yule, J.J. Chinn, The internal flow and exit conditions of pressure swirl atomizers, Atomization Sprays 10 (2) (2000) 121–146.

10.4 Paper IV

Comparison of numerical models for prediction of pressure-swirl atomizer internal flow

Milan Maly*[1], Jaroslav Slama[2], Ondrej Cejpek[1] and Jan Jedelsky[1]

[1]Brno University of Technology, Technicka 2, 616 69 Brno, Czech Republic

[2]Provyko s.r.o, Vinarska 460, 603 00 Brno, Czech Republic

*Corresponding author: milan.maly@vutbr.cz

Abstract

Numerical prediction of discharge parameters allows to design a pressure-swirl atomizer in fast and cheap manner. At the same time, the numerical approach must provide reliable results for a wide range of geometries and operating regimes. Many authors used different numerical setups for similar cases and often concluded opposite suggestions on turbulence model selection. This paper compares 2D axisymmetric, 3D periodic and 3D numerical models used for estimation of the internal flow characteristics of a pressure-swirl atomizer. The computed results are compared with experimental data in terms of spray cone angle (*SCA*), discharge coefficient (C_D), internal air-core dimensions, and velocity profiles.

The three-component velocity was experimentally measured using a Laser Doppler Anemometry in a scaled transparent model of the atomizer. The internal air-core was visualized at high temporal and spatial resolution by a high-speed camera with backlit illumination. Tested conditions covered a wide range of the Reynolds numbers within the inlet ports, Re = 1000, 2000, 4000.

The internal flow was numerically treated as both steady and transient two-phase flow. Both approaches yield similar results when time-averaged. The gas-liquid interface was captured with Volume of Fluid scheme. The numerical solver used laminar and several turbulence models, represented by k-ε and k-ω models, Reynolds Stress model (RSM) and Large Eddy Simulation (LES). The laminar solver was capable to predict the C_D, air-core dimensions and velocity profiles with an error less than 5% compared with the experimental results in both 2D and 3D simulation for the whole range of Re. The LES model performed similarly to the laminar solver for low Re but was superior for Re = 4000. The two-equation models k-ε and k-ω were sensitive to proper solving of the near wall flow and were not accurate for low Re except for the k-ε model, which returned valid results for Re = 4000. The 3D periodic simulation with steady laminar model is the most cost-effective combination.

Introduction

Pressure - swirl atomizers (PS) have a unique role in many industrial applications including combustion, spray cooling, spray drying, etc. A relatively simple geometrical design, resistance to clogging, wide spray cone angle and high atomization efficiency are among the favourable parameters. A typical PS atomizer contains tangential entry ports and a swirl chamber with an exit orifice. The liquid is fed via tangential ports into the swirl chamber where it gains high swirl velocity. The swirling liquid is discharged from the exit orifice in the form of a hollow conical liquid sheet which consequently disintegrates into filaments and ligaments. A ratio of the swirl to axial momentum determines the spray cone angle (*SCA*). Despite the simple geometry, the internal flow behaviour is complex. The swirling liquid creates a low-pressure zone along a centre line of the swirl chamber where the static pressure usually drops below the ambient pressure, and the air from the surrounding atmosphere is pulled inside the low-pressure zone, so an air-core is formed. The internal vortex behaves as a Rankine vortex since the swirl velocity has its maximum located at the air-core surface which behaves like a virtual solid

cylinder [1]. Secondary flow effects, as Görtler vortices, could be also presented in a boundary layer inside the swirl chamber [2, 3].

It is well known that the internal flow directly affects the parameters of the discharged liquid sheet, such as its thickness, stability, velocity, and *SCA*. These parameters consequently determine the sizes of ligaments and droplets. To understand the link between the atomizer performance and its design, the internal flow must be examined. Some authors used the exact analytical solution to predict the discharge parameters. Simple non-viscous treatment, reviewed in [4, 5], proved to be a useful tool for a basic insight into the flow behaviour, but it lacks accuracy for some atomizer geometries. A better agreement can be achieved when the viscous flow is assumed [6, 7], but still some aspects such as the liquid sheet temporal stability or secondary flow effects, are not resolved and their mathematical description is very extensive.

On the other hand, the numerical simulation has arisen in recent years due to an increase in a computational performance, and many commercial software are available in the market. These software tools for numerical simulations of the flow dynamics could be simply applied for the internal flow of the PS atomizer. However, many different geometrical, numerical and physical setup combinations can be used for the same atomizer and operating conditions. However, the numerical results should be still validated by an experiment.

In the past, many authors performed a CFD simulation of the internal flow of PS atomizer. An overview of some published papers is presented in Table 1. One of the first numerical studies of the PS atomizer was conducted in 1997 by Yule and Chinn [8]. They used a 2D axisymmetric geometry with a laminar solver and reported a deviation of discharge coefficient, C_D, from an experimental data to be less than 3%. A similar numerical setup was later used by Amini [6]. Even this simple 2D model yield better agreement with the experimental data than the analytical viscous solution. Note here that the author used the laminar solver even for values of Reynolds number within the inlet port, *Re* = 122,000. The complex nature of the internal flow does not allow for a simple conclusion whether the flow is turbulent or laminar, and many authors claim an opposite conclusion. A theoretical evaluation of turbulence evolution within the swirl chamber was made by Yule and Chinn [9, 10] who suggest that the flow is laminar even for very high *Re* due to the laminarization effect of the swirl dominant flow itself and also due to very short length scale where the turbulence has no time to develop.

A comparison of Large Eddy Simulation (LES) and laminar models was performed by Madsen et al. [11]. They used a scaled atomizer and operated it in range of *Re* = 12,000–41,000. Under these operating regimes, the laminar model had a slightly better agreement to the experimental data than LES. The authors also examined simple turbulence models represented by RNG and realizable k-ε models. However, these models were unable to predict the internal air-core. Galbiati et al. [12] compared the LES simulation with RNG k-ε and RSM models. They found an insignificant variation among the used models when compared to the deviation in the results from published empirical correlations. They also noted that the flow field was consistent for LES and k-ε model, while, surprisingly, the RSM had some discrepancies. Note here that the authors claim that the internal flow is fully turbulent based on Walzel Reynolds number, Re_W, defined as: $Re_w = \sqrt{2\rho_l p_l d_o}/\mu_l$, since it was much larger than a critical value of 5,000. However, the calculated *Re* = 1,700–3,800 assumes a rather laminar flow. Qian [13] found RSM to be superior over the laminar model at *Re* = 16,000, while Nouri-Borujerdi [14] found opposite conclusions for even larger *Re* in range of 18,000–40,000.

Baharanchi et al. [15] examined several schemes to capture the liquid-air interface using a 2D simulation with RNG k-ε turbulence model. A geo-reconstruct scheme was found to be the most suitable for capturing the air-core. They also discussed the necessity to model a surface tension and found that the surface tension had effect only if the Weber number is smaller than 204. From a practical point of view, it had a negligible effect on the developed flow. However, it affects the flow development process.

The difference between 2D and 3D computational models was examined by Sumer et al [16]. They used the laminar solver and found that the air-core diameter was about 5% smaller in the case of the 3D model. However, the frequency of waves on the air-core surface was predicted by both models closely and with good agreement to the experimental data. Vashahi et al. [17] compared RANS models *k-ε* and *k-ω*. The *k-ω* outperforms the *k-ε* in the *SCA* prediction and convergence speed.

Table 1 Review of published numerical setups

Author	Software	2D/3D	Transient /steady	Turbulence model	Interface	*Re*
Shaikh [18]	Fluent	2D, 3D		Laminar	VOF Geo-rec.	1000
Laurila [19]	OpenFOAM	3D Full	Transient	Implicit LES	VOF Geo-rec.	420-5300
Galbiati [12]		3D Full	Transient	LES, RSM, *k-ε* RNG	VOF	1700-3800
Ghate [20]	Fluent	2D	Transient	RSM	VOF PLIC	7×10^3–2×10^4
Ibrahim [21]	Fluent	2D		RSM	VOF Geo-rec	5×10^3–5×10^4
Amini [6]	Fluent	2D	Steady	Laminar	VOF	10^4–10^5
Dikshit [22]		3D	Steady	*k-ε*	VOF	~10^4
Madsen [23]	Fluent, CFX	3D		Laminar, LES	VOF	10^4–4×10^4
Bazarov [24]	CFX	3D	Steady	*k-ε*	VOF	>10^4
Sumer [25]	Fluent	2D, 3D	Transient	Laminar	VOF HRIC	$1{,}2\times10^4$
Qian [13]	OpenFOAM	2D		Laminar, RSM	VOF LS coupled	~$1{,}6\times10^4$
Nouri-Borujerdi [14]		2D	Steady /transient	Laminar, RSM	Level set	$1{,}8\times10^4$–4×10^4
Marudhappan [26]	Fluent	2D, 3D		Laminar	VOF HRIC	~2×10^4
Baharanchi [15]		2D	Transient	*k-ε* RNG	VOF	~$2{,}5\times10^4$
Mandal [27]	Fluent	2D		Laminar	VOF	~4×10^4
Vashahi [17]	CCM+	3D	Steady	*k-ε*, *k-ω*	VOF HRIC	

From the overview in Table 1, no clear conclusion can be made on the physical model selection, as both laminar and turbulence approaches were used by different authors for the entire range of *Re*. The most commonly used turbulence models are from the *k-ε* family and represented by realizable and renormalization group theory, RNG, models. The Reynolds stress model, RSM, is also widely used; the authors reported contradictory conclusions. The air-core interface is usually captured by Volume of Fluid (VOF) models.

Both the 2D and 3D simulation seems to provide accurate results; however, no comparison of the periodic 3D and full-scale 3D mesh was found. The majority of the 3D simulations used meshes, which contain tangential ports. This slows the mesh creation process, since the cells near the wall are usually very skewed. To overcome this, a no-port version is introduced here with the aim to provide a simpler and faster mesh creation process. Moreover, steady and transient approaches are compared here. This

paper aims to provide an overview of numerical setup for CFD prototyping of small pressure-swirl atomizers. The data presented here are validated by a comprehensive experiment performed in a wide range of *Re* from 1000 to 4000, which corresponds to a 16-times increase in the inlet pressure, p_l.

Experimental and numerical setup

The experiments were performed at specially designed facility for cold atomizer testing at Brno University of Technology, Czech Republic. A similar experimental setup was also used in our previous study where it is described in greater detail [28].

The atomizer design and test bench

The atomizer geometry was derived from a small-sized atomizer studied in our previous work [29]. However, three ports are used to improve the circumferential periodicity of the atomizer. The swirl chamber has a different converging part to aid manufacturing and mesh creation simplicity. The atomizer is manufactured as ten times scaled copy since the small dimension of the original atomizer does not allow for direct optical measurement. The transparent parts of the atomizer are made from cast polymethyl methacrylate, PMMA, which were ground and polished to achieve transparency. The operating conditions were partially derived from [29] where the original atomizer operated with JET A-1 at p_l = 0.5 MPa roughly yield *Re* = 1000. Other operating regimes, see Table 2, covered *Re* = 2000 and 4000. This range of *Re* values corresponds to the range of p_l from 0.5 to 8 MPa for the originally sized atomizer using JET A-1.

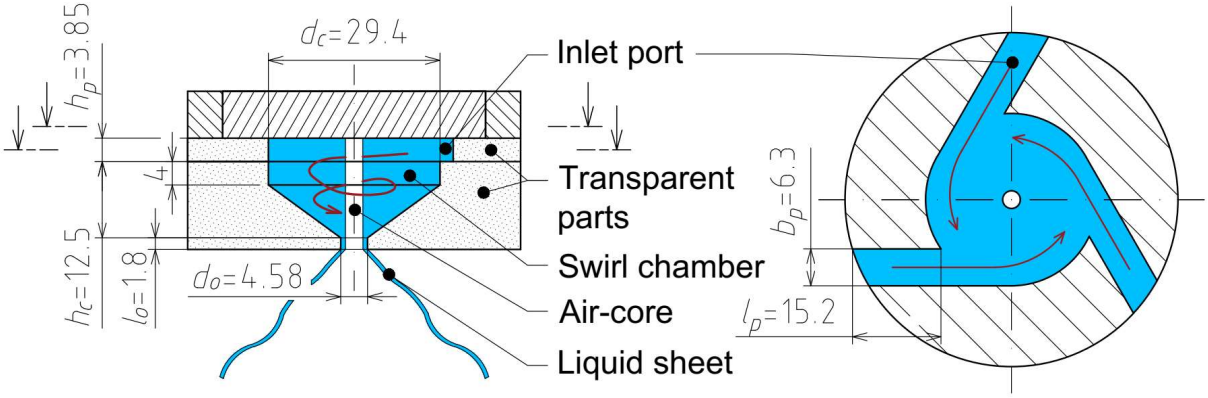

Figure 1 Atomizer schematic drawing with main dimensions in millimetres

Table 2 List of operating regimes

Re	p_l	$\dot{m}_p$	v_p	C_D	***Fr***	d_{aco}	d_{acc8}
[–]	**[kPa]**	**[kg/h]**	**[m/s]**	**[–]**	**[–]**	**[mm]**	**[mm]**
1000 ± 10	2.1	47.5	0.206	0.420	5.0	2.82	1.55
2000 ± 10	8.8	94.8	0.411	0.410	9.9	2.99	1.64
4000 ± 10	36.3	188.4	0.816	0.401	19.6	3.20	1.74

The operating liquid was p-cymene (1-Methyl-4-(propan-2-yl) benzene). It is one compound, colourless liquid, whose value of refractive index n = 1.49 is closely matched to the atomizer body which simplifies the optical measurement and reduces the measurement errors. The physical properties of the p-cymene at room temperature are as follows: surface tension σ = 0.028 kg/s^2, liquid dynamic viscosity μ_l = 0.00085 kg/(m·s), and liquid density ρ_l = 848 kg/m^3. The identical test bench as in [28] was used. The uncertainty in pressure sensing was 0.05 kPa and the calculated uncertainty of C_D was 0.25 % of actual value.

High speed imaging

A FASTCAM SA-Z high-speed camera (Photron, Japan) with long-distance microscope 12X Zoom lens (NAVITAR, New York, USA) which is composed of a 2X F-mount adapter (type 1-62922), a 12 mm F.F zoom lens (type 1-50486), and 0.25X lens (type 1-50011) was used to document the spatial and temporal behaviour of the air-core and discharged liquid sheet in one image with spatial dimensions of 31 × 31 mm. The camera frame rate was 20,000 frames per second, the resolution was 1024 × 1024 px and the shutter speed was set to 40 μs. A background light illuminated the atomizer using an LED panel. The air-core dimensions and the spray cone angle, SCA, were measured by an in-house MATLAB code using a threshold-based detection technique.

Laser Doppler Anemometry

Point-wise velocity measurements inside the swirl chamber were carried out using a 2D LDA FlowExplorer (Dantec Dynamics A/S, Skovlunde, DK), for setup details see [28]. The measurements were performed in four axial distances from the atomizer cap, see Figure 2. The refractive index of the atomizer body and working liquid differed by less than 0.005 for both wavelengths involved in the measurement. Therefore, the velocity error is expected to be less than 0.5 % [15, 24]. Nevertheless, the real position of the measurement volume inside the atomizer body had to be corrected as $S_2 = nS_1$, where S_2 is the real distance of the measurement volume from the atomizer wall and S_1 is the traversed distance of the measurement volume from the atomizer wall. The measurements near the air-core surface were affected by light reflections, which generate noise on the LDA signals and subsequent velocity estimates. Therefore, these data were processed by a filtration algorithm which seeks for a Gaussian distribution in the velocity histogram and calculates the mean velocity only from the data which satisfies the Gaussian distribution.

Flow tracer particles SL75 e-spheres with a mean diameter of 45 μm were used as tracers for the LDA measurements. Their Stokes number, based on the highest swirl velocity and air-core diameter, which is the worst scenario case for the particle movement, was less than 0.3 for $Re = 4000$ regime, which ensured a sufficiently flow fidelity.

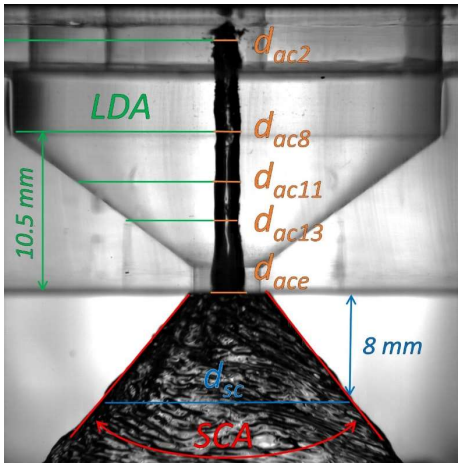

Figure 2 The typical high-speed image with measured positions

Numerical setup

The CFD simulations were made using commercial software Ansys Fluent 19.2. Four basic geometries, each representing a different level of simplification, were used; 2D axisymmetric model, 3D periodic model without inlet port, 3D periodic model with inlet port and full-scale 3D model with three inlet ports. The 2D axisymmetric model with the swirl component is the simplest approach, but widely used. Note here that the inlet velocity has to be set to conserve the mass flow rate in the radial direction and

conserve the angular momentum in the tangential direction. As it is later shown in this paper, this approach underestimates the swirl velocity magnitude. Thus, the second option used here is to set the mean velocity inside the inlet port, v_p, as the swirl velocity.

The geometrical design of the atomizer allows for the use of periodic boundary condition, since the atomizer can be divided into three identical parts, each 120° section. In this way, the 3D periodic model was created. Two periodic models are compared. The first one contains the inlet port and the second one is without the inlet port; a no-port version. The main advantage of the no-port version is simplicity in mesh generating process. The tangential connection of the port creates skewed elements near the swirl chamber wall. This could be overdone by slight displacement of the port towards the atomizer centreline or using the unstructured tetrahedral or polyhedral mesh. The pressure outlet was set to the outer boundaries and the no-slip condition was used on the internal wall boundaries for all cases. For the turbulent models, the value of turbulence intensity of 1 % and hydraulic diameter of 0.0049 mm were set on the inlet.

Pressure-velocity coupling was done using the PISO scheme for transient solution and the pseudo transient Coupled scheme for the steady solution. Turbulence and momentum used Second Order Upwind discretization. The liquid-air interaction was captured by a Volume of Fluid model with a geo-reconstruct scheme for transient models or Compressive scheme for the steady cases and LES. Surface tension between air and liquid was set as constant value. The air was treated with constant density. The gravity force was also considered.

The transient solution used variable time stepping with a Courant number 0.15. A typical time step size was approximately 2×10^{-6} s. After reaching a quasi-static solution, time averaging was applied, with minimum of 0.1 s recorded.

Several turbulence models based on a Reynolds-averaged Navier-Stokes (RANS) equation, LES and laminar solver were used and compared to achieve results comparable with the experiment. The mathematical description of the used methods and models is well known and can be found elsewhere [30].

Simple two-equation models represented by k-ε and k-ω were chosen for their good accuracy and versatile use for industrial applications. These models determine a turbulent length scale and a time scale by solving two separate transport equations. The k-ε model is based on a transport equation for kinetic energy k and dissipation rate ε. In this paper, the RNG and realizable k-ε models were used. The wall treatment was done using the scalable wall function for meshes without boundary layer and enhanced wall treatment (WT) was used for meshes with a boundary layer. The k-ω SST model with low-Re correction was used with meshes with boundary layer only. This model combines the standard k-ω model for near wall treatment and the k-ε model in the free stream flow.

The Reynolds Stress model (RSM) is among the most advanced RANS models for the swirl dominant flows as it solves all the transport equations for the Reynolds stresses. This model was used with low-*Re* and shear flow correction, with scalable wall function for meshes with wall y+ > 10 and omega-stress based for mesh with boundary layer.

Large Eddy Simulation (LES) was represented by Wall-Adapting Local Eddy Viscosity model (WALE). No perturbations were set at velocity inlet.

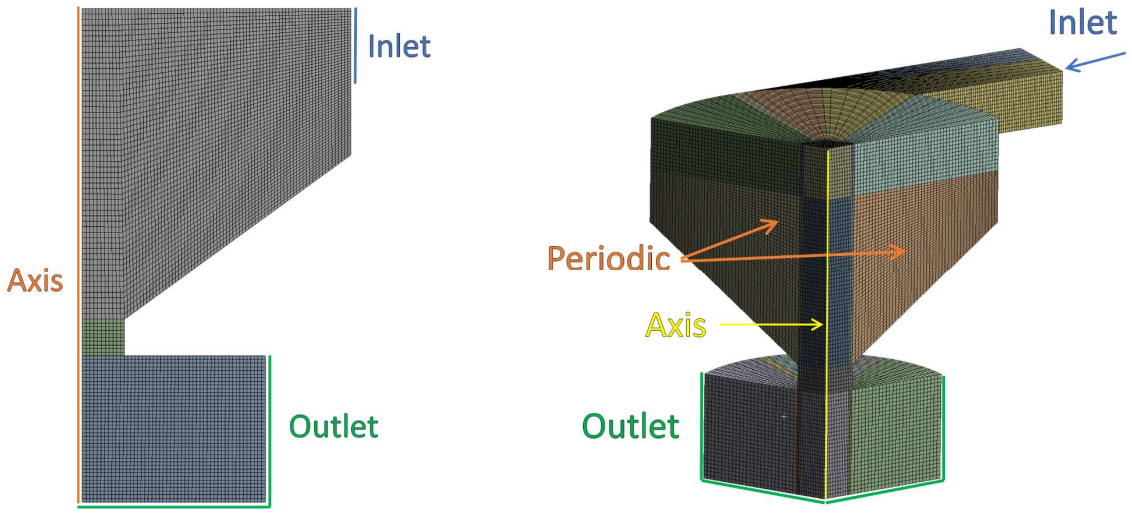

Figure 3 Left: 2D mesh. Right: 3D periodic mesh with inlet port

Results and discussion

In the results, the experimental data are presented first. Then, various numerical approaches are compared. The mesh dependence analysis is followed by a possibility of the geometry simplification. Then, several physical models are compared with the experimental data for various *Re*. The final part deals with the air-core temporal behaviour.

Experimental data

The high-speed imaging showed that the internal air-core is cylindrically shaped, being larger in diameter, with the exit orifice which is a well-known phenomenon [6, 31]. With increasing *Re*, the air-core diameter slightly increases as discussed in [32], see Table 2, where both d_{ace} and d_{ac11} grow almost linearly with increasing *Re*. The prominence of the surface waves and distortions decrease with *Re*.

The measured swirl velocity profiles are identical in all axial positions, see Figure 5. This is expected since it is a basic assumption of all inviscid models. The velocity profile represents a Rankine vortex; however, the viscous losses reduce its peak velocity. The measured velocity can be interpolated by a simple equation $wr^b=const,$ where b is an empirical constant which is proportional to the viscous losses [33].

With increasing *Re*, the relative swirl velocity slightly increases, which suggests smaller viscous losses with higher *Re*, see increasing values of b constant from 0.8 to 0.9 for Re = 1000 and 4000, respectively. Increasing relative swirl velocity causes the increase in the air-core diameter. This is in alignment with decreasing C_D, as shown in Table 2, which also well correlates with the enlarging air-core.

The axial velocity was measurable only in positions d_{ac8} and d_{ac11} due to limited optical access. It has a local maximum near the atomizer wall and a global maximum at the air-core surface. The position and relative value of both maxima remains the same for all measured regimes.

The turbulence intensity of the swirl velocity is between 7-9% with a slightly decreasing trend with *Re*, but with much higher values near the air-core and swirl chamber walls where it reaches the values above 30%. It was found independent of the axial position. The small influence of *Re* suggests that no transition effect occurs in the studied range of *Re* values between 1000 and 4000. However, the values of the turbulence intensity must be taken with respect to the long measuring volume of the backscatter LDA, which may introduce false turbulence measurement.

Figure 4 Typical results obtained from HS imaging. From left: Re= 1000, 2000 and 4000

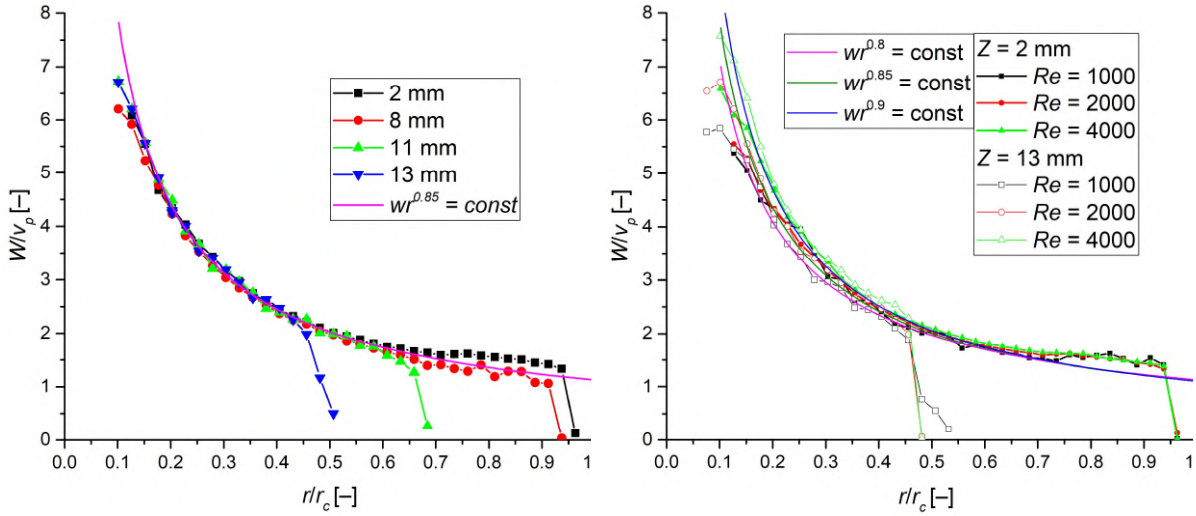

Figure 5 Swirl velocity profiles from LDA measurement, left for Re = 2000 and various Z positions. Right for Z = 2 and 13 mm for various Re.

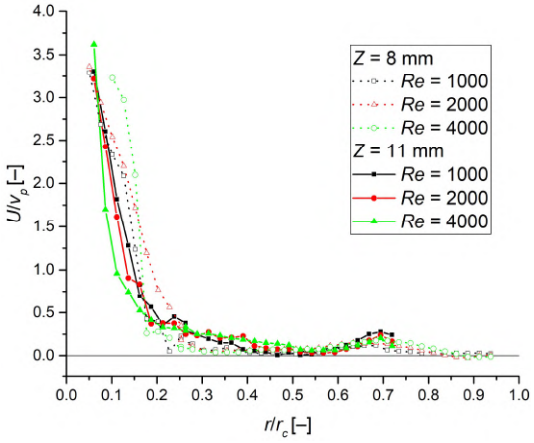

Figure 6 Axial velocity profiles from LDA measurements

Mesh independence test and comparison of steady and transient models

Several different mesh sizes were compared at *Re* = 2000 using the laminar solver for both steady and transient simulation, see typical results in Figure 7. The key parameter determining the simulation accuracy is the number of mesh cells across the exit orifice. With a low number of cells, the error of estimating the air-core dimension rises, which may harm the overall result of the simulation. The effect of cells number on C_D, *SCA* and the air-core dimension is shown in Figure 8 for 2D transient and 3D steady and transient simulations. Note that the meshes were evenly sized. Therefore, the overall number

of cells rises with a second power for 2D meshes from 6,784 to 106,206 cells for 11 and 42 cells in r_o, respectively, and with a third power for 3D meshes from 131,948 to 686,300 for 16 and 27 cells in r_o, respectively. The 3D mesh with 35 cells uses a similar cell size as the 27 cells version but contains 6 prismatic cells in the wall boundary layer to reach the wall y+ ~ 1 along the exit orifice. Moreover, three different dimensions of the outer outflow area were also compared, but the effect on the results was negligible. Thus, the middle sizes area was used for all the cases.

The steady simulation was found more prone to the mesh sizing and reached a maximum difference in C_D of 7 %. The transient simulation overperformed the steady one in proximity of results to the experimental data and showed a small effect of the mesh size. The sensitivity of the steady model can be explained by different VOF scheme; the steady simulations used a compressive scheme, while the transient one used a more accurate geo-reconstruct scheme [34]. Moreover, the steady simulations overestimated the air-core size, which leads to a decrease in C_D. The optimal mesh for both 2D and 3D has at least 20 cells in r_o, which is in line with other authors; however, a large variance was found in the literature. Ghate [20] suggests a mesh with roughly 13 cells in r_o, Ghate [20] used approximately 25 cells in r_o, Vashahi [17] similarly used around 25 polyhedral cells in r_o plus 7 layer of prismatic layer, while Galbiati [12] found a mesh independency for a much finer mesh, with roughly 40-50 cells in r_o and Nouri-Borujerdi [14] used even finer mesh with 80 cells in r_o. However, the overall effect of the mesh sizes is rather small and other effects, such as a turbulence model, time statistics or initial conditions, may have a greater effect.

The main advantage of the steady simulation is its time efficiency. It took between 5-8 hours for mesh with 686,300 cells on 16-cores machine to reach the quasi steady state. While the same case but transient took about 3-4 weeks to produce the same level of convergence. For practical usage, the steady simulations are much more suitable.

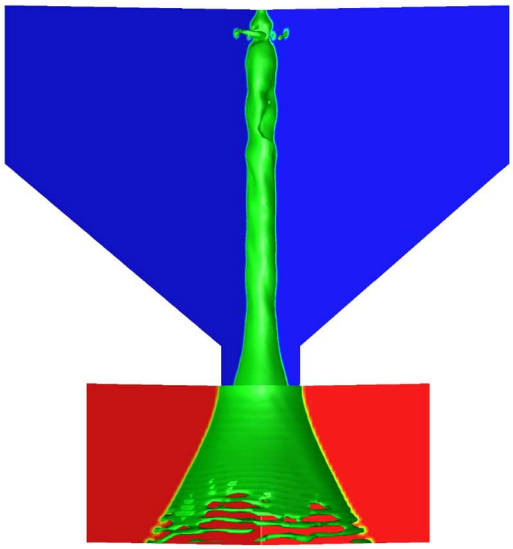

Figure 7 Typical results obtained from 3D periodic mesh with 27 cells in r_o, transient, Laminar simulation. Re = 2000, instantaneous image. Blue and red represents liquid and air respectively, green is an interface.

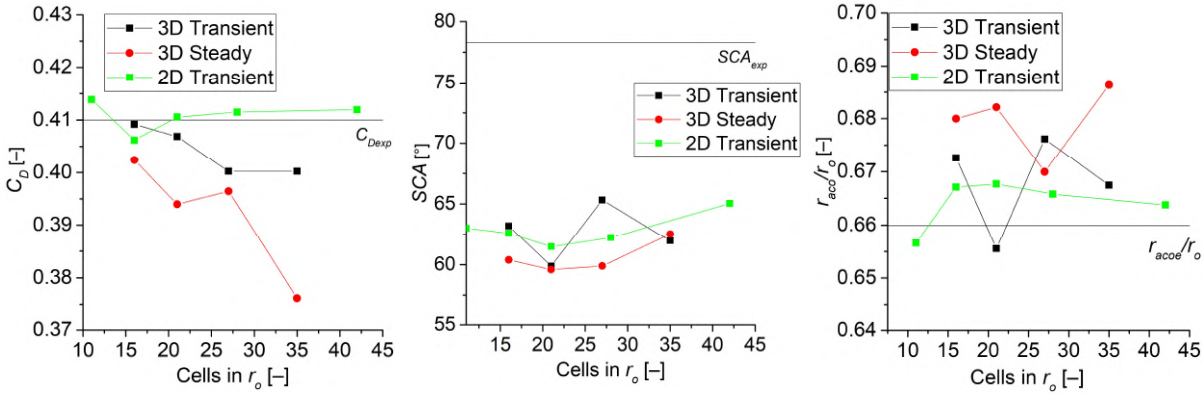

Figure 8 The effect of cell number in r_o. Laminar model, Re = 2000.

Atomizer geometry simplification

The atomizer geometry can by simplified in several steps, see Table 1. The most complex approach uses the full-scale atomizer model including the inlet ports. This model allows for the air-core to divert from the swirl chamber centreline. Since the atomizer used here can be divided into three identical parts, the periodic model can be easily created. This simplification ensures that the air-core axis is equal to the swirl-chamber centreline, which may subdue some large-scale flow instabilities. This model can be further simplified as the inlet port geometry can be substituted by an imprint of the inlet port on the wall of the swirl chamber to form the inlet boundary condition. However, the inlet velocity profile on the boundary of the swirl chamber is not trivial and it must be pre-calculated to yield correct results. This pre-calculation can be performed using a simple tetrahedron mesh with inlet port, a single-phase model and steady solution. This velocity profile must be interpolated on the no-port inlet boundary. The main advantage of the no-port mesh is the absence of highly skewed cells near the swirl chamber; therefore, the mesh creation process is much faster and the mesh quality is better. This can be also solved using unstructured meshes with tetrahedral or polyhedral cells.

The last possible simplification is to create a 2D axisymmetric model with the swirl velocity component. This model requires setting the inlet radial and swirling velocity as two independent components to keep the momentums in both directions. However, the results show that conserving the angular momentum can be inaccurate due to distortion of the inlet velocity profile, which leads to higher inlet angular momentum than assumed. This phenomenon is also well observed on the no-port version, which underestimated the air-core dimensions as well as the inlet pressure.

Table 3 Comparison of model geometry. Re = 2000, laminar model, transient.

Mesh	p_l	SCA	$d_{ac\text{-}exit}$	d_{a11mm}	U_l	V_l	C_D
	[Pa]	[°]	[mm]	[mm]	[m/s]	[m/s]	[–]
Experimental data	8800	78.0	2.99	1.67	3.1	2.2	0.41
2D Momentum	6900	56.1	2.88	1.48	3.4	1.7	0.46
2D v_p	8800	62.2	3.06	1.64	3.5	2.2	0.41
3D PER No-port	6700	56.7	2.83	1.47	3.5	1.9	0.47
3D PER No-port-profile	8550	63.0	2.98	1.49	3.6	2.4	0.42
3D PER	9200	65.3	3.07	1.85	2.9	2.6	0.40
3D Full	9350	61.3	3.10	1.66	3.7	2.4	0.40

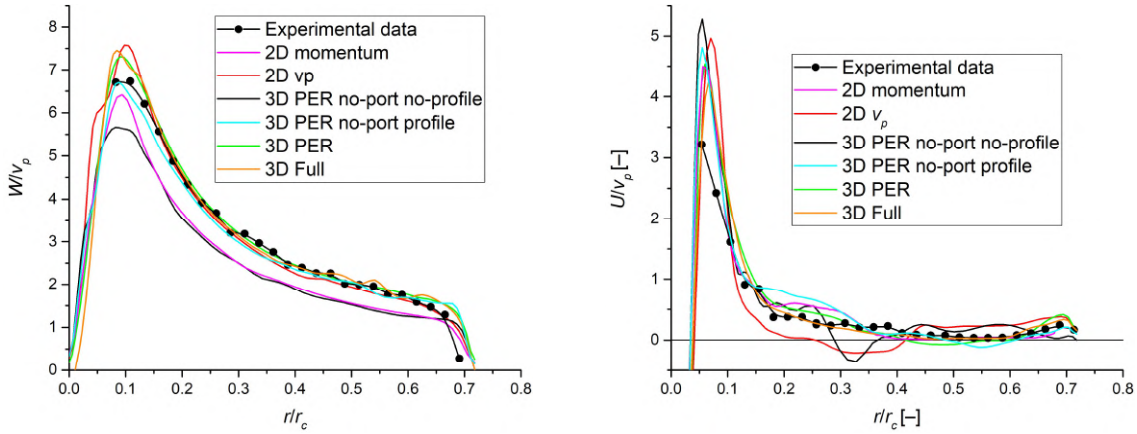

Figure 9 Mean swirl velocity profiles (left), axial velocity profiles (right). Z = 11 mm, Re = 2000

Physical models

Several physical models were compared for the 3D periodic mesh with the inlet port for all the regimes investigated. The results for both steady and transient ones are listed in Table 4 for $Re = 2000$. The effect of Re on the results from the selected models is shown in Figure 10.

Similarly, as in the mesh independence test, the steady simulation was found prone to selecting the model. The both versions of steady k-ε, RNG and Realizable, performed almost identically and their results were close to the experimental data. The steady RSM reached the largest deviance from the experimental data, since it was unable to predict the air-core within the swirl chamber. This model also failed on the mesh with a prismatic layer using Enhanced wall treatment. The same model, but omega-based RSM, properly captured the air-core but underestimated the C_D. The similar results were obtained by the steady k-ω–SST model. Both the k-ω –SST and omega-based RSM predicted C_D accurately in the transient simulation, where all the turbulence models return virtually identical results including LES. Only the omega-based RSM converged in the transient simulations, other variants diverged.

An improper setup of the wall function results in failure of the air-core prediction. The wall $y+$ must be carefully checked before selecting the proper wall function as the standard wall function failed in the all investigated cases. The turbulent models were able to closely predict flow characteristics even for $Re = 1000$, which is in good agreement with [12], where the k-ε model returns reliable results for $Re = 1600$. Note here that RSM model underperformed other turbulence models, similarly as in [12]. This result was not expected, since the RSM should be superior for flows with anisotropic turbulence, which is the case of swirl atomizer. It predicts the air-core only in the case of omega-based RSM, but its results were practically identical to the simpler k-ω.

The suitable models from Table 4were compared in the range of Re and the results are presented in Figure 10. No RSM model was able to predict the air-core for $Re = 1000$, thus these models are not presented here.

The C_D decreased in experiment slightly with Re as $C_D \propto Re^{-0.035}$ or with p_l as $C_D \propto p_l^{-0.016}$. It is in good agreement with several authors [35, 36] who found the similar decrease in C_D but some authors [37] claimed rather ascending C_D with p_l. Nevertheless, all the CFD models predicted the same descending trend, yet minor differences were observed. The steady k-ω model underpredicted the C_D, particularly for $Re = 1000$. The k-ε also suffer from difficulties with this regime, where it severely overpredicts the C_D and underpredicts the air-core dimension. The LES model returns the closest results of C_D, followed by the transient laminar model, which slightly diverts from the experimental data at $Re = 4000$. Note here that the empirical correlation for C_D proposed by Rizk and Lefebvre [38] gives a constant value of C_D of 0.41, which is in perfect agreement with the experimental data for $Re = 2000$.

Table 4 Comparison of different physical models. 3D periodic mesh with port, Re = 2000.

Mesh		Physical model	p_l	SCA	$d_{ac\text{-}exit}$	d_{a11mm}	U_l	V_l	C_D
			[pa]	[°]	[mm]	[mm]	[m/s]	[m/s]	[–]
Structured	Steady	Laminar	9200	59.9	3.08	1.82	3.85	2.41	0.40
Structured		*k*-ε - Realizable Scalable WF	8950	53.6	3.10	1.72	3.70	2.31	0.41
Structured		RSM Scalable WF	7400	59.9	2.51	0	2.69	1.66	0.45
Prismatic layer		*k*-ω -SST	10421	62.0	3.10	1.56	4.05	2.92	0.38
Prismatic layer		*k*-ε - Realizable Enhanced WT	8870	58.0	2.97	1.45	3.02	2.19	0.41
Prismatic layer		*k*-ε - RNG Enhanced WT	8800	57.2	2.95	1.40	2.99	2.16	0.41
Prismatic layer		RSM - Omega	10210	58.3	3.08	1.49	3.69	2.62	0.38
Prismatic layer		RSM Enhanced WT	Diverged						
Structured	Transient	Laminar	9300	65.3	3.07	1.85	2.92	2.64	0.40
Structured		*k*-ε - Realizable Scalable WF	8540	54.1	3.07	1.67	3.63	2.35	0.42
Structured		RSM Scalable WF	Diverged						
Prismatic layer		LES - WALE	8960	59.9	3.03	1.55	3.69	2.64	0.41
Prismatic layer		*k*-ω-SST	8840	57.6	3.01	1.50	3.02	2.66	0.41
Prismatic layer		*k*-ε - Realizable Enhanced WT	8050	52.0	2.87	1.22	3.11	2.25	0.43
Prismatic layer		RSM - Omega	9100	54.0	3.02	1.56	3.07	2.62	0.41
Prismatic layer		RSM Enhanced WT	Diverged						

The C_D value is usually related to the air-core diameter. Therefore, an increase in C_D should be accompanied with the growing air-core diameter, which is true for both experimental data and all the CFD models, see Figure 10, right. Only the *k*-ε model diverts for $Re = 1000$. Other models tend to slightly overestimate the air-core size for low *Re*.

The relative velocity of discharged liquid sheet, v_l/v_p (combined radial and axial velocity divided by the inlet velocity) is slightly increasing with *Re*. All CFD models captured the trend from the experiment well, but the velocity values were overestimated by most of them. The laminar model was closest to the experimental data for $Re = 1000$ and 2000, followed by the LES and *k*-ε. Slightly different results were obtained at the highest *Re*, where the LES outperformed the laminar model, but still overestimated the velocity by 5 %.

A huge disparity is found for the *SCA* results, where the value of experimental *SCA* is more than 20 % larger than the predicted one. The experimental *SCA* discussed here is measured directly after discharge as the apex angle of cone, which covers the liquid sheet, while the *SCA* from the CFD is based on the maximum in the liquid fraction inside the discharge liquid sheet. Nevertheless, both approaches should return very similar values of *SCA*. The *SCA* value grows rapidly in the experiment with *Re* as

$SCA \propto Re^{0.12}$, respectively with p_l as $SCA \propto p_l^{0.06}$, while it increases in transient laminar simulation as $SCA \propto Re^{0.06}$ or $SCA \propto p_l^{0.03}$ and it is constant for the LES simulation. The reason for these disparities is not exactly known, but it may be partially related to the flow of the surrounding air, which may slightly affect the liquid sheet formation as described in [39] and was not captured in CFD due to a relatively small outflow area. Also, manufacturing inaccuracies and different measuring methods may introduce some errors.

A widely used empirical correlation published by Rizk and Lefebvre [40] predicted much higher influence of the inlet pressure as $SCA \propto p_l^{0.11}$. However, this correlation was derived for liquids with higher viscosity and well captured the trends using higher viscous liquid in our previous study [28] using almost identical geometry as used here. Similarly, the experimental values of *SCA* were higher than expected. The viscous liquids typically exhibit larger influence of p_l on *SCA* since Ballester at al. [37] found $SCA \propto p_l^{0.39}$ for heating oil. The values of SCA based on the Rizk predictions are 46, 54 and 63° for Re = 1000, 2000 and 4000, respectively. These values are well below the measured values, but are much closer to the CFD prediction. Since the CFD predicts correctly other parameters of the internal flow, the differences in *SCA* might be linked with a different measurement technique, complex air-flow near the liquid sheet and wettability of the atomizer body.

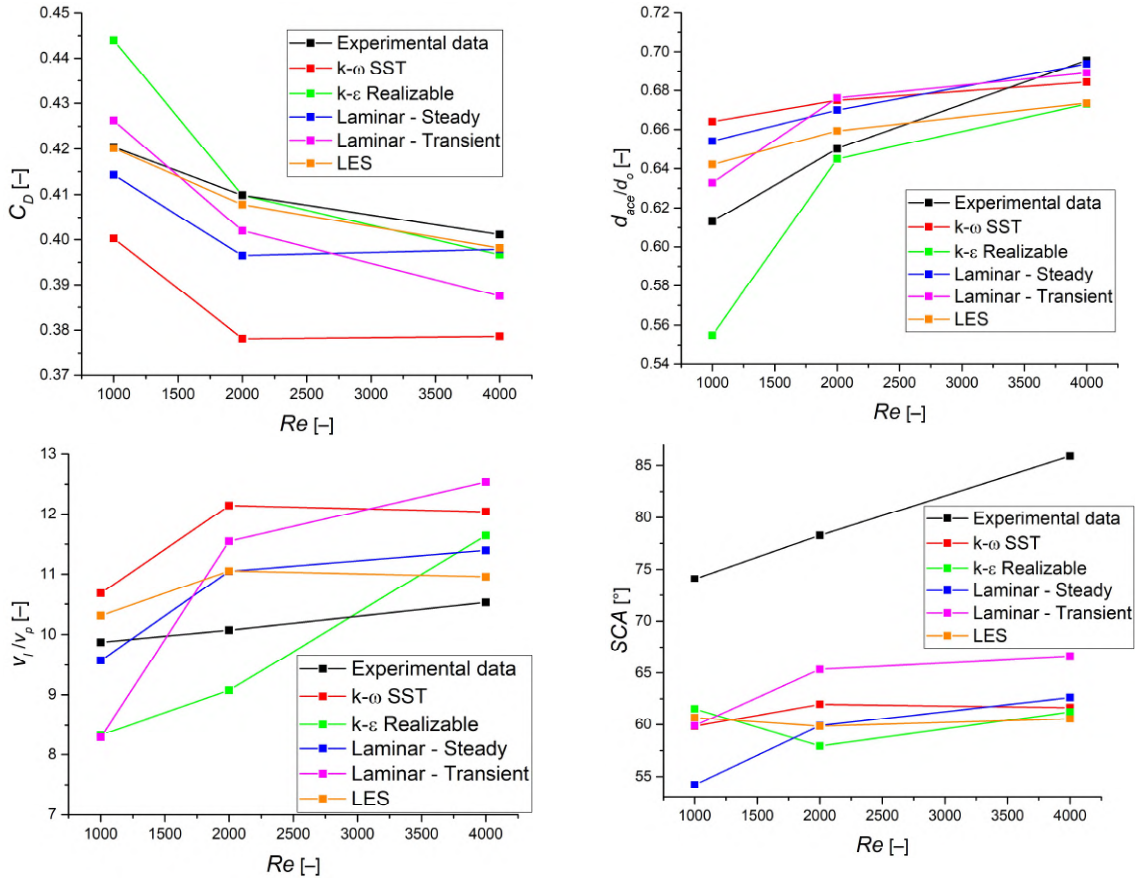

Figure 10 Effect of Re on C_D, SCA, liquid sheet velocity, v_l, and d_{ace} from various numerical setups.

Air-core dynamics

The mean parameters of the internal flow are important for the atomizer geometrical design. However, instabilities are commonly presented, and for some geometries, it may change the breakup nature or generate an unstable spray as documented elsewhere [1, 28, 29]. The steady simulations, in principle, can only indicate the calculation stability or the convergence rate, which may or may not be linked with real flow instabilities. Therefore, this part focuses only on the transient models. The simplest way to detect flow instabilities is to measure the rate of change of the air-core diameter or its position. From the experimental data, the most prominent are the air-core contractions and extractions at a given position. Its frequencies, shown in Figure 11 left, are almost identical along the air-core length and peaked roughly at f = 110, 240 and 480 Hz for Re = 1000, 2000 and 4000, respectively. This leads to a virtually constant value of Strouhal number over the range of Re values:

$$St = \frac{fD}{v_p} \tag{1}$$

where D is a characteristic dimension, which can be the swirl chamber diameter and is constant here. The same behaviour was documented elsewhere [41], where the value of St depended on the atomizer constant and was independent of the operating regime. Note here that no dominant frequency can be observed in our LDA data.

The CFD simulations are unable to predict any dominant frequency. The laminar model exhibits the largest amplitudes of the air-core fluctuations as reported in Figure 11 right. The turbulence models k-ε and k-ω subdued the air-core surface waves and almost no fluctuations can be detected.

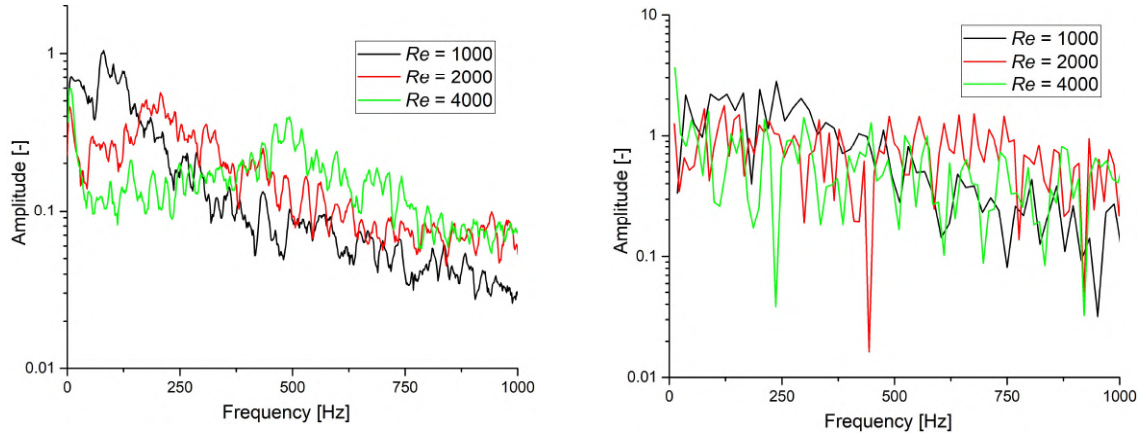

Figure 11 Frequency spectra of air-core diameter fluctuations at location d_{ac11}. Left: experimental data, right: laminar simulation.

Conclusion

The 2D and 3D numerical simulations of pressure-swirl atomizer internal flow were compared in transient and steady state with experimental data for Re = 1000, 2000 and 4000. Various numerical setups, including six turbulence models and several geometrical simplifications, were investigated.

The air-core was found stable and developed in all the tested regimes. The discharge coefficient C_D slightly decreased with Re as a result of lower relative viscous losses, which was confirmed by slight increase in the measured swirl velocity.

The steady simulations are comparable with the time-averaged transient ones; but their convergence rate is at least about an order of magnitude faster. No steady simulation setup was found stable for the 2D model.

From geometry simplification study, it is evident that the inlet port must be modelled to assure reliable results.

The laminar solver was capable to predict the C_D, air-core dimensions and velocity profiles with an error less than 5% compared with the experimental results in both 2D and 3D simulation for the whole range of Re. The LES model performed similarly to the laminar solver for low Re and was superior for Re = 4000. The two-equation models, k-ε and k-ω, were sensitive to proper solving of the near wall flow and were not accurate for low Re. However, all the models captured well the trends. The worst results were surprisingly obtained for RSM (Reynolds Stress Model), which diverged for Re = 1000 and 2000 or predicted the undeveloped air-core. For the unknown reason, the only parameter predicted with large error was the spray cone angle (SCA).

The air-core diameter fluctuations were observed and the dominant frequency was found rising with Re to keep a constant value of Strouhal number. However, the simulations provided only a wide range of frequencies without any significant peaks.

For the atomizer rapid CFD prototyping, the steady 3D simulation with laminar solver is the most efficient approach.

Acknowledgements

The authors acknowledge the financial support the project “Computer Simulations for Effective Low-Emission Energy Engineering” funded as project No. CZ.02.1.01/0.0/0.0/16_026/0008392 by Operational Programme Research, Development and Education, Priority axis 1: Strengthening capacity for high-quality research.

Nomenclature

A	area [m^2]
b	width [m]
B	experimental constant [–]
C_D	discharge coefficient [–]
d	diameter [m]
h	height [m]
k	Atomizer constant used in [4, 5] [–]
l_b	breakup length [m]
$\dot{m}$	mass flow rate [kg/h]
n	refractive index [–]
r	radial distance [m]
Re	Reynolds number [–]
S_1	virtual distance of the measurement volume [m]
S_2	real distance of the measurement volume [m]
SCA	spray cone angle [°]
SFR	Spill-to-Feed ratio [–]
t	liquid sheet thickness [m]
U	axial velocity [m/s]
V	radial velocity [m/s]
v	velocity [m/s]
W	swirl velocity [m/s]
We_g	gas Weber number [–]
X	ratio of air-core to of exit orifice area [–]
Z	axial distance [m]

Greek characters

p	pressure drop at the nozzle [Pa]
μ	dynamic viscosity [kg/(m·s)]
ρ	density [kg/m^3]
σ	liquid/gas surface tension [kg/s^2]

Subscripts and Superscripts

c	swirl chamber
cal	calculated
e	exit orifice
g	surrounding gas
l	atomized liquid
p	inlet port
ac	air-core
sc	spray cone

References

[1] Maly, M., Jedelsky, J., Slama, J., Janackova, L., Sapik, M., Wigley, G., and Jicha, M., 2018, "Internal flow and air core dynamics in Simplex and Spill-return pressure-swirl atomizers," International Journal of Heat and Mass Transfer, 123, pp. 805-814.

[2] Cooper, D., Yule, A., and Chinn, J., 1999, "Experimental measurements and computational predictions of the internal flow field in a pressure swirl atomizer," ILASS 1999.

[3] Qian, W., Hui, X., Zhang, C., Xu, Q., Lin, Y., and Sung, C.-J., 2017, "A Numerical Study of the Internal Flow in a Pressure Swirl Atomizer," (50848 C2 - Turbo Expo: Power for Land, Sea, and Air), pp. V04AT04A070-C071 - Volume 074A: Combustion, Fuels and Emissions.

[4] Chinn, J. J., 2009, "An appraisal of swirl atomizer inviscid flow analysis, Part 1: The principle of maximum flow for a swirl atomizer and its use in the exposition and comparison of early flow analyses," Atomization and Sprays, 19(3).

[5] Chinn, J. J., 2009, "An appraisal of swirl atomizer inviscid flow analysis, part 2: inviscid spray cone angle analysis and comparison of inviscid methods with experimental results for discharge coefficient, air core radius, and spray cone angle," Atomization and Sprays, 19(3).

[6] Amini, G., 2016, "Liquid flow in a simplex swirl nozzle," International Journal of Multiphase Flow, 79, pp. 225-235.

[7] Wimmer, E., and Brenn, G., 2013, "Viscous flow through the swirl chamber of a pressure-swirl atomizer," International Journal of Multiphase Flow.

[8] Yule, A., and Chinn, J., 1997, "Pressure swirl atomizer internal flow and performance," ILASS, Americas, pp. 205-209.

[9] Yule, A. J., and Chinn, J. J., 2000, "The internal flow and exit conditions of pressure swirl atomizers," Atomization and Sprays, 10(2), pp. 121-146.

[10] Chinn, J. J., 2008, "The numerics of the swirl atomizer," ILASS, p. 7.
[11] Madsen, J., Hjertager, B. H., and Solberg, T., 2004, "Numerical simulation of internal flow in a large-scale pressure-swirl atomizer," ILASS, pp. 183-188.
[12] C. Galbiati, S. Tonini, P. Conti, and Cossali, G. E., "Numerical Simulations of Internal Flow in an Aircraft Engine Pressure Swirl Atomizer," Journal of Propulsion and Power(6), p. 1433.
[13] Qian, W., Hui, X., Zhang, C., Xu, Q., Lin, Y., and Sung, C.-J., "A numerical study of the internal flow in a pressure swirl atomizer," Proc. ASME Turbo Expo 2017: Turbomachinery Technical Conference and Exposition, American Society of Mechanical Engineers Digital Collection.
[14] Nouri-Borujerdi, A., and Kebriaee, A., 2012, "Numerical simulation of laminar and turbulent two-phase flow in pressure-swirl atomizers," AIAA journal, 50(10), pp. 2091-2101.
[15] Abbasi Baharanchi, A., Nordin Darus, A., Ansari, M., and Abbasi Baharanchi, E., 2012, "An Optimum Method of Capturing Interface and a Threshold Weber Number for Inclusion of Surface Tension Force in Simulation of Nozzle Internal Flow in Pressure Swirl Atomizers," (ASME International Mechanical Engineering Congress and Exposition), p. 12.
[16] Sumer, B., Erkan, N., Uzol, O., and Tuncer, I., 2012, "Experimental and Numerical Investigation of a Pressure Swirl Atomizer," ICLASS.
[17] Vashahi, F., Dafsari, R. A., Rezaei, S., Lee, J. K., and Baek, B. J., 2019, "Assessment of steady VOF RANS turbulence models in rendering the internal flow structure of pressure swirl nozzles," Fluid Dynamics Research, 51, p. 045506.
[18] Shaikh, S., Banaszak, U., Von Lavante, E., Cooper, D., and Yule, A., "CFD prediction of the Effects of Viscosity on the Internal Flow of a Scale Pressure-swirl Atomiser," Proc. Proc. ILASS-Europe.
[19] Laurila, E., Roenby, J., Maakala, V., Peltonen, P., Kahila, H., and Vuorinen, V., 2019, "Analysis of viscous fluid flow in a pressure-swirl atomizer using large-eddy simulation," International Journal of Multiphase Flow, 113, pp. 371-388.
[20] Ghate, K., and Sundararajan, T., 2019, "Effects of orifice divergence on hollow cone spray at low injection pressures," Proceedings of the Institution of Mechanical Engineers, Part G: Journal of Aerospace Engineering, 233(11), pp. 4091-4105.
[21] Ibrahim, A., 2006, "Comprehensive study of internal flow field and linear and nonlinear instability of an annular liquid sheet emanating from an atomizer," University of Cincinnati.
[22] Dikshit, S. B., Kulshreshtha, D., and Chaniwala, S., 2011, "Numerical predictions of internal flow through pressure swirl atomizer," Indian Journal of Science and Technology, 4(2), pp. 72-75.
[23] Madsen, J., Hjertager, B. H., and Solberg, T., 2004, "Numerical simulation of internal flow in a large-scale pressure-swirl atomizer," Proc. ILASS-Europe 2004, pp. 183-188.
[24] Bazarov, V., Hinckel, J., and Villa Nova, H., 2008, "CFD Analysis of Swirl Atomizers," 44th AIAA/ASME/SAE/ASEE Joint Propulsion Conference & Exhibit, American Institute of Aeronautics and Astronautics.
[25] Sumer, B., Erkan, N., Uzol, O., and Tuncer, I., "Experimental and Numerical Investigation of a Pressure Swirl Atomizer."
[26] Marudhappan, R., Chandrasekhar, U., and Hemachandra Reddy, K., 2016, "Optimization of Simplex Atomizer Inlet Port Configuration through Computational Fluid Dynamics and Experimental Study for Aero-Gas Turbine Applications," Journal of The Institution of Engineers (India): Series C, pp. 1-12.
[27] Mandal, A., Jog, M., Xue, J., and Ibrahim, A., 2008, "Flow of power-law fluids in simplex atomizers," International journal of heat and fluid flow, 29(5), pp. 1494-1503.
[28] Maly, M., Cejpek, O., Sapik, M., Ondracek, V., Wigley, G., and Jedelsky, J., 2021, "Internal flow dynamics of spill-return pressure-swirl atomizers," 120, p. 110210.
[29] Maly, M., Sapik, M., Cejpek, O., Wigley, G., Katolicky, J., and Jedelsky, J., 2019, "Effect of spill orifice geometry on spray and control characteristics of spill-return pressure-swirl atomizers," Experimental Thermal and Fluid Science, 106, p. 12.
[30] Ansys®, 2017, Fluent Theory Guide, Release 18.2.
[31] Halder, M., Dash, S., and Som, S., 2002, "Initiation of air core in a simplex nozzle and the effects of operating and geometrical parameters on its shape and size," Experimental thermal and fluid science, 26(8), pp. 871-878.

[32] Wimmer, E., and Brenn, G., 2013, "Viscous flow through the swirl chamber of a pressure-swirl atomizer," International Journal of Multiphase Flow, 53, pp. 100-113.
[33] Khavkin, Y., 2004, The Theory and Practice of Swirl Atomizers, Taylor & Francis.
[34] Albadawi, A., Donoghue, D., Delauré, Y., Robinson, A., and Murray, D., 2012, "Numerical investigation of volume of fluid and level set interface capturing methods for bubble growth and detachment," 395, p. 012166.
[35] Halder, M., Dash, S., and Som, S., 2004, "A numerical and experimental investigation on the coefficients of discharge and the spray cone angle of a solid cone swirl nozzle," Experimental thermal and fluid science, 28(4), pp. 297-305.
[36] Som, S. K., 1983, "Theoretical and experimental studies on the coefficient of discharge and spray cone angle of a swirl spray pressure nozzle using a power-law non-Newtonian fluid," 12(1), pp. 39-68.
[37] Ballester, J., and Dopazo, C., 1994, "Discharge coefficient and spray angle measurements for small pressure-swirl nozzles," Atomization and sprays, 4(3).
[38] Rizk, N. K., and Lefebvre, A. H., 1985, "Internal flow characteristics of simplex swirl atomizers," Journal of Propulsion and Power, 1(3), pp. 193-199.
[39] Jedelsky, J., Maly, M., del Corral, N. P., Wigley, G., Janackova, L., and Jicha, M., 2018, "Air–liquid interactions in a pressure-swirl spray," International Journal of Heat and Mass Transfer, 121, pp. 788-804.
[40] Rizk, N. K., and Lefebvre, A. H., 1987, "Prediction of velocity coefficient and spray cone angle for simplex swirl atomizers," International Journal of Turbo and Jet Engines, 4(1-2), pp. 65-74.
[41] Donjat, D., Estivalezes, J.-L., Michau, M., and Lavergne, G., "Phenomenological study of the pressure swirl atomizer internal flow," Proc. 9th ICLASS Conference, Sorrento (Italy).

10.5 Paper V

Journal of Thermal Analysis and Calorimetry
https://doi.org/10.1007/s10973-018-7444-z

Effect of nanoparticles concentration on the characteristics of nanofluid sprays for cooling applications

M. Malý[1] · A. S. Moita[2] · J. Jedelsky[1] · A. P. C. Ribeiro[3] · A. L. N. Moreira[2]

Received: 25 January 2018 / Accepted: 27 May 2018

Abstract

This study addresses the effect of nanofluid synthesis on the rheological properties of the resulting fluid and their consequent effect on the characteristics (size and velocity distribution of droplets, spray cone angle, etc.) of the sprayed nanofluids. The results are discussed in the light of how the spray characteristics affect the use of the resulting nanofluid spray for cooling purposes. Nanoparticles of alumina (Al_2O_3) and zinc oxide (ZnO) are mixed in water-based solutions, for concentrations varying between 0.5% and 2 mass% for alumina and between 0.01% and 0.1 mass% for the zinc oxide particles. $FeCl_2{\cdot}4H_2O$ (0.1 mass%) was also used to infer on the effect of the nature (material) of the particles in the physicochemical properties of the resulting solutions. Among the various surfactants tested, citric acid (0.15%) was chosen for the final working mixtures, as it assured a stable behaviour of the solutions prepared during the entire study. The nanoparticles were characterized in detail, and the physicochemical properties of the fluid were measured before and after atomization, to evaluate any possible particle loss in the liquid feeding system or retention in the atomizer. The nanofluids were sprayed using a pressure-swirl atomizer at 0.5 MPa injection pressure. Droplet size and velocity in the spray were probed using phase Doppler anemometry. For the range of experimental conditions covered here, the results show that liquid viscosity is an important parameter in predetermining the spray characteristics of nanofluids, as it affects the primary liquid breakup. Despite this, only a mild increase is observed in the nanofluids viscosity, mainly for higher concentrations of alumina, which was not sufficient to significantly affect the spray characteristics, except for a small decrease in the spray cone angle and the size of the atomized droplets. Hence, for cooling purposes, the atomization mechanisms are not compromised by the addition of the nanoparticles and their using is beneficial, as they enhance the thermal properties without a significant deterioration of other fluid properties such as viscosity and spray characteristics. Present spray characteristics promote liquid adhesion to the cooling surfaces and droplet size and velocity are kept within a range that is appropriate for spray cooling, following the literature recommendations and our analysis.

Keywords Nanofluids · Pressure-swirl atomizer · Spray · PDA

Abbreviations

SCA	Spray cone angle (°)
SPAN	Relative span (–)

List of symbols

D_{20}	Surface mean diameter (μm)
D_{30}	Volume mean diameter (μm)
D_{32}	Sauter mean diameter (μm)
$D_{v0.1}$	10% volume diameter (μm)
$D_{v0.5}$	50% volume diameter (μm)
$D_{v0.9}$	90% volume diameter (μm)
f	Data rate (Hz)
ID_{32}	Integral Sauter mean diameter (μm)
r	Radial distance (mm)
Re	Reynolds number (–)

The present article is based on the lecture presented at ESNf2017 conference in Lisbon - Portugal on 8–10 October, 2017.

✉ A. S. Moita
anamoita@tecnico.ulisboa.pt

[1] Faculty of Mechanical Engineering, Brno University of Technology, Technicka 2896/2, 61669 Brno, Czech Republic

[2] IN+ - Center for Innovation, Technology and Policy Research, Instituto Superior Técnico, Universidade de Lisboa, Av. Rovisco Pais, 1049-001 Lisbon, Portugal

[3] Centro de Química Estrutural, Instituto Superior Técnico, Universidade de Lisboa, Av. Rovisco Pais, 1049-001 Lisbon, Portugal

Published online: 12 June 2018

U Axial velocity component (m s^{-1})
We Weber number (–)
w Liquid velocity at the exit orifice (m s^{-1})
Z Axial distance (mm)

Greek characters

μ_l Liquid dynamic viscosity (kg m^{-1} s^{-1})
ρ_l Liquid density (kg m^{-3})
σ_l Liquid/gas surface tension (kg s^{-2})

Introduction

Dissipating high heat loads is currently a challenge in many industrial applications, such as metallurgy, food processing, microelectronics, or even in solar energy applications [1–3]. As for the various liquid cooling techniques explored by the researchers within the last two decades, spray cooling is among the most popular, given the high heat transfer coefficients that can be achieved (of the order of 10^4–10^5 W m^{-2} K^{-1} or higher—[4]). Nevertheless, the efficient implementation of this strategy must cope with the increasingly demanding heat loads that are dissipated, so that continuous efforts have been put to further enhance the heat transfer processes. In this context, several authors addressed surface modification to enhance these processes, e.g. [2, 4], while others have explored the use of nanofluids to reach the same goal [5]. However, while many of these researchers dealt with nanofluids as being a single-fluid with novel thermophysical properties, mostly focusing on the effect of the nanoparticles addition on the thermal properties of the fluids [6–13] and on the heat transfer processes, often addressing convective heat transfer in internal flows [14–21], research on nanofluid droplets/sprays impacting on heated surfaces is still limited [8, 10] and the actual effects of adding nanoparticles in the fluid flow characteristics and, particularly in the mechanisms of atomization, are still scarcely reported. Hydrodynamic behaviour of the nanofluids slightly differs from that of the pure liquids, which is mainly related to physical modifications of the local and bulk properties of the nanofluids. Surface tension is affected by the nanoparticle concentration and size. Although this effect is less prominent in the bulk properties [22], it can be relevant for the wettability at the liquid–solid interface [23, 24]. The liquid density is expected to be slightly increased, as the nanoparticles have usually higher density compared to the base liquid. The viscosity of nanofluids depends on the size, shape, concentration and material of the added nanoparticles. Moreover, those parameters also determine if the nanofluids behave as Newtonian or non-Newtonian liquids. For instance, nanofluids with spherical particles are more likely to depict a Newtonian behaviour [25]. However, nanofluids rheology is a complex topic, as evidently shown in several studies reporting contradictory results. For instance, Jang et al. [26] report a dependency of the nanofluid viscosity on the tube size of flow domain at the microscale, which was neglected by other authors [27]. However, the wall friction coefficient is reported by others to slightly increase with the addition of nanoparticles [28].

Since all these properties are likely to affect the spray characteristics, a detailed characterization of the spray plays a paramount role in the heat transfer processes given the intricate correlation existing between droplet/spray characteristics and heat transfer processes. The pressure-swirl atomization excels in the generation of fine droplets at relatively low liquid pressure. In principle, the liquid is injected via tangential ports into a swirl chamber. The swirled liquid then leaves the exit orifice and spreads as a conical liquid sheet outside the atomizer. The liquid sheet consequently breaks up due to aerodynamic forces. The parameters of resulting droplets are dependent on the liquid sheet thickness and velocity. However, due to the complexity of the whole process, it is impossible to analytically predict the droplet sizes as they depend on the atomizer geometry, liquid properties and operating conditions. Many studies investigated the effect of liquid properties on the spray characteristics. Probably the most complex review of published work was reported by Lefebvre and McDonell [29]. Such studies mostly reveal that the liquid density has only a negligible role as its variation is usually small. The surface tension and the liquid viscosity have a similar impact on the atomization; however, both of them act differently. Hence, viscosity has a dominant effect on the liquid sheet breakup—a primary breakup. Its relative importance decreases in the region of the secondary breakup where the surface tension plays a dominant role. However, from the literature reviewed, the only known study related to the spray characteristics of nanofluids was conducted in 2017 by Kannaiyan and Sadr [30]; it concerns the effect of the concentration of alumina particles in kerosene.

In line with this, the present study addresses the effect of nanofluid synthesis on the local physical properties of the resulting nanofluid and their consequent effect on the atomization characteristics (droplet sizes, velocity distribution and spray cone angle, among others). The nature and the concentration of the nanoparticles of the base fluid are taken as influencing parameters, giving a particular emphasis on their effect on the interfacial mechanisms present in atomization. The results presented and discussed here focus on the consequences of the nanoparticle concentration on the atomization characteristics and how they can potentially affect the use of the resulting spray for cooling. Indeed, the cooling performance of the spray is strictly related to the complex interactions between droplets–droplets, droplets-spreading lamellas and droplets-deposited liquid film [1, 2], particularly when a liquid

phase change occurs, as a strong deposit of cold liquid may preclude the occurrence of phase change. In this case, the liquid renovation by droplet impingement may play an additional and important role in removing the heat flux, essentially by a convective single-phase process [1, 2]. Hence, fine/disperse sprays such as that used in the present work, may be preferred [1, 31] with optimized intermittent cycles, to better disperse the spray on the cooling area and to allow droplet spreading into thin lamellas, thus promoting liquid phase change [32, 33]. In such case, the impact outcomes (e.g. whether the droplet spreads or disintegrates after the impact) are directly dependent on the initial droplets sizes and velocities within the impinging spray. In any case, characterizing the spray prior to impact is mandatory, as characteristic size and velocity values of the spray droplets are directly used to compute representative non-dimensional numbers (Weber, Nusselt and Reynolds numbers, among others) [1, 2, 32, 33].

Experimental

Different nanofluids, obtained from alumina, zinc, copper and iron oxides in water are synthesized using co-precipitation and solvothermal methods [34], as detailed in the following section and are used to produce the sprays characterized in the present work.

The tested atomizer is a pressure-swirl type, as shown in Fig. 1. The atomizer is small-sized, with a discharge orifice of 0.42 mm in diameter and two tangential inlet ports with a square cross section of 0.6 × 0.6 mm^2.

The liquid was supplied from a small (3 L) pressure vessel, pressurized by air at 0.5 MPa. The liquid mass flow rate through the atomizer was approx. 7 kg h^{-1}. The atomized liquid was captured in a collection chamber and consequently re-used.

Table 1 Specification of the nanoparticles size

Samples	Diameter/nm	Brand
Al_2O_3	80	Fluka
ZnO	80	Sigma-Aldrich
CuO	50	Sigma-Aldrich
$FeCl_2{\cdot}4H_2O$	≥ 100	Sigma-Aldrich

Preparation of nanofluids and characterization of their thermophysical properties

A two-step process was used to prepare the nanofluids. The mixtures were prepared in the range of 0.01–2% mass percentages, mixed up on a base fluid of deionised water (DI) and a surfactant and were placed in the ultrasonic bath for 1 h. The characteristic sizes of the nanoparticles, which were mainly acquired from Fluka and from Sigma-Aldrich are summarized in Table 1. The main composition of the resulting solutions is shown in Table 2.

As briefly explained in the introduction, particular interaction phenomena may occur at the interface between the nanoparticles and the surface to cool during spray impact. However, prior to impact, and for the low concentrations used in this study, the main influence of the particles on the spray is related to the possible sedimentation and agglomeration, which may locally affect the thermal and the physicochemical properties of the solutions. In all samples, the dispersion was observed and maintained when a surfactant was added to the mixture. Different surfactants were tested (e.g. citric acid, oleic acid, CTAB—cetyl trimethylammonium bromide) to infer on their effect in the stability

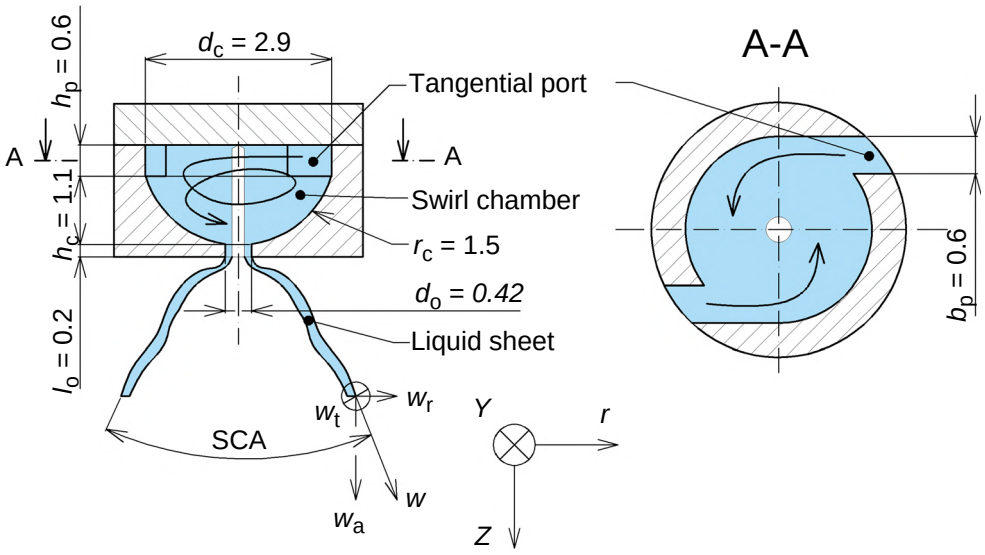

Fig. 1 Schematic of the pressure-swirl atomizer with the main dimensions in millimeters

Table 2 Specification of the nanofluids composition

Sample number	Mass percentage/%				
	Surfactant		Oxide		Deionized water
1	Citric acid	0.15	–		99.85 (pure)
2	Citric acid	0.15	Al_2O_3	2	97.85 (pure)
3	Citric acid	0.15	Al_2O_3	0.5	99.35 (pure)
4	Citric acid	0.15	ZnO	0.5	99.35 (pure)
5	Citric acid	0.15	ZnO	0.01	99.84 (pure)
6	Citric acid	0.15	CuO	0.1	99.75 (pure)
7	Citric acid	0.15	$FeCl_2{\cdot}4H_2O$	0.1	99.75 (pure)

of the nanofluids. The mixtures showing the most stable behaviour were prepared with citric acid; therefore those mixtures were used to show the results presented and discussed here. The stability of the low concentrated nanofluids (up to 0.5 mass%) was achieved within hours, then sedimentation was observed. However, the nanofluid with 2 mass% of Al_2O_3 had a limited stability as the sedimentation appears in approx. 15 min. The measurement duration was about 10 min for one liquid batch, so it was not affected by sedimentation. After hand re-shacking, the sedimented part was dissolved, and the stability was restored. In order to prevent the sedimentation, the liquid supply vessel was shaken every minute.

The morphology was analysed by scanning and transmission electron microscopy, which also gives information about the phase structures and chemical composition, complemented by Fourier transform infrared spectroscopy, X-ray diffraction, Raman and X-ray photoelectron spectroscopy. Surface wetting was then quantified with an optical tensiometer (THETA from Attension), by the apparent equilibrium and quasi-static advancing and receding macro-contact angles, following the procedures described in [35, 36]. The accuracy of the contact angle measurements is of the order of $\pm$ 1°. Care was taken to perform a high number of measurements (of the order of 15 measurements) for which the values dispersion was at most of the order of $\pm$ 5°.

As for the thermophysical properties of the nanofluids, the present study considered the measurement of the density ρ_l, dynamic viscosity μ_l and surface tension σ_l. The density was evaluated from the concentration of the solution, by mass conservation principles and was very close to that of water, for all the samples tested (ρ_l = 998 kg m^{-3}). The viscosity was evaluated with an ATS RheoSystems (a division of CANNON® Instruments, Co) under controlled temperature conditions, with an accuracy of $\pm$ 5%. The surface tension was measured under controlled temperature conditions (20 $\pm$ 2 °C) with an optical tensiometer THETA (Attention), using the pendant drop method. The value taken for the surface tension of each solution was averaged from 15 measurements, with a maximum standard deviation of the mean of 0.04 mN m^{-1}. A detailed description of the measurement procedures is provided in [37].

The properties of the nanofluids were measured before and after atomization, since if particle trapping would occur in the liquid feeding system or in the atomizer, it would affect the properties of the fluids and the atomization mechanisms. Also, the images taken with the high-speed camera were qualitatively analysed to check for possible modifications in the spray morphology caused by any significant loss of particles. No significant changes were observed, either in the liquid properties or in the spray morphology that could indicate any problem related to the loss of particles.

Spray characterization

The measurements of droplets velocity and size were performed using a two-component Phase Doppler anemometer by Dantec Dynamics A/S (Skovlunde, Denmark) which consists of 55× transmitting optics, 57 × 10 receiving optics and multi-line Ar-ion + laser Spectra-Physics type 177-G0232. The optical configuration is summarized in Table 3. Burst signal processor P80 was used to process the measured signal. BSA flow software v5.20 was used to control the data acquisition and the following setting was

Table 3 Outline of the phase Doppler optical configuration

	Value
Transmitting optics	
Laser power/mW	400
Laser wavelengths/nm	514 and 488
Beam spacing/mm	60
Frequency shift/MHz	40
Transmitter focal length/mm	310
Receiving optics	
Scattering angle/°	69
Receiver focal length/mm	500
Micrometre/mm	0.500

used: Photomultiplier sensitivity 1180–1500 V, signal gain 22 dB, velocity centre 15 ms^{-1}, velocity span 30 ms^{-1}. Although the PDA is capable of 2D measurement, only the axial velocity component U was evaluated for this part of the study.

The measurement grid uses a radial system, as defined in Fig. 2, where $r = 0$ mm corresponds to the centre of the spray cone. Measurements are reported for $Z = 10$ mm and $Z = 20$ mm, being $Z = 0$ mm, positioned at the atomizers exit orifice. Extensive measurements were then performed for $-20\text{ mm} < r < 20\text{ mm}$ and $-20\text{ mm} < y < 20$ mm in 2 mm steps on two radially orthogonal axes. The measurement was limited to 50,000 samples acquired or to 15-s acquisition duration at each measured point.

Characteristic droplet sizes statistically evaluated from the sampled droplets include average values and characteristic diameters representing the volume ratios and the area to volume ratios. These characteristic diameters are usually more representative of the actual droplet size distribution across the spray, as they weigh the relative importance of larger droplets. These characteristic diameters are also important as they can help us to understand the most suitable spray characteristics promoting heat transfer.

The present work mostly evaluates the Sauter mean diameter or D_{32}, $D_{v0.1}$, $D_{v0.5}$ and $D_{v0.9}$. The quantities $D_{v0.1}$, $D_{v0.5}$ and $D_{v0.9}$ represent the particle diameters below which 10, 50 and 90%, respectively, of the total volume is contained. The Sauter mean diameter or D_{32} is the ratio between the area and the volume of the droplets measured. From this, the Integral Sauter mean diameter (ID_{32}) can be calculated as a single parameter providing the global representation of D_{32} by its mass weighted averaging over the entire radial profile [38]:

$$ID_{32} = \sum_{i=1}^{n} r_i f_i D_{30,i}^3 \Big/ \sum_{i=1}^{n} r_i f_i D_{20,i}^2 \quad (1)$$

where f_i is data rate, D_{30} is volume mean diameter and D_{20} is surface mean diameter in the position with radial distance r_i from the atomizer centre.

There are many aspects which affect the precision of the PDA measurement e.g.: fluctuations in the operating pressure of the atomizer, uncertainty of the atomizer positioning respective to the PDA measurement volume and the error of the PDA instrument itself. As it is almost impossible to evaluate these phenomena separately, standard deviations (SD) of main evaluated parameters were calculated as quantities revealing the repeatability error. This procedure was based on five measurements with pure water. Those measurements were performed randomly during the measurement series. The SD was found to be $\pm$ 0.2–1 ms^{-1} for velocity, depending on the measurement position, $\pm$ 1–3.5 μm for D_{32}, $\pm$ 1.5 μm for ID_{32} and $\pm$ 1.5° for PDA based measurements of the spray cone angle (SCA). The error bars are not displayed in the plots for clarity, as the variation of the results is low.

The nanofluids with a nanoparticle concentration of 0.5 mass% or higher were optically opaque. Spherical validation was about 75–85% for the opaque liquids which is slightly lower compared to the validation rate of 88–92% of transparent liquids. As long as the inhomogeneities inside the droplets are small compared with the wavelength of the laser light (514 nm), the measurement accuracy should be undisturbed [39], but signal blur may occur and decrease the validation and data rate.

High-speed visualization using a high-speed camera Phantom v4.2 and image post-processing complement the PDA measurements to qualitatively characterize the shape and morphology of the sprays and to evaluate the SCA. Images were taken at 15 kHz, with a resolution of 192 × 192 px^2. The SCA was captured by an in-house MATLAB code based on the Canny edge detector.

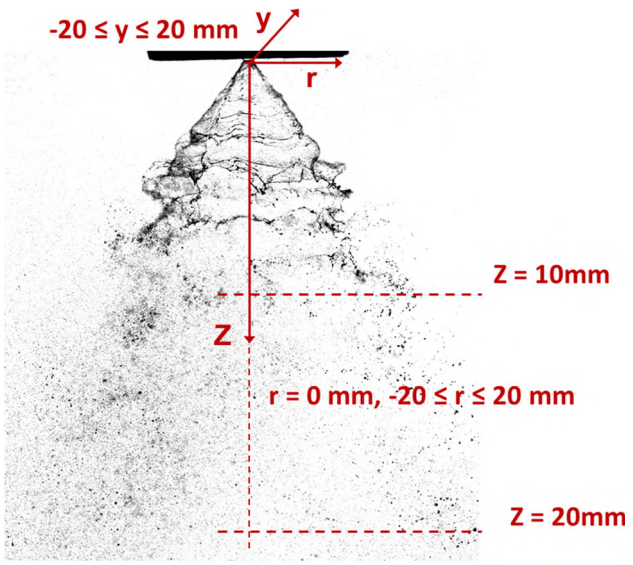

Fig. 2 System of coordinates used in the measurements with the phase Doppler anemometer

Results and discussion

The first part of this study evaluates the effect of nanoparticles concentration on the thermophysical properties of the nanofluids. Then, it is followed by the analysis of their consequent effects on the spray characteristics and how they can affect the suitability of the spray for cooling applications. Hence, this possible effect was firstly evaluated in the surface tension and in the viscosity, as they are paramount properties affecting the spray angle and the

atomization processes. The results in Fig. 3 show a minor influence of the nanoparticles concentration on the surface tension of the mixtures (Fig. 3a), but evidence a trend of the viscosity to increase with the particles concentration (Fig. 3b), particularly when the alumina particles are used.

The properties of the nanofluids resulting from the mixture with CuO and $FeCl_2{\cdot}4H_2O$ particles show no significant effect of adding the nanoparticles on the properties of the resulting solution. So, for the solution water + CuO (0.1%) + citric acid (0.15%), the surface tension was measured to be 72 mN m^{-1} and the dynamic viscosity was 1.05×10^{-3} μ_l/kg m^{-1} s^{-1}. For the solution water + $FeCl_2{\cdot}4H_2O$ (0.1%) + citric acid (0.15%), the surface tension was 71 mN m^{-1}, while the dynamic viscosity was 1.04×10^{-3} μ_l/kg m^{-1} s^{-1}.

The surface tension and the viscosity of the mixtures are divided by the values of the base liquid (water + surfactant) to isolate the effect of adding the nanoparticles from that of adding the surfactant. This effect of the nanoparticles on the nanofluids viscosity agrees with several studies in the literature, e.g. [10]. However, the variation of surface tension was less than 3%; thus, this effect can be neglected.

The possible effect of the liquid viscosity on the spray characteristics, the SCA, droplets characteristic sizes and representative velocities were analysed. SCA, was determined both from the high-speed images and from the PDA measurements (Fig. 4). The measures taken from the post-processing of the high-speed images were mainly used to validate the PDA measurements.

The PDA based SCA was determined as the apex angle of a virtual cone which covers 90% of the liquid volume flux inside the spray. It was derived from a radial profile of the normalized cumulative liquid distribution across the spray (Fig. 5). Thus the SCA values taken from the PDA measurements do not match perfectly to those obtained from the high-speed images. However, the differences between the extreme angle values are very small—2% for camera-based SCA and ± 6% for PDA based SCA, which allows validating the PDA measurements. A linear correlation with correlation coefficient $R^2 = 0.85$ shown in Fig. 4 can be obtained.

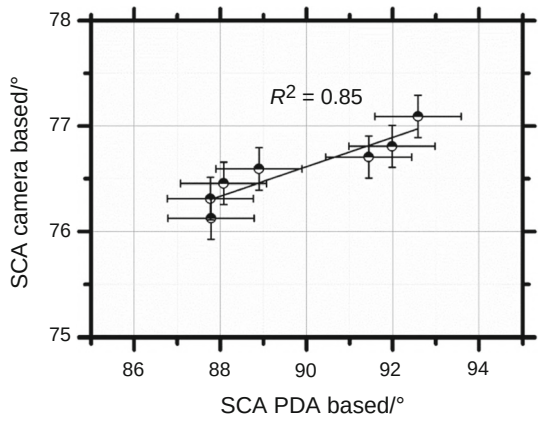

Fig. 4 Comparison between the SCA values evaluated from the PDA measurements and taken from the post-processing of the high-speed images

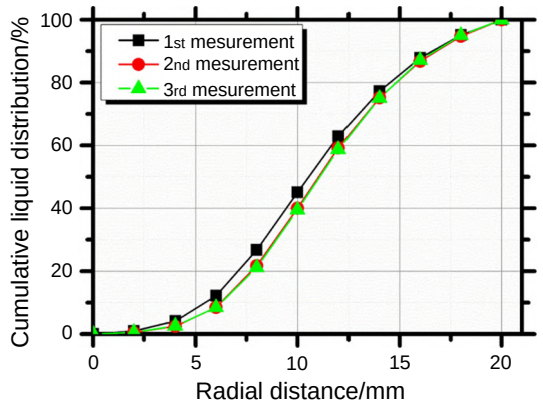

Fig. 5 Cumulative liquid distribution in the spray for three consequent measurements using ZnO 0.01 mass%

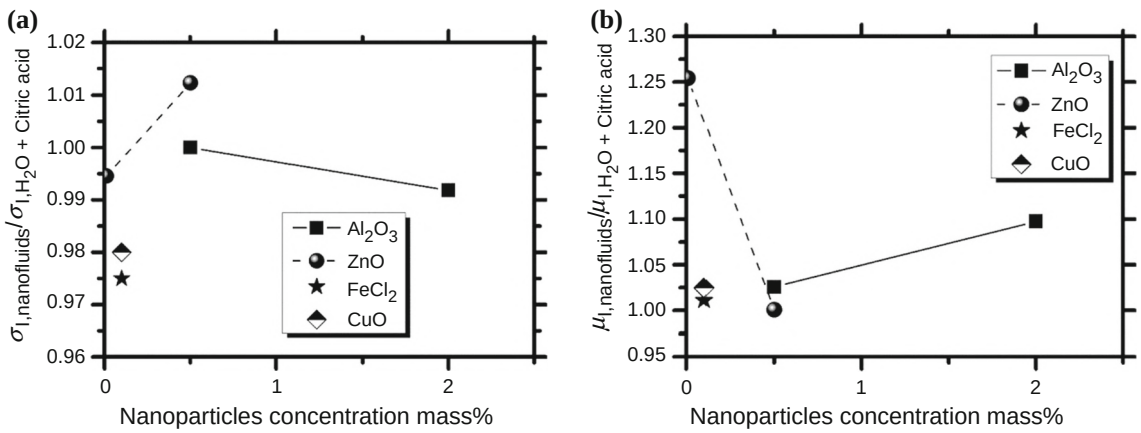

Fig. 3 Effect of the nanoparticles concentration on: **a** surface tension of the nanofluids, **b** dynamic viscosity of the nanofluids

The liquid sheet breakup length based on the high-speed images was about 5–7 mm with no obvious correlation with the nanofluid used. The image resolution was not sufficient to distinguish it more precisely. The PDA measurements at $Z = 10$ mm are conducted just after the primary breakup.

Each nanofluid was atomized and measured several times. However, the spray characteristics were slightly different between the first and the second measurement. This effect is illustrated in Fig. 5, for the nanofluid obtained with 0.01 mass% of ZnO particles, where the liquid distribution in the spray is shifted towards the spray centre for the first measurement. Similar behaviour was observed for all the nanofluids tested here. Hence, for further analysis, only the first measurement is considered, which nevertheless is still statistically representative [40].

Figure 6 shows the evolution of the axial velocity and D_{32} along the spray radial coordinate, at $Z = 20$ mm. The axial velocity reaches its maximum in the positions where the liquid sheet is expected ($r = 6$–8 mm). This velocity profile is typical for pressure-swirl atomizers. From the figure, it can be inferred that higher nanoparticles concentration tends to form a spray with lower axial velocities and smaller droplets, especially in the spray centre where, however, there is a very low droplet mass flow rate (see Fig. 7). Al_2O_3 with 2 mass% presents the lowest values of both the axial velocity and D_{32}, being followed by Al_2O_3 with 0.5 mass% and ZnO 0.5 mass%. These differences become less relevant as the measurements were performed further from the spray centre. These results are in agreement with those reported in [30] where the nanofluids with higher concentration formed droplets with lower axial velocity and slightly lower D_{32}.

The droplet size and velocity are linked together, as larger droplets have higher momentum and thus their velocity remains high, further downstream from the atomizer.

The liquid volume distribution across the spray, as illustrated in Fig. 7, shows a negligible effect of the nanoparticle concentration. Hence, mild differences are only observed for the largest nanoparticle concentration (2 mass%), for which there is more liquid concentrated further from the spray centre. This is evident for both axial distances ($Z = 10$ and 20 mm). For $Z = 10$ mm, both nanofluids with 0.5 mass% have a slightly more liquid concentrated further from the spray centre. This is not

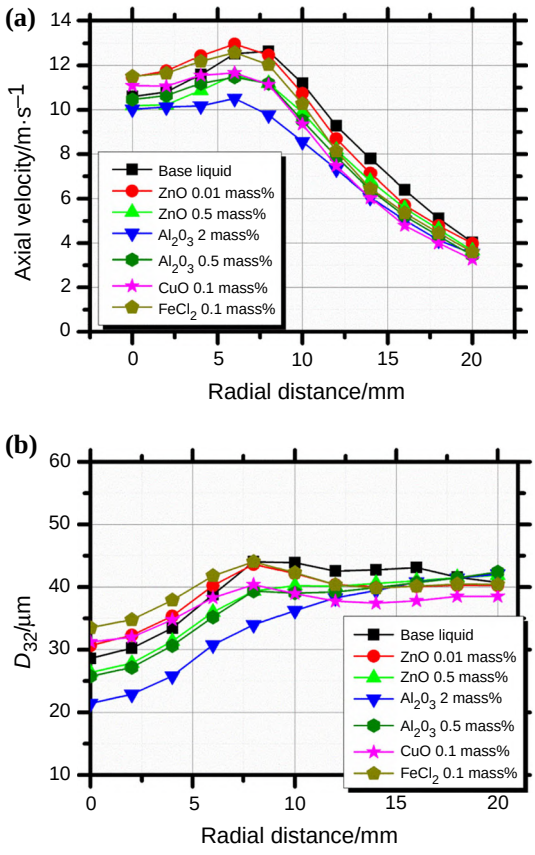

Fig. 6 Spray profile characteristics measured at $Z = 20$ mm: evolution of **a** droplets axial velocity and of **b** D_{32} along the radial coordinate of the spray

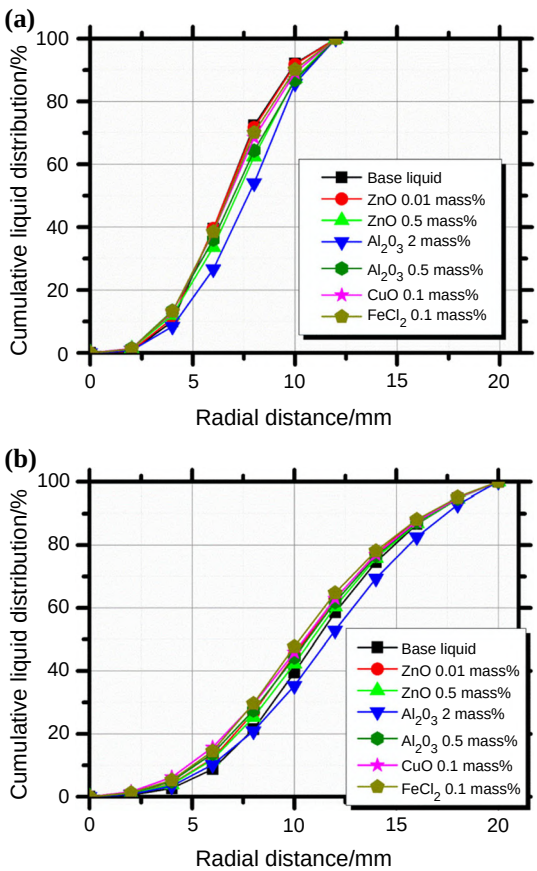

Fig. 7 Liquid volume distribution across the spray (i.e. along the radial coordinate r) at: **a** $Z = 10$ mm and **b** $Z = 20$ mm

evident for higher axial distance. Thus, the same amount of the liquid is distributed along the radial axis even when the droplets have a slightly different characteristic D_{32} or axial velocities. The highest liquid flow rate at $Z = 20$ mm was found at $r = 10$–14 mm where D_{32} (Fig. 6) was almost independent of the liquid used. However, the axial velocity reached a maximal value at $r = 6$–8 mm which corresponds to the inner edge of the liquid sheet as the liquid flow rate sharply increases in those positions.

A clearer perspective of the liquid distribution can be provided by the fractional volume diameters, which, as aforementioned, represent the particle diameters below which 10% ($D_{v0.1}$), 50% ($D_{v0.5}$) or 90% ($D_{v0.9}$) of the total volume is contained—see Fig. 8. Therefore, $D_{v0.1}$ represents a volume fraction of the smallest particles. In the spray centre, up to $r = 10$ mm, the nanofluids with the highest nanoparticle concentration have a larger fraction of smallest droplets. For positions further than $r = 10$ mm, all the nanofluids tested depicted a very similar $D_{v0.1}$. On the other hand, $D_{v0.9}$ which is mostly affected by large particles depicts a similar trend to that shown by D_{32}: $D_{v0.9}$ reaches a maximal value at $r = 8$ mm as there are large droplets in the disintegrated liquid sheet. For the positions on the very edge of the spray, the highly concentrated nanofluids have a relatively larger $D_{v0.9}$, which indicates a higher number of large droplets. This trend is in agreement with the small increase in D_{32} for these nanofluids in Fig. 6.

Relative SPAN, calculated as SPAN = $(D_{v0.9} - D_{v0.1})/D_{v0.9} - D_{v0.1})\ D_{v0.5}$. $D_{v0.5}$ was also evaluated but showed only small deviations with no obvious correlation with the nanofluid used.

To deeply evaluate the drop-size distribution in the single measured positions, the cumulative droplet volume fraction was calculated and plotted against the droplet size at two different radial distances. In the position $r = 2$ mm from the spray centre, the nanofluids with higher nanoparticle concentration formed a larger number of small droplets and thus a lower D_{32}, as shown in Fig. 9. No significant difference was observed between the nanofluids with different material particles. Hence, the nanoparticle material does not affect the characteristics of the resulting nanofluid spray. A similar trend is observed when analysing the measurements performed in radial positions further from the spray centre, even when the overall D_{32} of all liquids is almost the same. The number of the small

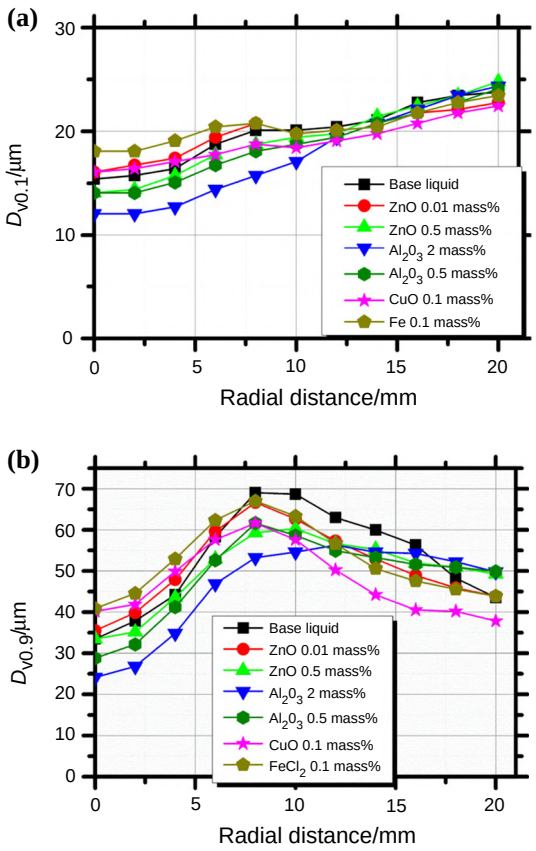

Fig. 8 Spray profile characteristics measured at $Z = 20$ mm: **a** $D_{v0.1}$, **b** $D_{v0.9}$

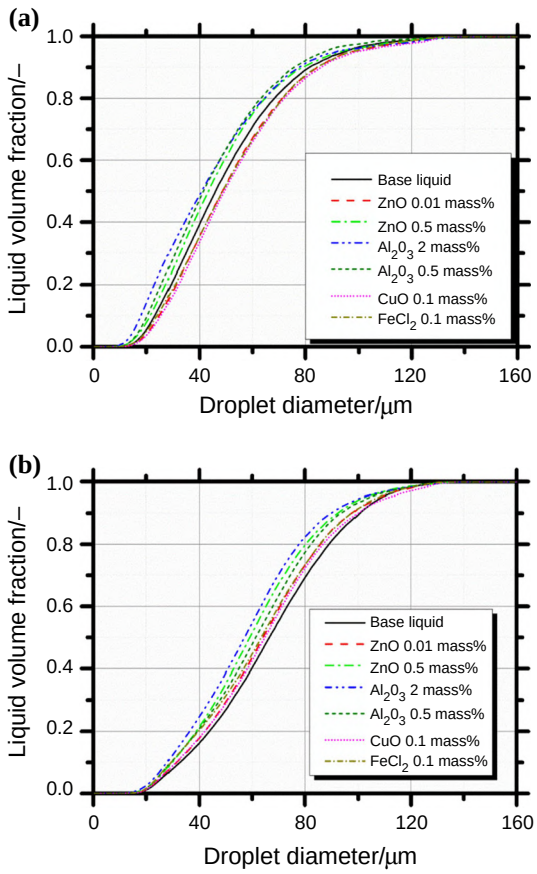

Fig. 9 Cumulative liquid volume fraction evaluated at $Z = 20$ mm. Measurements are taken at: **a** $r = 2$ mm and **b** $r = 12$ mm

particles is lower here due to higher overall D_{32}. Droplets smaller than 50 μm contain 39% liquid volume for the nanofluid produced with the Al_2O_3 particles, which is higher than 26% obtained for the base liquid.

To explain the velocity and size profiles, the droplet dynamics has to be considered. The droplets, formed from the liquid sheet, interact with surrounding air by transforming their momentum to the air and inducing its motion [41]. This process intensifies with increasing droplet surface [42], so it is more effective for sprays with smaller ID_{32} like the 2 mass% Al_2O_3, than for those depicting larger ID_{32} (0.1 mass% $FeCl_2{\cdot}4H_2O$).

This entrained air flows through the spray cone towards the centreline in the downstream direction. It causes a redistribution of the smallest droplets from the outer spray regions to the centreline. This effect explains three outcomes: (1) the generally high number of small droplets present in the centreline, that should have been, for the hollow-cone spray, free of droplets; (2) the difference between the shapes of the size profiles of individual liquids (Figs. 6b, 8). If a higher number of small droplet fraction shifts to the spray centreline, the outer spray part contains mainly the large droplets and the D_{32} keeps high. (3) The droplets decelerate preferably in the axial direction, which causes widening of the SCA. This is documented in Fig. 7, where the 2 mass% Al_2O_3 shows the liquid volume spread over larger radial positions when compared with 0.1 mass% $FeCl_2{\cdot}4H_2O$.

Despite this trend of the nanofluid sprays with higher particles concentration to form smaller droplets near the spray centre, with increased viscosity, the nanofluids form sprays with larger droplets due to larger droplets in position downstream the disintegrated liquid sheet, as clearly evidenced for $Z = 10$ mm in Fig. 10, which depicts the Integral Sauter Mean Diameter ID_{32} as a function of the dynamic viscosity. This effect is less evident for fully developed spray at $Z = 20$ mm where the ID_{32} varies in poor correlation with $R^2 = 0.27$ as $ID_{32} \sim \mu_l^{0.16}$. This correlation has similar exponent as in [43] where a very similar atomizer was tested over a very wide viscosity range of oil-based fuels. For the simplex atomizers, other published data (e.g. as reviewed in [29] and [44]) reported several correlations varying from $ID_{32} \sim \mu_l^{0.118}$ to $ID_{32} \sim \mu_l^{0.25}$, depending on the atomizers and liquids used. For a given range of viscosities, the change in ID_{32} is thus expected to be less than 2 μm which is smaller than the measurement uncertainty. [30] also observed shorter breakup length of the liquid with high nanoparticle concentration.

The SCA was observed to decline with the increase in the nanofluids viscosity for $Z = 10$ mm; however, virtually no effect was found at $Z = 20$ mm (Fig. 11). Increasing viscous forces tends to lower the velocities inside the swirl

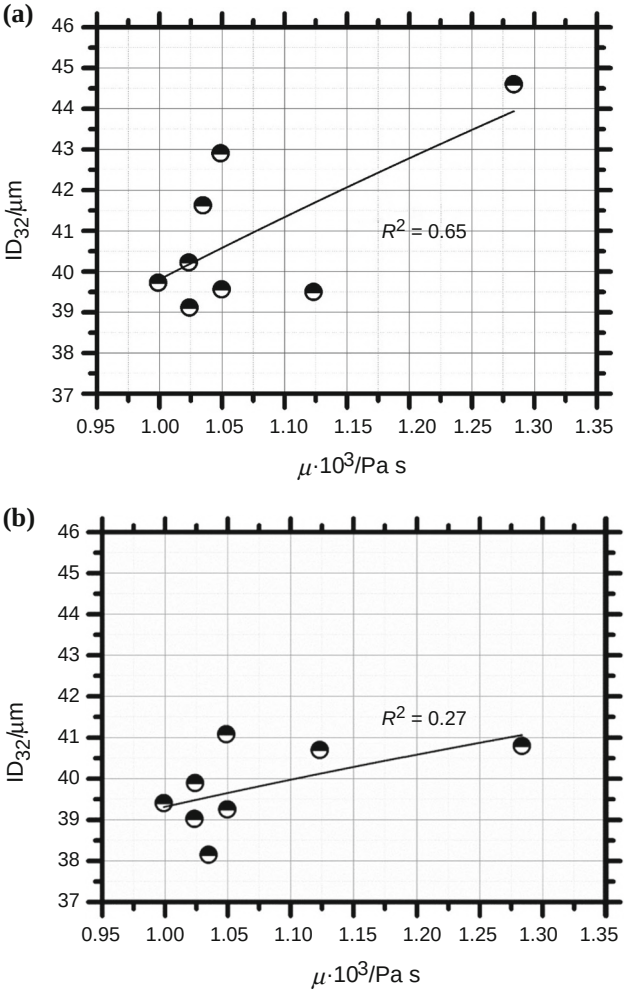

Fig. 10 Effect of the nanoparticles concentration (represented in the nanofluids viscosity) on the characteristic size of the spray droplets. PDA measurements performed at **a** $Z = 10$ mm. **b** $Z = 20$ mm

chamber, thus causing the SCA to decrease. Data reported in [29] reveals that the SCA slightly decreases with viscosity as SCA $\sim \mu_l^{-0.13}$, which should result in only a decline by about 1° in the SCA, in this case. However, it is difficult to detect this small change which is below the measurement uncertainty. These results are in agreement with those observed in [29].

Two forces act against the liquid disintegration: surface tension and viscosity. A relative importance of viscous and surface tension forces can be estimated by the ratio of the liquid phase Weber (ratio between the surface tension and inertial forces) and Reynolds (ratio between the inertial and viscous forces) numbers at the nozzle exit [45]: $We/Re = w \cdot \mu/\sigma$ where w is the liquid velocity at the exit orifice. It is mainly this ratio that gives the relative importance of the surface tension and the viscous forces. For our cases, this ratio is roughly 0.35–0.5, depending on the nanofluid used. This value, much smaller than unity, suggests the

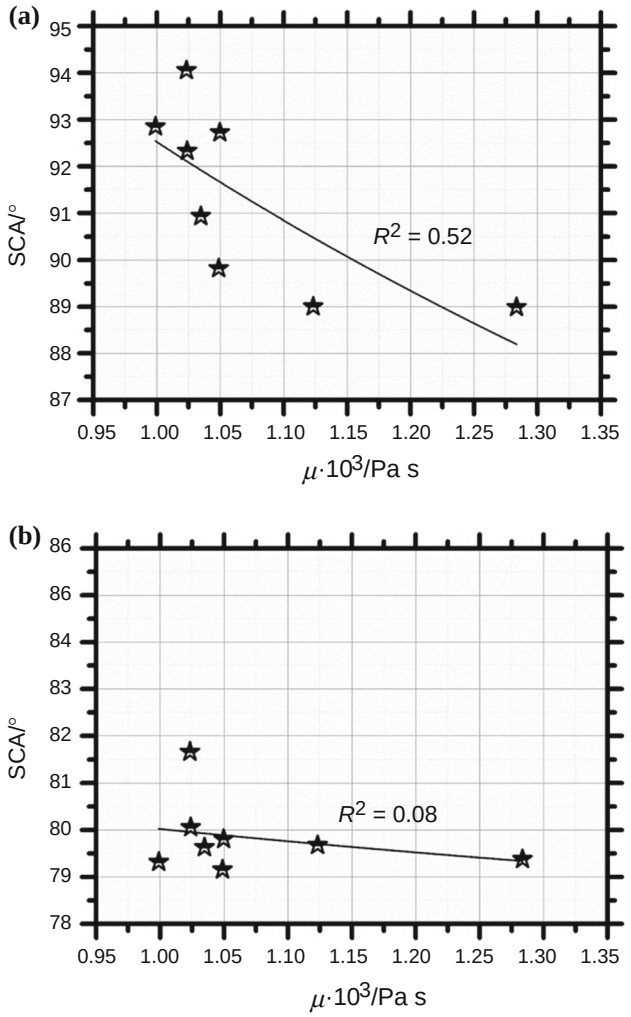

Fig. 11 Effect of the nanoparticles concentration (represented in the nanofluids viscosity) on the SCA at **a** Z = 10 mm. **b** Z = 20 mm

dominance of the surface tension forces over the viscous forces during the spray formation. Hence, it partially explains why the change in viscosity has a very small effect on the droplet sizes for Z = 20 mm. On the other hand, the liquid sheet breakup during the primary breakup is affected mostly by the viscosity [29] as the measurements analysed for Z = 10 mm show a strong dependence on the viscosity. This also indicates that the liquid breakup is not completely finished at Z = 10 mm.

Up to this point, the analysis has mainly focused on the spray characteristics and how they are affected by the nanoparticle concentration. The spray characteristics are intricately related to the cooling performance of the spray. In this context, one of the most obvious characteristics affecting the heat transfer is the SCA. The results analysed in the previous paragraphs show a trend for the higher nanoparticles concentration to mildly reduce the SCA at the exit of the nozzle orifice, due to the increase in the nanofluid viscosity. However, as also explained, this effect is fainted approximately at 20 mm below the atomizer orifice, so to avoid any influence on the spray wetted area and consequently on the heat flux one can mainly recommend the atomizer to be positioned at 20 mm or higher from the surface to cool.

Relating the spray mechanisms and characteristics with its cooling performance is far more complex and the detailed evaluation of the cooling performance of the spray must be analysed upon its impingement on the surface to cool. However, one may predict the contribution of the spray characteristics a priori to the cooling performance. The mechanism explained in the previous paragraphs leading to the appearance of smaller droplets at the centre of the spray region, which is more likely to occur in sprays with smaller ID_{32} like the 2 mass% Al_2O_3 actually contributes to distribute the sprays droplets on the surface area, allowing a more homogeneous wetting and cooling. The heat fluxes to dissipate depend on the application that is being considered, but, for instance for electronic cooling, they easily achieve heat fluxes up to 1 MW m^{-2}, which is enough for the impinging liquid to boil. If the injection period is large enough to create a liquid film, the pinching of the droplets contributes to the renovation of the cooling liquid on the surface, in a cooling process that is majorly convective and possibly occurring without phase change [1, 32, 33], which is precluded by this mechanism, as the local cooling precludes the occurrence of a stable nucleate boiling regime. While this mechanism is more effective depending on the inertial effects [2, 32], which are higher for larger droplets, the fact that these sprays have smaller droplets may actually be beneficial, since splashing and interaction mechanisms, which take the fluid away from the surface, are less likely to occur [2, 32]. If the injection period is not high enough to create a liquid film upon impingement, the cooling occurs as the spray droplets impact and spread on the surface. The size and velocity of the spray droplets directly influences the possible outcomes, as they impact on the surface, namely they can stick on the surface and spread along a thin liquid film called lamella, or they can breakup, if the inertial forces at impact are high enough to overcome surface tension forces [2, 46]. There are several criteria to establish the critical conditions for the occurrence of this immediate droplet disintegration upon impact, but the majority of them is a function of the Weber number, which is usually reported to be larger than 250, for the occurrence of disintegration, e.g. [32]. In the present study and particularly for the nanofluids with the smaller ID_{32} the Weber number is always lower than this critical value, thus the spray droplets are more likely to stick and spread on the surface, contributing to the convective heat transfer, than to disintegrate, taking away the liquid mass from the surface. Also, under this scenario, as

the droplets spread on thin lamellas of the liquid film, they are more likely to vaporize, thus allowing to take advantage of the latent heat of evaporation to cool the surface.

Conclusions

This paper addresses the effect of nanoparticles concentration on the characteristics of nanofluid sprays, which in turn may affect the spray performance in cooling applications. Different particles were added to water-based mixtures within a range of concentrations varying between 0.01 and 2 mass%. The particles are mainly alumina, zinc, copper and iron oxides.

The liquid viscosity was found to be an important parameter in predetermining the spray characteristics of the nanofluids, as it affects the primary breakup. On the other hand, surface tension was found to be a dominant force in the secondary breakup process.

However, for the range of nanoparticle concentrations studied here, the thermophysical properties of the nanofluids were not significantly changed in comparison with the base fluid. Hence, only a mild increase was detected in nanofluids viscosity, mainly observed for higher concentrations of alumina, which was not sufficient to affect the spray characteristics, except for a small decrease in the cone angle of the spray and in the diameter of the atomized droplets. However, the differences were in the same order of magnitude as the measurement uncertainty. Hence, for the conditions studied here, the addition of the nanoparticles positively contributes to the spray cooling performance as they may alter the thermal properties of the resulting nanofluid without significantly affect the hydrodynamic spray characteristics. The results also suggest that further investigation should be focused on very high particle concentrations, as the liquid physical properties will be influenced in a more significant way. In this context, the analysis of spray/surface interactions will also provide complementary information of the cooling performance of the resulting nanofluid sprays.

Acknowledgements This work has been supported by the project No. 18-15839S funded by the Czech Science Foundation. The authors are also grateful to Fundação para a Ciência e Tecnologia (FCT) for partially financing the research under the framework of the project RECI/EMS-SIS/0147/2012 and for supporting M. Malý with a research fellowship, during his stage at IN+. A. S. Moita acknowledges FCT for financing her contract and exploratory research project through the recruitment programme FCT Investigator (IF 00810-2015).

References

1. Kim J. Spray cooling heat transfer: the state of the art. Int J Heat Fluid Flow. 2007;28(4):753–67.
2. Moreira ALN, Moita AS, Panão MR. Advances and challenges in explaining fuel spray impingement: How much of single droplet impact research is useful? Prog Energy Combust Sci. 2010;36:554–80.
3. Mahian O, Kianifar A, Kalogirou SA, Pop I, Wongwises S. A review of the applications of nanofluids in solar energy. Int J Heat Mass Transf. 2013;57:582–94.
4. Bostanci H, Daniel R, John K, Louis C. Spray cooling with ammonia on microstructured surfaces: performance enhancement and hysteresis effect. J Heat Transf. 2009;131:071401.
5. Duursma G, Sefiane K, Kennedy A. Experimental studies of nanofluid droplets in spray cooling. Heat Transf Eng. 2017;30(13):1108–20.
6. Das SK, Choi US, Yu W, Pradeep Y. Nanofluids: science and technology. New York: Wiley; 2008.
7. Buongiorno J, Venerus DC, Prabhat N, McKrell T, Townsend J, Christianson R, Tolmachev YV, Keblinski P, Hu L-W, Alvarado JL, Bang IC, Bishnoi SW, Bonetti M, Botz F, Cecere A, Chang Y, Chen G, Chen H, Chung SJ, Chyu MK, Das SK, Di Paola R, Ding Y, Dubois F, Dzido G, Eapen J, Escher W, Funfschilling D, Galand Q, Gao J, Gharagozloo PE, Goodson KE, Gutierrez JG, Hong H, Horton M, Hwang KS, Iorio CS, Jang SP, Jarzebski AB, Jiang Y, Jin L, Kabelac S, Kamath A, Kedzierski MA, Kieng GL, Kim C, Kim J-H, Kim S, Lee SH, Leong KC, Manna I, Michel B, Ni R, Patel HE, Philip J, Poulikakos D, Reynaud C, Savino R, Singh PK, Song P, Sundararajan T, Timofeeva E, Tritcak T, Turanov AN, Van Vaerenbergh S, Wen D, Witharana S, Yang C, Yeh W-H, Zhao X-Z, Zhou S-Q. A benchmark study on the thermal conductivity of nanofluids. J. Appl. Phys. 2009;106:094312.
8. Chen R-H, Phuoc TX, Martello D. Effects of nanoparticles on nanofluid droplets evaporation. Int J Heat Mass Transf. 2010;53:3677–82.
9. Mehrali M, Sadeghinezhad E, Rashidi MM, Akhiani AR, Latibari ST, Mehrali M, Metselaar HSC. Experimental and numerical investigation of the effective electrical conductivity of nitrogen-doped graphene nanofluids. J. Nanoparticle Res. 2015;17(6):267.
10. Hsieh S-S, Liu H-H, Yeh Y-F. Nanofluids spray heat transfer enhancement. Int J Heat Mass Transf. 2016;94:104–18.
11. Esfe MH, Saedodin S, Yan W-M, Afrand M, Sina N. Study on thermal conductivity of water-based nanofluids with hybrid suspensions of CNTs/Al2O3 nanoparticles. J Therm Anal Calorim. 2016;124:455–60.
12. Selvam C, Lal DM, Harish S. Thermal conductivity and specific heat capacity of water–ethylene glycol mixture-based nanofluids with graphene nanoplatelets. J Therm Anal Calorim. 2017;129:947–55.
13. Zyla G. Viscosity and thermal conductivity of MgO–EG nanofluids: experimental results and theoretical models predictions. J Therm Anal Calorim. 2017;129:171–80.
14. Kakaç S, Pramuanjaroenkij AA. Review of convective heat transfer enhancement with nanofluids. Int J Heat Mass Transf. 2009;52:3187–96.
15. Nield DA, Bejan A. Convection in Porous Media. 4th ed. New York: Springer; 2013.

16. Kherbeet ASh, Mohammed HA, Salman BH, Ahmed HE, Alawi OA, Rashidi MM. Experimental study of nanofluid flow and heat transfer over microscale backward- and forward-facing steps. Exp Therm Fluid Sci. 2015;65:13–21.
17. Shenoy A, Sheremet MA, Pop I. Flow and heat transfer past wavy surfaces: viscous fluids, porous media and nanofluids. New York: Taylor & Francis Group; 2016.
18. Sheikholeslami M, Ganji DD. Nanofluid convective heat transfer using semi analytical and numerical approaches: a review. J. Taiwan Inst. Chem. Eng. 2016;65:43–77.
19. Hosseinzadeh M, Heris SZ, Beheshti A, Shanbedi M. Convective heat transfer and friction factor of aqueous Fe3O4 nanofluid flow under laminar regime: an experimental investigation. J Therm Anal Calorim. 2016;124:827–38.
20. Raei B, Shahraki F, Jamialahmadi M, Peyghambarzade SM. Experimental study on the heat transfer and flow properties of c-Al2O3/water nanofluid in a double-tube heat exchanger. J Therm Anal Calorim. 2017;127:2561–75.
21. Akbari OA, Afrouzi HH, Marzban A, Toghraie D, Malekzade H, Arabpour A. Investigation of volume fraction of nanoparticles effect and aspect ratio of the twisted tape in the tube. J Therm Anal Calorim. 2017;129:1911–22.
22. Sharma AK, Tiwari AK, Dixit AR. Rheological behaviour of nanofluids: a review. Renew Sustain Energy Rev. 2016;53: 779–91.
23. Vafaei S, Borca-Tasciuc T, Podowski MZ, Purkayastha A, Ramanath G, Ajayan PM. Effect of nanoparticles on sessile droplet contact angle. Nanotechnology. 2006;17:2523–7.
24. Wasan DT, Nikolov AD. Spreading of nanofluids on solids. Nature. 2003;423:156.
25. Chinnam J, Das DK, Vajjha RS, Satti JR. Measurements of the surface tension of nanofluids and development of a new correlation. Int J Therm Sci. 2015;98:68–80.
26. Jang SP, Lee J-H, Hwang KS, Choi SUS. Particle concentration and tube size dependence of viscosities of water nanofluids flowing through micro- and minitubes. Appl Phys Lett. 2007;91: 243112.
27. Ayela F, Chevalier J. Comment on "Particle concentration and tube size dependence of viscosities of water nanofluids flowing through micro- and minitubes. [Appl. Phys. Lett. 91, 243112 (2007)]". Appl Phys Lett. 2009;94:066101.
28. Singh PK, Harikrishna PV, Sundararajan T, Das SK. Experimental and numerical investigation into the hydrodynamics of nanofluids in microchannels. Exp Therm Fluid Sci. 2012;42: 174–86.
29. Lefebvre AH, McDonell VG. Atomization and sprays. 2nd ed. London: Taylor & Francis; 2017.
30. Kannaiyan K, Sadr R. The effects of alumina nanoparticles as fuel additives on the spray characteristics of gas-to-liquid jet fuels. Exp Thermal Fluid Sci. 2017;87:93–103.
31. Teodori E, Moita AS, Pontes P, Moura M, Moreira ALN, Bai Y, Li X, Liu Y. Application of bioinspired superhydrophobic surfaces in two-phase heat transfer experiments. J Bionic Eng. 2017;14(3):506–19.
32. Panão MRO, Moreira ALN, Durão DFG. Thermal-fluid assessment of multijet atomization for spray cooling applications. Energy. 2011;36:2302–11.
33. Panão MRO, Moreira ALN, Durão DFG. Transient analysis of intermittent multijet sprays. Exp Fluids. 2012;53:105–19.
34. Pastrana-Martínez LM, Pereira N, Lima R, Faria JL, Gomes HT, Silva AMT. Degradation of diphenhydramine by photo-Fenton using magnetically recoverable iron oxide nanoparticles as catalyst. Chem Eng J. 2015;26:45–52.
35. Pereira P, Moita AS, Monteiro G, Prazeres DMF. Characterization of English weed leaves and biomimetic replicas. J Bionic Eng. 2014;11(3):346–59.
36. Moita AS, Teodori E, Moreira ALN. Enhancement of pool boiling heat transfer by surface micro-structuring. J Phys Conf Ser. 2012;395:012175.
37. Moita AS, Laurência C, Ramos JA, Prazeres DMF, Moreira ALN. Dynamics of droplets of biological fluids on smooth superhydrophobic surfaces under electrostatic actuation. J Bionic Eng. 2016;13(2):220–34.
38. Jedelsky J, Jicha M. Energy considerations in spraying process of a spill-return pressure-swirl atomizer. Appl Energy. 2014;132:485–95.
39. Manasse U, Wriedt T, Bauckhage K. Phase-Doppler sizing of optically absorbing liquid droplets: comparison between Mie theory and experiment. Part Spray Syst Charact. 1992;9(1–4):176–85.
40. Albrecht H-E, Borys M, Damaschke N, Tropea C. Laser Doppler and phase Doppler measurement techniques. Berlin: Springer; 2003.
41. Santolaya JL, García JA, Calvo E, Cerecedo LM. Effects of droplet collision phenomena on the development of pressure swirl sprays Int. J. Multiph. Flow. 2013;56:160–71.
42. Jedelsky J, Maly M, del Corral MO, Wigley G, Janackova L, Jicha M. Air–liquid interactions in a pressure-swirl spray. Int J Heat Mass Transf. 2018;121:788–804.
43. Maly M, Janackova L, Jedelsky J, Jicha M. Impact of alternative fuel rheology on spraying process of small pressure-swirl atomizer. AIP Conf Proc. 2016;1745:020031.
44. Lefebvre AH. The prediction of Sauter mean diameter for simplex pressure-swirl atomisers. At Spray Technol. 1987;3(1): 37–51.
45. Yule AJ, Dunkley JJ. Atomization of melts for powder production and spray deposition. Oxford: Clarendon Press; 1994.
46. Moita AS, Moreira ALN. Experimental study on fuel drop impacts onto rigid surfaces: morphological comparisons, disintegration limits and secondary atomization. Proc Combust Inst. 2007;31:2175–83.